HIGH-PERFORMANCE VISIBLY TRANSPARENT LUMINESCENT SOLAR CONCENTRATORS

By

Chenchen Yang

A DISSERTATION

Submitted to
Michigan State University
in partial fulfillment of the requirements
for the degree of

Materials Science and Engineering – Doctor of Philosophy

2022

ABSTRACT

HIGH-PERFORMANCE VISIBLY TRANSPARENT LUMINESCENT SOLAR CONCENTRATORS

By

Chenchen Yang

Visibly transparent solar harvesting surfaces provide an exciting new approach to harvesting solar energy around buildings and mobile electronics, effectively improving their energy utilization efficiency and autonomy while maintaining the aesthetics of the surfaces underneath. Transparent luminescent solar concentrators (TLSC), a key branch of transparent photovoltaic (TPV) technologies, selectively harvest the ultraviolet (UV) and near-infrared (NIR) portion of the incident solar irradiance, and optically transport the solar energy conversion to edge-mounted photovoltaic cells by waveguided photoluminescence. Due to the absence of electrodes, busbars, and collection grids over the solar harvesting area, the device structural simplicity enables these devices to achieve the highest levels of visible transparency and aesthetic quality.

In the first part of this work, the theoretical efficiency limits of TLSCs are derived and practical considerations are outlined to approach these limits. In deriving these limits, key material and engineering challenges are identified to fully optimize TLSCs. Guided by this simulation work as a roadmap, three classes of fluorescent organic molecules (cyanine dyes, non-fullerene acceptors and BODIPYs) are designed, synthesized, and modified as luminophores for NIR selective-harvesting TLSC to improve the corresponding photoluminescence quantum yields, enhance the NIR spectral coverage, and suppress the reabsorption losses. The power conversion efficiency (*PCE*) of the corresponding NIR TLSCs have been significantly improved from 0.4% to 1.5%. To maximize the light harvesting in the invisible portion of the solar spectrum for higher *PCE*s, massive-downshifting nanoclusters (NC) with surface ligand modification were synthesized

and combined with organic molecules into a dual-band TLSC system as UV and NIR selective harvesting luminophores, respectively. The resulting TLSC exhibits a record *PCE* over 3.0% with high visible transparency and is the first demonstration of this type of device which can effectively harvest both UV and NIR ranges selectively. Additionally, a practical method to seamlessly integrate these TLSCs onto arbitrary surfaces is developed to expand future deployment. Finally, standard protocols for assessing, characterizing, and reporting both the photovoltaic performance and aesthetic quality of TPVs and LSCs are also described. Collectively, these efforts highlight the promising potential of the TLSC technology for widespread adoption, effectively supplying the ever-growing energy demand on-site.

Copyright by CHENCHEN YANG 2022

ACKNOWLEDGEMENTS

There are many individuals to whom I would like to express my sincere gratitude throughout my doctoral program. First, I want to thank my academic advisor, Dr. Lunt, who offered me the opportunity to work in the Molecular and Organic Excitonics (MOE) Lab. I have gained incredible knowledge and extensive experience from your inspiration, encouragement, and guidance during my graduate study at MSU. Thank you, Dr. Lunt, for everything. I also want to thank my committee members Dr. Morelli, Dr. Lai, and Dr. Hogan for their valuable feedback on my thesis.

I am grateful to my fellow graduate students and post-docs in the MOE Lab: Peggy, thank you for being one of my best friends, your passionate attitude for both work and life is always remarkable, and I will always appreciate our friendship; Chris Traverse, you are a wonderful teammate to work with, your knack for troubleshooting and maintaining laboratory instruments and equipment is truly amazing; Paddy, thanks for helping with my nanocluster synthesis, we have also built up our friendship during the collaboration; Pei, you are calm and optimistic all the time, and I enjoyed our chats and meals together, thanks for being a good companion in the lab; Alex, an enthusiastic photographer and biker, I really enjoyed our collaboration on all the 3D printing designs and waveguide paintings together; Matt, we have worked on many projects together, many of which would not have been published without your valuable input; Chris Herrera and Isaac, I really appreciate our Zoom chats after the group meeting every week, which alleviates my pressure and loneliness during this pandemic time; Dianyi, we have also collaborated on many projects during your postdoctoral research here, and I loved coming to your apartment for food with your lovely family, thank you for being the paradigm of a good researcher for me.

I also gratefully acknowledge our collaborators: Dr. Sophia Lunt, Hyllana and Deanna from the Department of Biochemistry and Molecular Biology; Dr. Borhan, Dr. Levine, Wei, Jun, Mehdi, Aria, Wei-Tao and Fangchun from the Department of Chemistry; Dr. Anthony from the Department of Mechanical Engineering; Dr. Runkle from the Department of Horticulture; Per, Mike, and Brian from the Composite Materials and Structure Center; Scott from the Department of Chemistry Glass Shop; Rob and Tom from the Department of Physics and Astronomy Machine Shop; Tony from the Mass Spectrometry Facility. I also appreciate the support and help from our CHEMS office, many thanks to Jennifer, Nikki, Tiffany, Jessica, Kim, Brad, Heather, and Donna; and I want to thank Dr. Katy Colbry from the MSU College of Engineering for her help all the time.

I also want to thank my friends around MSU. I have so many fond memories with you guys: Hank, Xing, Junchao, Yubo, Xinting, Zhongyu, Zeyang, Ruiqiong, Yang, Yuelin, Chuanpeng, Yaozhong, Xiaolu, Alice, Chi, Bowen and Tianjiao. Thanks for your companionship, it made my graduate school life colorful and joyful.

Finally, acknowledgments are not complete without thanking my beloved family. My parents always support me with their consistent encouragement through the highs and lows in my graduate study at MSU. Thank you for your love and care. This thesis is dedicated to you.

TABLE OF CONTENTS

LIST OF TABLES	ix
LIST OF FIGURES	X
KEY TO SYMBOLS AND ABBREVIATIONS	XV
Chapter 1 Introduction to Molecular and Organic Excitonic Photovoltaics	1
1.1 Overview of Semiconductor Physics	2
1.2 Working Principles of Solar Cells	
1.3 Molecular and Organic Excitonic Semiconductors	9
1.4 Incident Solar Spectrum	
1.5 Wavelength-Selectivity and Shockley-Queisser Limits	14
Chapter 2 Introduction to Visibly Transparent Luminescent Solar Concentrators	20
2.1 Working Principles of Luminescent Solar Concentrators	20
2.2 Theoretical Efficiency Limits of Transparent Luminescent Solar Concentrators	24
2.3 Efficiency Limits of Transparent Luminescent Solar Concentrators with Finite Width	ı and
Stokes Shift Emitters	30
2.4 Practical Efficiency Limits of Transparent Luminescent Solar Concentrators	31
2.5 Practical Consideration for Scaling of Transparent Luminescent Solar Concentrators	32
2.6 Photoluminescence Mechanisms in Luminescent Solar Concentrators	34
2.7 Luminophore Material Candidates for Luminescent Solar Concentrators	36
Chapter 3 Standard Characterization Protocols for Transparent Photovoltaics	42
3.1 Transparent Photovoltaic Performance Characterization	42
3.2 Transmittance, Reflectance and Absorptance Spectra Measurements	45
3.3 Figures of Merit for Visible Transparency and Aesthetic Quality	50
3.4 Quantitative Assessment of TPV Aesthetics	57
3.5 Measurement Validation	58
3.6 Summary	60
Chapter 4 Standard Characterization Protocols for Luminescent Solar Concentrators	s 61
4.1 Photophysical Properties Measurements	
4.2 <i>J-V</i> Characteristics of LSC/TLSC Systems	
4.3 EQE_{LSC} Measurement and Matching Integrated J_{SC}	
4.4 Position-dependent EQE_{LSC} for Reabsorption Loss Analysis	
4.5 Figures of Merit for Aesthetic Quality of LSCs	
4.6 Measurement Validation, Data Completeness and Self-Consistency	
4.7 Detailed Mathematical Description of LSC Performance Parameters	
4.8 Summary	
	00
Chapter 5 Comprehensive Analysis of Transparent, Semitransparent, and Colorful Luminescent Solar Concentrator Aesthetics	84

5.1 Visual Impact Resulted from Escaped Photoluminescence	84
5.2 Optical Model	86
5.3 Results	
5.4 Discussion	108
5.5 Summary	
Chapter 6 Integration of Luminescent Solar Concentrators onto Arbitrary Surfaces	113
6.1 Introduction	
6.2 Experimental Section	
6.3 Results	
6.4 Discussion	
6.5 Summary	
Chapter 7 Impact of Stokes Shift on the Performance of Near-Infrared Harvesting	
Transparent Luminescent Solar Concentrators	
7.1 Introduction	
7.2 Experimental Section	130
7.3 Results	132
7.4 Discussion	139
7.5 Summary	145
Chapter 8 Near-Infrared Harvesting Transparent Luminescent Solar Concentrators by	
on Non-Fullerene Acceptors	
8.1 Introduction	
8.2 Experimental Section	
8.3 Results	
8.4 Discussion	
8.5 Summary	161
Chapter 9 Ultraviolet and Near-Infrared Selective Harvesting Dual-Band Transparen	
Luminescent Solar Concentrators	
9.1 Introduction	
9.2 Experimental Section	
9.3 Results	
9.4 Discussion	
9.5 Summary	197
Chapter 10 Future Outlook and Conclusions	
10.1 Future Outlook	198
10.2 Final Conclusions	206
APPENDICES	208
APPENDIX A Checklist for Luminescent Solar Concentrator Manuscripts	
APPENDIX B An Overview of Literature Reports for LSC/TLSC Devices	
RIRI IOCDAPHV	210

LIST OF TABLES

Table 2.1 Representative summary of the absorption λ_{max} , emission λ_{max} and $PLQY$ s of typical luminophores and dye emitters used in LSCs and TLSCs
Table 3.1 Photovoltaic parameters of an example TPV cell tested with different backdrops 44
Table 3.2 Summary of aesthetic quality parameters of various samples including commercial tinted glass (C-Glass)
Table 4.1 Comparison of photovoltaic parameters of the TLSC with and without mask 71
Table 4.2 Summary of aesthetic quality parameters of various samples
Table 7.1 Summary of the absorption λ_{max} , emission λ_{max} , Stokes shifts (<i>S</i>) and quantum yields (<i>PLQY</i> s) of Cy7-CA, Cy7-NEt ₂ -I and Cy7.5-NEt ₂ -I in DCM and polymer films
Table 7.2 Summary of photovoltaic parameters and overlap parameters
Table 8.1 Photovoltaic and aesthetic quality parameters of the TLSCs
Table 8.2 Wavelength selective absorption ratio, QY and $Int. J_{SC}$ comparison
Table 8.3 Summary of Photovoltaic parameters for TLSCs with different edge-mounted PV, <i>G</i> factor and luminophores as shown in Figure 8.5
Table 9.1 Photovoltaic and aesthetic quality parameters of the TLSCs
Table A.1 State-of-the-art LSC/TLSC work for reference

LIST OF FIGURES

Figure 1.1 Semiconductor energy band diagrams	5
Figure 1.2 Working principle of a photovoltaic device.	7
Figure 1.3 Energy level diagrams of a conjugated molecule and a D/A heterojunction	11
Figure 1.4 Incident AM 1.5G solar irradiance.	13
Figure 1.5 Visibly transparent photovoltaics realized by various approaches	16
Figure 1.6 Efficiency limits as a function of visible transparency.	17
Figure 2.1 Operating principle of transparent luminescent solar concentrators.	20
Figure 2.2 Component efficiencies in LSC operation.	22
Figure 2.3 Ideal absorption, emission spectra and corresponding SQ efficiency limits of TLS	
Figure 2.4 Ideal configurations of UV-only selective-harvesting TLSCs.	26
Figure 2.5 Ideal configurations of TLSCs with multiple waveguide components	28
Figure 2.6 Practical configuration of TLSCs with finite Stokes shift and emission width	30
Figure 2.7 Practical consideration for scaling of TLSCs.	33
Figure 2.8 Jablonski energy diagrams of various photoluminescence mechanisms utilized in design.	
Figure 2.9 Representative absorption and emission spectra (normalized) of typical emitters applied in LSCs and TLSCs	36
Figure 3.1 Standard characterization of TPV device photovoltaic performance	43
Figure 3.2 Schematic showing how to measure the transmittance spectra of TPV devices	46
Figure 3.3 Schematic showing how to measure the reflectance spectra of TPV devices by usidouble-beam method.	_
Figure 3.4 Transmittance spectra comparison.	49
Figure 3.5 Transmittance spectra for AVT calculation	51

Figure 3.6 Color rendering.	. 52
Figure 3.7 Exemplary commercial tinted glass samples.	. 55
Figure 3.8 Exemplary commercial tinted glass samples.	. 58
Figure 4.1 Photoluminescence spectrometer layout for <i>PLQY</i> measurement	. 62
Figure 4.2 Equivalent layouts for <i>J-V</i> measurement for a TLSC system.	. 66
Figure 4.3 Schematic protocols for LSC characterization.	. 67
Figure 4.4 Photographs of actual LSC device assembly and characterization.	. 69
Figure 4.5 LSC Photovoltaic performance.	. 70
Figure 4.6 Equivalent layouts for <i>EQE</i> measurement for a TLSC system	. 73
Figure 4.7 Visible transparency and aesthetic quality of TLSC systems.	. 76
Figure 4.8 TLSCs Photon balance check.	. 78
Figure 5.1 Schematic showing the impact of escaped photoluminescence on the aesthetics of L systems.	
Figure 5.2 A survey on 365 commercially available (grey dots) and top 50 mass-market (red dots) architectural glass products.	. 88
Figure 5.3 UV/VIS and VIS/NIR cutoffs determined by comprehensive consideration of all aesthetic quality parameters.	. 89
Figure 5.4 Idealized absorption and emission characteristics used in the optical model	. 90
Figure 5.5 Schematic showing multiple reflection and transmission events	. 91
Figure 5.6 Schematic showing the transmitted and reflected light (orange arrows) and the escaped photoluminescence (red arrows).	. 98
Figure 5.7 Visual impact of photoluminescence on aesthetic parameters of TLSCs on the transmitted side.	101
Figure 5.8 Visual impact of photoluminescence on aesthetic parameters of TLSCs on the reflected side.	103
Figure 5.9 The impact of escaped photoluminescence from up-conversion (UC) and quantum-cutting (QC) processes on the aesthetics on the transmitted side	

Figure 5.10 The impact of escaped photoluminescence from up-conversion (UC) and quantum cutting (QC) processes on the aesthetics on the reflected side	
Figure 5.11 The impact of escaped photoluminescence from DS processes of LSCs with purposeful coloration on the transmitted side.	106
Figure 5.12 The impact of escaped photoluminescence from DS processes of LSCs with purposeful coloration on the reflected side.	108
Figure 6.1 Conceptual schematic showing a TLSC integrated onto arbitrary surfaces	114
Figure 6.2 NIR luminophore utilized in this study.	118
Figure 6.3 Photovoltaic performance.	119
Figure 6.4 Normalized position-dependent <i>EQE_{LSC}</i> .	119
Figure 6.5 Transmittance spectrum and photon balance check.	121
Figure 6.6 Extracted and normalized peak EQE_{LSC} value as a function of distance (d)	123
Figure 6.7 Product of the reflection and trapping efficiencies as a function of refractive index waveguide.	
Figure 7.1 Normalized absorption and emission spectra of cyanine dyes	132
Figure 7.2 Molecular structure, HOMO and LUMO electronic orbitals	133
Figure 7.3 Photographs of the TLSCs	133
Figure 7.4 Photovoltaic performance of the TLSCs.	136
Figure 7.5 Photon balance check.	137
Figure 7.6 Position-dependent <i>EQE_{LSC}</i> spectra.	138
Figure 7.7 Overlap integral and scalability prediction	142
Figure 8.1 Non-fullerene acceptor utilized in this study	147
Figure 8.2 Optical Properties of the NFA utilized in this study.	149
Figure 8.3 Photovoltaic performance of CO _i 8DFIC TLSCs	152
Figure 8.4 Absolute absorption and <i>EQE_{LSC}</i> spectra for TLSCs.	153

Figure 8.5 EQE_{LSC} and the averaged integrated J_{SC} comparison of TLSCs with different edge mounted PVs, G factors and luminophores.	
Figure 8.6 Photon balance check.	157
Figure 8.7 CIELAB color coordinates, LUEs and TLSCs with GaAs edge-mounted PV	158
Figure 8.8 Photographs of all the TLSC devices.	158
Figure 8.9 TLSC with a similar NFA IEICO-4F.	160
Figure 9.1 General synthesis of CO _i 8DFIC.	166
Figure 9.2 General synthesis of BODIPY	166
Figure 9.3 Working Principle and Luminophores of the Dual-band TLSCs	169
Figure 9.4 X-ray Diffraction pattern of Cs ₂ Mo6I ₁₄ nanocluster powder	170
Figure 9.5 Mass spectrometry patterns of various nanoclusters.	171
Figure 9.6 Photovoltaic Performance of the Dual-band TLSCs.	174
Figure 9.7 Position-dependent EQE_{LSC} spectra.	177
Figure 9.8 Single-pane NIR-only TLSCs.	179
Figure 9.9 Optical simulation for TLSC scalability	180
Figure 9.10 Optical simulation for TLSC scalability	181
Figure 9.11 Impact of optical isolation on the performance of dual-band TLSCs	182
Figure 9.12 Aesthetic Quality of the Dual-band TLSCs	183
Figure 9.13 Photon balance check.	184
Figure 9.14 Comprehensive Analysis of Photovoltaic Performance and Aesthetic Quality	186
Figure 9.15 CO _i 8DFIC+NC and BODIPY+NC dual-band TLSCs.	191
Figure 9.16 Photostability study of dual-band TLSCs	193
Figure 9.17 Photostability study of dual-band TLSCs	194
Figure 9.18 Photostability test setup.	195

Figure 10.1 Mechanically flexible TLSC prototype.	199
Figure 10.2 TLSCs with Micro-segmented PV, greenhouse application and photon management of the property of the	
Figure 10.3 TLSCs performance enhancement via spectral conversion approaches	203
Figure 10.4 Photodynamic therapy for on-site cancer curing	205

KEY TO SYMBOLS AND ABBREVIATIONS

 $A(\lambda)$ Absolute optical absorptance spectrum

 A_1 Single-pass absorptance within the waveguide medium

 A_{Active} Active area of a solar cell which receive the incident solar power

AC Alternating current

 A_{Edge} Luminescent solar concentrator total waveguide edge area

 A_{LSC} Luminescent solar concentrator total waveguide front surface area

AM 1.5G Air-mass 1.5 global solar spectrum

AOI Angle of incidence

AVLH Average visible luminescent haze

AVR Average visible reflectance

AVT Average visible transmittance

BE Binding energy

BIPV Building-integrated photovoltaic

BODIPY Boron-dipyrromethene

C Concentration

CCT Correlated color temperature

CdSe/CdS Cadmium selenide/cadmium sulfide

CIELAB International Commission on Illumination (CIE) color space defined by

lightness (L) and chromaticity coordinates (a^*, b^*)

CIELUE International Commission on Illumination color space defined by

lightness (L) and chromaticity coordinates (u, v)

CIEXYZ International Commission on Illumination color space defined by

chromaticity coordinates (X, Y, Z)

CIGS Copper indium gallium selenide

CO_i8DFIC Also known as NFA146, PCE146, O6T-4F, a commonly used non-

fullerene acceptor used in organic photovoltaics

CRI Color rendering index

Cyanine, an organic dye category with polymethine structures

d The centerline distance between the excitation beam and the edge-

mounted solar cell in luminescent solar concentrator characterization

D/A Donor/acceptor combination or heterojunction

D65 A commonly used standard illuminant defined by the CIE

DC Direct current

DCM Dichloromethane

DS Down-shifting photoluminescence mechanism

DSSC Dye-sensitized solar cell

e Elementary charge, $\approx 1.60217662 \times 10^{-19}$ C (Coulombs)

 E_C Conduction band

 E_V Valance band

 E_{FI} Fermi level of intrinsic semiconductors

 E_{FN} Fermi level of N-type semiconductors

 E_{FP} Fermi level of P-type semiconductors

 E_g Bandgap energy of semiconductors

 $EQE_{LSC}(\lambda)$ External quantum efficiency spectrum of luminescent solar concentrators

 $EQE_{PV}(\lambda)$ External quantum efficiency spectrum of the edge-mounted solar cell

eV Electron-volt, $\approx 1.60217662 \times 10^{-19}$ J (Joules)

f(E) Fermi-Dirac function

FF Fill factor of a solar cell

FRET Förster resonance energy transfer

Geometric factor, used as a correction factor in EQE_{LSC} measurement

GaAs Gallium arsenide

Ge Germanium

h Planck's constant, 6.626×10^{-34} m² kg/s

 \hbar Modified Planck's constant, $\hbar = h/2\pi \approx 1.05 \times 10{\text{-}}34 \text{ m}^2 \text{ kg/s}$

HOMO Highest occupied molecular orbital

IEICO-4F Another commonly used non-fullerene acceptor in OPVs

IGU Insulated glass units

IPCE Internal power conversion efficiency, equivalent to *EQE*

IQE Internal quantum efficiency

IR Infrared

I_{SC} Short-circuit current

J Current density

 J_0 Reverse saturation current density

 J_{Ph} Photogenerated current density

 J_{SC}^{Int} Integrated short-circuit current density

J-V Current density-voltage characteristic

 k_B Boltzmann constant, $\approx 1.38064852 \times 10\text{-}23 \text{ m}^2 \text{ kg s}^{-2} \text{ K}^{-1}$

L Luminescent solar concentrator waveguide length

LSC Luminescent solar concentrator

LUE Light utilization efficiency

LUMO Lowest unoccupied molecular orbital

m Multiplication factor of photoluminescence mechanisms

 m_e^* Effective mass of the electron

MEG Multi-exciton generation

MF Spectral mismatch factor

n Ideality factor in Shockley equation

NC Nanocluster

n_{cladding} Refractive index of LSC cladding

NFA Non-fullerene acceptor

NIR Near infrared

 n_{Sub} Refractive index of the waveguiding substrate

OI Overlap Integral

OPV Organic photovoltaic

 P_0 Incident solar power density

PBMMA Polybutylmethylmethacrylate

PCE Power conversion efficiency

PDT Photodynamic therapy

PKSC Perovskite solar cell

PL Photoluminescence

PLQY Photoluminescence quantum yield

 P_{max} Maximum output power density of a solar cell

PV Photovoltaic

QC Quantum-cutting

QD Quantum dot

QY Quantum yield

 $R(\lambda)$ Reflectance spectrum

 R_S Series resistance in Shockley equation

 R_{Sh} Shunt resistance in Shockley equation

 R_f Front surface reflectance

S₀ Ground state in Jablonski energy diagrams

S₁ Excited singlet molecular orbital

SF Singlet fission

Si Silicon

SQ Shockley-Queisser

SS Stokes shift

SWCNT Single-walled carbon nanotube

 $S(\lambda)$ Output spectrum of the solar simulator

T Temperature, in the unit of Kelvin (K)

t Thickness

 $T(\lambda)$ Transmittance spectrum

T₁ Excited triplet molecular orbital

TBA Tetrabutylammonium

TLSC Transparent luminescent solar concentrator

TPU Thermoplastic polyurethane

TPV Transparent photovoltaic

TTA-UC Triplet-triplet annihilation up-conversion

UV Ultraviolet

 $V(\lambda)$ Photopic response of the human eye

Voc Open-circuit voltage

W Emission peak width

XRD X-ray diffraction

 ε_0 Dielectric constant of free space

Relative dielectric constant ε_r Solar spectrum absorption efficiency η_{Abs} Overall power conversion efficiency of the LSC-PV system η_{LSC} Optical efficiency of the LSC η_{Opt} Photoluminescence efficiency of the luminophore in the matrix material η_{PL} Efficiency of the edge-mounted PV cell under photoluminescence η_{PV}^* Efficiency of suppressing reabsorption loss η_{RA} Reabsorption probability in LSC scalability model η_{RAP} Waveguide light trapping efficiency η_{Trap} Critical angle determining the emission cone in LSC waveguide θ_C

Wavelength of light

λ

Chapter 1 Introduction to Molecular and Organic Excitonic Photovoltaics

Harvesting incident solar irradiance to generate electric power provide a viable and sustainable approach to curb the world's ever-growing energy demand.^{1,2} Deployment of conventional photovoltaic (PV) modules in solar farms or on building rooftops has experienced rapid growth in the last decade. To further fulfill the potential of solar energy, one of the most effective strategies is to seamlessly integrate PV devices onto arbitrary surfaces of the built environment and facilities, converting these surfaces into ubiquitous power-generating sources or autonomous units.^{3,4} Consequently, such a deployment strategy simultaneously enables on-site renewable energy generation and reduces electricity loss in transmission and distribution, dramatically improving the overall energy utilization efficiency. For these ubiquitous deployment opportunities, aesthetic quality is often equality important as power conversion efficiency (*PCE*) since it determines the threshold for PVs to be deployed in practical applications (e.g., glazing systems, mobile surfaces, etc.). Visibly transparent photovoltaics (TPV) predominately harvest the ultraviolet (UV)⁵⁻⁷ and near-infrared (NIR)^{4,8} portion of the incident solar irradiance, and allow the visible (VIS) light to pass though, minimizing the visual impact and enabling adoption in areas inaccessible with conventional solar technologies. 2,3,9,10

This thesis comprehensively covers various aspects of the visible transparent solar concentrator (TLSC, a key TPV technology) development, including background knowledge, reporting standards and performance improvement. In Chapter 1, an overview of semiconductor physics and background knowledge of photovoltaic technologies is provided, and the comparison between opaque photovoltaics and transparent photovoltaics is described. In Chapter 2, the working principles of luminescent solar concentrators (LSC) and are introduced, the theoretical and practical power conversion efficiency (*PCE*) limits of LSC and transparent luminescent solar

concentrators (TLSC) are investigated, photoluminescence mechanisms applied in LSC design are reviewed, and luminophore material candidates are surveyed. In Chapter 3, key performance metrics of TPVs are defined, and exemplary TPV devices are comparatively measured to highlight the standardized characterization protocols, a method to check TPV data consistency is also included. In Chapter 4, key performance metrics of TLSCs are defined, and exemplary TLSCs are comparatively measured in both erroneous and correct ways to highlight the best and most accurate characterization methods. In Chapter 5, the impact of the escaped photoluminescence on the aesthetics of LSCs are quantitatively and systematically analyzed. Chapter 6 introduces an approach to seamlessly integrate TLSC devices onto arbitrary surfaces while maintaining the waveguide functionality of the TLSC. In Chapter 7, modified cyanine dyes are demonstrated and incorporated into NIR selective-harvesting TLSCs with improved photovoltaic performance. In Chapter 8, to enhance the utilization of the NIR spectrum, non-fullerene acceptors are incorporated into the NIR selective-harvesting TLSCs, further improving the corresponding photovoltaic performance. Chapter 9 describes the development of combined UV and NIR dual-band selectiveharvesting TLSC systems. The last chapter, Chapter 10, provides an outlook on TLSC devices for future development and a comprehensive summary of this work.

1.1 Overview of Semiconductor Physics

As the interatomic distance decreases in an ensemble of atoms, the electronic wave functions of each atom start to overlap and interact with each other. This interaction or perturbation results in the splitting of the discrete quantized energies and the formation of energy band structure. As a result, electronic materials can be categorized as conductors, insulators, and semiconductors

according to their electrical conduction and energy band structures. Conductors exhibit high electrical conductivity due to the corresponding conduction band partially filled with delocalized electrons. Insulators and semiconductors share similar energy band structures: the valance band is fully filled with electrons while the conduction band is completely empty. The energy difference between the bottom of the conduction band (E_C) and the top of the valance band (E_V) is known as the bandgap energy (E_g), which is also called forbidden energy band. Typically, an insulator exhibits E_g values over 3 eV where it becomes non-conductive, while the E_g value of a semiconductor is between $k_B T$ (e.g., 0.0258 eV, k_B is the Boltzmann constant, $\approx 1.38064852 \times 10^{-23} \text{ m}^2 \text{ kg s}^{-2} \text{ K}^{-1}$, and T is the temperature, at room temperature, T = 300 K) and $\sim 3.0 \text{ eV}$.

When a semiconductor is illuminated by incident light beam, photons with energy lower than E_g are transmitted through the semiconductor, whereas photons with energy higher than the E_g value can be absorbed by the semiconductor. The absorbed energy excites an electron from valance band to the conduction band, leaving behind a positively charged vacancy, i.e., a hole, in the valance band. An electron-hole pair is therefore formed and bound by coulombic forces. Similar to the hydrogen atom, the Bohr model is used to estimate the binding energy (BE) of the electron-hole pair:

$$BE = \frac{e^4 m_e^*}{2\varepsilon_0^2 \varepsilon_r^2 \hbar^2} \tag{1.1}$$

where \hbar is the reduced Planck constant ($\hbar = h/2\pi$), m_e^* is the effective mass of the electron, ε_0 is the dielectric constant of free space and ε_r is the relative dielectric constant of the semiconductor materials. Therefore, the BE is proportional to $1/\varepsilon_r^2$. Typically, ε_r values of inorganic semiconductors are relatively large, e.g., for Si, the $\varepsilon_r(\text{Si})$ is ~11.7, and the corresponding BE(Si) value is 14.7 meV, therefore, the electron-hole pair formed in inorganic semiconductors can be

readily dissociated at room temperature (T = 300 K, $k_BT = 25.7 \text{ meV}$, and k_B is the Boltzmann constant). As a result, electrons and holes can be considered free charge carriers in many inorganic semiconductors at room temperature upon a photo-excitation process.

As fermions, electrons and holes in semiconductors follow Fermi-Dirac statistics, the probability of finding an electron in a state with energy (E) can be calculated by Fermi-Dirac function:

$$f(E) = \frac{1}{1 + \exp\left(\frac{E - E_F}{k_B T}\right)}$$
(1.2)

where E_F is a constant called the Fermi energy, or Fermi level, which is the highest energy level an electron can occupy at the absolute zero temperature (T = 0 K).

A pure semiconductor crystal is called an intrinsic semiconductor, and the corresponding Fermi level (E_{FI}) is close to the middle of the energy gap ($E_{FI} \approx E_g/2$) as shown in **Figure 1.1**A. The electronic properties of semiconductor materials can be modified by doping process, and the doped semiconductors are called extrinsic semiconductors: by doping impurities into intrinsic semiconductor to donate excess electrons to the conduction band, the doped extrinsic semiconductor is then called N-type, and the Fermi level of N-type is above the mid-gap ($E_{FN} > E_{FI}$); similarly, by doping impurities to donate excess holes to the valence band, the doped extrinsic semiconductor is then called P-type, and the Fermi level of P-type is below the mid-gap ($E_{FP} < E_{FI}$).

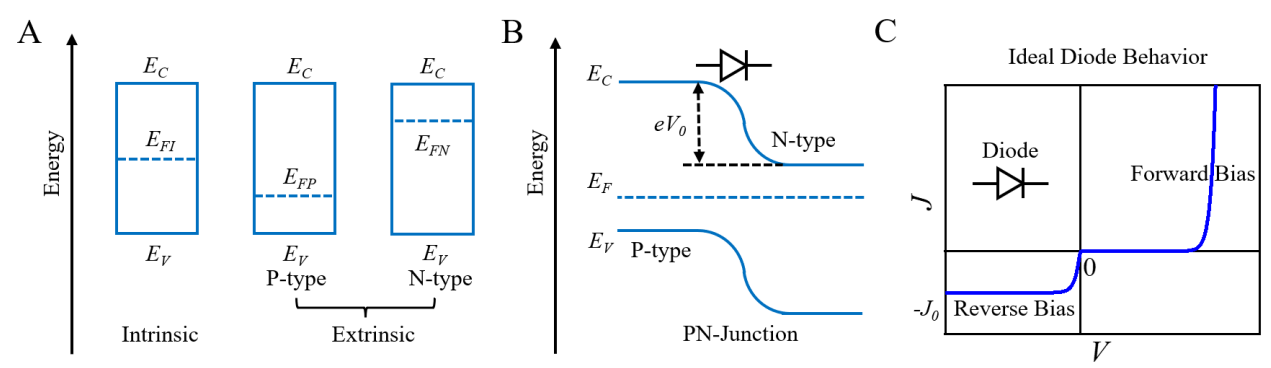


Figure 1.1 Semiconductor energy band diagrams.

Energy band diagrams for (A) intrinsic and extrinsic (P-type and N-type) semiconductors. (B) Energy band diagram for a P-N junction at equilibrium, a potential energy barrier, eV_0 , is formed at equilibrium. (C) Current density (J) - voltage (V) characteristic of an ideal P-N junction (i.e., an ideal diode), the scale of Y-axis is adjusted under reverse bias (V < 0) to illustrate the reverse saturated current density (J_0) for clarity.

A P-N junction formed by combing a N-type semiconductor and a P-type semiconductor is called a P-N junction or a diode. Once the P-N junction is formed, excess carriers (electrons and holes) from the respective sides will diffuse into the others, resulting in a space charge layer, i.e., depletion region, or transition region. An equilibrium state is reached when the Fermi level is constant across the junction as shown in Figure 1.1B, and the drift currents driven by the built-in electric field is finally balanced by the diffusion currents caused by carrier concentration gradients. Eventually, a potential barrier is formed at the P-N junction (eV_0) and permits current flow only in forward direction, and Shockley equation (i.e., diode equation) is used to describe this ideal diode behavior of a P-N junction:

$$J = J_0 \left[\exp\left(\frac{eV}{k_B T}\right) - 1 \right] \tag{1.3}$$

where J_0 is the reverse saturation current density, J is the current density, V is the voltage applied on the P-N junction. According to Equation 1.3, when a P-N junction is under forward bias (V > 0), the potential barrier is reduced by the amount of applied bias, V. As a result, the electrons at E_C and the holes at E_V can readily overcome the reduced potential barrier, $e(V_0 - V)$, and diffuse

to the other side, respectively. Thus, the overall current density increases exponentially as forward bias increases. On the contrary, when a P-N junction is under reverse bias (V < 0), the corresponding potential barrier is increased by the amount of (-V), and the first term quickly become negligible compared to the second term as negative bias continue to decrease in Equation 1.3, which results in the overall reverse current density, $J \rightarrow -J_0$ as shown in Figure 1.1C. This is also the reason why J_0 is called the reverse saturation current density. This unidirectional rectifying behavior is the basic characteristic of a diode.

1.2 Working Principles of Solar Cells

The equivalent circuit of a solar cell device is shown in **Figure 1.2**A, a current source and a diode are connected in parallel to supply the external load. A modified Shockley equation is used to describe the overall current density (J) – voltage (V) characteristic of this circuit:

$$J = J_0 \left\{ \exp \left[\frac{e(V - AJR_S)}{nk_B T} \right] - 1 \right\} + \frac{V - AJR_S}{AR_{Sh}} - J_{Ph}$$
 (1.3)

where n is the ideality factor of the diode, A is the active area of the solar cell, R_S is the series resistance, R_{Sh} is the shunt resistance, and J_{Ph} is photogenerated current density. Notably, the reverse saturation current density, J_0 , is strongly temperature-dependent, which originates from the thermal generation of minority carriers in the neutral regions diffusing into the depletion region and the thermal generation of electron-hole pairs in the depletion region. J_0 increases as T increases, a common rule of thumb is that J_0 doubles for every 10 K rise in temperature. The ideality factor, n (typically between 1 and 2), is a measure of how closely the solar cell under dark condition behaves as an ideal diode: n = 1 when the current is due to minority carrier diffusion in the neutral

regions and there is no recombination within the depletion region, whereas n = 2 when the recombination in the depletion region dominates the current. For a good solar cell, the corresponding n should be close to 1, which mimics an ideal diode behavior in the dark; J_0 should be small due to minimized carrier recombination within the device, resulting a high output voltage; the R_S should be small to minimize the energy loss; and the R_{Sh} should be large so that the photogenerated charge carriers (electrons and holes) can be effectively collected by the respective electrodes with minimum recombination, maximizing the output J_{Ph} .

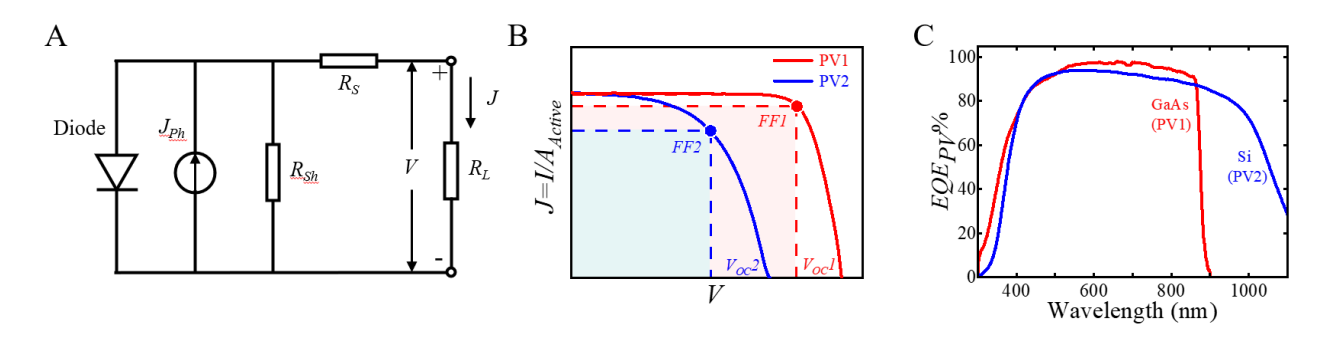


Figure 1.2 Working principle of a photovoltaic device.

(A) The equivalent circuit of a solar cell device. (B) Exemplary current density (J) - voltage (V) characteristic curves of two solar cells with different bandgap. (C) The corresponding external quantum efficiency spectra (EQE_{PV}) of a silicon and GaAs PV cells.

The first key data for reporting a PV system is the measurement of the corresponding J-V characteristics under standard illumination (incident AM 1.5G solar spectrum, and it will be discussed in a latter section), which are necessary to report the corresponding power conversion efficiency (PCE) of the device. Three key photovoltaic performance parameters can be extracted from the J-V curve: short-circuit current density (J_{SC}), which equals the current (I_{SC}) value acquired at zero voltage bias (V = 0) divided by $A = I_{SC}/A$. V_{OC} is the voltage at open-circuit condition (I = 0). The maximum output power (I_{Max}) is the maximum product value of the (I_{SC}) represents the

"squareness" of the J-V curve. Therefore, the PCE is given as the ratio of maximum output power density ($P_{max,out}$) to the incident power density:

$$PCE = \frac{P_{max,out}}{P_0} = \frac{V_{OC} \cdot J_{SC} \cdot FF}{P_0}$$
 (1.4)

The *J-V* curves of two exemplary PV systems (PV1 vs. PV2) are plotted in Figure 1.2B: any *PCE* difference of these PV systems can result from the differences in the corresponding V_{OC} , FF and J_{SC} .

The second key data for the characterization of any PV system is the reporting of the corresponding external quantum efficiency (EQE_{PV}) or internal power conversion efficiency (IPCE) spectrum. The EQE_{PV} is defined as the ratio of the number of photogenerated electrons collected at the electrode to the number of incident photons at each wavelength. The exemplary EQE_{PV} spectra of a silicon and a GaAs PV cells are shown in Figure 1.2C. EQE_{PV} is used to calculate any spectral mismatch factors (MF), which ensures the equivalent 1 sun intensity applied to the J-V measurement of the test cells for a fair comparison between different reports (i.e., different test cell/reference cell combinations and various solar simulators with different output spectra). The MF can be calculated as:

$$MF = \frac{\int AM \ 1.5G(\lambda) \cdot EQE_{Ref}(\lambda)d\lambda}{\int S(\lambda) \cdot EQE_{Ref}(\lambda)d\lambda} \times \frac{\int S(\lambda) \cdot EQE_{PV}(\lambda)d\lambda}{\int AM \ 1.5G(\lambda) \cdot EQE_{PV}(\lambda)d\lambda}$$
(1.5)

where $AM\ 1.5G(\lambda)$ is the photon flux spectrum, $S(\lambda)$ is the output spectrum of the solar simulator, $EQE_{Ref}(\lambda)$ is the external quantum efficiency spectrum of the reference cell, and $EQE_{PV}(\lambda)$ is the external quantum efficiency spectrum of the test cell under investigation. It is necessary to calculate the corresponding MF value to properly set the testing lamp intensities prior to J-V

measurements or to correctly report the illumination conditions. Therefore, a complete PV performance report should also include the corresponding *MF*.

The internal quantum efficiency (IQE_{PV}) is the ratio of the number of electrons collected by the electrode to the number of photons absorbed by the PV cell at each wavelength. Thus, these two quantum efficiencies are related through:

$$EQE_{PV}(\lambda) = \eta_{Abs}(\lambda) \cdot IQE_{PV}(\lambda) \tag{1.6}$$

where η_{Abs} is the PV absorption efficiency at each wavelength. The integrated photocurrent density (J_{SC}^{Int}) can be calculated as:

$$J_{SC}^{Int} = e \cdot \int EQE_{PV}(\lambda) \cdot AM1.5G(\lambda)d\lambda \tag{1.7}$$

For the same PV device, this integrated current density value should match the J_{SC} extracted from the corresponding J-V characteristic, which is the most important consistent check in PV characterization.^{3,11,12} The details of PV characterization protocols will be covered in the later chapters.

1.3 Molecular and Organic Excitonic Semiconductors

Organic materials are carbon-based compound, which may also contain other atoms such as hydrogen, nitrogen, oxygen, sulfur, phosphorous, fluoride or even metals. Depending on the molecular weight and complexity of the organic molecules, organic materials can be categorized into three classes: small molecules, polymers, and biological molecules. Small molecules typically have molecular weight less than 1000 and well-defined molecular structures; polymers are long-

chain large molecules consisting of undefined numbers of repeating units with corresponding molecular weight spanning from few thousands to a million; and biological molecules, such as DNAs and RNAs, usually exhibit the highest molecular complexity due to their biological origins and functionalities.

The term organic semiconductors applied in electronic and optoelectronic applications typically refer to small molecules and polymers with π -conjugated molecular structures. A carbon atom has six electrons outside of the nucleus. In ground state, the electronic configuration of a carbon atom is 1s²2s²2p²: the two 1s electrons are the core electrons and do not participate in chemical bonding. The fully occupied 2s orbital can mix with the 2p orbitals to form spⁿ hybridized orbitals: e.g., sp¹, sp² and sp³ orbitals, depending on the number of p orbitals participating into hybridization with 2s orbital. These hybridized orbitals can therefore form covalent bonds with other atoms. Figure 1.3 shows the energy level diagram of the simplest conjugated molecule, ethane, as a typical example of the π -conjugated system: each carbon atom in ethane is sp² hybridized, resulting in three identical sp² orbital and one p_z orbital. As the atomic distance of two carbon atoms decreases, two sp² orbitals from each carbon atom form a σ -bond and the other four left sp² orbitals form four σ -bonds with the four s orbitals of four hydrogen atoms. Additionally, a π -bond is formed based on the two p_z orbitals. The interatomic interaction leads to the splitting of both the σ -bond and the π -bond into bonding and anti-bonding molecular orbitals, and the strength of π -bond is weaker than that of the σ -bond, due to less overlap between the two p_z orbitals. As the energy levels shown in Figure 1.3A, which shows the sequence: $E(\sigma^*) > E(\pi^*) > E(\pi) > E(\sigma)$. The smallest electronic transition in conjugated molecules is the π - π * transition due to the lower energetic separation, therefore, the π molecular orbital is called the highest occupied molecular orbital (HOMO) and the π^* molecular orbital is called the lowest unoccupied molecular orbital

(LUMO). Compared to inorganic semiconductors in discussed in the prior section, the HOMO and LUMO in organic semiconductors are analogous to the VB and CB in inorganic semiconductors, electron donor and acceptor correspond to P-type and N-type semiconductors, respectively. Such nomenclature differences originate from the different mechanisms forming the band structures in organic and inorganic semiconductors, respectively. Similarly, the energy difference between HOMO and LUMO is defined as the energy bandgap (E_g) of organic semiconductors. The optical and electrical properties of organic semiconductors can be finely tuned by designing and modifying the corresponding molecular structures, conjugation, and crystallinity. Small molecule and polymer organic semiconductors have alternating single (σ -bond) and double bonds (π -bond) in their corresponding molecular structures, which are also called π -conjugated systems.

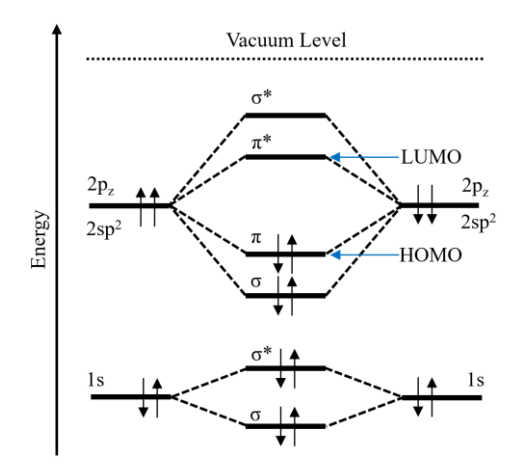


Figure 1.3 Energy level diagrams of a conjugated molecule and a D/A heterojunction. The π molecular orbital is called the highest occupied molecular orbital (HOMO) and the π^* molecular orbital is called the lowest unoccupied molecular orbital (LUMO), respectively.

Similar to inorganic semiconductors, when organic semiconductor molecules are illuminated by incident light beam, photons with energy higher than the E_g value can be absorbed by these molecules. The absorbed energy can excite an organic semiconductor molecule and generates a coulombically bound electron-hole pair. This electrically neutral quasiparticle formed in organic semiconductors is called an exciton.

As shown in Equation 1.1, the *BE* of electron-hole pair is proportional to $1/\varepsilon_r^2$. In contrast to relatively large ε_r values in their inorganic counterparts, the ε_r values of organic semiconductor is relatively small (~2-4), and therefore the *BE*s of organic semiconductors typically range from ~0.1 to 2 eV and much larger than $k_BT \approx 25.7$ meV. Therefore, in contrast to the electron-hole pair formed in inorganic semiconductor, an exciton cannot be readily dissociated into free carriers after generation at room temperature.

There are two types of motion mechanisms of generated excitons within the organic semiconductors: Förster resonant energy transfer (FRET) and Dexter energy transfer. The FRET process can occur at longer distances, typically in the range of 10 to 200 Å; and the Dexter process occurs typically at few Å length scale via direct orbital overlap. Health and have been widely utilized in organic electronics design, such as organic photovoltaics, organic light emitting diodes, and luminescent solar concentrators, etc.

Charge transport is another important property in organic optoelectronic devices. The position of the alternating single and double bonds can be switched, resulting in a resonant structure. Electrons in π -orbitals become delocalized, enabling intramolecular and intermolecular charge transfer.

1.4 Incident Solar Spectrum

Photovoltaics function under the illumination of solar irradiance. Hence, to optimize and modify solar devices for best output power and functionalities, it is important to understand the incident solar spectrum. In our solar system, the Sun is the only star which isotropically emits electromagnetic radiation into the space. The Sun, with an effective surface temperature of ~5800

K, can be considered as a black body radiator. The Earth is surrounded by an atmosphere which attenuates the overall intensity of the incident solar irradiance. The air mass coefficient is defined as the ratio of the direct optical path through the Earth's atmosphere to the optical path length at the zenith angle (AM 1 at 0°) as shown in **Figure 1.4**A. Among all the air mass coefficient cases, AM 0 represent the solar irradiance outside the atmosphere at zenith angle, and solar cells used in outer space, for example, the communication satellites are characterized by using AM 0; AM 1 represents the solar irradiance after travelling through the atmosphere to the sea level at zenith angle, which is useful to characterize solar cells working in equatorial regions; AM 1.5G has been widely adopted as the test standard in PV characterization since the 1970s, and it represents the terrestrial solar irradiation at mid-latitudes where the world's major population centers locate, the power intensity of AM 1.5G is 1000 Wm⁻² or 100 mWcm⁻² (i.e., 1 sun intensity).

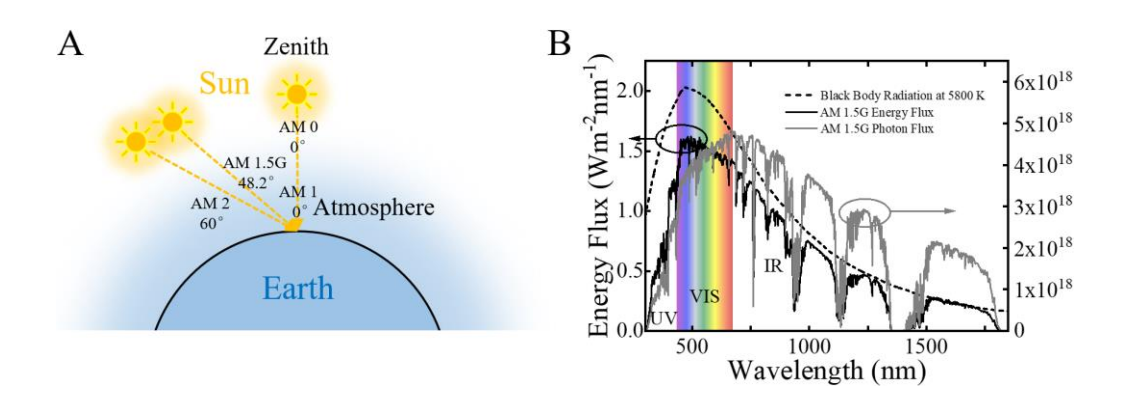


Figure 1.4 Incident AM 1.5G solar irradiance.

(A) Schematic showing the definitions of various air mass coefficients based on zenith angles. (B) The comparison of spectra of black body radiation at $5800 \, \text{K}$, AM $1.5 \, \text{G}$ energy flux and AM $1.5 \, \text{G}$ photon flux. The defined visible range ($435-675 \, \text{nm}$) is also indicated as the rainbow band as the background.

In Figure 1.4B, black body radiation spectrum at 5800 K is compared with AM 1.5G energy spectrum, the dips along the AM 1.5G curve stem from the combination of the optical absorption of chemicals in the Earth's atmosphere (such as water vapor, molecular oxygen, nitrogen, and carbon dioxide) and the optical absorption of chemical elements in the Sun's photosphere

(Fraunhofer lines). The AM 1.5G energy flux can be readily converted into photon flux by applying Planck-Einstein relation, and the AM 1.5G photon flux is also plotted in Figure 1.4B for comparison. For single-junction PVs, photon flux is a more frequently used spectrum to quantify the photovoltaic performance of a solar cell, since the amount of incident photons directly correlates to the number of generated electrons. For transparent photovoltaic applications, we define wavelength range lower than 435 nm as UV, wavelength range between 435 nm and 675 nm as VIS, and wavelength range above 675 nm as IR.3,9,10 The cutoff wavelengths between UV/VIS and VIS/IR are chosen to optimize invisible light harvesting and TPV aesthetic quality, which will be discussed in the latter chapter. With the AM 1.5G energy flux, 11% is in the UV, 34% is in the VIS and the rest 55% is in the IR; in AM 1.5G photon flux, 4% of the photons are in the UV, 23% of the photons are in the VIS and the rest 73% of the photons are in the IR. Thus, a majority of the solar energy and solar photons are present in the invisible portion of the incident solar spectrum, offering great potential for the development of wavelength-selective transparent photovoltaic technologies. Single-junction PV cell design focuses more on photon flux, which directly determines the number of potential photogenerated carriers; whereas multi-junction PV cell focuses on the optimization of overall solar energy utilization, therefore, energy flux is more relevant in such case.

1.5 Wavelength-Selectivity and Shockley-Queisser Limits

In recent years, see-through PVs have been developed as an approach to make building-integrated photovoltaics (BIPV) that can help achieve net-zero-energy consumption buildings. Current see-through PV technologies can be categorized into two main groups: non-wavelength-

selective and wavelength-selective, depending on their corresponding absorption profiles. These groupings are important as they have different fundamental theoretical limits. Solar cells based on conventional inorganic semiconductors, such as Si, GaAs, Ge, are opaque photovoltaic devices. The continuum in the density of states of these inorganic semiconductors results in continuous absorption profile across the entire VIS range, and no visible photons can transmit through unless these materials are made thin enough. When these layers are thin enough, this thin-film approach results in a severe tradeoff between transmission and power production (can achieve mostly one or the other) and often results in tinted color on the transmitted or reflected sides, substantially degrading the aesthetics and applications of the corresponding TPVs. Therefore, such approach is sometimes referred to as "semitransparent". Alternatively, visible transparency can be realized by segmenting opaque solar cells as shown in **Figure 1.5**A, the opaque PV area is dispersed in microscale so that the space in between allows optical transmission (referred to as the "non-wavelength-selective approach).

In comparison, wavelength-selectivity can be realized with excitonic materials in TPV designs. As we defined in the previous section, wavelength-selective TPVs predominantly (or only) harvest UV (< 435 nm) and NIR photons (> 675 nm), enabling the highest visible transparency and best color metrics. ^{3,9,10} Inorganic photoactive materials, such as perovskites, quantum dots, the corresponding bandgaps can be tuned for UV harvesting and VIS transmitting; as for NIR spectrum, optical absorption of organic semiconductors originates from the transition from ground state to excited molecular orbitals. The gap between these excited molecular orbitals results in discontinuity in density of states. With purposeful design and modification of the molecular structures, conjugation, and crystallinities of organic semiconductors, these gaps can be tuned to

match the visible spectrum, which allows the transmission of VIS photons to create visible transparency as shown in Figure 1.5D.

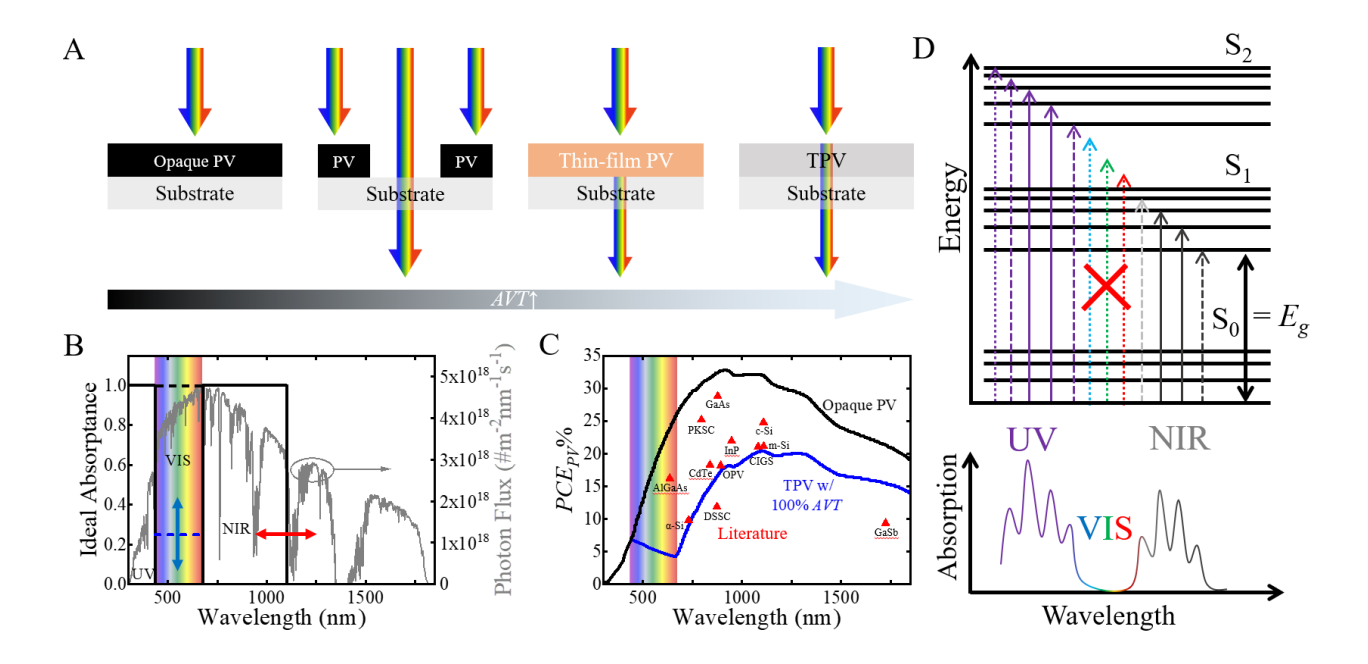


Figure 1.5 Visibly transparent photovoltaics realized by various approaches.

(A) Schematics showing conventional opaque PV, non-wavelength-selective TPV with spatially micro-segmented structure, non-wavelength-selective TPV with VIS absorbing thin-film, and wavelength-selective TPV. (B) Idealized step-function absorption profile of UV and NIR wavelength-selective TPV with various degree of visible contribution and adjustable NIR absorption cut-off. (C) Corresponding Shockley-Queisser (SQ) efficiency limits for opaque PV and wavelength-selective PV. Best research cell efficiencies are also added as the background. (D) Wavelength-selective TPVs realized by molecular and organic excitonic semiconductor materials.

When developing new kinds of solar cells, such as with TPVs and TLSCs, it can be quite useful to understand the theoretical power conversion efficiency limits to guide further development. For PV technologies (transparent or otherwise), this discussion begins with the Shockley-Queisser (SQ) single-junction limit. SQ limit is derived based on several ideal conditions: 1) the intensity of the incident solar irradiance is unconcentrated AM 1.5G; 2) the absorption profile (or EQE_{PV}) of the PV cell is a step-function as shown in Figure 1.5B, only one electronhole pair (exciton) is generated per incoming photon with energy higher than the E_g , and the excess energy after the excitation process is lost to thermalization; 3) the solar cell is a black body, and

therefore, the only recombination process in the PV cell is radiative recombination; and 4) the generated charge carriers (both electrons and holes) have infinite mobility, which can all be effectively collected by the respective electrodes. SQ limits as a function of E_g are plotted in Figure 1.5C, the *PCE* limit of an opaque single-junction is calculated to be 33.1% with a E_g of ~1.34 eV under AM 1.5G standard illumination. 11,17–19 A number of photovoltaic systems are now closely approaching the SQ single-junction limit, as references, the best research PV cells (including representative GaAs, Si, CIGS, OPV, perovskite solar cell (PKSC), copper indium gallium selenide (CIGS), etc.) are also included in Figure 1.5C. With wavelength-selectivity, the degree of visible transparency (visible optical absorption or visible contribution) can be adjusted according to practical requirements as shown in Figure 1.5B. With near 100% visible transparency, the *PCE* limit of single-junction TPVs is constrained thermodynamically to 20.6% with a E_g of ~1.12 eV. 3.9,10

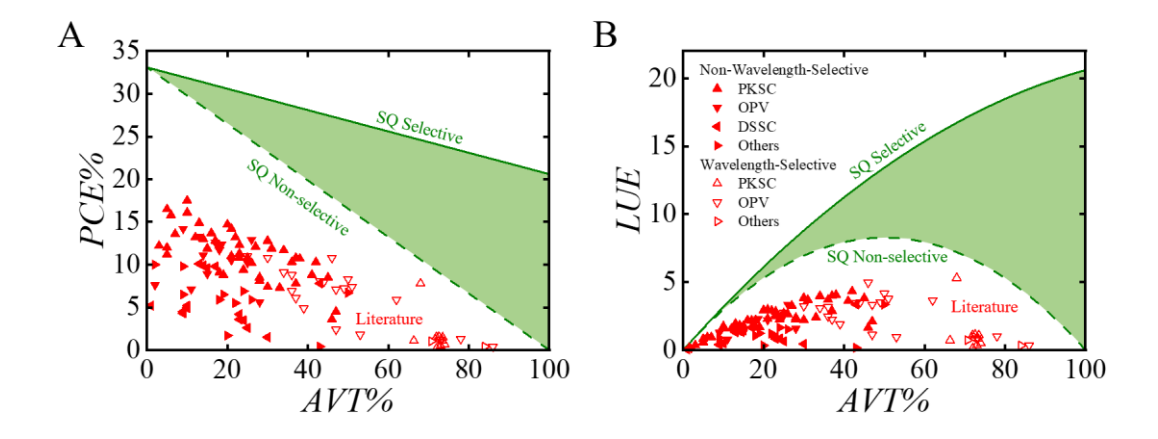


Figure 1.6 Efficiency limits as a function of visible transparency.

(A) Power conversion efficiency (PCE) versus average visible transmission (AVT). (B) Light utilization efficiency ($LUE = PCE \times AVT$) versus AVT. Note: the olive dash line is the SQ PCE (or LUE) limit for non-wavelength-selective TPV with partial visible transmittance (via microsegmentation or VIS absorbing thin-film approaches). The olive solid line is the SQ PCE (or LUE) limit for wavelength-selective TPV. The shaded green region between the two limit lines indicates the theoretically achievable PCE (or LUE) and AVT combination with the wavelength-selective approach only. Literature reports are included in both plots for comparison, including perovskite solar cells (PKSC), organic photovoltaics (OPVs), dye-sensitized solar cells (DSSC), and other TPV technologies.

The SQ PCE limit lines for non-wavelength-selective and wavelength-selective TPVs are plotted in **Figure 1.6**A.² For the non-wavelength-selective TPV approach, there is a direct tradeoff between photovoltaic performance and visible transmission. Therefore, the SQ PCE limit of a non-wavelength-selective TPV decreases from 33.1% (completely opaque) to 0% (completely transparent) as the corresponding AVT approaches 100%. In reality/practice, this limit will reach 0% at more modest AVTs around 80% due to losses related to reflections and recombination dynamics. In comparison, for wavelength-selective TPVs, the corresponding SQ PCE limit decreases from the same 33.1% (completely opaque) to 20.6% with an AVT > 99%. The dark shaded green area between the two limit lines indicates the theoretically achievable *PCE* and *AVT* combination with the wavelength-selective approach only. Thus, wavelength-selective approaches lead to a near infinite enhancement in the PCE as the AVT approaches 100% and 4-fold enhancement at an AVT of ~70%. A representative literature survey of various emerging TPVs (including PKSCs, OPVs, DSSCs and micro-segmented conventional or thin-film PVs) is shown in Figure 1.6A, it is obvious that most non-wavelength-selective TPVs show slightly higher PCEs but with AVTs below 50%, and higher AVTs are generally only achieved with wavelength-selective approaches.9,10

Another important metric that should be reported is the light utilization efficiency (LUE), which is the product of AVT and PCE ($PCE \times AVT$). The LUE provides a metric for comparing TPVs with different overall levels of AVT on the same scale. The LUE limits are 20.6% and 36.6% for single-junction and multi-junction TPVs with near 100% AVT, respectively. Reporting LUE enables a fair performance comparison between different TPV technologies and theoretical limits which can be used as a metric to evaluate the ability of a TPV technology to simultaneously optimize both visible transparency and power conversion, track the best utilization of light, and

assess progress in this field.³ Figure 1.6B shows the SQ *LUE* limit lines for non-wavelength-selective and wavelength-selective TPVs limits, and similarly, the dark shaded green area between the two limit lines indicates the theoretically achievable *LUE* and *AVT* combination with the wavelength-selective approach only. The literature survey is also included in this plot for reference. As the TPV technology with wavelength-selective approach develops, more data points are expected to appear and advance in the dark shaded green area, pushing this technology towards greater commercial potential and greater practical deployment in more applications in the near future.

Chapter 2 Introduction to Visibly Transparent Luminescent Solar Concentrators

As a key TPV technology, transparent luminescent solar concentrators (TLSC) selectively harvest the UV, NIR or partially and neutrally across the VIS portion of the incident solar spectrum. The device structural simplicity enables TLSCs to achieve the highest levels of visible transparency and aesthetics, unparalleled scalability, mechanic flexibility, and affordability. Consequently, the question of the efficiency limits has emerged in these new systems. In this chapter, the working principle of TLSC is introduced, and the theoretical efficiency limits of these concentrator systems are derived. Then practical considerations are outlined to approach these limits. In deriving these limits, key material and engineering challenges are identified to fully optimize TLSCs that can push them towards greater commercial potential.

2.1 Working Principles of Luminescent Solar Concentrators

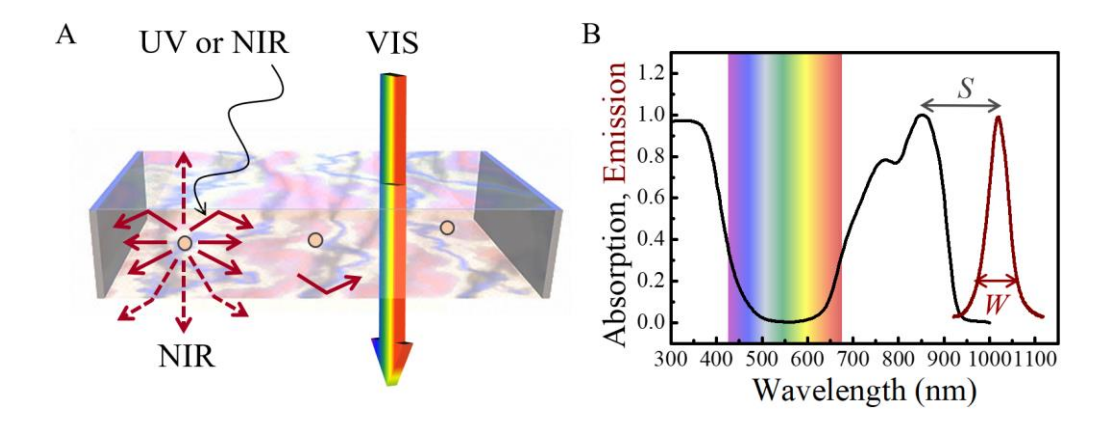


Figure 2.1 Operating principle of transparent luminescent solar concentrators.

(A) Schematic showing a transparent luminescent solar concentrator (TLSC) that selectively harvests ultraviolet (UV) and near-infrared (NIR) light while passing visible light. (B) Typical absorption and emission spectra of luminophores for transparent LSCs highlight two key parameters: the Stokes or down-conversion shift, S, and the width of the luminescent peak emission, W.

As shown in **Figure 2.1**A, luminescent solar concentrators (LSC, transparent or not) operate based on the following mechanisms: a portion of incident solar spectrum is absorbed the luminophores embedded in a transparent waveguide. That absorbed solar energy is then re-emitted at another at another wavelength isotropically in all directions within the waveguide, provided the oscillators are not preferentially oriented. Due to the refractive index difference between the waveguide and the ambient environment the re-emitted photons are predominately trapped by total internal reflection, causing these re-emitted photons to be directed towards the waveguide edges where they can be converted to electrical power in an edge mounted PV cell. The overall *PCE* of the LSC-PV system, η_{LSC} is given mechanistically by:^{9,21}

$$\eta_{LSC} = \eta_{Ont}^* \cdot \eta_{PV}^* = (1 - R) \cdot \eta_{AbS} \cdot \eta_{PL} \cdot \eta_{Tran} \cdot \eta_{RA} \cdot \eta_{PV}^* \tag{2.1}$$

where η_{0pt}^* is the overall optical efficiency (number of photons reaching the waveguide edge)/(number of photons incident on the waveguide), R is the front face reflection, η_{Abs} is the total solar spectrum absorption efficiency of the luminophore, η_{PL} is the photoluminescence efficiency of the luminophore, which equals the measured photoluminescence quantum yield (QY or PLQY) value of the luminophore embedded in the waveguide material, η_{Trap} is the waveguide light trapping efficiency, and η_{RA} is the efficiency of suppressing reabsorption loss. ^{21,22} The light trapping efficiency can be approximated for simple waveguides with isotropic emitters as η_{Trap} = $\sqrt{1-1/n_{Sub}^2}$ and $R=(n_{Sub}-1)^2/(n_{Sub}+1)^2$ excited at normal incidence (the only case considered in this work), where n_{Sub} is the refractive index of the waveguiding substrate (see **Figure** 2.2B). The absorption efficiency, defined is η_{Abs} , $\eta_{Abs} =$ $\int_{300nm}^{E_G^{Lum}} AM1.5G(\lambda) \cdot A(\lambda) \, d\lambda / \int_{300nm}^{\infty} AM1.5G(\lambda) \, d\lambda \,, \text{ where } A(\lambda) \text{ is the single-path absolute}$ absorptance profile of the LSC, E_G^{Lum} is the bandgap of the luminophore (in wavelength), and AM

1.5G is the air mass 1.5 global photon flux spectrum. The *PCE* of the edge mounted PV cell, η_{PV} (reported for illumination under AM 1.5G) must be normalized by its solar spectrum absorption efficiency and EQE_{PV} at the luminophore wavelength to account for monochromatic conversion as:

$$\eta_{PV}^* = \left(\frac{\eta_{PV}(AM1.5G)}{\eta_{Abs}^{PV}(AM1.5G)}\right) \cdot \frac{\int EQE_{PV}(\lambda')PL(\lambda')d\lambda}{\int PL(\lambda')d\lambda}$$
(2.2)

where $PL(\lambda')$ is the luminophore photoluminescence emission spectrum as a function of wavelength, $EQE_{PV}(\lambda')$ is the external quantum efficiency of the edge-mounted PV cell at the emission wavelength range (λ') , and $\eta_{Abs}^{PV}(AM1.5G)$ is the absorption efficiency of the PV material (rather than the luminophore). The thermodynamic limiting monochromatic η_{PV}^* is shown in Figure 2A where this scaled efficiency only accounts for the V_{OC} and FF losses as a function of the corresponding PV bandgap. Because of the light intensity dependence of η_{PV}^* , this correction will typically be dependent on the geometrical gain of the collector but is not considered here. Thermodynamic limiting PV efficiencies for edge mounted cells are derived based on the SQ detailed balance limit. 11,17,23

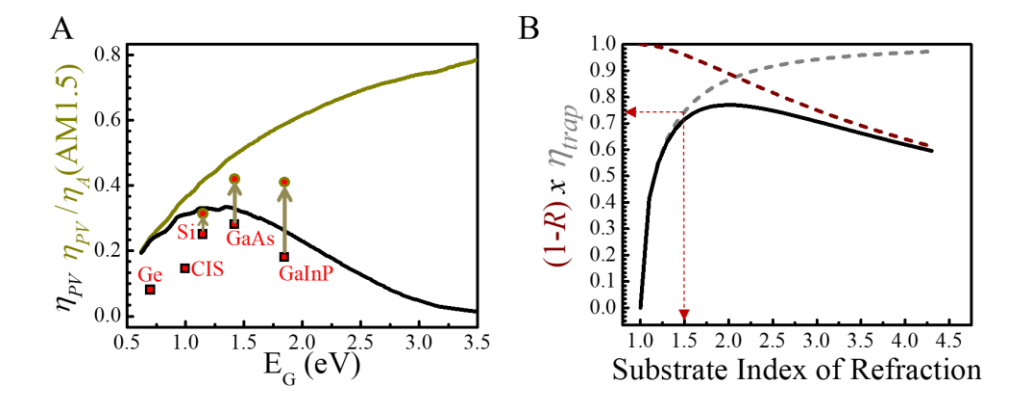


Figure 2.2 Component efficiencies in LSC operation. (A) Theoretical (black line) and best-performance solar cell efficiency (data points) as a function of bandgap under AM1.5G (η_{PV}) and normalized by the AM1.5G absorption efficiency (η_{PV}/η_{Abs} (AM1.5G), gold line).

Figure 2.2 (cont'd)

This efficiency represents the limits of the PV efficiency as a function of only FF and V_{OC} losses. (B) Reflection (red, dashed line) and trapping efficiency (grey, dashed line) as a function of the index of refraction of the substrate (n_{Sub}) for simple optical waveguiding. The maximum of the product of the reflection losses and trapping efficiency (blacked line) is at $n_{Sub} = 2.0$ for simple optical waveguiding of isotropic emitters.

Accounting for multiple reabsorption and emission events, the efficiency of suppressing reabsorption loss is then defined as:²⁴

$$\eta_{RA} = \frac{1 - \eta_{RAP}}{1 - \eta_{RAP}\eta_{PL}\eta_{Trap}} \tag{2.3}$$

where the reabsorption probability, η_{RAP} , is integrated over all emission angles and the absorptive path length is corrected for each take-off angle in a rectilinear system as:

$$\eta_{RAP} = \frac{\int_{0}^{\infty} d\lambda \int_{\theta_{crit}}^{\pi/2} d\theta \int_{-\pi/4}^{\pi/4} \sin(\theta) PL(\lambda) \left(1 - exp\left[-\varepsilon(\lambda)C\frac{Lt}{2t_{0}\sin(\theta)\cos(\varphi)}\right]\right) d\varphi}{\int_{0}^{\infty} d\lambda \int_{\theta_{crit}}^{\pi/2} d\theta \int_{-\pi/4}^{\pi/4} \sin(\theta) PL(\lambda) d\varphi}$$
(2.4)

where the critical angle (emission cone) is $\theta_{crit} = sin^{-1}(1/n_{sub})$, θ is the azimuth relative to the normal of the LSC waveguide, t is the thickness of the film with the luminophore coated on the front surface of the waveguide, t_0 is the waveguide thickness, and φ is the in-plane rotation angle integrated from $-\pi/4$ to $\pi/4$ to aid in the rectilinear conversion (e.g., with the path length $L/\cos(\varphi)$). In the case of the luminophore being embedded directly in the matrix (without an additional coated film on the front surface of the LSC waveguide), $t = t_0$ (as drawn in Figure 2.1A). The reabsorption losses then depend on plate length, PL efficiency, waveguiding efficiency, absorption coefficient, and degree of spectral overlap.²⁴

Finally, the maximum concentration ratio, C, (incident photon energy)/(photon energy redirected through a single aperture) has been derived previously for luminescent solar concentrators with a detailed balance assuming typical incident illumination around 1 sun as: 23,25

$$C = \frac{E_2^3}{E_1^3} exp\left(\frac{E_1 - E_2}{kT}\right) \tag{2.5}$$

where E_I is the energy at the edge of the absorption, E_2 is the energy of the emission onset. G describes the maximum concentration achievable considering the entropy balance between absorption-emission, and the energy distribution for a boson gas (i.e., photons) - that is, there is an entropy cost to concentrating diffuse light. This concentration is fundamentally limited by the constraint that the concentrated light cannot effectively exceed the source temperature (i.e., it is not possible to radiate more energy than the black body source at equilibrium). ²⁵ In Equation 2.5, $(E_1 - E_2)$ is proportional to the Stokes shift, S, defined in Figure 2.1B (so that $E_1 - E_2 = S \cdot hc/(\lambda_1\lambda_2)$) or sometimes defined as $(v_1 - v_2)$ and a system with four-sided apertures would have an additional factor of 4 in the denominator that acts to reduce the level of light concentration. For reference, the maximum concentration for diffuse concentrators without spectral shifting is $C = (n_2/n_1)^2$.

2.2 Theoretical Efficiency Limits of Transparent Luminescent Solar Concentrators

Considering the process described by Equation 2.1, it is clear that any power producing LSC is fundamentally limited by the PV efficiency of the edge-mounted photovoltaic cells. Thus, this discussion necessarily begins with the SQ single-junction PV limit.¹¹ In Figure 2.1B, typical emission and absorption shapes and characteristics of a luminophores are provided. Two key parameters are highlighted: the Stokes shift (or downshift), *S*, defined as the difference between the absorption and emission peaks; and the emission full width at half the maximum, *W*.²⁶

We begin by analyzing the limiting cases, where the emission and absorption characteristics of ideal luminophores are shown schematically in **Figure 2.3**A. Using this as a starting point, the limits of TLSCs are derived as a function of key parameters outlined below. The AM1.5G solar spectrum is integrated without the visible spectrum and as a function of bandgap. The color rendering index (CRI) and average visible transparency (AVT) can be used to determine the visible spectrum range to avoid; the range of 435-675 nm provides CRI > 95 and AVT > 99.5%. As a result, we utilize 435-675 nm as the visible range for this calculation. Although the human eye can sense the light from 390 to 435 nm and from 675 to 720 nm if bright enough, these ranges do not contribute significantly to our overall perception of color.

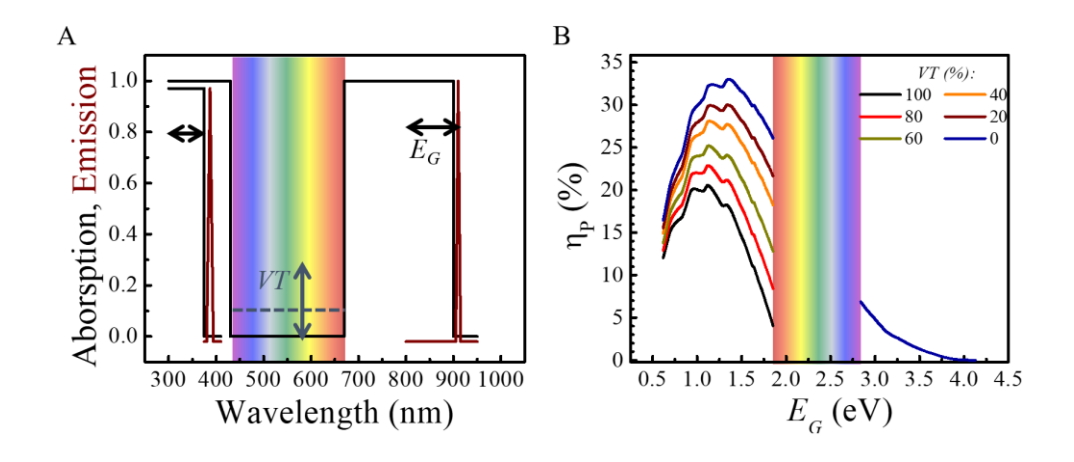


Figure 2.3 Ideal absorption, emission spectra and corresponding SQ efficiency limits of TLSCs.

(A) Schematic of idealized absorption and emission characteristics $(W \rightarrow 0, S \rightarrow 0)$ for selectively harvesting luminophores for theoretically-limited transparent LSCs with single waveguide cells. Configurations for both UV-only and UV+NIR harvesting are drawn. (B) Corresponding efficiency limits for the profiles in (A) as a function of the luminophore bandgap and degree of visible transparency (AVT). Note that the limit for AVT = 0 is just that of the Shockley–Queisser theoretical single-junction PV limit.

The ideal transparent solar concentrator then requires the following conditions: 1) the PL efficiency of the luminophore is unity; 2) the PV mounted around the edge has a PCE and EQE_{PV} equal to the SQ limit; 3) there are no reflection losses into the luminescent absorber or at the

waveguide edge; 4) there are no waveguiding losses (perfect light trapping); 5) there is no overlap between the emission and absorption (no reabsorption losses – this also plays an important role in the light concentration and scaling); 5) there is no diverging intensity dependence from the ideal limits of the edge mounted PV; 6) the absorption edges are sharp cutoffs around the visible spectrum; and 7) the emission width (W) is perfectly narrow. Given these restrictions, the theoretical limits of transparent luminescent solar concentrators are then described Equation 2.1, which reduces to $\eta_{Opt}^* = \eta_{Abs}$ and $\eta_{LSC} = \eta_{Abs}(E_G^{Lum}) \cdot \eta_{PV}^*(E_G^{Lum}) = \eta_{PV}(E_G^{Lum})$, where all the incident photons absorbed by the luminophores are subsequently converted to the same number of photons absorbed by the edge-mounted PV cell. In the absence of any concentrating effects, the single-junction thermodynamic efficiency limits are shown in Figure 2.3B. Although these ideal requirements represent a significant challenge, it is conceivable that all of the criteria outlined above can be satisfied (or nearly so) to meet this limit. For example, all reflections could be eliminated with the use of antireflection coatings; perfect waveguiding achieved with tailored and selectively reflecting photonic mirrors; luminophores with near unity η_{PL} and emission widths < 5nm have been demonstrated; and PV cells are now closely approaching the SQ limit.

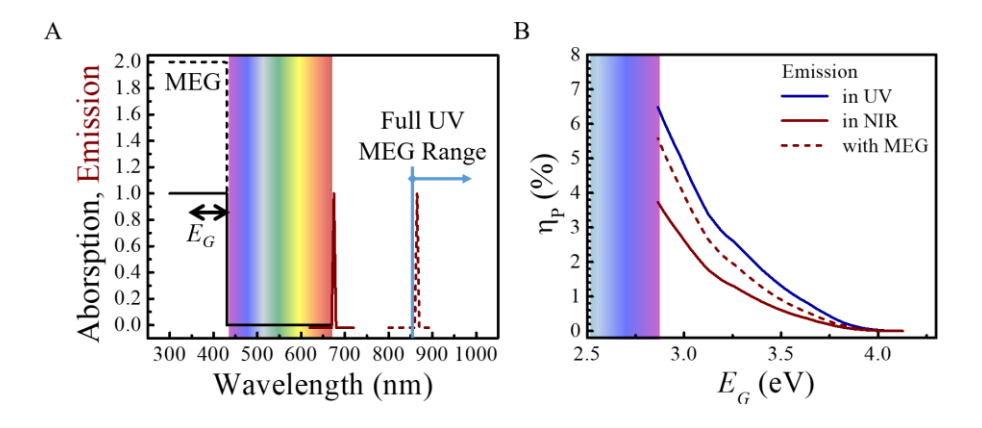


Figure 2.4 Ideal configurations of UV-only selective-harvesting TLSCs.

(A) Schematic and (B) corresponding efficiency limits as function of luminophore bandgap for two alternative UV-only harvesting transparent LSCs designs. The first configuration harvests UV light and down-converts this energy into the NIR to prevent coloring from escape cone emissions.

Figure 2.4 (cont'd)

The second configuration uses a multiexciton (MEG) UV harvesting luminophore with emission at half of the energy of the UV cutoff to enable emission of two photons from one high energy UV photon. Note that these two configurations place varying restrictions on the maximum VOC and FF of the edge-mounted PV. (B) The case of UV harvesting and UV emission with no spectral overlapping is also included.

Notably, in this idealized case there are multiple ways to configure selective UV harvesting for transparent devices. Provided the emission is perfectly narrow and non-overlapping with the absorption, the UV-only TLSC efficiency limits are plotted in Figure 2.4, yielding a maximum efficiency of 6.9% with an ideal cutoff at 435nm. We reiterate that the formation of color in these systems stems from both absorptive filtering and any luminescence in the visible range. It is therefore necessary to design emitters with either emission with S=0 and W=0 (e.g., a delta function), or large downshifted emission past the visible spectra into the near-infrared. The latter case is more advantageous for both reducing the formation of colorful glow and eliminating reabsorption losses over large areas. This larger downshift, while beneficial for scaling, also results in drop of the UV-only efficiency limit to 3.7%. However, because the downshift required in this scenario is so large, it is possible to consider the application of multiexciton generation (MEG) mechanisms^{27–33} or singlet fission (SF) to overcome some of this thermal loss as shown in Figure 2.4A. In singlet fission, one high energy singlet excited state can decay to form two triplet excitons and is well known to be nearly 100% efficient in many molecule systems. 27,34-38 This process is thermodynamically endothermic if the triplet energy is less than or equal to the singlet energy, providing the minimum emission wavelength (870nm), and corresponding PV bandgap, requirement. In this case the UV-only efficiency limits (with emission in the NIR and SF) increases from 3.7% to 5.6% as shown in Figure 2.4B. Thus, there is a surprising amount of potential in harvesting the UV-only portion of the solar spectrum, particularly if the full photon energy can be fully exploited.

For the case of combined UV/NIR harvesting, the entire spectrum of incident UV and NIR photons would ideally be selectively absorbed. Then the same number of UV/NIR photons are remitted via photoluminescence resulting in the generation of equal number of electrons. Hence, the relationship between absorptance (A) and transmittance (T) of TLSC $A(\lambda) + T(\lambda) = 100\%$ for UV/NIR wavelengths becomes $EQE_{LSC}(\lambda) + T(\lambda) = 100\%$. Since the emission edge borders the absorption edge with ideally no overlap between emission and absorption the ideal bandgap for the edge-mounted PV can be selected resulting in no voltage loss in this edge-mounted PV. As a result, the thermodyanic efficiency limits for TLSC are essentially identical to theoretical limits for TPVs. With increasing transparency from 0% to 100% in visible range, the maximum efficiency of TLSC is modestly reduced from 33.1% (SQ limit of opaque photovoltaics) to 20.6% (thermodynamic efficiency of wavelength-selective fully transparent LSCs). TLSCs are then just another version of a transparent solar cell which shift the solar energy conversion optically to the edges.

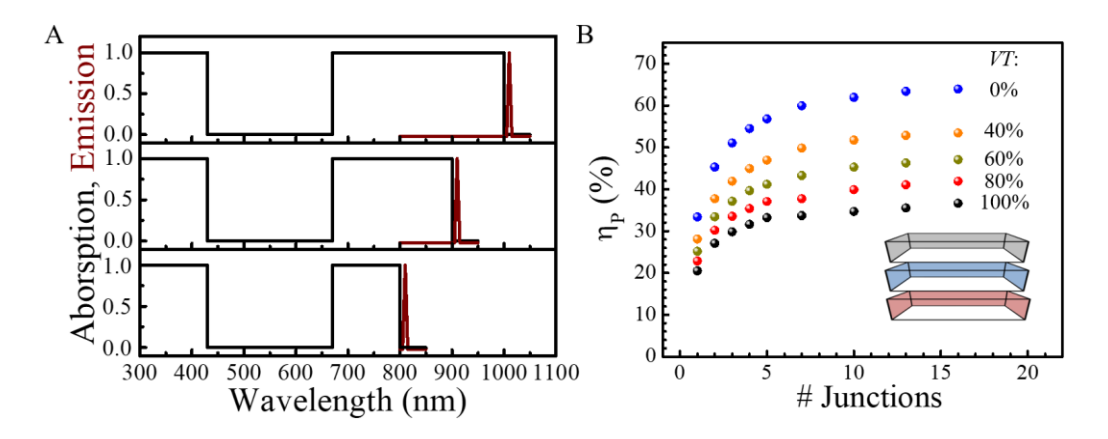


Figure 2.5 Ideal configurations of TLSCs with multiple waveguide components. (A) Schematic of idealized absorption and emission characteristics $(W \rightarrow 0, S \rightarrow 0)$ for selectively harvesting luminophores for theoretically-limited transparent LSCs with multiple (multi-junction) waveguide cells. (B) Corresponding efficiency limits for the profiles in (A) as a function of the waveguide cells and degree of visible transparency (AVT) for series-matched currents.

To completely reduce the energy losses associated with thermal relaxation ideal multipanel (or multi-junction) LSC devices are also considered.^{26,39} It is important to appreciate that the narrow band emission of the luminophore requires edge-mounting of single-junction photovoltaics (as opposed to ultra-high efficiency multi-junctions) as it will be particularly difficult to current or voltage match all of the PV sub-cells with essentially only monochromatic light. However, it is still possible to form multi-panel LSC devices where each subpanel is separated by an air gap or photonic mirror, and harvests light from a particular section of the solar spectrum, with a PV bandgap matched to the emitter in each subpanel. We analyze this configuration in **Figure 2.5**A, again in the absence of waveguiding losses and assuming all sub-cells are photocurrent matched. The efficiency then increases to 36.6% for fully transparent multi-panel devices as shown in Figure 2.5B.

In all of these idealized cases, we further consider the light concentration limitation imposed by Equation 2.5 based on the Heaviside and delta function approximations of the absorption and emission profiles, respectively. This leads to $E_1 = E_2$ and results in a maximum concentration of G = 1. This means that for the idealized profile in Figure 2.3A, no additional light concentration above the incoming solar flux intensity would be possible, thus limiting the size and geometry constraints of such an ideal system. However, this entropy cost is not so severe and small Stokes shifts of even 45meV in Equation 2.5 can lead to G > 5 (a value typical of the best demonstrated LSCs with only a slight reduction (< 5% at the peak) to the limiting efficiency curves in Figure 2.3B.²² For reference, a Stokes shift of 100 meV leads to G > 35 across the spectral range above 0.9eV, much greater than has been demonstrated in actual LSC systems due to other parasitic reabsorption losses. Thus this entropy driven limitation to scalability quickly becomes negligible when further considering the more practical scenarios below, i.e., in practical LSC design and developlemt, this concentration limitation does not play an important role. However, it

is a more important design parameter in concentrated solar power systems where complicated optics and light tracking systems are utilized for maximized power output.

2.3 Efficiency Limits of Transparent Luminescent Solar Concentrators with Finite Width and Stokes Shift Emitters

We next turn our attention to the practical considerations of the performance of TLSCs. This discussion becomes dependent on a greater number of parameters and thus follows a discussion for a number of cases as the idealized parameters are relaxed.²⁶

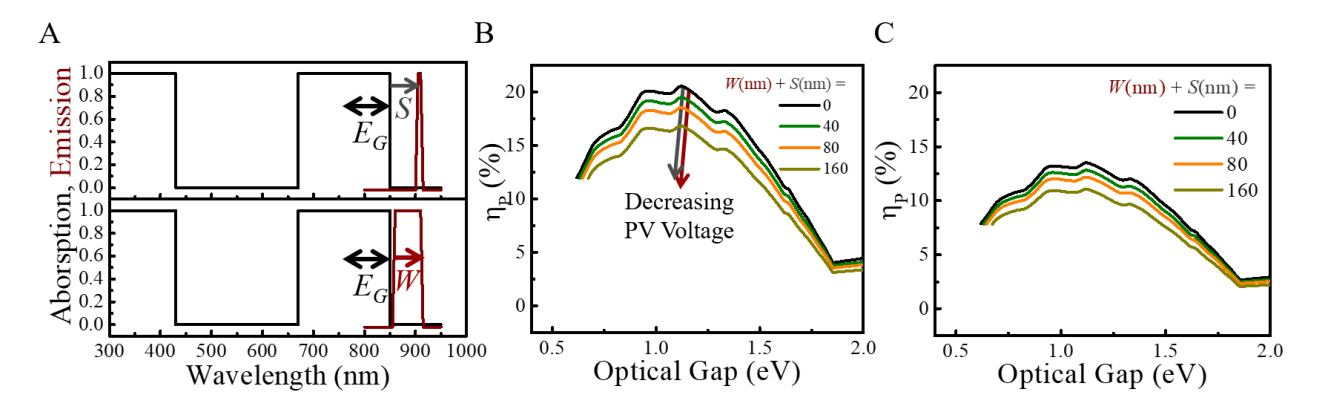


Figure 2.6 Practical configuration of TLSCs with finite Stokes shift and emission width.

(A) Schematic and (B) corresponding efficiency limits as function of luminophore bandgap, idealized Stokes shift (S), and idealized emission width (W). Note that as W or S increases, the corresponding PV bandgap and voltage must decrease, thus reducing the efficiency limit. In this idealized configuration S and W are essentially equivalent. In practice, there is a distinct advantage to small W and large S in reducing reabsorption losses and increasing scalability since there is typically at least some spectral overlap. (C) Corresponding efficiency limits as function of luminophore bandgap, idealized Stokes shift (S), and idealized emission width (W) with practical light trapping considerations.

This discussion is further extended to less ideal systems where emitters have a fixed finite emission width (*W*) with a varied Stokes shift (*S*), and vice versa. This case is one of the first key areas of loss as it confines the solar spectral range that can be harvested for a given PV bandgap and dictates the voltage loss required in selecting a particular PV cell bandgap. For example, given

a particular molecule emitter with a defined absorption, the smaller the W, the higher voltage PV that can be selected. For reference, a range of emission widths have been demonstrated for organic molecules $(30\text{-}100\text{nm})^{24,40\text{-}43}$ nanoclusters $(50\text{-}300\text{nm})^{7,44}$ J-aggregates $(15\text{-}40\text{nm})^{45,46}$ nanocrystals $(15\text{-}30\text{nm})^{47}$ rare-earth ions $(<5\text{-}20\text{nm})^{48,49}$ and single diameter carbon nanotubes $(8\text{-}15\text{nm})^{50}$ suggesting that such losses can, in fact, be minimized. Nonetheless, for the most efficient emitters, this value of W is typically around 20-100nm. As shown in **Figure 2.6A**, finite values of W and S require a smaller bandgap at the edge-mounted $PV:E_G^{PV} \leq [E_G^{Lum} - (S+W)]$. Consequently, the output PV voltage (Voc) will become lower. As W+S increase from 0 to 160 nm, the corresponding efficiency limit will decrease from 20.6% to 16.8% due to this "voltage loss" as shown in Figure 2.6B. In practical TLSC design, since there will be at least some overlap between absorption and emission, large S with small W is preferable than large W with small S in scaling up, which will be discussed in detail below.

2.4 Practical Efficiency Limits of Transparent Luminescent Solar Concentrators

For the practical efficiency limit, we then apply more realistic limitations to Equation 2.1. For example, we use the practical reflection and waveguiding optimization as shown in Figure 2B where the optimum of the product of the reflection and waveguiding efficiencies of simple waveguides leads to $(1-R)\cdot\eta_{Trap} = 0.77$ for a substrate with $n_{Sub} = 2.0$. It is reiterated that this can, in theory, be improved to near 1.0 with higher complexity optical designs that also add considerable cost, e.g., with antireflection coatings, ⁵¹ distributed Bragg reflectors (DBRs, also known as 1D photonic mirrors) with tunable stop bands. ^{52,53} Given that a number of photovoltaic systems are now closely approaching the SQ single-junction limit (e.g., Si and GaAs as shown in

Figure 2.2A),⁵⁴ and the current trajectory of improvement will be limited over the next few decades. We can use the current state of the art in lab-scale performance as a practical module limit for the foreseeable future. We then fix the quantum efficiency of the PV cell in Equation 2.2 to EQE_{PV} = 95% since this is among the highest average quantum efficiencies reported for a lab-scale single-junction cell (i.e., GaAs). Similarly, we can assume a factor of 0.9 reduction in the monochromatic PV efficiency considering the slight divergence of FF and V_{OC} from the SQ limit. Combining all the PV losses leads to an overall reduction of 85.5% of the SQ limit (33.1%) of the PV cell, which is close to the record single-junction cell reported for GaAs. Finally, we include finite widths to the emission and Stokes shift as variables in Figure 2.6C. For W = 80nm and S = 80nm (S+W = 160 nm), this results in a practical efficiency limit ~11% for an emitter bandgap of 1.12eV. Thus, the practical efficiency limits track surprisingly close to that for transparent photovoltaics which was estimated to be 11%, also with a bandgap of 1.1eV. 10

2.5 Practical Consideration for Scaling of Transparent Luminescent Solar Concentrators

In reality, reabsorption losses are one of the most significant sources of efficiency and scaling reduction. To explore this effect, we integrate Equations 2.3 and Equation 2.4 numerically as a function of length, luminophore quantum yield, and Stokes shift to evaluate practical transparent LSC system efficiencies. 42,55,56 Light emitted by the luminophore in the waveguide must traverse the length of the waveguide before being reabsorbed by the luminophore or waveguide to reach the edge-mounted PV and produce electric power. These losses are critically dependent on the QY of the luminophore, the waveguiding efficiency (η_{Trap}), the overlap (or Stokes shift, S) of the luminophore emission-absorption, and the overall waveguide dimensions (L). Waveguide roughness and optical transparency also play an important role as waveguides are

scaled to around square meters areas, where both can act as reabsorption or scattering losses. Absorption coefficients of < 0.01/cm are ideal for eliminating waveguide absorption in the NIR and are in this range for many polymer based waveguides (e.g., polymethmethracalate, polycarbonate, etc.).

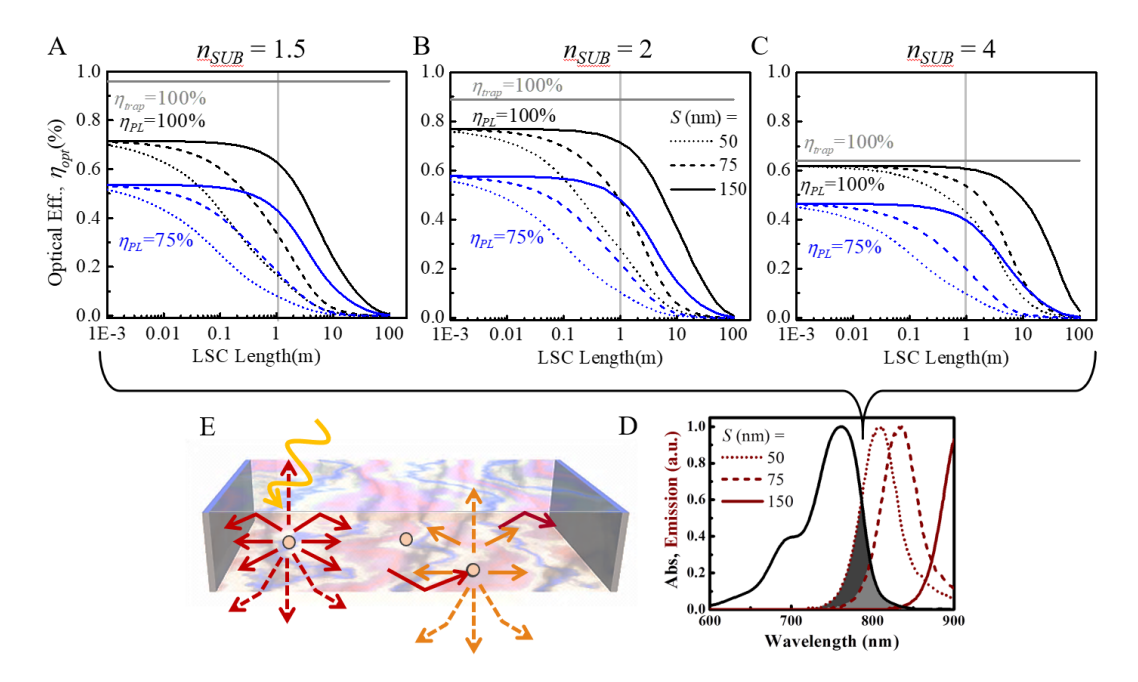


Figure 2.7 Practical consideration for scaling of TLSCs.

Practical optical efficiency (η_{Opt}) as a function of PL efficiency (η_{PL}), Stokes shift (S), and LSC length for substrate index (n_{Sub}) of (A) 1.5, (B) 2.0, (C) 4.0 given (D) the more realistic spectral overlap profiles and (E) device schematic emphasizing reabsorption events. Note that the varying degrees of spectral overlap are highlighted in (D) with the grey shaded area associated with each S. The situation of perfect light trapping is also shown for reference (e.g., using wavelength selective mirrors), the optical efficiency is still reduced by (1–R) and which shows perfect scaling only when the PL efficiency is unity.

Even for luminophores with 100% QY, reabsorption losses can become dominant for luminophores with small Stokes shift in large waveguides but only modest waveguiding efficiency since each absorption/emission event leads to a reduction of photon flux through cone emission from the front of the waveguide that effectively act as scattering events as shown in **Figure 2.7**E, unless the waveguiding efficiency is 100%. These cone losses for each reabsorption/emission event for perfect emitters (luminophore with 100% QY) still follows (η_{trap}) N , where N is the number

of reabsorption/scattering events and this behavior is already captured in Equation 2.4. For example, for an ideal TLSC with $\eta_{PL} = 1$ and $n_{Sub} = 1.5$ ($\eta_{Trap} = 0.745$), over 90% of the photons would be lost after being scattered (or re-emitted) by the embedded luminophores after just 8 scattering or re-emission events due to cone losses. If the the quantum efficiency of the luminophore is less than 100%, the photon flux reduction will be more significant after each scattering or reabsorption event. Shown in Figure 2.7A to C is the scaling for a practical case accounting for reabsorption losses given the spectral characteristics shown. For reference, the case of both $\eta_{Trap} = \eta_{PL} = 1$ is also plotted, leading to $\eta_{Opt}^* = (1-R)$ at all plate lengths. Considering the data in Figure 2.7D, a reasonable target for the practical performance and scalability would be to target larger Stokes shifts in the range 100 nm < S < 160 nm combined with emission widths that are as narrow as possible. Figure 2.7A also highlights that the Stokes shift is just as important as η_{PL} , if not more so, particularly for the largest area scaling. This can be seen in any of the three subplots, where for a substrate index of 1.5 and 1m² plate size the larger Stokes of 150nm combined with the lower η_{PL} of 75% results in 25% higher optical efficiency than for system with a Stokes shift of 75nm combined with a η_{PL} of 100%.

2.6 Photoluminescence Mechanisms in Luminescent Solar Concentrators

Down-shifting (DS) is the most widely adopted photoluminescence mechanism in LSC/TLSC design as shown in **Figure 2.8**A, optical absorption of high energy photons excites the luminophores from ground states to excited states (e.g., $S_0 \rightarrow S_1$, $S_0 \rightarrow S_2$, etc.), and photoluminescence with longer wavelengths results from down-shifting radiative recombination processes (via fluorescence or phosphorescence). Notably, in organic and molecular semiconductors, the gap between the excited molecular orbitals (S_1 and S_2) results in discontinuity

in the density of states, which can be tuned to overlap with the visible spectrum to create visible transparency.

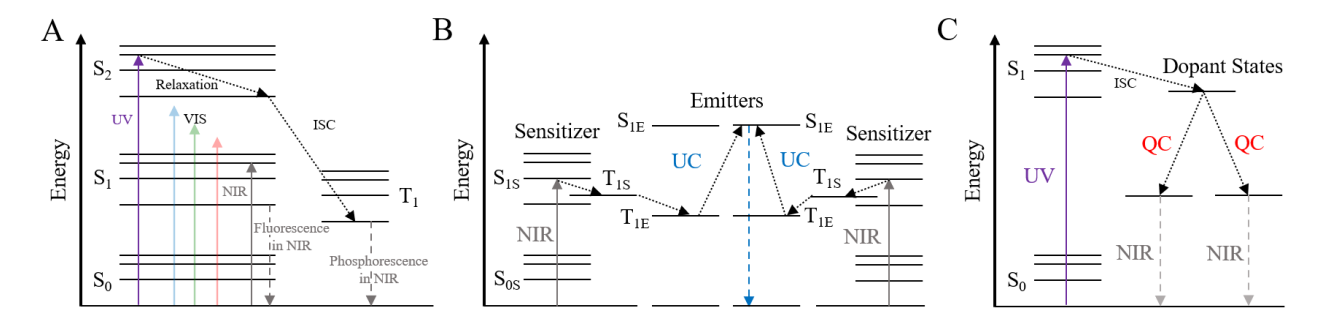


Figure 2.8 Jablonski energy diagrams of various photoluminescence mechanisms utilized in LSC design.

(A) Down shifting (DS) process. (B) Triplet-triplet annihilation up-conversion (TTA-UC) process. (C) Quantum-cutting (QC) process.

SQ limit successfully predicts the maximum achievable efficiency for a single-junction PV device. Minimizing the following two key losses can further improve the overall photovoltaic performance of the LSC-PV system: 1) transmission loss due to incomplete solar spectrum absorption; 2) thermalization of high energy photons in the form of excess heat, i.e., thermalization loss. Spectral conversion of the incident solar spectrum provides promising routes to effectively reduce these losses.

Up-conversion (UC) of low-energy photons above the energy bandgap of the edge-mounted PV cells reduces the transmission loss, effectively expanding the solar spectral coverage not achievable with conventional DS process.^{57–59} Among several UC approaches, triplet-triplet annihilation up-conversion (TTA-UC) is suitable for photovoltaic applications due to its superior optical absorption and relatively high *PLQY*s.^{60–62} Figure 2.8B shows the energy transfer process of TTA-UC: the sensitizer molecules are excited from the ground state (S₀₈) to the excited state (S₁₈) by absorbing low-energy photons, then the excited sensitizer passes to a long-lived triplet state (T₁₈) via intersystem crossing (ISC). Subsequently, the excited energy transfers from

sensitizer triplet state (T_{1S}) to emitter triplet state (T_{1E}) via a Dexter process, and triplet-triplet annihilation (TTA) occurs between two emitters in close proximity to form a higher emitter singlet state (S_{1E}), then radiative decay of such higher energy state leads to the emission of one upconverted high-energy photon.⁵⁷

Quantum-cutting (QC) one absorbed high-energy photon into two or multiple low-energy photons provides an alternative approach to reduce thermalization loss. $^{63-67}$ The energy diagram for QC process is shown in Figure 2.8C: upon absorbing one high-energy photon, the excited singlet state (S₁) undergoes ISC to dopant states, where the QC process takes place and subsequently emits two low-energy photons. This spectral conversion approach enables effective utilization of high-energy UV photons in LSC application with an ideal QY value of 200%. Notably, demonstrations of TTA-UC and QC mechanisms in LSC systems have both been reported in literature, the impact of QC mechanism on LSC aesthetics and photovoltaic performance will be discussed in Chapter 5 and Chapter 10, respectively.

2.7 Luminophore Material Candidates for Luminescent Solar Concentrators

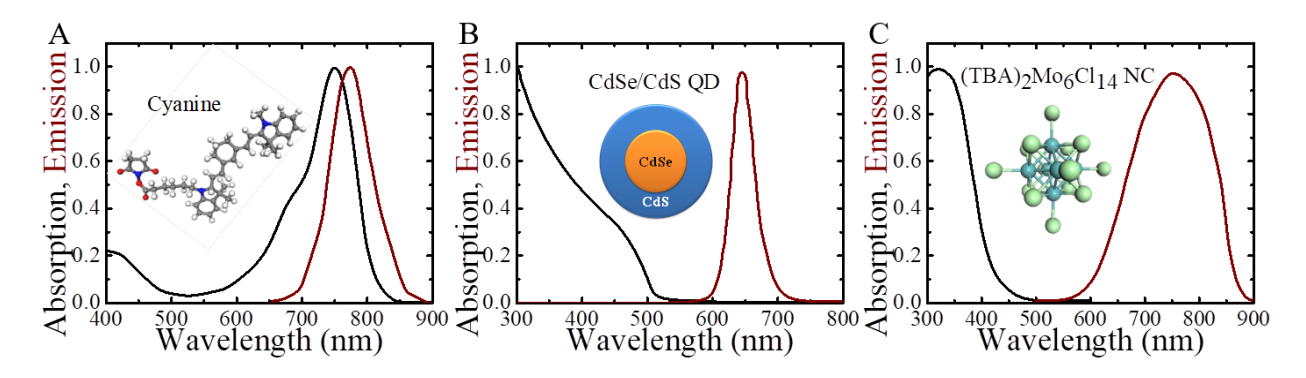
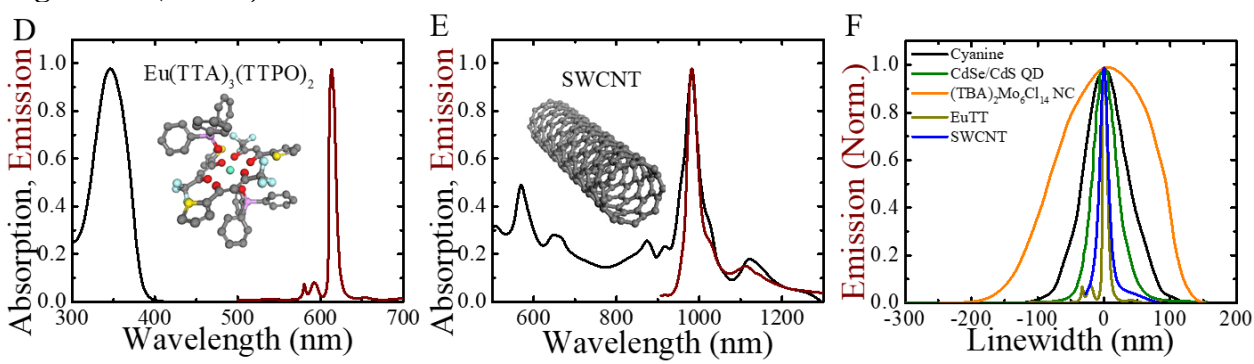


Figure 2.9 Representative absorption and emission spectra (normalized) of typical emitters applied in LSCs and TLSCs.

The molecular structures or nanostructures are included as insets for (A) Cyanine salt. (B) CdSe/CdS quantum dots. (C) $(TBA)_2Mo_6Cl_{14}$ nanoclusters.

Figure 2.9 (cont'd)



(D) Eu(TTA)₃(TTPO)₂ rare-earth ion complex. (E) Single-walled carbon nanotube. (F) Emission linewidth (W) comparison of different emitter species. Note that small W (< 5 nm), and a wide range of S (5- 500 nm) have been reported.

Key representative emitter materials applied in LSCs/TLSCs are reviewered in this section, the corresponding absorption and emission spectra are shown in **Figure 2.9**A to E. The excitonic nature of organic dyes stems from their π -conjugated molecular structure, enabling tunable and selective harvesting in various parts of the solar spectrum that is key for selective NIR harvesting. The most common organic dyes for LSC include rhodamines, ^{68–74} coumarins, ^{73,75–77} lumogens, ⁴ cyanine salts, ^{8,78} and perylenebismides derivatives, ^{79–82} etc (see **Table 2.1**). While the Stokes shifts of organic dyes are usually small (< 100 nm), recent efforts have resulted in S > 100 nm for both fluorescent and phosphorescent emitters. Another challenge is that the QYs of emitters in NIR range are typically lower (< 50%).^{8,78} Nonethless, selective NIR harvesting TLSCs have been demonstrated based on variations of these cyanine salts with system efficiencies of 0.4% efficiency combined with an AVT of 86% and little tinting. Looking forward, these NIR-selevtive TLSCs show potential for efficiencies up to 10% as described in the efficiency limits above. Thus, while there are a number of challenges in designing these materials to selectively harvest invisible photons with high quantum yield and Stokes shift, organic chemistry affords massive design space to solve many, if not all, of these challenges. In Chapter 6, Chapter 7 and Chapter 9, newly

designed and syenthesized NIR selective harvesting organic dye molecules will be presented to fullfill their promise for higher TLSC photovoltaic performance and aestthtic quality.

Table 2.1 Representative summary of the absorption λ_{max} , emission λ_{max} and PLQYs of typical luminophores and dye emitters used in LSCs and TLSCs.

Luminophore	Absorption	Emission	PLQY	Visible Colored	Reference	
Lummophore	λ_{max} (nm)	λ_{max} (nm)	(%)	Visible Cololed		
Rhodamine 6G	528	558	95	Yes	68	
Lumogen F Red 305	578	613	98	Yes	83	
Perylene Derivative	577	674	70	Yes	84	
Cyanine Salt	742	772	20-30	No	8	
CdSe/CdS QDs	< 500	650	86	Yes	85	
Mn ²⁺ doped ZnSe/ZnS NCs	400	600	37	Yes*	86	
CuInSe _x S _{2-x} /ZnS QDs	500	960	40	Yes	87	
$CdSe/Cd_{x}Pb_{1\text{-}x}S\ QDs$	460	625	40	Yes	88	
$(TBA)_xMo_6Cl_{14}\ NCs$	325	750	75	No	7	
$Eu(TTA)_3(TPPO)_2$	577	674	70	Yes*	89	

^{*}Molecules that are visibly colored due to emission peaked in the visible spectrum.

Another class of emitters are quantum dots (QD) and nanocrystals. ^{90–92} By controlling the reaction condition, the variation of their particle sizes, structures, ligand species and compositions results in the tunability of both absorption and emission spectra. However, the limited oscillator strength of these materials near their bandgap typically prevents their use as NIR selective harvester, making them more suitable for selective UV harvesting or semitransparent (colored or opaque) applications. ^{5,6,93} Currently, several strategies have been developed to increase the downshift. One promising approach is the use of core/shell structured nanocrystals, forming quasitype II heterojunction where the shell has larger energy bandgap and acts as a light absorbing antenna that transfers the absorbed energy to the core crystal as the light emitter. ^{56,85,88,94,95} Impurity-doping and alloying are both alternative approaches to tackle the reabsorption problem.

For example, in Mn-doped ZnSe/ZnS core/shell NCs, small amount (0.1-1%) of Mn²⁺ introduces new localized excited energy states within the bandgap of ZnSe resulting in exhibit enhanced downshifted luminescence.⁸⁶ Ternary or quaternary compound semiconductors are also introduced in core/shell QDs, such as CdSe/Cd_xPb_{1-x}S⁹⁴ and CuInSe_xSe_{2-x}/ZnS QDs.⁸⁷

Among the nanostructured emitters, a new class of emitter materials has been reported recently based on 0D nanoclusters and nanocrystals for these applications. Such nanoclusters include hexanuclear metal halide salts $A_2B_6X_{14}$ (e.g., $A=K^+$, $B=Mo^{2+}$, W, and $X=Cl^-$, Br^- , or I^-). The $(TBA)_2Mo_6Cl_{14}$ (IBA: tetrabutylammonium) nanocluster, for example, was shown to selectively absorb the UV portion of the solar spectrum (300-435 nm) and emit in the NIR (centered at 750nm) with a massive phosphorescent downshift of around 400 nm that was one of the first examples to eliminate reabsorption losses. ^{7,44} Since both the absorption and emission are outside the visible range, these materials provide the highest level of aesthetic quality with a reported AVT over 85% combined with a device efficiency of 0.44% that is predicted to exceed 1% at larger scales.

Rare-earth ions and ion-complexes are also an important class of potential emitters for LSCs and TLSCs. ^{84,89} Historically, these have been used in fluorescent lighting and downconverting phosphors. ^{48,49,96-99} In LSC applications, organic emitters such as europium tris(2-thenoyl trifluoro acetonate)-di(triphenylphosphine oxide (Eu(TTA)₃(TPPO)₂) have been demonstrated, where light is absorbed by the central organic ligand, energy is transferred to Eu³⁺ and then emitted as photons by the Eu³⁺ ion. ⁸⁹ There have also been a number of demonstrations of rare-earth ions (e.g. Ce³⁺, Eu²⁺, Eu³⁺, Sm²⁺, and Tm²⁺) directly embedded into a variety inorganic hosts. ^{100–103} While the UV absorption combined with large luminescent downshifts (> 200 nm) and sharp emission peaks (< 20 nm) makes Eu(TTA)₃(TPPO)₂ and other ions potentially

suitable for the UV LSC, the emission spectrum shown to date peak in the visible range that results in luminescence based tinting combined with narrow absorption bands (insufficient solar harvesting). Moving forward, efforts are needed to further increase the emission outside of the visible range and expand the absorption bands to make them more compelling for TLSC applications.

Single-walled carbon nanotubes (SWCNTs) consist of 1-D rolled graphene sheets of varying tube diameter and chirality. SWCNTs exhibit both metallic and semiconducting characteristics, which strongly depend on their (*n*, *m*) chiral indexes and diameters. ^{104,105} While these materials are notably difficult to sort (metallic, semiconducing, diameter, chirality, etc.) and to process at large scale, ^{106,107} they have attracted tremendous attention due to their outstanding optoelectronic properties. ¹⁰⁸ Semiconducting SWCNTs have direct bandgap, and many diameters/chiralities exhibit tunable photoluminescence in the NIR range (wavelengths of emission peaks spanning from 1.0 to 1.6 μm), which makes them promising TLSCs emitter candidates. ^{50,105} Recently, several methods including oxygen atom doping and sp³ defect doping have been developed to enhance the quantum yield by reducing the nonradiative recombination rates. ^{20,109,110} While CNTs have notably small Stokes shifts (see Figure 2.9E), these could be enhanced through energy transfer of bundled CNTs with progressively smaller bandgaps.

As final note on the use of the word "concentrator", we highlight that traditional solar concentrators have been developed to focus light onto PVs to enhance PV performance using, for example, optical lenses, parabolic troughs, mirrors, etc. where the thermodynamic limits of efficiency are well known to increase with higher intensity. Unlike with these traditional "solar concentrators" the goal of the TLSC is not typically to get enhanced light concentration to increase the efficiency limits but to provide a low cost solar harvesting system. Practically, this effect is of

limited importance because the concentrating effect is often offset by losses dictated by reabsorption and wavegude trapping losses as the concentrator is scaled to very large areas needed to collect more light. In ideal systems, however, this concentration effect may eventually become an important enhancing effect in TLSCs. Ultimately, the calculation of theoretical and practical efficiency limits of TLSC systems provides guidelines for the future development of ideal mateirals and properties for the realization of the full potential of this new clear photovoltai technique.

Chapter 3 Standard Characterization Protocols for Transparent Photovoltaics

Emerging TPV technologies have exhibited tremendous growth in the past 6-7 years.³ As introduced in Chapter 1, current TPV technologies can be categorized into two main groups: non-wavelength-selective TPVs have exceeded *PCE* of 12%¹¹¹ with perovskites and ~10%¹¹² with organic and excitonic materials with *AVT*s around 20-30% and *LUE*s of 2-3; and wavelength-selective TPVs fabricated with organic layers have demonstrated *PCE*s between 5-10% for *AVT*s between 40-55% and *LUE* of 2.5-4.^{3,113,114} Despite the rapid development in TPV research, new characterization challenges have led to less reliable reporting of performance metrics. Thus, it is imperative to adopt standard characterization protocols for these new types of devices, which can provide an unbiased comparison among the reported performance values.¹¹⁵

In this chapter, several example TPVs are used to comparatively measure all the key performance metrics and consistency checks to highlight the best TPV characterization protocols. Common measurement pitfalls are also emphasized, which can lead to inflated performance results. Key parameters to evaluate the visible transparency and aesthetic quality of TPV devices are given along with an overview of the method to measure and calculate them. Finally, the photon balance consistency check is illustrated for data acquired from independent measurements, which helps validate the data and significantly alleviate concerns over experimental errors.

3.1 Transparent Photovoltaic Performance Characterization

The *PCE* of TPVs is defined and calculated the same way as any other PV technology from current density-voltage (*J-V*) characteristics under a standard illumination as expressed in Equation 1.1, which applies to all TPVs and LSCs/TLSCs. It is noted that the characterization protocols for

device characterization of LSCs and TLSCs are outlined in the next chapter. The incident solar spectrum (P_0) should always be the AM 1.5G spectrum as the standard input power for both non-wavelength-selective and wavelength-selective TPV devices. Standard protocols for spatial uniformity of beam illumination, ¹¹⁶ light intensity calibration ¹¹⁷ and spectral mismatch correction of the solar simulator can be found elsewhere. ¹¹⁸

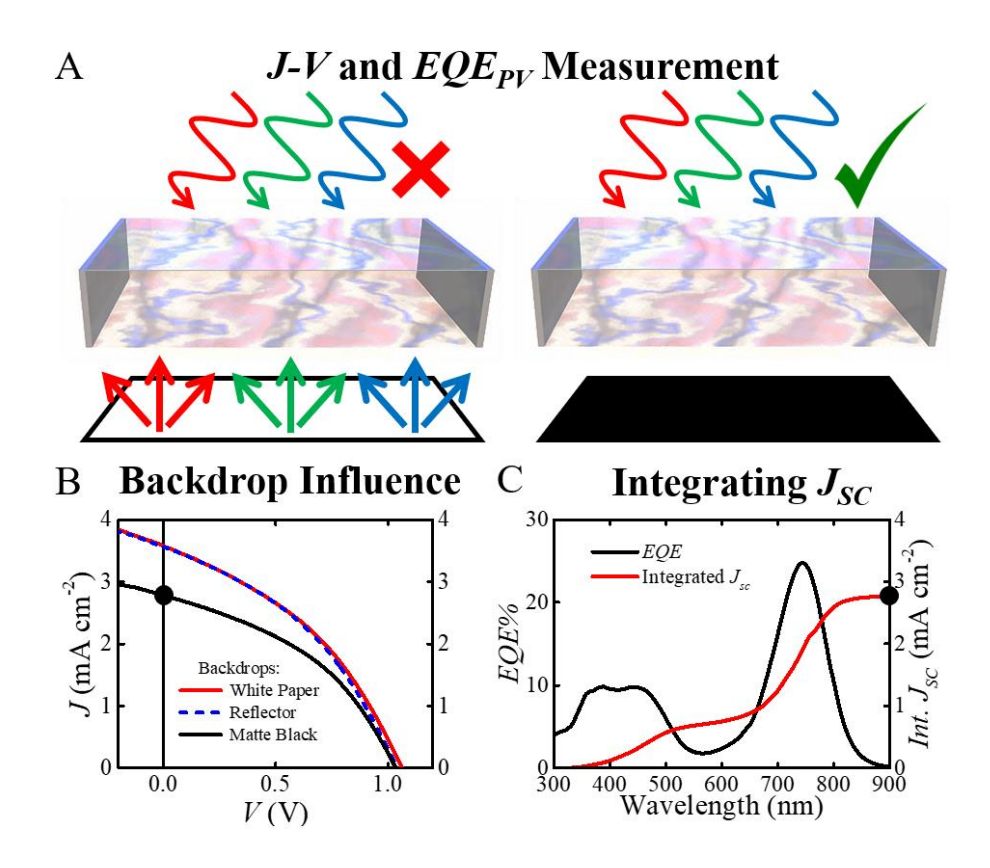


Figure 3.1 Standard characterization of TPV device photovoltaic performance.

(A) Schematic showing the bifacial nature of TPVs that leads to a "double-pass" effect in J-V and EQE measurements. A matte black backdrop is necessary to avoid overestimation. (B) J-V characteristic comparison of the same NIR-selective harvesting TPV device using different backdrop conditions. J-V data are measured under simulated AM1.5G solar illumination (xenon arc lamp with the spectral mismatch factor of 0.97 \pm 0.03). (C) J_{SC} integrated from the EQE_{PV} matches the J_{SC} extracted from J-V characteristics with the matte black backdrop.

Nonetheless, there are still key nuances that are introduced with TPVs compared to traditional opaque cells. Additional consideration for J-V and EQE_{PV} measurements of TPVs are required. For example, TPV devices are intrinsically bifacial, which allows illumination from both

sides as shown in **Figure 3.1**A. A matte black background should be placed behind the tested device during J-V and EQE_{PV} measurements to eliminate backside illumination or reflection ("double-pass" effect) from the test environment. In an uncontrolled environment where there is a scattering or reflective surface behind the device, significantly overestimated J-V data can be obtained as shown in Figure 3.1B. Additional measurements with different surfaces behind the device (mirrors, scattering layers, etc.) at specified distances can be reported but should supplement (not replace) the standard single-pass measurement. To illustrate the effect of different backdrops on J-V measurements, a single NIR-selective TPV cell with large active area is tested with a masked area of 6.45 cm². Three different backdrop conditions (white paper, broadband reflector and matte black) are used while testing the J-V characteristics under illumination. All these scans are taken in a darkroom to eliminate contribution from other light sources. The results are shown in Figure 1B, and parameters are summarized in **Table 3.1**. With a white scattering layer or mirror reflector as the backdrop, the measured current densities are nearly 30% higher than the scans with black matte backdrop, which leads to an overestimated overall PCE of 47% from additional V_{OC} and FF overestimation. The inflated result originates from the "double-pass" effect, which is essentially the same in magnitude for either a reflective mirror or a scattering backdrop.

Table 3.1 summarizes the *J-V* characteristic parameters of the same TPV under different backdrop conditions, which highlight the impact from "double-pass" effect.

Table 3.1 Photovoltaic parameters of an example TPV cell tested with different backdrops.

Backdrops	J_{SC} (mAcm ⁻²)	$V_{OC}(V)$	FF%	PCE%	AVT%	CRI
White Paper	3.58±0.08	1.06±0.01	39±1	1.46±0.03		
Reflector	3.56 ± 0.07	1.03±0.01	39±1	1.43 ± 0.02	58.8	89.4
Black Paint	2.78 ± 0.09	1.03±0.01	41±1	1.17±0.04		

In addition to the impact from the backdrop effect, the overestimation of the photocurrent can also stem from a number of other sources, including mismeasurements of the device area. For example, certain layers can exhibit relatively large conductivity, which leads to collected charge from outside of a patterned electrode area or even from the entirety of the substrate area. If multiple devices are tested on a substrate, such "edge effects" can potentially result in unrecognized device connection (either from inter-device connection or electrode overlap from poor shadow masking). In such cases, multiple devices simultaneously contribute to the photocurrent while a single device area is utilized in the corresponding *PCE* calculation, and this leads to a substantial overestimation of the photocurrent density and inflated *PCE*. To alleviate this concern, an opaque mask with a single aperture with well-defined area value should be attached to the front surface of the PV cell being tested to minimize this photocurrent overestimation (whether there is one or more device on a substrate). 115–117

One of the first and most important consistency checks for a traditional PV cell is the comparison of the photocurrent density extracted from J-V and from the integrated EQE_{PV} . The EQE_{PV} therefore should be reported for all TPVs and LSCs/TLSCs. This further eliminates concern over photocurrent overestimation. The convolution of the EQE_{PV} with the AM 1.5G photon flux should strictly match the J_{SC} from J-V measurements for the same PV device as shown in Equation 1.6. As a typical example, the EQE_{PV} of the same NIR-selective TPV used to compare the influence of the backdrops is shown in Figure 3.1C, where the integrated J_{SC} matches that from the J-V measurement with the matte black backdrop. The integrated J_{SC} from the EQE_{PV} spectrum should be provided as a consistency check for all future TPV performance reports.

3.2 Transmittance, Reflectance and Absorptance Spectra Measurements

Transmittance Measurement

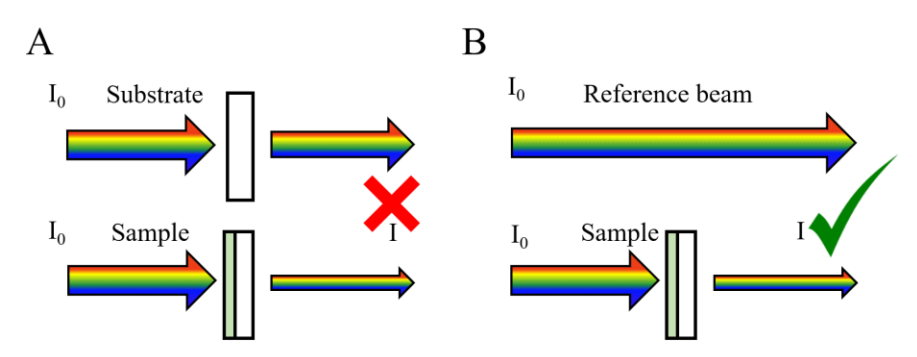


Figure 3.2 Schematic showing how to measure the transmittance spectra of TPV devices. Note that no reference sample should be utilized in double-beam spectrometers, and the reflectance spectrum should be measured separately.

To enable adoption in practical applications (e.g., architectural window glass and mobile surfaces), aesthetic quality is just as important as photovoltaic performance for TPV devices. Aesthetic quality can be quantitatively evaluated from three main figures of merit: the AVT, color rendering index (CRI), and CIELAB color coordinates (a^*, b^*) . Both the AVT and color coordinates are often the first metrics assessed for many glasses, greenhouses, and electronics (display) industries and are utilized as go-no-go criteria for practical integration or deployment (regardless of *PCE*). The calculation of *AVT*, *CRI*, and color coordinates requires the transmittance spectrum of the TPV as input data.³ The addition of this measurement has created substantial confusion and actually requires reporting of both $T(\lambda)$ and the reflectance spectrum, $R(\lambda)$. Historically, solution-based transmittance measurements have utilized solvent-only cuvettes in the double-beam spectrometer as a reference to (nearly perfectly) subtract all reflectance and arrive at absorptance spectra as shown in Figure 3.2A. However, reflections are not so easily referenced from solid films due to complex optical interference and reflections for the tested device compared to reference pieces of glass. Thus, no reference sample should be used for TPV (or thin-films) in double-beam spectrometers as shown in Figure 3.2B. Reflectance spectra should then be measured separately and reported via direct reflectance measurements from each fully assembled TPV.

Reflectance spectra are critical to both the photon balance and as a secondary measure of the *CRI* and color coordinates.

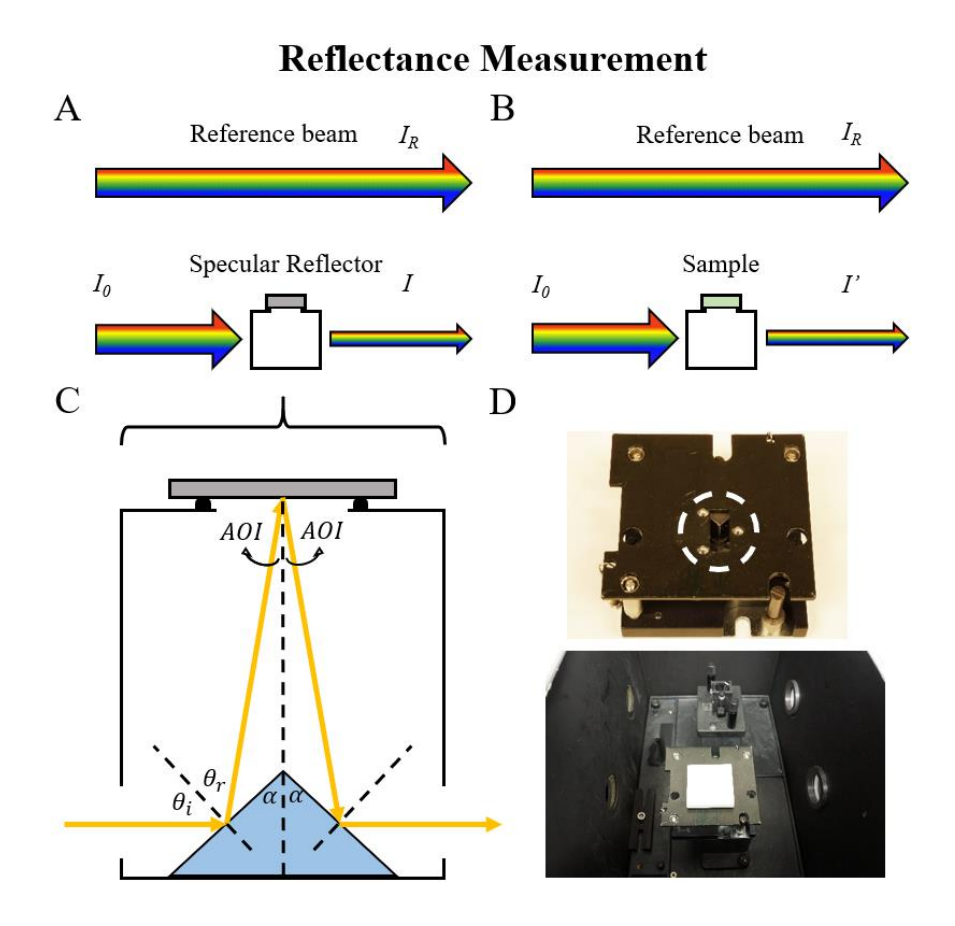


Figure 3.3 Schematic showing how to measure the reflectance spectra of TPV devices by using double-beam method.

(A) Background correction. (B) Sample testing. (C) Ray diagram inside the specular reflectance accessory. (D) Upper photograph: specular reflectance accessory alone. The dashed circle highlights the 3-dot sample support and the aperture for mounting the reflector or sample; Lower photograph: double-beam measurement setup in reflectance testing mode.

Similar to the transmittance spectrum ($T(\lambda)$) measurement shown in Figure 3.2B, the double-beam UV/VIS/NIR spectrometer can also be used to measure reflectance ($R(\lambda)$). With double-beam measurements a near-normal specular reflectance accessory is installed on the sample beam side as shown in **Figure 3.3**A. A planar specular reflector with known reflectance spectrum ($R_{SR}(\lambda)$) is applied to run the background correction calibration. It is recommended to re-

measure the same planar specular reflector after calibration to confirm this gives an $R(\lambda)$ of 100% at every scanned wavelength. Then the TPV sample can be measured as shown in Figure 3.3B. $R^*(\lambda)$ is acquired based on the assumption of 100% reflectance background correction after the calibration, however, metal-coated and dielectric optical mirrors used as the planar specular reflector in the calibration do not have a constant 100% R at every wavelength. Therefore, the reflectance of the sample is corrected as:

$$R(\lambda) = R_{SR}(\lambda) \cdot R^*(\lambda), \tag{3.1}$$

where R_{SR} is the known reflectance spectrum of the calibrating reflector. Figure 3.3C illustrates the simplified ray diagram inside the near normal specular reflectance accessory, where the term "near normal" implies a small angle of incidence (AOI). The angles satisfy these relations:

$$\alpha = \theta_i = \theta_r$$

$$2\alpha = 90^{\circ} + AOI \tag{3.2}$$

The isosceles triangular mirror has an obtuse 2α angle slightly larger than 90°, which ensures that $R(\lambda)$ data is acquired at near normal angle. On the other hand, the $R_{SR}(\lambda)$ data is usually provided by the supplier at small AOI. As long as the "near normal" condition is satisfied ($AOI < 15^\circ$, usually between 6° to 12°), the variation of $R_{SR}(\lambda)$ between 6° - 10° and 0° is negligible and the $R_{SR}(\lambda)$ difference between p-wave and s-wave is very small in the 300-1200 nm range according to Snell's Law. Therefore, $R(\lambda)$ measured by this method is accurate enough to be used for aesthetic quality parameter calculation or utilized in the photon balance. Figure 3.3D shows the photographs of the specular reflectance accessory alone and the double-beam setup in reflectance testing mode. It is noted that the sample should be held parallel to the fixture without any tilting that could lead to inaccurate measurements. It is also note that the aperture should be entirely covered by the test

sample area of the TPV, otherwise inaccuracy or inconsistency of the measurement can be generated.

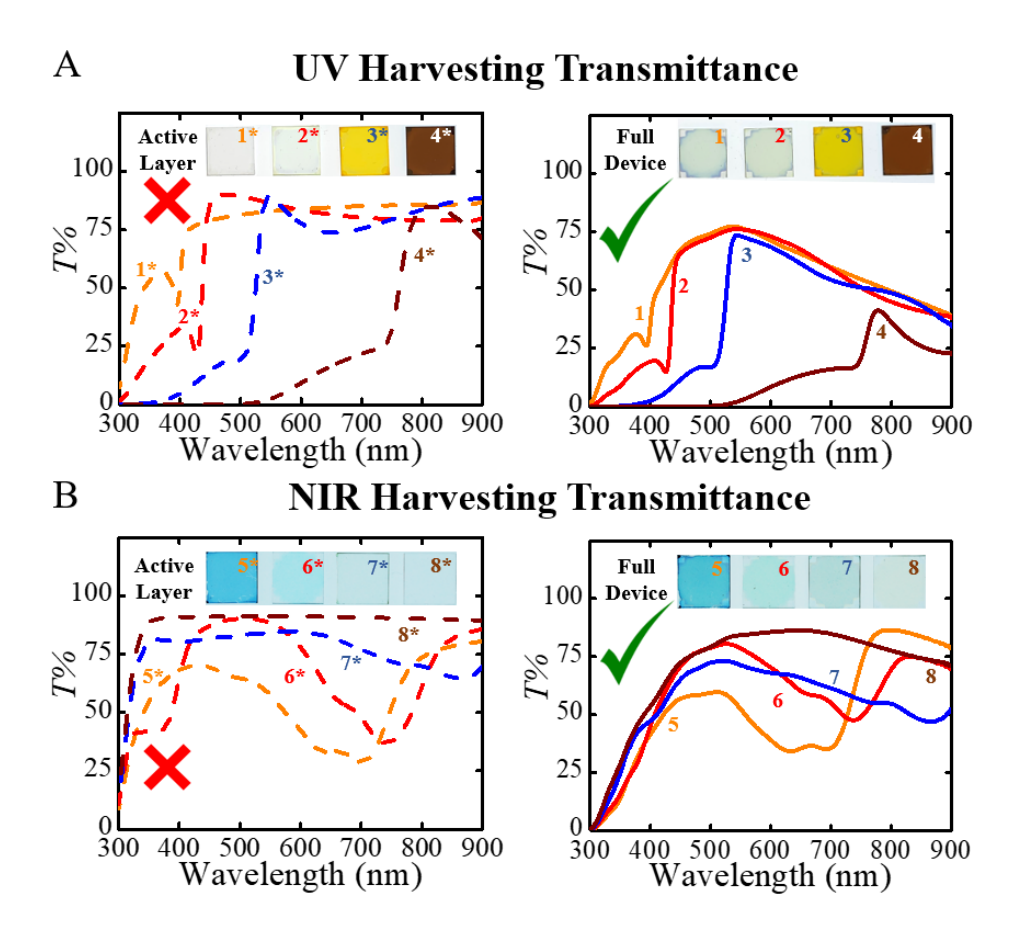


Figure 3.4 Transmittance spectra comparison.

(A) Transmittance spectra of various UV and blue-absorbing perovskite active-layer films with different composition (1*-4*) and complete perovskite TPV devices (1-4). Inset: photograph of the corresponding films or devices. (B) Transmittance spectra of various NIR-red-absorbing active-layer films (5*-7*; 8* is the glass substrate) and devices (5-7 are complete devices, and 8 does not have an active layer). Device 8 is fabricated to show the impact on the TPV transmittance from carrier transport layers and electrodes. Inset: images of the corresponding films and devices photographed in transmission mode.

We emphasize that when reporting AVT, CRI and CIELAB color coordinates of any TPV device, the transmittance and reflectance measurements should always be made through the entire device architecture with the beam spot confined within the device area. If the test beam spot is bigger than the device active area, a portion of the incident light can be directly collected by the

detector, which can lead to an overestimated $T(\lambda)$ or an underestimated $R(\lambda)$. The best practice is to measure the AVT and PCE on the same device. However, a suitable alternative is to test small area devices for the PCE while using un-patterned larger area devices for optical measurements, as long as the devices are made side-by-side. As an example, **Figure 3.4**A and B shows transmittance spectra of various compositions of halide perovskite active layer films (1^*-4^*) , NIR selective-harvesting active layer films (5^*-7^*) and complete TPV devices (1-4 for perovskite PVs and 5-7 for NIR-selective harvesting PVs). We emphasize that there is a significant difference in the transmittance spectra between the film and complete PV devices due to additional reflectance and optical interference.

3.3 Figures of Merit for Visible Transparency and Aesthetic Quality

Key figures of merit for visible transparency and aesthetic quality will be discussed in this section: AVT (also commonly referred to as visible transmittance, "VT", or visible light transmittance, "VLT") is independent of any defined visible wavelength range and relies solely on the photopic response of the human eye ($V(\lambda)$). The AVT should be reported as the integration (first moment) of the transmittance spectrum and AM 1.5G photon flux weighted against the photopic response of the human eye:

$$AVT = \frac{\int T(\lambda) \cdot V(\lambda) \cdot AM1.5G(\lambda)d\lambda}{\int V(\lambda) \cdot AM1.5G(\lambda)d\lambda}$$
(3.3)

This is also the definition long utilized by the window industry and recently introduced into the PV community. ¹⁰ The transmitted photon flux (AM $1.5G \cdot T(\lambda)$) and $V(\lambda)$ are plotted in **Figure 3.5**A and B for both perovskite and NIR-selective PVs, which illustrates that both the shape and absolute

value of $T(\lambda)$ can affect how the incident photon flux is attenuated (especially for wavelengths where $V(\lambda)$ is largest) and thus impacts the AVT. Photographs of various compositions of halide perovskite active layer films, different NIR harvesting active layer films and the corresponding TPVs are also shown in the inset of Figure 3.4A and B.

AVT Calculation A B $\frac{7}{80} 5 \times 10^{18}$ $\frac{4}{4} \times 10^{18}$ $\frac{1}{1} \times 10^{18}$ $\frac{1}{1} \times 10^{18}$ $\frac{1}{1} \times 10^{18}$ $\frac{3}{1} \times 10^{18}$ $\frac{3} \times 10^{18}$ $\frac{3} \times 10^{18}$ $\frac{3} \times 10^{18}$ $\frac{3} \times 10^{18}$ $\frac{3}$

Figure 3.5 Transmittance spectra for AVT calculation. AM 1.5G photon flux, transmitted photon fluxes through PV devices 1–8, and photopic response function $V(\lambda)$. We note that photon flux should be utilized for the AVT calculation.

In addition to the AVT, two key figures of merit for TPV aesthetics that should be reported are the CRI and CIELAB color space parameter set (a^*, b^*) , which quantify the rendered color fidelity of objects from a test light source and indicate relative color with respect to a reference illumination source. However, in applying this analysis to TPVs, there are nuances that need to be noted. In particular, it is a combination of both color coordinates and CRI that define the acceptable range of optical properties for window applications. The CRI is commonly utilized in the lighting and display industries to assess how closely an artificial light source resembles a blackbody radiator spectrum of a particular color temperature. CRI varies between 0 and 100: a value of > 90 is generally considered to be of excellent quality for the lighting industry but has different requirements that are dependent on color coordinates for TPVs. For CRI calculations, the

transmitted energy flux, $P(\lambda)$, i.e., AM 1.5G· $T(\lambda)$ is treated as the "test light source", and AM 1.5G should always be used as the "reference illumination source" rather than the Planckian blackbody radiator with closest correlated color temperature (CCT) to the transmitted source. We emphasize that because of the way the CRI calculations and color functions are defined, it is the energy flux that needs to be utilized for AM 1.5G and not the photon flux as might be expected given how human vision works. Chromatic adaption should also be applied when necessary.

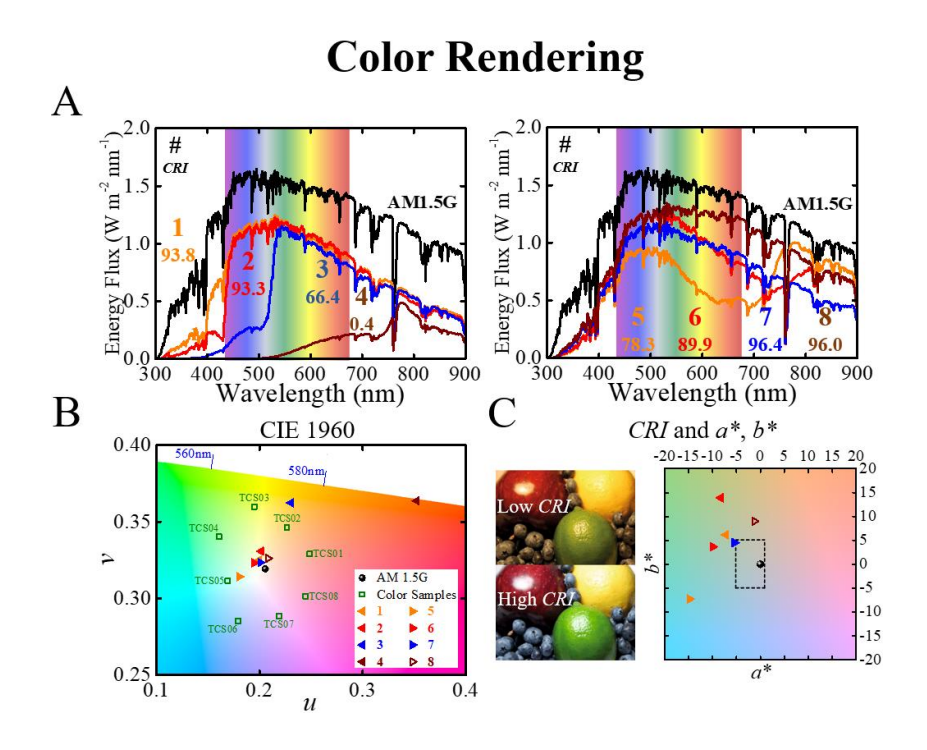


Figure 3.6 Color rendering.

(A) AM 1.5G energy flux and transmitted energy fluxes of PV devices 1–8. We note that it is energy flux that should be utilized for CRI calculations based on the construction of the CRI formalism. Note that as the UV absorption cut-off increases beyond 435 nm or the NIR absorption peaks decreases below 675 nm, the CRI drops quickly, as outlined in Table S3.2, resulting in strongly tinted films and devices. On the UV side, this leads to positive values of $(b^* \text{ or } a^*)$, while on the NIR side, this leads to negative values $(b^* \text{ or } a^*)$, where modestly negative values of a^* and b^* are more acceptable to the window industry. (B) CIE1960 color space used to calculate CRI with test color samples (TCS01–TCS08) and PV devices 1–8. AM 1.5G is also included as the "reference light source." (C) Comparison of objects illuminated by high and low CRI light source (left): under low CRI conditions; for example, blueberries look like blackberries. CIELAB color space (right): the dashed box illustrates the region of acceptable tinting for many massmarket architectural glass products. Note: PV devices 3 and 4 are strongly tinted in visible and their corresponding (a^*, b^*) coordinates are outside of the shown scale.

Integrating the CIE 1931 XYZ color matching functions with these source spectra (i.e., AM 1.5G or AM 1.5G· $T(\lambda)$) as shown in **Figure 3.6**A) gives the corresponding sets of (X, Y, Z) tristimulus values, and tristimulus values are then converted to determine the coordinates (x, y) in CIE 1931 color space (CIEXYZ). The (x, y) coordinate of AM 1.5G is (0.3322, 0.3439) with *CCT* of ~5513 K. For *CRI* calculations, the tristimulus values of various light sources are further converted into (u, v) coordinates of various light sources in CIE 1960 uniform color space (CIELUV) as shown in Figure 3.6B. As the selective harvesting cutoff blue-shifts into the UV range (from device 4 to 1 in Figure 3.4A) or as the selective harvesting peaks red-shift to the NIR range (from device 5 to 7 in Figure 3.4B), in CIELUV the (u, v) coordinates approach the "reference source" point AM 1.5G with minimized tinting and improved visible transparency.

The definition of color includes both chromaticity (u, v) and luminous intensity L ("brightness" for light source and "lightness" for physical objects). A color sample (i) will exhibit color differences consisting of chromaticity differences (Δu_i^*) and lightness differences (ΔL_i^*) when illuminated with the reference source or a transmitted source. Since the shape of $T(\lambda)$ determines how well a transmitted source can maintain the color rendering of AM 1.5G, the geometrical distance between the point of a transmitted source and the point of the reference AM 1.5G in the chromaticity coordinate system illustrates the chromaticity difference. There are 8 standard test-color samples used as a basis for these chromaticity and lightness differences that are averaged to calculate the CRI:

$$CRI = \frac{1}{8} \sum_{i=1}^{8} \left[100 - 4.6 \cdot \sqrt{(\Delta u_i^*)^2 + (\Delta v_i^*)^2 + (\Delta L_i^*)^2} \right]$$
(3.4)

In CIELAB color space, the calculation of (a^*, b^*) coordinates also starts from the tristimulus values of the reference source (X_0, Y_0, Z_0) and the transmitted source (X_t, Y_t, Z_t) , which can then be transformed into a set of (L^*, a^*, b^*) values by:

$$L^* = 116 \cdot f\left(\frac{Y_t}{Y_0}\right) - 16$$

$$a^* = 500 \cdot \left[f\left(\frac{X_t}{X_0}\right) - f\left(\frac{Y_t}{Y_0}\right) \right]$$

$$b^* = 200 \cdot \left[f\left(\frac{Y_t}{Y_0}\right) - f\left(\frac{Z_t}{Z_0}\right) \right]$$
(3.5)

where,

$$f(t) = \begin{cases} \sqrt[3]{t} & \text{if } t > (\frac{6}{29})^3 \\ \frac{841}{108} \cdot t + \frac{4}{29} & \text{if } t \le (\frac{6}{29})^3 \end{cases}$$

Note that reference source (X_0 , Y_0 , Z_0) is also called the "white point", which should be the AM 1.5G spectrum. The calculation of L^* is the same for both CRI and CIELAB. AM 1.5G has been used as the test standard for incident power since 1970s, and it is therefore the AM 1.5G energy flux that should always be the reference spectrum for CRI calculation in TPV applications (additional spectrum, e.g., the spectra of a backlit display, can also be utilized in these calculations as a supplement for display mounted TPVs). The AM 1.5G and transmitted energy fluxes (AM 1.5G· $T(\lambda)$) for various PVs (device 1-8) are plotted in Figure 3.6A as the "reference source" and "test sources" power spectra. ¹²⁰

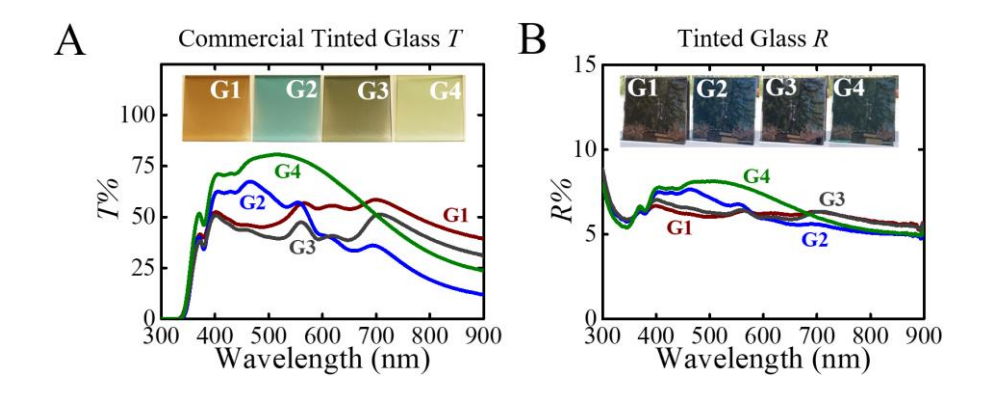


Figure 3.7 Exemplary commercial tinted glass samples.

T and R spectra of commercial tinted glass sheets: bronze (1), blue (2), grey (3), and green (4). A summary of CRI and (a^*, b^*) values are provided in Table S2. Inset: photographs of the transmitted and reflected color of C1–C4 glass samples.

A comparison of objects illuminated with low and high *CRI* light sources is shown in Figure 3.6C (left). We note that *CRI* is not a function of *AVT*, but rather the shape of the spectrum through the visible (i.e., it is possible to have an *AVT* of 10% and a *CRI* of 100 if the transmittance spectrum is flat through the visible). Transmittance and reflectance spectra of several commercial tinted glass samples are plotted in **Figure 3.7**A and B, respectively. **Table 3.2** summarizes the aesthetic quality parameters of various films, TPVs and glass samples included in this discussion.

Table 3.2 Summary of aesthetic quality parameters of various samples including commercial tinted glass (C-Glass).

Samples	AVT%	CRI	CIELAB (a*, b*)
AM 1.5G	100	100	(0, 0)
UV-Film-1*	83.0	96.4	(-0.04. 3.04)
UV-Film-2*	85.3	94.8	(-7.36, 8.59)
VIS-Film-3*	70.2	66.3	(-2.29. 69.6)
VIS-Film-4*	4.9	0	(30.0, 42.9)
Red-Film-5*	52.8	73.7	(-13.4, -14.1)
NIR-Film-6*	85.9	85.2	(-10.5, -2.0)

Table 3.2 (cont'd)

Samples	AVT%	CRI	CIELAB (<i>a</i> *, <i>b</i> *)
NIR-Film-7*	84.1	98.4	(-0.6, 1.6)
Substrate-8*	91.4	99.9	(-0.2, 0.1)
UV-Device-1	73.9	93.8	(-7.2, 6.2)
UV-Device-2	73.8	93.3	(-8.3, 13.9)
VIS-Device-3	60.0	66.4	(-1.7. 67.6)
VIS-Device-4	4.6	0.4	(25.7, 41.9)
Red-Device-5	38.1	78.3	(-14.8, -7.3)
NIR-Device-6	63.6	89.9	(-9.9, 3.6)
NIR-Device-7	66.0	96.4	(-5.4, 4.5)
Ctrl-Device-8	85.7	96.0	(-1.3, 9.0)
C Glass-1 T	52.8	93.1	(2.4, 6.4)
C Glass-2 T	51.2	77.6	(-10.8, -12.2)
C Glass-3 T	42.2	93.5	(-0.5, -1.7)
C Glass-4 T	76.3	90.8	(-7.7, 1.0)
C Glass-1 R	N/A	98.8	(0.4, -0.1)
C Glass-2 R	N/A	90.1	(-2.0, -3.8)
C Glass-3 R	N/A	94.6	(-0.4, -1.4)
C Glass-4 R	N/A	92.6	(2.6, -0.6)

Note that most widespread commercial is much less tinted than the C-Glass samples. Also note the progression of *CRI* as the transitions move from the UV to VIS and VIS to NIR.

In the window industry, CRI is applied to evaluate the ability of portraying a variety of colors of the transmitted daylight through glazing compared to those observed directly under daylight without the glazing. Threshold values for the CRI in the window industry depend on the position of the color coordinates described below: the CIELAB color space coordinates (a^*, b^*)

(Figure 3.6C (right)) are typically the first metric utilized to assess acceptable ranges of color tinting for mass market architectural glass products. While u and v are used to calculate CRI, we recommend reporting a^* and b^* to characterize position in the color space, which is the standard in the window industry. On this scale, a^* and b^* at the origin (0, 0) is colorless. The color coordinate box that defines the region of acceptable tinting for many mass-market architectural glass products is -5< a^* <1 and -5< b^* < 5. 121 Tinted glass with values near the origin (neutral or grey) or negative values of a^* (greenish) and negative b^* (blueish) are found to be more visually acceptable for modern window deployment than positive values of a^* (reddish) and positive b^* (yellowish). CRI is interdependent with a^* and b^* as all parameters are defined by the same transmittance spectrum; therefore, the CRI threshold requirements for one corner of the acceptable color coordinate box will differ from the CRI requirements in other regions. For example, bluetinted coatings (i.e., negative a^* and b^*) only require CRI > 90 because the color of the tint is more acceptable; whereas less desirable yellow- or red-tinted coating (e.g., a^* or b^* close to 0 or positive) require higher CRI > 95 to remain in an acceptable color range. For this reason, it is imperative that both values are reported.

3.4 Quantitative Assessment of TPV Aesthetics

Similar considerations can also be applied to reflected color, and both transmission and reflection effects should be considered to compose representative photographs for publication. Assessing aesthetic parameters in transmission mode qualitatively captures the aesthetics perceived when viewing the scenery through a window and the quality of natural daytime lighting provided into a building. The same methodology can be applied and reported in reflection mode

(using the reflection spectra). The glass-side reflection characterizes the aesthetic of a building when viewed from the outside during the day when external reflected light dominates, whereas the coating-side reflection characterizes the color of glass perceived from inside the building at night when internal reflection dominates. It is particularly important to be aware of such factors when qualitatively assessing the aesthetics of TPVs in reported photographs. Photographs on a white background primarily capture the transmitted aesthetic (inset of Figure 3.7A), photographs on black background primarily capture the reflected aesthetic of the surface facing the observer (inset of Figure 3.7B), and photographs with scenery behind the TPV are combination weighted by the specific lighting in the photograph (insets of **Figure 3.8**A and B). We recommend at minimum publishing photographs with a white background, where the unobstructed background is visible for color reference (i.e., should look white), with other compositions used to supplement.

3.5 Measurement Validation

A B 100 T+R+EQE 80 300 400 500 600 700 800 900 Wavelength (nm) B 100 T+R+EQE 60 60 700 800 900 Wavelength (nm)

Photon Balance Check

Figure 3.8 Exemplary commercial tinted glass samples.Photon balance check for a UV-selective harvesting (left) and NIR-selective harvesting TPVs (right). Inset: photographs of the corresponding TPV devices.

In addition to the integrated J_{SC} consistency check described in Section 3.6, the photon balance (at every wavelength) should be used to check all key TPV devices:

$$A(\lambda) + R(\lambda) + T(\lambda) = 1 \tag{3.6}$$

where $A(\lambda)$ is the absorption spectrum of the entire TPV device. However, since it is difficult to directly measure $A(\lambda)$ and $EQE_{PV}(\lambda) \leq A(\lambda)$ we can take the limit of internal quantum efficiency $IQE_{PV}(\lambda) \leq 1$ (unless multiple exciton generation (MEG) exists) so that the following relation should be satisfied at every wavelength with independent measurements of $EQE_{PV}(\lambda)$, $T(\lambda)$ and $R(\lambda)$:

$$EQE_{PV}(\lambda) + T(\lambda) + R(\lambda) \le 1$$
 (3.7)

In the case that MEG is present, the EQE_{PV} term in Equation 3.7 must be replaced with EQE_{PV}/IQE_{PV} . In the case of multi-junction devices, the IQE_{PV} is reduced in exchange for an increase in output voltage (multiple absorbed photons generate one electron/hole pair to obtain higher potential), so that the EQE_{PV} in Equation 3.7 should be replaced by the summation of the EQE_{PV} spectrum of all sub-cells. Thus, the photon balance consistency check should be applied to every type of TPV. Two examples of this simple consistency check are shown for both UV- and NIR-selective harvesting TPVs in Figure 3.8A and B, respectively. It is noted that this balance can also be used to estimate the IQE_{PV} (replacing EQE_{PV} in Equation 3.7 with EQE_{PV}/IQE_{PV}) in the same report, provided Equation 3.7 is still shown to be met. We also encourage reporting of parasitic losses (e.g., parasitic absorption losses from transport layers and electrodes) whenever possible. At a minimum, all reports on TPVs should provide independent $EQE_{PV}(\lambda)$, $T(\lambda)$ and $R(\lambda)$ measurements and provide such validation checks for each emphasized device to minimize potential experimental errors.

3.6 Summary

In summary, various emerging TPV technologies provide a compliment to traditional PVs to help meet the growing energy demand of the world. A rapid increase in TPV reports indicate excitement for this emerging field. However, a misunderstanding of the measurements needed to characterize these new devices and the target metrics for widespread adoption has created substantial confusion in the literature. In this chapter, standard protocols of TPV characterization are clearly outlined, and common pitfalls are described. While the PCE for TPVs should be measured in similar fashion to the opaque counterparts, there are additional nuances to their measurement. Further, we discuss the additional measurements required for characterizing TPV devices. AVT, CRI, and (a^*, b^*) are critical figures of merits that are as important as PCE and EQE_{PV} , if not more so. We describe how to accurately measure and report AVT, CRI, and (a^*, b^*) metrics, outline key targets for these properties in the window industry, and show these calculations for a number of TPV materials and devices. In addition, the photon balance is used as a tool to validate independent spectral measurements of EOE_{PV} , transmittance, and reflectance. This work outlines necessary approaches for characterizing and reporting TPVs which are an exciting new paradigm for PV research that can enable new opportunities and new applications for solar energy harvesting.¹²

Chapter 4 Standard Characterization Protocols for Luminescent Solar Concentrators

Although LSC, TLSC, and thin-film TPV technologies as shown in Chapter 3 share some similarities in the methods for device characterization, ¹² LSC/TLSC characterization is filled with a greater range of possible measurement errors. LSCs/TLSCs appear to be simple devices, and because of this, researchers from many fields including materials science to chemistry, optics, physics, and electrical engineering have joined the LSC research community. However, the characterization of LSCs is surprisingly nuanced and more challenging than that of conventional PVs or TPVs. The purpose of this chapter is to demonstrate standardized LSC characterization protocols by comparatively measuring the key performance parameters in both correct and erroneous approaches. Simplifications of the device measurements are outlined, while yielding reliable results. Common mistakes in the measurements are pinpointed with analysis of possible causes that can inflate performance. Parameters to evaluate the visible (VIS) transparency and aesthetic quality of LSC and TLSC devices are given with several examples. Finally, validation and consistency checks from independent experimental measurements are illustrated, which should be included in future LSC reports.

4.1 Photophysical Properties Measurements

As introduced in Chapter 2, luminophore materials with various photoluminescence mechanisms play a key role in LSC systems, which determine the corresponding photovoltaic performance, aesthetic quality, spectral selectivity. The photophysical properties of the luminophores are the first part of dataset to be collected in LSC/TLSC characterization and reporting protocols, which include the absolute absorptance $(A(\lambda))$ and normalized emission

spectra $(PL(\lambda))$ and photoluminescence quantum yield (QY) of the luminophore in the waveguide (either coated as luminophore/matrix thin-film or embedded within the transparent waveguide matrix).

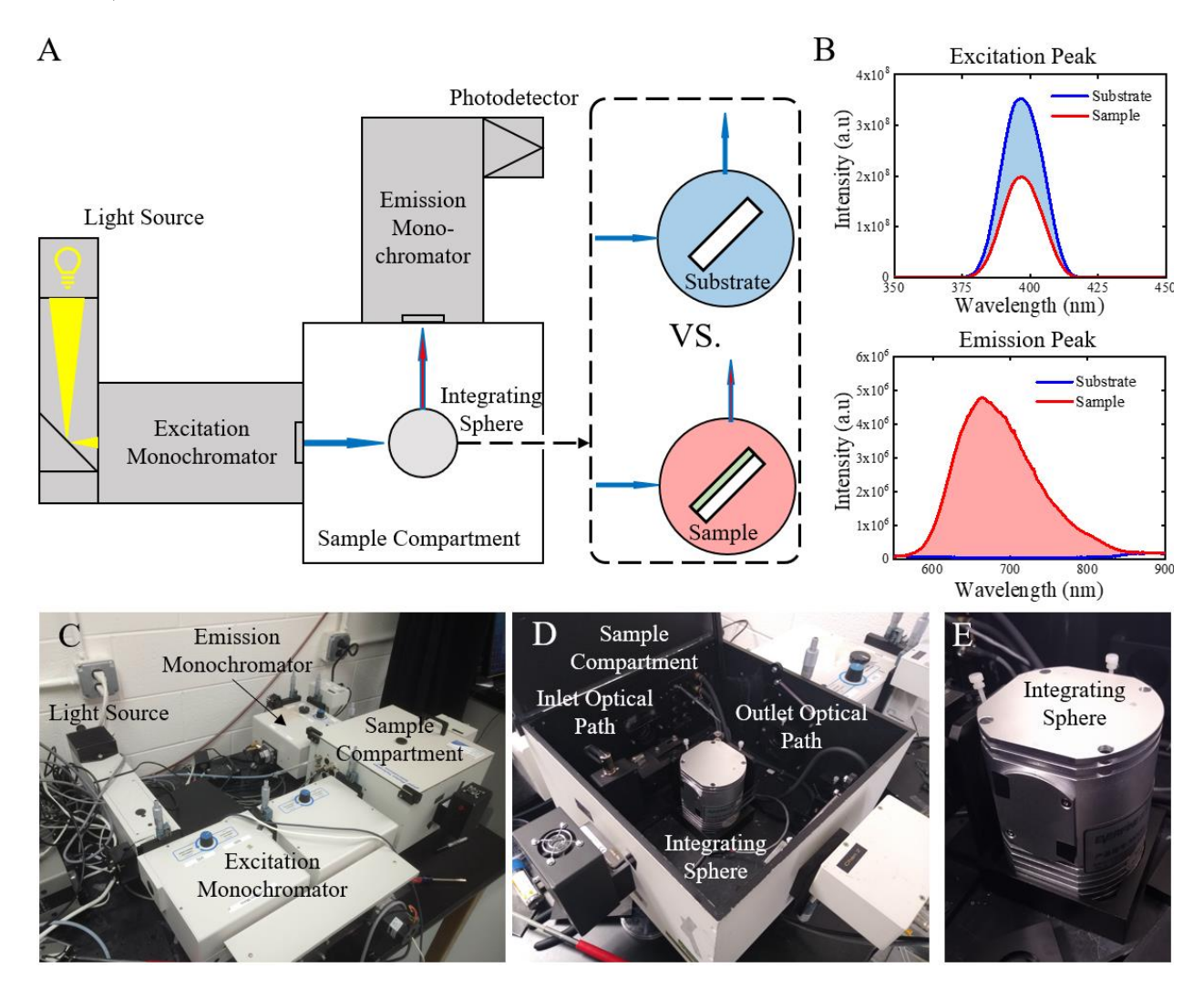


Figure 4.1 Photoluminescence spectrometer layout for *PLQY* **measurement.**(A) Schematic of photoluminescence spectrometer for *PLQY* measurement. (B) Exemplary absorption and emission profiles of *PLQY* calculation. (C) Photograph of photoluminescence spectrometer in MOE lab. (D) Photograph of the inside sample compartment. (E) Zoomed-in photograph of integrating sphere.

The $A(\lambda)$ can be calculated as $A(\lambda) = 1 - T(\lambda) - R(\lambda)$ as addressed in Equation 3.6. The $PL(\lambda)$ spectrum can be measured with photoluminescence spectrometer. The typical layout of a photoluminescence spectrometer is shown in **Figure 4.1**A: the light source provides panchromatic

incident light, and then the excitation monochromator mechanically selects and transmits a single-wavelength of light to excite the sample (solution cuvette or thin-film sample coated onto a substrate) located in the sample compartment. Then the emitted photoluminescence from the sample enters the emission monochromator in an emission scan mode and is collected by the attached photodetector. A background scan is performed for each sample with the same excitation and emission wavelength setting so that the emission spectrum is accurately measured. Optical filters (including both short-pass filters and long-pass filters) are necessary tools to minimize the influence from the background noise and false signals (e.g., wavelength doubling). Filters can be placed at either the entrance or exit of the sample compartment according to the certain excitation/emission combination.

The QY of a luminophore is defined as the ratio of number of emitted photons per absorbed photon. Therefore, for luminophores with conventional downshifting photoluminescence mechanism, the maximum QY value is 100%; for luminophores with quantum-cutting or multi-exciton generation mechanism, the maximum QY value is 200%; and for luminophores with upconversion mechanism, the maximum QY value is 50%. To accurately measure the absolute QY value of a sample, an integrating sphere located within the sample compartment is required: an integrating sphere is an optical instrument consisting of a hollow spherical cavity with the interior surfaces covered with nearly ideal diffusive reflective coating. With small holes functioning as entrance and exit ports, all entered or emitted light can uniformly distribute everywhere on the inner surface within the integrating sphere due to multiple scattering, diffusive and reflective events. Therefore, the effects of original direction of entered or emitted light are minimized, which serves for the purpose of QY measurement as shown in Figure 4.1A: two emission scans need to be performed for each QY measurement with the same excitation/emission configuration. The first

scan is performed with a reference substrate or a cuvette containing only the solvent in the integrating sphere, which is used to measure the total excitation light intensity. The second scan is performed with testing samples to determine the emission light intensity. Notably, the emission scan range should include both the excitation and emission wavelength ranges. To calculate the absolute QY value, the reference scan is subtracted from the sample scan at both the excitation and emission wavelength ranges. Figure 4.1B shows an example of this calculation: the shaded blue area indicates the intensity difference of the excitation light between the reference scan and the sample scan, whereas the shaded red area indicates the intensity difference of the emission light between the reference scan and the sample scan. With both light intensities recorded, the absolute QY can then be calculated as:

$$QY = \frac{N_{Emission}}{N_{Absorption}} = \frac{\alpha(\lambda) \cdot \int \frac{\lambda}{hc} \left[I_{Sample}(\lambda') - I_{Reference}(\lambda') \right] d\lambda}{\alpha(\lambda) \cdot \int \frac{\lambda}{hc} \left[I_{Reference}(\lambda) - I_{Sample}(\lambda) \right] d\lambda}$$
(4.1)

where $N_{Absorption}$ and $N_{Emission}$ represent the number of absorbed photons at excitation wavelength range and the number of emitted photons at emission wavelength range, respectively. $A(\lambda)$ is the calibration factor for the measurement setup, which can be acquired with a standard illumination light source with known emission spectrum. h is the Planck's constant and c is the speed of light. Notably, λ indicates the excitation wavelength range and λ' indicates the emission wavelength range, which is consistent with the definitions in Equation 2.2. Therefore, $I_{Sample}(\lambda')$ is the light intensity of the sample scan at the emission wavelength range, $I_{Reference}(\lambda')$ is the light intensity of the reference scan at the excitation wavelength range, and $I_{Reference}(\lambda)$ is the light intensity of the reference scan at the excitation wavelength range, and $I_{Reference}(\lambda)$ is the light intensity of the reference scan at the excitation wavelength range, and $I_{Reference}(\lambda)$ is the light intensity of the reference scan at the excitation wavelength range, and $I_{Reference}(\lambda)$ is the light intensity of the reference scan at the excitation wavelength range, and $I_{Reference}(\lambda)$ is the light intensity of the reference scan at the excitation wavelength range, and $I_{Reference}(\lambda)$ is the light intensity of the reference scan at the excitation wavelength range, and $I_{Reference}(\lambda)$ is the light intensity of the reference scan at the excitation wavelength range, and $I_{Reference}(\lambda)$ is the light intensity of the reference scan at the excitation wavelength range.

luminophore, a plot of $A(\lambda)$ vs. $PL(\lambda)$ should be provided with the PLQY value of the luminophore in the waveguide matrix.

4.2 J-V Characteristics of LSC/TLSC Systems

Similar to any other PV systems, the first key data for reporting the photovoltaic performance of LSCs/TLSCs is the *J-V* characteristics acquired under standard illumination as addressed in Chapter 1. We emphasize that such data are necessary for all PV and LSC reports, despite many LSC reports missing such data. The overall *PCE* of an LSC system is the product of the two component efficiencies:^{9,124}

$$\eta_{LSC} = \eta_{Opt}^* \cdot \eta_{PV}^* = \frac{J_{SC} \cdot V_{OC} \cdot FF}{P_0}$$
(4.2)

Equation 4.2 is based on the combination of Equation 1.4 and Equation 2.1, where η_{PV}^* is the efficiency of the edge-mounted PV cell under the downshifted flux of the luminophore and η_{Opt}^* is the overall optical efficiency. The two component efficiencies η_{PV}^* and η_{PV}^* are helpful to understand the working principle of the LSC system. However, we emphasize that any LSC or TLSC system should be treated the same as any other photovoltaic device – reporting only the overall optical efficiency (η_{Opt}^*) or optical efficiency at a specific wavelength ($\eta_{Opt}(\lambda)$) is not a sufficiently reliable way to represent the *PCE* of an LSC system (η_{LSC}) as we explain below. The best approach to acquire η_{LSC} is directly from current density-voltage (J-V) characteristics with connections made to edge-mounted PVs (in series or parallel) under standard illumination AM 1.5G. ^{125,126} In Equation 4.2, J_{SC} is the short-circuit current density, V_{OC} is the open-circuit voltage, FF is the fill factor, and P_0 is the incident solar power density (in Wm⁻²nm⁻¹) (i.e., AM 1.5G energy

flux as the standard input). Since the area receiving incident power is the front surface of the waveguide, the measured short-circuit current density (J_{SC}) should always be divided by the area of the waveguide front surface rather than the area of the edge-mounted PV cells (a common mistake in J_{SC} and η_{LSC} calculations for LSCs).

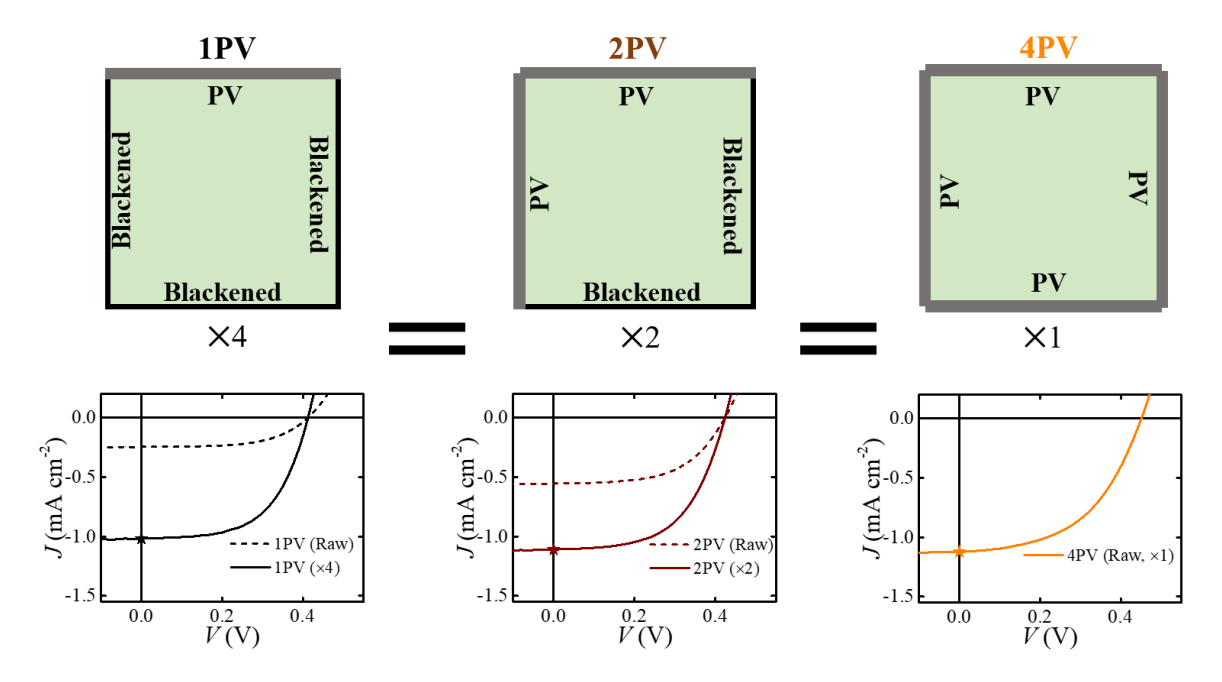


Figure 4.2 Equivalent layouts for *J-V* **measurement for a TLSC system.**Both the raw and corrected *J-V* curves are also shown in the same plot for these three layouts, respectively.

In real-world applications, all four edges would typically be mounted with PV cells to maximize the output electrical power. For research purposes, an appropriate simplification (due to the symmetry) is to mount two edges with PV cells in parallel to make the configuration less complicated, simplify the wiring connections, and make the system less susceptible to losses from current matching cells that can stem from PV cell-to-cell variability and cell dimension variations. In this case, the other two edges should be painted black to prevent any reflection from inside or outside the waveguide. It is also acceptable to mount one edge with a PV cell with the rest three painted black. The overall η_{LSC} can then be corrected by multiplying the current density by 2 or 4 for these two scenarios. **Figure 4.2** illustrates the equivalent layouts for *J-V* measurement for LSC

systems. By applying the corresponding corrections ($\times 4$ for "1PV", $\times 2$ for "2PV" and $\times 1$ for "4PV"), all three of the *J-V* equivalent layouts should lead to very similar photovoltaic performance.

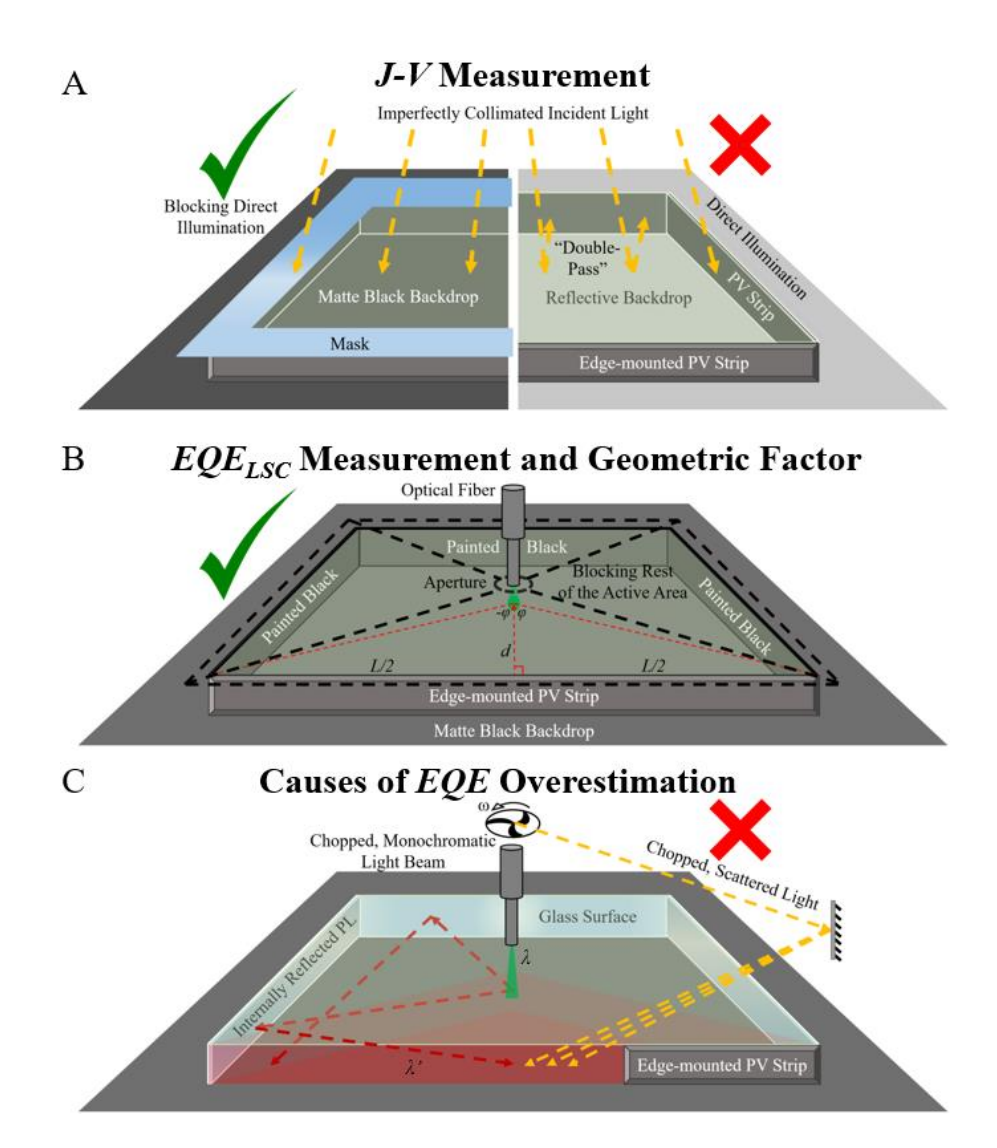


Figure 4.3 Schematic protocols for LSC characterization.

(A) Schematic illustrating how to measure the *J-V* characteristic of LSC systems. A matte black backdrop and an opaque mask are necessary to avoid photocurrent overestimation from "double-pass" and "direct illumination" effects. (B) Schematic showing the correct setup and the geometric factor for position-dependent EQE_{LSC} measurement. Note that only the incident beam is illuminated onto the front surface of the LSC waveguide, while the rest of the active area is masked. Three edges should be painted black to apply geometric correction (× g at each d) when only one edge is mounted with PV cell for easy connection. (C) Schematic showing the possible causes of EQE_{LSC} overestimation. Without masking, the edge-mounted PV can pick up signal from chopped light scattered by the test environment

Figure 4.3 (cont'd)

(yellow, dashed arrows) and internal reflected PL from any unpainted edges (red, dashed arrows), causing inflated EQE_{LSC} data. Note that the edge-mounted PV should extend across the entire length of the LSC but has been shortened in the schematic for clarity.

Figure 4.3A illustrates both appropriate and erroneous ways to conduct *J-V* measurements. Most LSC devices are also intrinsically bifacial, which allows illumination from both sides. Therefore, light scattering or reflection behind the tested device can contribute to the total light absorption. It is necessary to place a matte black backdrop behind the tested LSC to eliminate the double-pass of light. As noted in Chapter 3, nearly 30% overestimation of the J_{SC} can be made with a reflective or scattering backdrop, ¹² but this can be even greater for LSC since scattering from any reflective backdrop can result in direct illumination of the edge-mounted PV. For any LSC system, the electrical characterization should only account for the contribution from the waveguided photoluminescence reaching to the edge-mounted PV. As shown in Figure 4.3A, if the edge-mounted PVs are directly illuminated by an imperfectly collimated incident light, the overestimation of η_{LSC} (mainly from overestimated J_{SC}) can be substantial. Therefore, an opaque mask with well-defined area value should be closely placed in front of the LSC system to block any direct illumination. Such direct illumination not only leads to overestimation of the η_{LSC} but does so preferentially at smaller device areas so that the performance will not be representative of the scaling to larger area devices. To illustrate the direct illumination effect on J-V measurements, a NIR-selective harvesting TLSC (waveguide length (L) = 50.8 mm, front active area = 25.8 cm²) is edge-mounted with 1, 2, and 4 Si-PV cells (each PV cell has dimension of 50.8 mm by 6.35 mm) as outlined above (with detailed layouts illustrated in Figure 4.2).

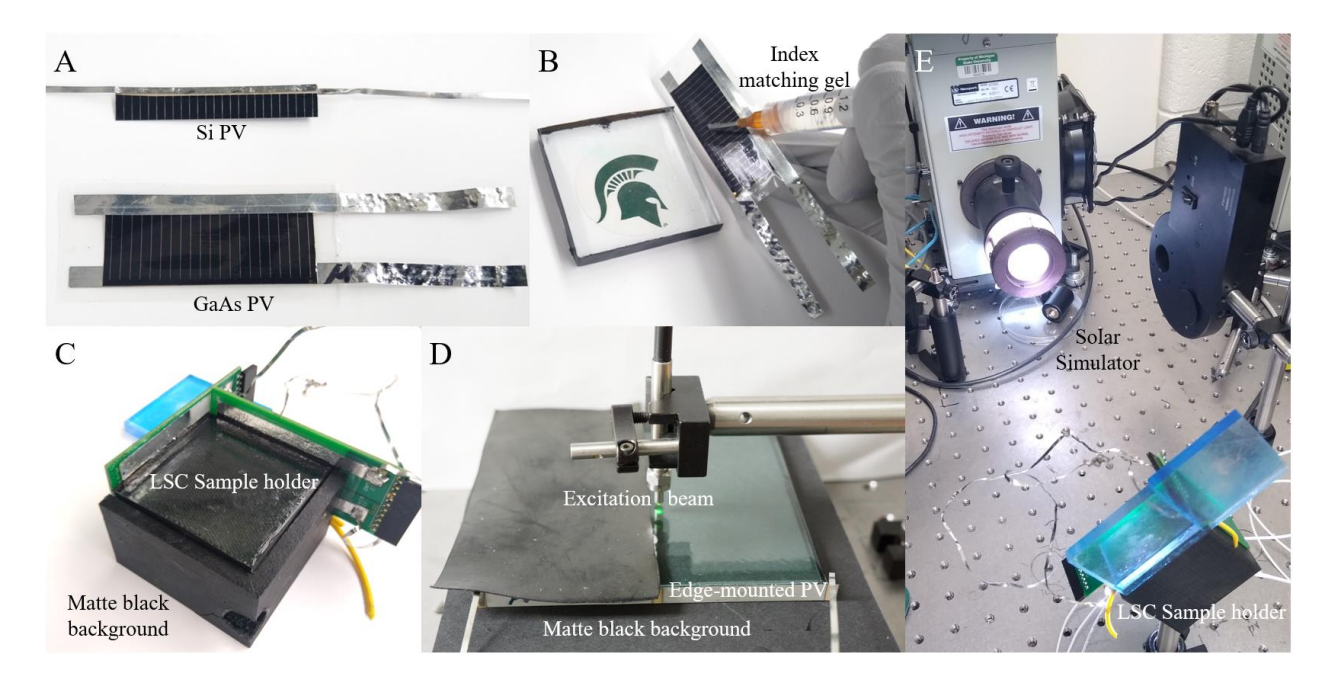


Figure 4.4 Photographs of actual LSC device assembly and characterization.

(A) Photograph of a Si PV cell and a GaAs PV cell. (B) Index gel is used to attach the PV cell onto the LSC waveguide edge. (C) Fully assembled LSC-PV system with two edge-mounted GaAs PV cells in a sample holder for *J-V* measurement. (D) Fully assembled LSC-PV with one edge-mounted Si PV for EQELSC measurement, excitation beam is moved along the waveguide centerline for position-dependence test, the left half of the TLSC waveguide front surface area is masked for comparison. (E) LSC-PV system inside the sample holder under illumination of solar simulator for *J-V* measurement.

Index matching gel (or glue) is applied to couple the PV cells to the waveguide edges to reduce flux loss between the waveguide edge and the PV cells as shown in **Figure 4.4**. The remaining unmounted edges are painted black to block the inlet and reflection of light. The raw current density curves are multiplied by 4, 2, and 1 as a correction, when mounting 1, 2, and 4 PV cells, respectively. The corresponding results are plotted in **Figure 4.5**A with parameters tabulated in **Table 4.1**.

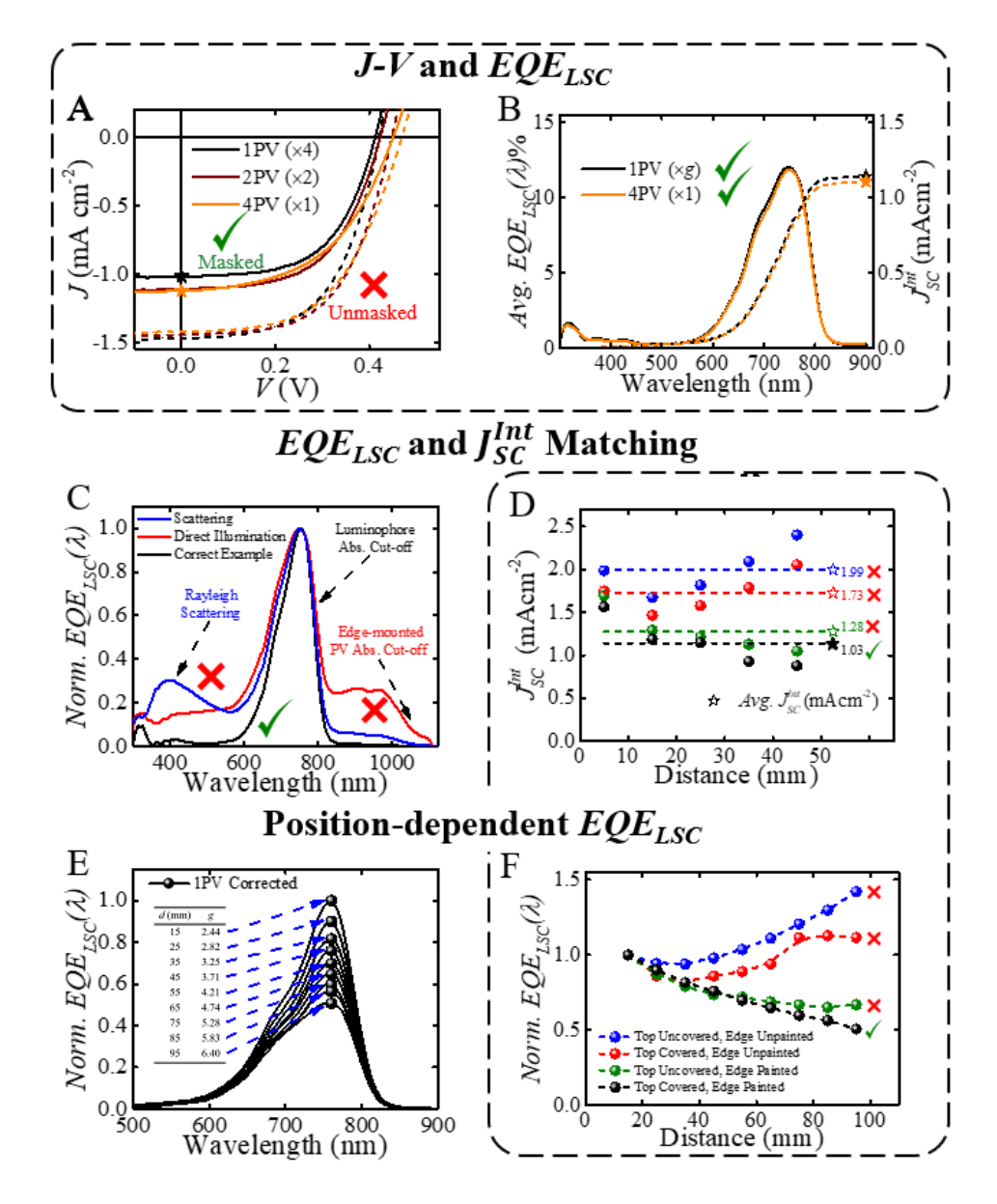


Figure 4.5 LSC Photovoltaic performance.

(A) J-V comparison of the same NIR-selective harvesting TLSC using different numbers of edge-mounted PV strips (wired in parallel) with and without applying a mask. J-V data are measured under simulated AM 1.5G solar illumination (xenon arc lamp with the spectral mismatch factor of 0.97 ± 0.03). Following the recommended protocols, the number of PV cells used should not significantly affect the result by more than 5% to 10%. (B) Comparison of $EQE_{LSC}(\lambda)$ spectra acquired from 1 (5 points along the centerline, corrected by \times g, then averaged) and 4 edge-mounted PV cells (averaged from 13 symmetrical positions on the waveguide with no correction). Both of the corresponding J_{SC}^{Int} match the J_{SC} extracted from J-V characteristics with matte black backdrop and mask shown in (A). (C) Common errors can be directly seen in $EQE_{LSC}(\lambda)$ measurement including scattering (sloped background) and direct illumination of the PV cell (additional offset with the PV bandgap cut-off visible). (D) J_{SC}^{Int} from $EQE_{LSC}(\lambda)$ at different positions (d: 5–45 mm with 10 mm interval, corrected by \times g, as spheres) and the corresponding averaged J_{SC}^{Int} (dashed lines pointing the stars).

Figure 4.5 (cont'd)

Various appropriate and inappropriate scenarios are included: blue (waveguide front surface uncovered and edges unpainted), red (waveguide front surface covered and edges unpainted), olive (waveguide front surface uncovered and edges painted), and black (waveguide front surface covered and edges painted, the only correct scenario). Note the severity of "internally reflected PL" effect originates from unpainted edges, "chopped and scattered light" effect originates from uncovered waveguide front surface, and both combined can affect the $EQE_{LSC}(\lambda)$ for J_{SC}^{Int} calculation.

Table 4.1 Comparison of photovoltaic parameters of the TLSC with and without mask.

Approaches	J_{SC}	J_{SC}^{Int}	V_{OC}	FF	η_{LSC}
(XCorrection)	(mAcm-2)	(mAcm ⁻²)	(V)	(%)	(%)
1PV Masked (X4)	1.02±0.09	1.14 (×g, Avg.)	0.41±0.01	59±1	0.24±0.02
1PV Unmasked (X4)	1.47 ± 0.08	1.14 (Ng, Avg.)	0.42 ± 0.01	57±2	0.35 ± 0.01
2PV Masked (X2)	1.11 ± 0.07	N/A	0.42 ± 0.01	57±1	0.26 ± 0.02
2PV Unmasked (×2)	1.44 ± 0.04	IV/A	0.44 ± 0.01	58±1	0.37 ± 0.02
4PV Masked (X1)	1.12±0.08	1 11 (Aug.)	0.44 ± 0.01	51±1	0.25 ± 0.02
4PV Unmasked (×1)	1.42±0.01	1.11 (Avg.)	0.46±0.01	54±1	0.36±0.01

The slight variation in J-V between 1, 2, and 4 edge-mounted PVs (with masking) stems from slight variability in the PV cells and the impact of slight differences in the wiring on the FF. The unmasked current densities can be more than 40% higher than the ones from the masked scans despite similar V_{OC} and FF values, resulting in dramatic η_{LSC} overestimation.

4.3 EQE_{LSC} Measurement and Matching Integrated J_{SC}

As with any other PV measurement, it is typically necessary to measure EQE_{PV} first, to be able to measure mismatch factors and set lamp intensities appropriately prior to the measurement. This is the case for any solar cell or concentrator device that is certified. While the mismatch can be applied after the measurement to correct the illumination intensity, it is preferable to apply it

first. Additionally, the comparison of the photocurrent densities extracted from J-V characteristic and integrated from EQE_{PV} is the most important consistency checks for any photovoltaic device. Thus, EQE spectra should also be provided in all LSC reports even though many articles fail to report such data. ^{12,115–117}

For EQE measurements of LSC systems ($EQE_{LSC}(\lambda)$), several key nuances should be noted. The most reliable way to measure $EQE_{LSC}(\lambda)$ is to mount all four edges with the same PV cells (material, size, etc.) in parallel, and take multiple scans at symmetrical positions all over the waveguide active area so that the average of these EQE_{LSC} spectrum can represent the whole waveguide for photocurrent integration. An example of this approach is plotted as orange curve in Figure 4.5B. However, to avoid unnecessarily complicated wire connections by mounting all four edges with PV cells in parallel, Figure 4.3B shows a simplified alternative to effectively measure EQE_{LSC} by mounting one edge with PV cell and painting the rest of the three edges black. Multiple raw EQE_{LSC} scans are taken at various distances between the excitation beam and edge-mounted PV cell (d) along the centerline. Then the $EQE_{LSC}(\lambda)$ at each d is calculated by multiplying the raw spectral data by the geometric factor (g):8.22.24

$$g = \frac{2\pi}{2\varphi} = \frac{\pi}{\tan^{-1}\left(\frac{L}{2d}\right)} \tag{4.3}$$

where 2φ is the angle facing the edge-mounted PV and L is the length of the waveguide as shown in both Figure 4.3B. This correction is only applicable along the centerline and when the other edges are required to be painted black. An evenly spaced series of corrected measurements can then be averaged into one $EQE_{LSC}(\lambda)$ spectrum to represent the whole LSC device, which can be integrated with the AM 1.5G to compare with the corresponding J_{SC} extracted from J-V measurements. As an example, the averaged $EQE_{LSC}(\lambda)$ from the five EQE_{LSC} scans (d: 5-45 mm

alone the centerline, 10 mm interval) of the same NIR-selective TLSC (with waveguide length, L = 50.8 mm) is plotted in Figure 4.5B. The corresponding integrated J_{SC} (J_{SC}^{Int}) values at each d are shown as black spheres in Figure 4.5D. The J_{SC}^{Int} matches the J_{SC} from J-V measurement with masking. With the same TLSC, Figure 4.5B also illustrates that the 1 and 4 edge-mounted PVs in EQE_{LSC} measurement are equivalent to each other (note the black and orange solid stars in Figure 4.5A and B).

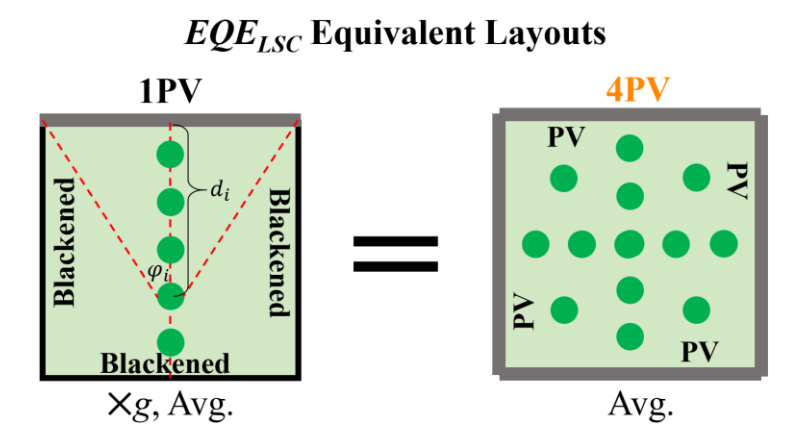


Figure 4.6 Equivalent layouts for *EQE* measurement for a TLSC system.

Figure 4.6 compares the 1PV- and 4PV-approaches: for 1PV-approach, 5 scans are taken along the center lines with 10 mm interval, then each EQE_{LSC} spectrum is corrected by multiplying the corresponding g value at each d, then these 5 corrected spectra (after $\times g$) are averaged as the representative $EQE_{LSC}(\lambda)$ for the whole TLSC device; for the 4PV-approach, 13 scans in total are taken in the symmetrical positions all over the waveguide front surface, 13 EQE spectra are averaged as the $EQE_{LSC}(\lambda)$ and no correction is needed in this 4PV scenario. These two approaches are equivalent and result in very similar J_{SC}^{Int} values as compared in Figure 4.5B, which match the J_{SC} from 1PV, 2PV and 4PV approaches for J-V measurement. Notably, Table 4.1 summarizes the photovoltaic parameters of this TLSC. Note the difference between the conditions with and

without the mask applied. The integrated short-circuit current density values (J_{SC}^{Int}) with 1 or 4 edge mounted PV cell(s) are also provided for comparison.

Several common errors in EQE_{LSC} measurements can be directly identified from the spectrum. For example, nanoparticles may be generated in the fabrication process. These nanoparticles function as Rayleigh scattering centers within the LSC waveguide. While scattering increases the light harvesting for small device sizes it creates two detrimental effects: 1) haze, which is unacceptable in many applications, and 2) increased outcoupling of waveguided light that results in outcoupling loss that dominate performance as devices increase in size beyond several centimeters. To highlight the presence of such an effect, nanoparticles are purposely introduced into a NIR-selective TLSC in Figure 4.5C. Rayleigh scattering decreases as wavelength increases, which is reflected in the EQE_{LSC} spectrum as an inclined "background" superimposed to the EQE_{LSC} of the luminophores (blue curve). If the excitation beam is not well focused and instead diverges (most optical fibers), the PV cell can be directly illuminated by the monochromatic excitation. In this case, a level background will also appear in the EQE_{LSC} spectrum (red curve in Figure 4.5C) that extends to the absorption cutoff of the edge-mounted PV. Therefore, the integrated J_{SC} will be significantly overestimated.

4.4 Position-dependent EQE_{LSC} for Reabsorption Loss Analysis

The wavelength-dependent EQE_{LSC} spectrum of an LSC system can be expressed as: 127,128

$$EQE_{LSC}(\lambda) = \eta_{Opt}(\lambda) \cdot \frac{\int EQE_{PV}(\lambda')PL(\lambda')d\lambda'}{\int PL(\lambda')d\lambda'}$$
(4.4)

where $\eta_{Opt}(\lambda)$ is the position-dependent LSC optical efficiency, which is defined as the ratio of the number of emitted photons waveguided to the edge to the number of photons incident onto the front active area at the absorption wavelength of the luminophore (λ) . The integral term represents the EQE_{PV} of the edge-mounted PV cell over the emission wavelengths of the luminophore, and $PL(\lambda')$ is the luminophore photoluminescence emission spectrum in waveguide matrix as a function of wavelength. If the edge-mounted PV shows a nearly constant $EQE_{PV}(\lambda')$ in the photoluminescence (λ') range, Equation 4.4 simplifies to $EQE_{LSC}(\lambda) = \eta_{Opt}(\lambda) \cdot EQE_{PV}$. Then the position-dependent $EQE_{LSC}(\lambda)$ is proportional to $\eta_{Opt}(\lambda)$, which can be used to calculate the optical efficiency and predict the scalability of LSC systems. As an example, the normalized $EQE_{LSC}(\lambda)$ of a NIR-selective TLSC (L=101.6 mm) spectra as a function of d (from 15 mm to 95 mm along the centerline, with 10 mm interval) are plotted in Figure 4.5E and the peak values are extracted and plotted in Figure 4.5F to emphasize the "roll-off" or reabsorption loss behavior.

As shown in Figure 4.3B, we emphasize that it is important to: 1) keep the fiber close and perpendicular to the LSC front surface, which can minimize the diverge of the excitation beam; 2) blacken the rest of the three edges, which eliminates any incident light from outside and PL reflection from inside of the waveguide edges; 3) mask the active area while leaving a small aperture to allow the excitation into the waveguide, which prevents the edge-mounted PV from collecting chopped and scattered light from the testing environment. Correct $EQE_{LSC}(\lambda)$ measurements should only allow the waveguided PL signal to be collected by the edge-mounted PV cell. Due to the amplification of the correction applied (g) when using the simplified approaches, ignoring such detail can lead to severe overestimation of the J_{SC}^{Int} and incorrect roll-off behavior of the $EQE_{LSC}(\lambda)$, which are plotted in Figure 4.5D and F for comparison. For a fair

comparison, we encourage J-V, averaged $EQE_{LSC}(\lambda)$, matched J_{SC}^{Int} and $EQE_{LSC}(\lambda)$ as a function of d to be provided in all LSC reports, which are highlighted in the dashed-line box in Figure 4.5.

4.5 Figures of Merit for Aesthetic Quality of LSCs

Aesthetic quality is equally important as η_{LSC} since it determines the threshold for TLSCs to be deployed in practical applications (e.g., glazing systems, mobile surfaces, etc.). Similar to any other TPV technologies, AVT, CRI and CIELAB color coordinates (a^*, b^*) are the three main figures of merit to quantitatively evaluate aesthetic quality of an LSC/TLSC device. AVT is used to evaluate the overall visible transparency of a TLSC device, and CRI with (a^*, b^*) is to quantify the rendered color fidelity of the transmitted light. Standard protocols to measure and calculate these key parameters are outlined in Chapter 3. ^{12,120,124} Several UV- and VIS- and NIR-selective harvesting LSC and TLSCs are provided as examples for aesthetic quality analysis as shown in **Figure 4.7**.

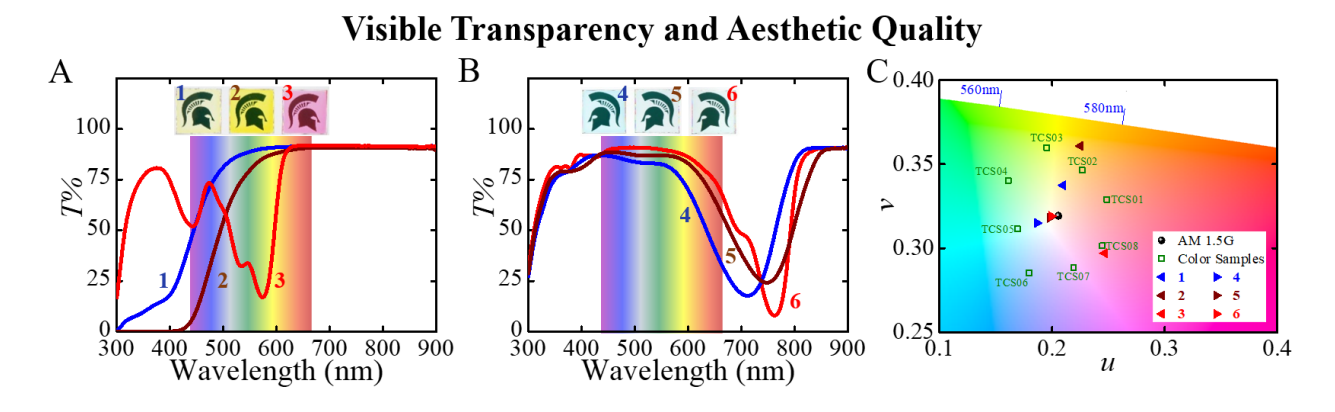


Figure 4.7 Visible transparency and aesthetic quality of TLSC systems. Transmission spectra of various (A) UV- and VIS- (1–3) and (B) NIR-selective (4–6) harvesting LSC and TLSCs. Inset: images of the corresponding LSC and TLSC devices photographed in transmission mode. (C) CIE 1960 color space used to calculate CRI with test color samples (TCS01 to TCS08) and LSC and TLSC devices 1–6. AM 1.5G is also included as the "reference light source" point.

The absence of electrodes and complex optical interference enables both higher levels of visible transparency and color tuning for LSC and TLSCs. LSCs can be designed to be colorful (for exteriors) or invisible (for windows and displays) by tuning the absorption wavelength range of the embedded luminophores. The transmission spectrum ($T(\lambda)$) of an LSC or TLSC is the input data for its AVT, CRI and color coordinates calculation. As an example, Figure 4.7A and B show $T(\lambda)$ of several LSC and TLSC systems embedded with various luminophores (1 to 2 for UV-, 3 for VIS-, 4 to 6 for NIR-selective harvesting).

Table 4.2 Summary of aesthetic quality parameters of various samples.

Samples	AVT%	CRI	CIELAB (a^*, b^*)
AM 1.5G	100	100	(0, 0)
UV-TLSC-1	87.7	90.8	(-5.8, 25.2)
UV-TLSC-2	77.8	69.9	(-5.1, 68.7)
VIS-LSC-3	43.6	27.7	(33.3, -17.9)
NIR-TLSC-4	76.6	77.4	(-12.4, -6.9)
NIR-TLSC-5	84.5	90.3	(-5.3, -2.2)
NIR-TLSC-6	87.9	92.8	(-4.9, -0.9)

By applying a series of mathematical transformation, $T(\lambda)$ can be converted into (u, v) coordinates in CIE 1960 uniform color space (CIELUV) as shown in Figure 4.7C, where the chromaticity coordinate distance between the point of the reference AM 1.5G and the point of the transmitted source determines the chromaticity difference and the corresponding CRI. Alternatively, the input $T(\lambda)$ can also be converted into (a^*, b^*) coordinates as the report of color rendering property as tabulated in **Table 4.2**. As the selective harvesting cutoffs blue-shift into UV (from device 3 to 1 in Figure 4.7A) or as the selective harvesting peaks red-shift from into NIR (from device 4 to 6 in Figure 4.7B), the corresponding AVT and CRI increase, and the (u, v) coordinates approach the AM 1.5G reference source point. The inset photographs of the LSC and

TLSCs concomitantly agree with such trend: the observed colors change from pinkish to light-yellow from device 3 to 1 and from light-blue to nearly colorless from device 4 to 6. Therefore, these figures of merit should be reported in the future LSC works if aesthetics are considered as their properties.

4.6 Measurement Validation, Data Completeness and Self-Consistency

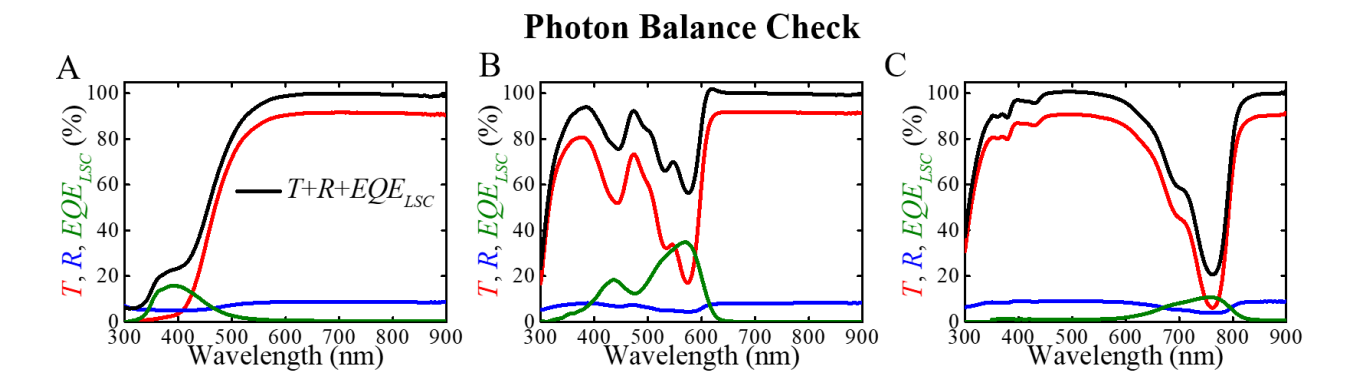


Figure 4.8 TLSCs Photon balance check.(A) UV-, (B) VIS-, and (C) NIR-selective harvesting LSC and TLSC device examples.

Analogous to TPVs,^{12,20} the photon balance at every wavelength should also be satisfied for LSC systems with independent measurements of $EQE_{LSC}(\lambda)$, $T(\lambda)$ and $R(\lambda)$:^{78,124}

$$EQE_{LSC}(\lambda)/m + R(\lambda) + T(\lambda) \le 1$$
 (4.5)

where m is the number of emitted photons per absorbed photon. This relation is valid since $EQE_{LSC}(\lambda)/m \leq A(\lambda)$, where $A(\lambda)$ is the absolute absorption spectra of the LSC as introduced in Section 4.1. For down-shifting luminophores, there is only one emitted photon per absorbed photon (m = 1). For down-converting luminophores that exhibit multiple exciton generation (MEG), a quantum-cutting (QC) or singlet fission (SQ), the luminophore can emit more than one photon (m > 1) per absorbed photon. If these luminophores also exhibit high PL quantum yield

(QY > 100%), the $EQE_{LSC}(\lambda)$ of the corresponding LSC systems can exhibit $EQE_{LSC}(\lambda) > 100\%$ at absorption peak wavelengths. Equation 4.5 is still valid for cases with m > 1 since $EQE_{LSC}(\lambda)/m$ is $\leq A(\lambda)$. Examples of this consistency check are shown for UV-, VIS- and NIR-selective harvesting LSC and TLSC in **Figure 4.8**A to C, respectively. We note that the highest $EQE_{LSC}(\lambda)$ (acquired at the smallest d value) in the position-dependent EQE_{LSC} spectra should be used in Equation 4.5 to ensure the whole EQE_{LSC} series can satisfy the photon balance.

4.7 Detailed Mathematical Description of LSC Performance Parameters

Currently, multiple LSC protocols are applied by researchers in LSC community. These nonstandard protocols have generated a full range of errors and poor reporting that have promulgated the literature. As a final note, the mathematical relation between several performance parameters is derived in this section to clarify these entanglements. As introduced in Chapter 2, the efficiency of the edge-mounted PV cell, η_{PV}^* , is the efficiency of the PV under the waveguided PL spectra and intensity of the luminophore. To a first approximation, it can be estimated by the efficiency of the PV at AM 1.5G normalized by its solar spectrum absorption efficiency and external quantum efficiency (EQE_{PV}) at the luminophore PL wavelength to account for photon downshifting:

$$\eta_{PV}^* = \left(\frac{\eta_{PV}(AM\ 1.5G)}{\eta_{Abs}^{PV}(AM\ 1.5G)}\right) \cdot \frac{\int EQE_{PV}(\lambda') \cdot PL(\lambda')d\lambda'}{\int PL(\lambda')d\lambda'}$$
(4.6)

where $\eta_{PV}(AM\ 1.5G)$ is the power conversion efficiency of the edge-mounted PV cell under AM 1.5G illumination, $PL(\lambda')$ is the luminophore photoluminescence emission spectrum in waveguide

matrix as a function of wavelength, and $\eta_{Abs}^{PV}(AM\ 1.5G)$ is the absorption efficiency of the PV active material (not the luminophore), which is defined as:

$$\eta_{Abs}^{PV}(AM\ 1.5G) = \frac{\int AM\ 1.5G(\lambda) \cdot A_{PV}(\lambda)d\lambda}{\int AM\ 1.5G(\lambda)d\lambda}$$
(4.7)

where $A_{PV}(\lambda)$ is the absolute absorption spectrum of the PV active layer (no parasitic absorption of other layers), and AM 1.5 $G(\lambda)$ is the AM 1.5G photon flux. Equation 4.6 assumes that there is an equivalent photon flux at the waveguide edge as on the front surface from AM 1.5G. However, this is rarely the case – the flux is typically much lower at the waveguide edge so that η_{PV}^* is light intensity dependent and its value will vary significantly (including the subcomponents of V_{OC} and FF) with the degree of concentration, luminophore QY, reabsorption loss, etc.

The overall optical efficiency, η_{Opt}^* , is defined as the ratio of number of emitted photons reaching the waveguide edge to the number of solar photons incident onto the waveguide front active surface across all incident wavelengths. Different from the overall optical efficiency $\eta_{Opt}^*(\lambda)$ is the optical efficiency at each specific wavelength λ , which is important for considering the quantum efficiency. From Equation 2.1, $\eta_{Opt}(\lambda)$ is the product of several component efficiencies:^{21,78,124}

$$\eta_{Opt}(\lambda) = (1 - R_f(\lambda)) \cdot A(\lambda) \cdot \eta_{PL} \cdot \eta_{Trap} \cdot \eta_{RA}$$
 (4.8)

where η_{Opt}^* and $\eta_{Opt}(\lambda)$ are related by:

$$\eta_{Opt}^* = \frac{\int AM \ 1.5G(\lambda) \cdot \eta_{Opt}(\lambda) d\lambda}{\int AM \ 1.5G(\lambda) d\lambda}$$
(4.9)

Combining Equation 4.2, Equation 4.6 and Equation 4.9 to derive the equation for power conversion efficiency of the LSC system (η_{LSC}):

$$\begin{split} \eta_{LSC} &= \eta_{Opt}^* \cdot \eta_{PV}^* \\ &= \left[\eta_{PV} (AM \ 1.5G) \cdot \frac{\int AM \ 1.5G(\lambda) d\lambda}{\int AM \ 1.5G(\lambda) \cdot A_{PV}(\lambda) d\lambda} \cdot \frac{\int EQE_{PV}(\lambda') \cdot PL(\lambda') d\lambda'}{\int PL(\lambda') d\lambda'} \right] \\ &\cdot \left[\frac{\int AM \ 1.5G(\lambda) \cdot \eta_{Opt}(\lambda) d\lambda}{\int AM \ 1.5G(\lambda) d\lambda} \right] \end{split}$$

which can be further simplified to:

$$\eta_{LSC} = \eta_{PV}(AM\ 1.5G) \cdot \frac{\int AM\ 1.5G(\lambda) \cdot \eta_{Opt}(\lambda) d\lambda}{\int AM\ 1.5G(\lambda) \cdot A_{PV}(\lambda) d\lambda} \cdot \frac{\int EQE_{PV}(\lambda') \cdot PL(\lambda') d\lambda'}{\int PL(\lambda') d\lambda'}$$
(4.10)

Equation 4.10 essentially takes the equation for the $\eta_{PV} = V_{OC} \cdot J_{SC} \cdot FF/P_0$ and corrects the J_{SC} to account for the downshifting and waveguiding of part of the solar spectrum by the luminophore. The derivation above is valid only if the photon flux at the solar cell edge is the same as the front surface.

Thus, reporting only the overall optical efficiency (η_{Opt}^*) or optical efficiency at a specific wavelength $(\eta_{Opt}(\lambda))$ is not a sufficiently reliable way to represent the *PCE* of an LSC system (η_{LSC}) . While there are a number of reports that only give the optical efficiency or calculate the η_{LSC} based on assumptions of the edge-mounted PV (η_{PV}^*) , this often leads to misleading reports as η_{PV}^* is also often misunderstood and the performance of the edge-mounted PVs is intrinsically light intensity dependent (and therefore light concentration dependent). Even with the same PV cell applied (same $\eta_{PV}(AM\ 1.5G)$), η_{PV}^* can still vary for different LSC systems, since the η_{Opt}^*

will determine the intensity and the wavelength of the waveguide photon flux onto the edge-mounted PV. Moreover, it is not clear to many researchers whether η_{Opt}^* in Equation 4.9 is defined on an energy or photon basis (typically it should be on photon basis as this is how PVs and LSCs work). This correspondingly depends on how η_{PV}^* is defined, often making comparisons between optical efficiencies very difficult. Instead of calculating η_{PV}^* and η_{Opt}^* with such complicated derivations from Eq. S1 to Eq. S5, the most straightforward approach to acquire η_{LSC} is directly from J-V characteristics with connections made to edge-mounted PVs (in series or parallel) under standard illumination AM 1.5G.

Notably, the definition of optical efficiency (η_{Opt}) is used in some literature based on the comparison of the short-circuit current values collected with and without the LSC waveguide:

$$\eta_{Opt} = \frac{I_{LSC}}{I_{PV} \cdot G}, \text{ where } G = \frac{A_{LSC}}{A_{PV}}$$
(4.11)

 η_{Opt} is defined as the number of photons emitted from the LSC edge over the total number of photons impinging on the LSC through the top surface. We note that Equation 4.11 can be used as an estimation. However, a particular problem that arises with this approach is the potential convolution of monochromatic and broad spectrum measurements so that this equation is just an estimation based on the assumption that EQE_{PV} is a constant at all wavelengths. Under broad spectrum illumination, this equation fails to capture the differing mismatch factors (and therefore equivalent intensities) from the light source for each current response in the ratio. Moreover, to make these measurements a PV cell must have already been mounted around the waveguide edges so it is better to simply measure and report EQE_{LSC} , J-V, and η_{LSC} . Thus, while this method can be used as a quick estimate, we recommend instead providing the η_{LSC} and EQE_{LSC} .

4.8 Summary

In summary, this chapter provides standard protocols to characterize the performance of LSCs/TLSCs with a particular emphasis on the simplification and challenges of performing J-V and EQE_{LSC} measurements. Key parameters to evaluate the visible transparency and aesthetic quality of LSC devices are outlined by using several LSCs/TLSCs examples. In addition, methods for confirming the self-consistency of LSC data are described. We reemphasize that all reports on LSCs should provide independent measurements of η_{LSC} , $EQE_{LSC}(\lambda)$, $T(\lambda)$, $R(\lambda)$, $A(\lambda)$, $PL(\lambda)$ and OY for data completeness and show self-consistency checks to minimize potential experimental errors. In addition, AVT, LUE, and (a^*, b^*) should be reported to so that aesthetics can be quantitatively compared. As a service to our LSC-PV research community, we provide a "Checklist for Luminescent Solar Concentrator Manuscripts" in the Appendices Section. By doing so, we encourage authors to provide the details from the LSC-PV checklist in their submitted research articles. As an added benefit, such reporting will enable inclusion of the reported data to the "Reporting Device Efficiency of Emerging PV Materials" database. We also encourage authors to submit their LSC-PVs for third-party certification when claiming record values of efficiency. We hope that the use of this checklist will become standard for all LSC-PV reports, allowing published results to be readily comparable between reports (among LSC-PV reports, and between LSC-PV and other PV technologies). We emphasize that adopting the metrics outlined in this checklist will help the community achieve its goal of accelerating reproducible and robust advances in the development of LSC-PV devices.

Chapter 5 Comprehensive Analysis of Transparent, Semitransparent, and Colorful Luminescent Solar Concentrator Aesthetics

Widespread solar adoption requires LSCs to simultaneously achieve high photovoltaic performance and excellent aesthetic quality.³ With most research efforts focusing on efficiency improvements, the significance of LSC aesthetics has been understated. Particularly, escaped photoluminescence has the potential to strongly impact visual aesthetics in several different ways and has been particularly overlooked. In this chapter, we define and analyze key figures of merit for LSC aesthetics by incorporating the impact of the photoluminescence. Additionally, a new metric analogous to haze, termed the "average visible haze", is defined to describe the visual impact of the escaped photoluminescence on human perception. The main mechanisms of photoluminescence utilized in LSC design, including down-shifting, up-conversion and quantum-cutting are systematically assessed within this framework. In identifying these key aspects, this perspective can help guide future research in semitransparent, colorful, and transparent LSC designs.

5.1 Visual Impact Resulted from Escaped Photoluminescence

To adequately fulfill the promise of these new PV adoption opportunities, comprehensive understanding beyond photovoltaic performance is required in additional factors such as scalability, reliability, affordability, and most importantly, aesthetic quality.² The aesthetics of and LSC or any TPV device can be observed from both the transmitted and the reflected sides. Intuitively, the key figures, the key figures of merit for TPV aesthetic quality introduced in Chapter 3 can be readily transferred to the evaluation of LSC aesthetics. For simple waveguides with isotropic

emitters and typical waveguide index of fraction (~1.5), ~25.5% of the total emitted photoluminescence photon flux $(PL^{Total}(\lambda))$ escapes from the emission cone (θ_C) from both sides of the LSC waveguide as illustrated in **Figure 5.1**. P.21 The escaped photoluminescence $(PL^{Back}(\lambda))$ or $PL^{Front}(\lambda)$, ~12.75% of $PL^{Total}(\lambda)$ on each side) combined with the transmitted or reflected solar spectrum $(AM\ 1.5G(\lambda)\cdot T(\lambda))$ or $AM\ 1.5G(\lambda)\cdot R(\lambda)$ determines the total photon flux on each side. If the photoluminescence $(PL(\lambda))$ resides within the VIS range, then the escaped photoluminescence becomes visually prominent and appears as if it were a "colorful haze".

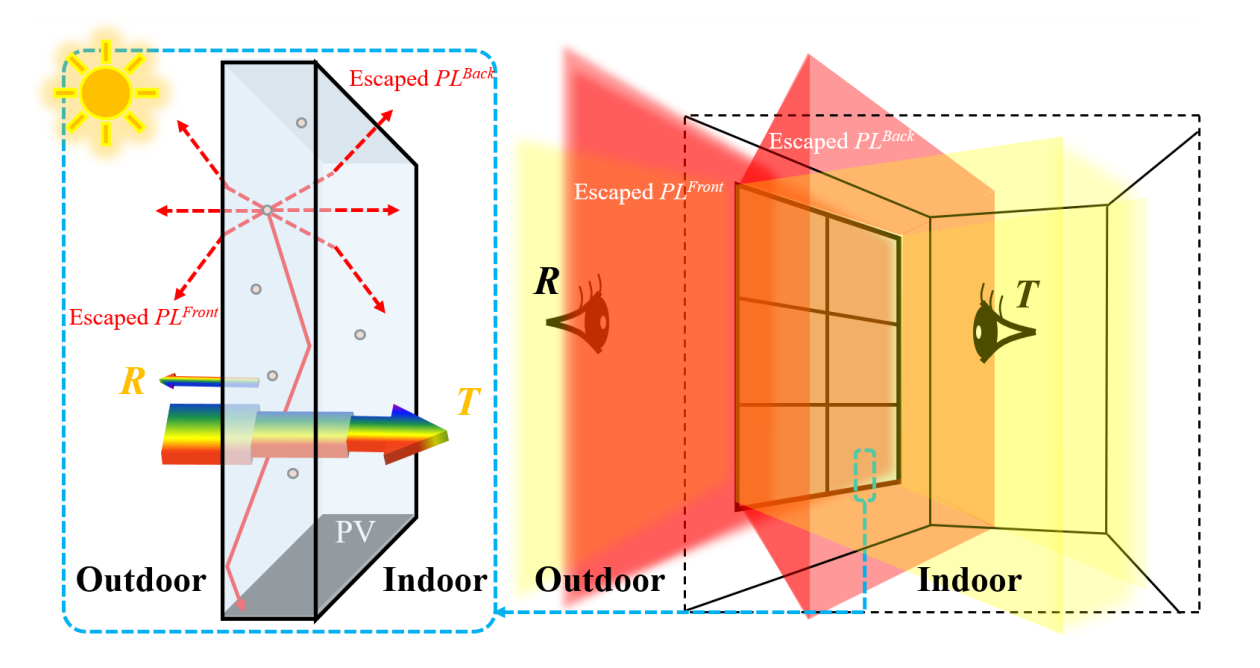


Figure 5.1 Schematic showing the impact of escaped photoluminescence on the aesthetics of LSC systems.

The incident sunlight beam is transmitted and reflected only in the normal direction (in light yellow), whereas the un-trapped photoluminescence escapes from both waveguide surfaces in all directions (in red) which creates a "glowing" effect to observers on both sides. Therefore, the transmitted solar spectrum combined with the escaped photoluminescence spectrum (AM $1.5G(\lambda) \cdot T(\lambda) + PL^{Escaped}(\lambda)$) determines the aesthetic parameters of the LSC on the transmitted side (i.e., indoor), and the reflected solar spectrum combined with the escaped photoluminescence spectrum (AM $1.5G(\lambda) \cdot R(\lambda) + PL^{Escaped}(\lambda)$) determines the aesthetic parameters of the LSC on the reflected side (i.e., outdoor).

5.2 Optical Model

Typically, the aesthetics of TPVs are quantitatively evaluated by using three key figures of merit: average visible transmittance (AVT_{\perp}), color rendering index (CRI) and CIELAB color coordinates (a^*, b^*) . The AVT_{\perp} is used to evaluate the overall visible transparency (weighted by the photopic response) of a given TPV device and is widely utilized in the window industry. CRI and (a^*, b^*) can be utilized to quantify the rendered color fidelity and indicate relative color of the light transmitted or reflected by the device as test light source with respect to a reference illumination source, and both are utilized in the lighting and window industries. Color purity (i.e. color saturation) is another metric to quantitatively evaluate the degree of closeness of the tinted color compared to the dominant monochromatic color. ¹²⁰ In the CIE 1931 chromaticity diagram, monochromatic colors are located along the perimeter of the chromatic diagram, which is also referred as spectral locus. The (x, y) coordinates of AM 1.5G (0.332, 0.344), CIE standard illuminated D65 (0.313, 0.329) and equal energy point (1/3, 1/3) are also included in the CIE 1931 plot: the corrected color temperature (CCT) of the AM 1.5G and D65 are ~5513 K and ~6504 K along the proximity of Planckian locus, respectively, which are both very close to the equal energy point. AM 1.5G energy flux (with the unit of [~W m⁻²nm⁻¹]) is the standard input power intensity widely adopted by solar industry, whereas D65 is a unitless spectrum profile based on blackbody radiation curve at ~6500 K that is commonly used as the standard illuminant to represent daylight illumination in both lighting and window industries. As TPV technologies develop, photovoltaic performance and aesthetic quality become equally important for practical deployment, requiring the mergence of the PV and CIE standards. In TPV deployment, these devices are illuminated by an incident solar spectrum simultaneously dictate both the PCE and aesthetics. Therefore, it is only

logic to apply one unified spectrum standard with the unit of power per area only for all measurements and both purposes.^{3,12,124,131}.

To design transparent photovoltaics (TPV) that simultaneously maximize the light harvesting (power conversion efficiency (PCE)) and minimize the corresponding visual impact, it is necessary to define the proper visible spectral range by considering the three key aesthetic parameters. Since the air-mass 1.5 global (AM 1.5G) under 1 sun intensity (1000 Wm⁻²) has been widely adopted as the test standard for incident solar irradiation in PV characterization since the 1970s, ^{2,12,116} we use AM 1.5G as the reference spectrum (reference illumination source) for the calculation of all the aesthetic parameters (i.e., AM 1.5G alone as the input test light source yields an AVT_{\perp} of 100%, a CRI of 100 and the (a^*, b^*) at the origin (0, 0)). Idealized step-function transmittance profiles with varying cutoffs are utilized to confirm the practical visible range (VIS) for TPVs. In the prior chapters, the visible range had been defined for the purposes of optimizing TPVs with minimal visual impact as 435 - 675 nm based on CRI > 95 only. Here we consider and assess the color metrics of both CRI and (a^*, b^*) in depth. We first survey 50 of the top massmarket architectural low-E glass products to determine the industry targets for the majority of transparent window products as shown in **Figure 5.2**. From this analysis we find that $CRI \ge 85$, and $-7 < a^* < 0$, $-3 < b^* < 7$ are key levels for widespread product deployment where the (a^*, b^*) become the key constraining factor over the CRI.

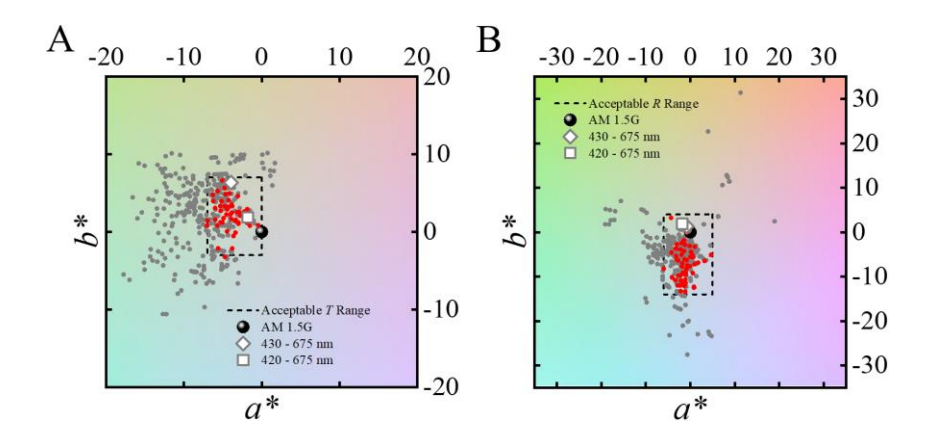


Figure 5.2 A survey on 365 commercially available (grey dots) and top 50 mass-market (red dots) architectural glass products.

This survey determines the acceptable ranges for CIELAB color coordinates: $(a^*, b^*)_T$: -7 < a^* < 0 and -3 < b^* < 7; and $(a^*, b^*)_R$: -6 < a^* < 5 and -14 < b^* < 4 on the transmitted side and reflected side, respectively. The visible transmissive ranges 430 – 675 nm (grey square) are also included in both plots.

As shown in **Figure 5.3A** and B, transmitting photons in the range of 430 - 675 nm with no light absorption provides a *CRI* of 96.70 and (a^*, b^*) of (-3.95, 6.37), adequately meeting these requirements while maximizing the solar harvesting in the invisible range. We note that the transmissive range is only slightly changed from 435 nm to 430 nm on the blue/UV side so that the corresponding b^* value slightly decreases from 9.17 to 6.37 and falls within the acceptable range. When the long-wavelength cutoff is fixed at 675 nm, redshifting the short-wavelength cutoff from 430 nm quickly decreases *CRI* and rapidly increases b^* in the positive direction, resulting in perceptible yellow/orange tinting; similarly, with fixed short-wavelength cutoff at 430 nm, blue-shifting the long-wavelength cutoff from 675 nm into VIS also quickly decreases *CRI*, and rapidly decreases $a^* < 0$, resulting in blue tinting. Thus, any further reduction in this defined VIS range imparts substantial visual impact on the corresponding TPVs. Additionally, we note that blue-shifting the UV/VIS cutoff from 430 nm to 420 nm while maintaining the NIR cutoff at 675 nm results in the (a^*, b^*) of (-1.80, 1.87), moving much closer to the CIELAB origin with a slightly higher *CRI* of 97.5 for the highest aesthetic demands. Any absorption or reflection peak located

within the defined VIS range of 430 - 675 nm, particularly near the photopic response $(V(\lambda))$ peak as shown in Figure 5.3A, results in significant colored tinting, which dramatically reduces AVT_{\perp} and CRI values and moves (a^*, b^*) far from the origin.

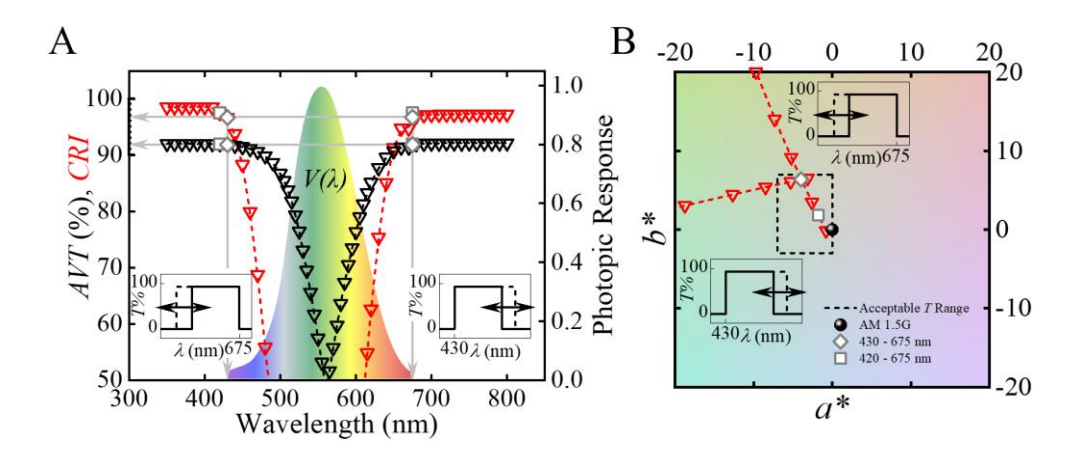


Figure 5.3 UV/VIS and VIS/NIR cutoffs determined by comprehensive consideration of all aesthetic quality parameters.

(A) Color rendering index (CRI_T , red triangle) and average visible transmittance (AVT_\perp , black triangle) of the TPVs as a function of short and long idealized visible transmission wavelength cutoff shown in the insets. The photopic response ($V(\lambda)$) is also included as the background. AM 1.5G solar spectrum is used as the reference light source, which results in a CRI_T value of 100. (B) CIELAB color coordinates (a^* , b^*)_T as a function of short and long idealized visible transmission wavelength cutoff shown in the insets. The acceptable (a^* , b^*)_T range based on mass-market architectural glass products is plotted as the dashed box: $-7 < a^* < 0$ and $-3 < b^* < 7$, and the reference spectrum AM 1.5G is at the origin (0, 0). With comprehensive consideration of both color metrics, the visible range is therefore defined as 430 - 675 nm, which results in CRI_T of 96.70 and (a^* , b^*) of (-3.95, 6.37) (indicated as grey diamond in (A) and (B)), a more strict definition of visible range, 420 - 675 nm, results in CRI_T of 97.51 and (a^* , b^*) of (-1.80, 1.87) (indicated as grey square in (A) and (B)).

Based on the defined VIS range, the idealized step-function absorption profiles in the invisible spectral ranges are determined, the same normalized emission profile is shifted to create photoluminescence as a function of wavelength ($PL(\lambda)$) in blue, cyan, green, orange, red and NIR) as shown in **Figure 5.4**A. We note $PL(\lambda)$ is the photoluminescence spectral profile normalized by its peak value, which is used for schematic purpose, whereas $PL^{Total}(\lambda)$, $PL^{Front}(\lambda)$ and $PL^{Back}(\lambda)$ are the absolute photoluminescence photon fluxes, which share the same unit with AM 1.5G

photon flux [~# of photons m $^{-2}$ nm $^{-1}$ s $^{-1}$] and therefore are directly used as input photon fluxes for the calculation of various color metrics. Varying degrees of visible absorption are included. To isolate the impact from the photoluminescence only, we fix any visible absorption profile to be flat across the entire VIS to create color-neutral transmission. The multiplication factor (m) is defined as the number of emitted photons per absorbed photon, and the total impact is then assessed based on down-shifting (m = 1), up-conversion (m = 0.5), and quantum-cutting (m = 2) photoluminescence mechanisms, respectively, as described in Chapter 2.

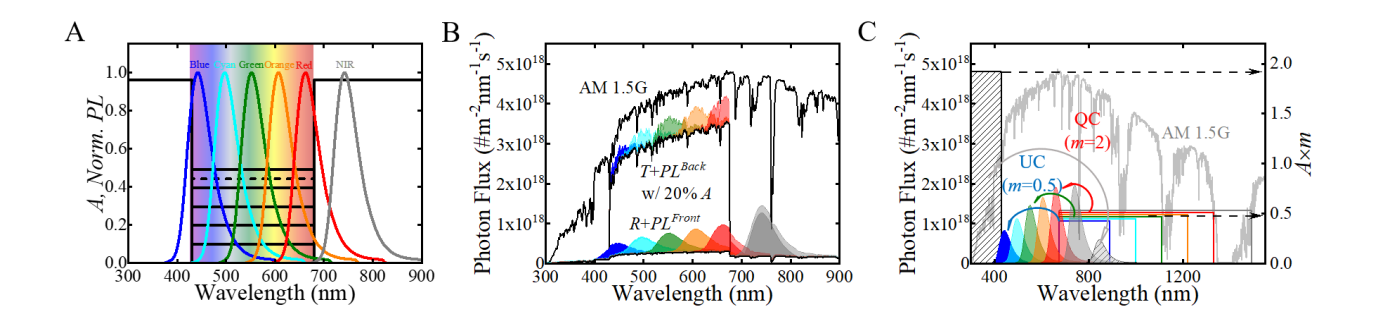


Figure 5.4 Idealized absorption and emission characteristics used in the optical model.

(A) Schematic of idealized absorption and emission characteristics with step-function absorptance profiles with various degrees of visible contribution between 430-675 nm are drawn. The emission profile is manually shifted to create photoluminescence as a function of wavelength $(PL(\lambda))$ in blue, cyan, green, orange, red and near-infrared (NIR)) in the optical model. (B) An example to show the impact of escaped down-shifting photoluminescence on the combined spectra on transmitted and reflected sides of an LSC system with 20% visible neutral single-pass absorptance (A_I) . (C) Idealized absorption and emission characteristics of spectral conversion approaches in LSC design: UV photons are quantum-cut with emission in NIR; the usable IR range expands as the up-converted emission wavelength redshifts $(PL(\lambda))$ manually shifted from blue to NIR). Note that the product of the corresponding absolute absorptance heights (A) and the multiplication factors (m) is used as the right axis $(A \times m)$ to signify these spectral conversion mechanisms. AM 1.5G photon flux is also included as background for comparison.

Detailed calculation of total absorptance $(A(\lambda))$, reflectance $(R(\lambda))$ and transmittance spectra $(T(\lambda))$ is based on a single-pane see-through PV illuminated by incident solar irradiance, the light beam experiences multiple reflection and transmission events at the two air/PV interfaces. As shown in **Figure 5.5**, the sum of the total reflected intensity and total transmitted

intensity determines the total reflectance (R) and transmittance (T) of the see-through PV device, respectively. Here we derive the relationship between overall absorptance, transmittance, and reflectance for a single-pane module where the absorbing material is uniformly dispersed throughout the waveguide media.

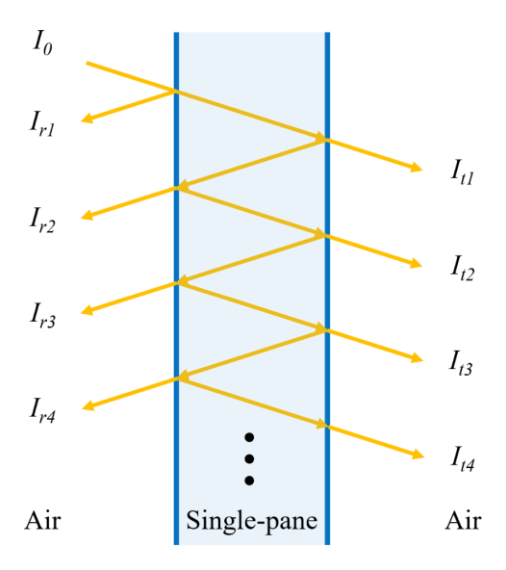


Figure 5.5 Schematic showing multiple reflection and transmission events.

The incident light beam (I_0) experiences multiple reflection and transmission events when it interacts with a single-pane see-through PV device.

With refractive index, n = 1.5 of the see-through PV, the reflectance at the air/front surface interface (R_f) is:

$$R_f = \left(\frac{n-1}{n+1}\right)^2 = 0.04\tag{5.1}$$

According to the Beer-Lamber law, when incident light beam transmits through a uniform attenuating medium with absorptivity (α), the single-pass transmittance (T_I) with an optical path length of d can be expressed as the ratio of transmitted light beam intensity (I_0) as:

$$T_1 = \frac{I_t}{I_0} = \exp(-\alpha \cdot d) \tag{5.2}$$

Therefore, the single-pass absorptance starting from within the media (A_I) is:

$$A_1 = 1 - T_1 = 1 - \exp(-\alpha \cdot d) \tag{5.3}$$

For a single-pane see-through PV with multiple reflection and transmission events, the light beam intensity of each reflection and transmission event can be expressed as:

1st-order:

$$I_{r1} = I_0 \cdot R_f$$

$$I_{a1} = I_0 \cdot (1 - R_f) \cdot A_1$$

$$I_{t1} = I_0 \cdot (1 - R_f) \cdot (1 - A_1) \cdot (1 - R_f) = I_0 \cdot (1 - R_f)^2 \cdot (1 - A_1)$$

2nd-order:

$$I_{r2} = I_0 \cdot (1 - R_f) \cdot (1 - A_1) \cdot R_f \cdot (1 - A_1) \cdot (1 - R_f) = I_0 \cdot R_f \cdot (1 - R_f)^2 \cdot (1 - A_1)^2$$

$$I_{a2} = I_0 \cdot (1 - R_f) \cdot (1 - A_1) \cdot R_f \cdot A_1 + I_0 \cdot (1 - R_f) \cdot (1 - A_1) \cdot R_f \cdot (1 - A_1) \cdot R_f \cdot A_1$$

$$= I_0 \cdot (1 - R_f) \cdot A_1 \cdot [R_f \cdot (1 - A_1)] + I_0 \cdot (1 - R_f) \cdot A_1 \cdot [R_f \cdot (1 - A_1)]^2$$

$$I_{t2} = I_0 \cdot (1 - R_f) \cdot (1 - A_1) \cdot R_f \cdot (1 - A_1) \cdot R_f \cdot (1 - A_1) \cdot (1 - R_f)$$

$$= I_0 \cdot (1 - R_f)^2 \cdot R_f^2 \cdot (1 - A_1)^3 = I_{t1} \cdot R_f^2 \cdot (1 - A_1)^2$$

3rd-order:

$$I_{r3} = I_0 \cdot (1 - R_f) \cdot (1 - A_1) \cdot R_f \cdot (1 - A_1) \cdot R_f \cdot (1 - A_1) \cdot R_f \cdot (1 - A_1) \cdot (1 - R_f)$$

$$= I_0 \cdot (1 - R_f)^2 \cdot R_f^3 \cdot (1 - A_1)^4 = I_{r2} \cdot R_f^2 \cdot (1 - A_1)^2$$

$$I_{a3} = I_{0} \cdot (1 - R_{f}) \cdot (1 - A_{1}) \cdot R_{f} \cdot (1 - A_{1}) \cdot R_{f} \cdot (1 - A_{1}) \cdot R_{f} \cdot A_{1} + I_{0} \cdot (1 - R_{f}) \cdot (1 - A_{1}) \cdot R_{f} \cdot (1 - A_{1}) \cdot R_{f} \cdot (1 - A_{1}) \cdot R_{f} \cdot A_{1}$$

$$= I_{0} \cdot (1 - R_{f}) \cdot A_{1} \cdot \left[R_{f} \cdot (1 - A_{1}) \right]^{3} + I_{0} \cdot (1 - R_{f}) \cdot A_{1} \cdot \left[R_{f} \cdot (1 - A_{1}) \right]^{4}$$

$$I_{t3} = I_{0} \cdot (1 - R_{f}) \cdot (1 - A_{1}) \cdot R_{f} \cdot (1 - A_{1})^{2}$$

4th-order:

$$I_{r4} = I_{0} \cdot (1 - R_{f}) \cdot (1 - A_{1}) \cdot R_{f} \cdot (1 - A_{1}) \cdot R_{f}$$

$$\cdot (1 - A_{1}) \cdot (1 - R_{f}) = I_{0} \cdot (1 - R_{f})^{2} \cdot R_{f}^{5} \cdot (1 - A_{1})^{6} = I_{r3} \cdot R_{f}^{2} \cdot (1 - A_{1})^{2}$$

$$I_{a4} = I_{0} \cdot (1 - R_{f}) \cdot (1 - A_{1}) \cdot R_{f} \cdot (1 - A_{1})^{2}$$

$$I_{t4} = I_{0} \cdot (1 - R_{f}) \cdot (1 - A_{1}) \cdot R_{f} \cdot (1 - A_{1})^{2}$$

$$= I_{t3} \cdot R_{f}^{2} \cdot (1 - A_{1})^{2}$$

• • •

nth-order:

$$I_{rn} = I_{rn-1} \cdot R_f^2 \cdot (1 - A_1)^2$$

$$I_{tn} = I_{tn-1} \cdot R_f^2 \cdot (1 - A_1)^2$$

Both I_r and I_t are geometric sequences with common ratio of $R_f^2 \cdot (1 - A_1)^2 < 1$. It is noted that the R geometric sequence starts from the 2nd-order. The total reflectance and transmittance as the sum of the geometric sequences can therefore be calculated:

$$\sum_{i=1}^{\infty} I_{ri} = I_0 \cdot R_f + I_0 \cdot R_f \cdot (1 - R_f)^2 \cdot (1 - A_1)^2 + I_0 \cdot R_f \cdot (1 - R_f)^2 \cdot (1 - A_1)^2$$

$$\cdot \left[R_f^2 \cdot (1 - A_1)^2 \right] + I_0 \cdot R_f \cdot (1 - R_f)^2 \cdot (1 - A_1)^2 \cdot \left[R_f^2 \cdot (1 - A_1)^2 \right]^2 + I_0 \cdot R_f$$

$$\cdot (1 - R_f)^2 \cdot (1 - A_1)^2 \cdot \left[R_f^2 \cdot (1 - A_1)^2 \right]^3 + \cdots$$

$$R = \frac{\sum_{i=1}^{\infty} I_{ri}}{I_0} = R_f + \frac{R_f \cdot (1 - R_f)^2 \cdot (1 - A_1)^2}{1 - R_f^2 \cdot (1 - A_1)^2}$$

Similarly,

$$\sum_{i=1}^{\infty} I_{ti} = I_0 \cdot (1 - R_f)^2 \cdot (1 - A_1) + I_0 \cdot (1 - R_f)^2 \cdot (1 - A_1) \cdot [R_f^2 \cdot (1 - A_1)^2] + I_0$$

$$\cdot (1 - R_f)^2 \cdot (1 - A_1) \cdot [R_f^2 \cdot (1 - A_1)^2]^2 + I_0 \cdot (1 - R_f)^2 \cdot (1 - A_1)$$

$$\cdot [R_f^2 \cdot (1 - A_1)^2]^3 + \cdots$$

$$T = \frac{\sum_{i=1}^{\infty} I_{ti}}{I_0} = \frac{(1 - R_f)^2 \cdot (1 - A_1)}{1 - R_f^2 \cdot (1 - A_1)^2}$$
(5.4)

 I_a is also a geometric sequence with a different common ratio of $R_f \cdot (1 - A_1)$, and the total absorptance can be calculated as:

$$\sum_{i=1}^{\infty} I_{ai} = I_0 \cdot (1 - R_f) \cdot A_1 + I_0 \cdot (1 - R_f) \cdot A_1 \cdot [R_f \cdot (1 - A_1)] + I_0 \cdot (1 - R_f) \cdot A_1$$

$$\cdot [R_f \cdot (1 - A_1)]^2 + I_0 \cdot (1 - R_f) \cdot A_1 \cdot [R_f \cdot (1 - A_1)]^3 + I_0 \cdot (1 - R_f) \cdot A_1$$

$$\cdot [R_f \cdot (1 - A_1)]^4 + I_0 \cdot (1 - R_f) \cdot A_1 \cdot [R_f \cdot (1 - A_1)]^5 + I_0 \cdot (1 - R_f) \cdot A_1$$

$$\cdot [R_f \cdot (1 - A_1)]^6 + \cdots$$

$$A = \frac{\sum_{i=1}^{\infty} I_{ai}}{I_0} = \frac{(1 - R_f) \cdot A_1}{1 - R_f \cdot (1 - A_1)}$$
 (5.5)

To confirm A + T + R = 1, the consistency derivation is shown below:

$$\begin{split} A + T + R &= \left[\frac{\left(1 - R_{f}\right) \cdot A_{1}}{1 - R_{f} \cdot (1 - A_{1})} \right] + \left[\frac{\left(1 - R_{f}\right)^{2} \cdot (1 - A_{1})}{1 - R_{f}^{2} \cdot (1 - A_{1})^{2}} \right] + \left[R_{f} + \frac{R_{f} \cdot \left(1 - R_{f}\right)^{2} \cdot (1 - A_{1})^{2}}{1 - R_{f}^{2} \cdot (1 - A_{1})^{2}} \right] \\ &= \frac{\left(1 - R_{f}\right) \cdot A_{1} \cdot \left[1 + R_{f} \cdot (1 - A_{1})\right] + \left(1 - R_{f}\right)^{2} \cdot (1 - A_{1}) + R_{f} \cdot \left(1 - R_{f}\right)^{2} \cdot (1 - A_{1})^{2}}{1 - R_{f}^{2} \cdot (1 - A_{1})^{2}} + R_{f} \\ &= \frac{\left(1 - R_{f}\right) \cdot A_{1} \cdot \left[1 + R_{f} \cdot (1 - A_{1})\right] + \left(1 - R_{f}\right)^{2} \cdot (1 - A_{1}) \cdot \left[1 + R_{f} \cdot (1 - A_{1})\right]}{1 - R_{f}^{2} \cdot (1 - A_{1})^{2}} + R_{f} \\ &= \frac{\left(1 - R_{f}\right) \cdot \left[1 + R_{f} \cdot (1 - A_{1})\right] \cdot \left[A_{1} + \left(1 - R_{f}\right) \cdot (1 - A_{1})\right]}{1 - R_{f}^{2} \cdot (1 - A_{1})^{2}} + R_{f} \\ &= \frac{\left(1 - R_{f}\right) \cdot \left[1 + R_{f} \cdot (1 - A_{1})\right] \cdot \left[1 - R_{f} + R_{f} \cdot A_{1}\right]}{1 - R_{f}^{2} \cdot (1 - A_{1})^{2}} + R_{f} \\ &= \frac{\left(1 - R_{f}\right) \cdot \left[1 + R_{f} \cdot (1 - A_{1})\right] \cdot \left[1 - R_{f} + R_{f} \cdot A_{1}\right]}{1 - R_{f}^{2} \cdot (1 - A_{1})^{2}} + R_{f} \\ &= \frac{\left(1 - R_{f}\right) \cdot \left[1 + R_{f} \cdot (1 - A_{1})\right] \cdot \left[1 - R_{f} \cdot (1 - A_{1})\right]}{1 - R_{f}^{2} \cdot (1 - A_{1})^{2}} + R_{f} \\ &= \frac{\left(1 - R_{f}\right) \cdot \left[1 - R_{f}^{2} \cdot (1 - A_{1})\right] \cdot \left[1 - R_{f} \cdot (1 - A_{1})\right]}{1 - R_{f}^{2} \cdot (1 - A_{1})^{2}} + R_{f} \end{aligned}$$

$$= \frac{\left(1 - R_f + R_f\right) \cdot \left[1 - R_f^2 \cdot (1 - A_1)^2\right]}{1 - R_f^2 \cdot (1 - A_1)^2} = \frac{1 - R_f^2 \cdot (1 - A_1)^2}{1 - R_f^2 \cdot (1 - A_1)^2} = 1$$

In our optical model, different A_I values in visible range (430 - 675 nm) are input (e.g., A_I = 0, 0.1, 0.2···) to create various idealized step-function absorptance profile (A) as shown in Figure 3B: for example, with A_I = 0.2 in visible range, the calculated R = 0.064, T = 0.738, and A = 0.198; and with A_I = 1 outside of visible range, R = 0.04, T = 0, and A = 0.96, which is the absorptance profile for Figure 5.4A.

For indoor aesthetics, it is assumed that the window is the primary light source during the day of a given room as shown in Figure 5.1. Thus, the visible $PL^{Back}(\lambda)$ impacts the rendered color fidelity of the transmitted sunlight and creates luminescent haze can be observed as if the window is "glowing" in the color of the photoluminescence. A similar effect, but with differing magnitude, is expected for the outdoor aesthetics from $PL^{Front}(\lambda)$ that will impact the exterior appearance of the building. To comprehensively assess the aesthetics of LSC devices, these PL spectra are used to correct the AM $1.5G(\lambda) \cdot T(\lambda)$ and AM $1.5G(\lambda) \cdot R(\lambda)$ input spectra (i.e., test light sources) to calculate the rendered color with respect to the standard AM 1.5G spectrum (i.e., reference illumination source) on each side. Modified color rendering indexes (CRI_T and CRI_R) and CIELAB color coordinates ($(a^*, b^*)_T$ and $(a^*, b^*)_R$) are used to quantify the rendered colors on each side. The detailed CRI and (a^*, b^*) calculation approaches have been described in Chapter 3. We note that the calculation of average visible transmittance (AVT_L) remains the same, which is still reported as the integration of the $T(\lambda)$ measured at normal incidence and weighted against the photopic response ($V(\lambda)$) of the human eye. 12,124

For window products, scattering (in the bulk or on the surfaces of the glass sheet due to microscopic imperfections or textures during fabrication) can cause haze that reduces optical quality and the transmission of optical information. Scattering haze is defined as the ratio of the transmitted light that is diffuse to the total transmitted light (the sum of specular transmittance and diffusive transmittance). In the case of photoluminescence, we incorporate $V(\lambda)$ into the definition of a new parameter, the average visible luminescent haze ($AVLH_T$ and $AVLH_R$ for the transmitted and reflected sides, respectively), to quantify the glowing haze of escaped photoluminescence for human perception.

Comprehensive tunability in $A(\lambda)$, $T(\lambda)$, $R(\lambda)$ and $PL(\lambda)$ can be effectively utilized and combined to purposefully create colored surfaces. In these cases, there color is imparted by transmission and reflection, as well as escaped PL. To demonstrate such design, we further modify the idealized step-function absorption profiles in VIS and combine them with the VIS DS photoluminescence to purposefully create various transmitted and reflected colors. The same DS photoluminescence profiles shown in Figure 5.4A are paired with these VIS absorption profiles, and the corresponding results of purposeful coloration are calculated with the same method as described for the transparent applications.

As illustrated in **Figure 5.6**, the incident light beam is transmitted and reflected only in normal direction, which determines the corresponding average visible transmittance (AVT_{\perp}) and the average visible reflectance (AVR_{\perp}) , respectively. Whereas the un-trapped photoluminescence escapes from both sides of the waveguide in all directions, i.e., isotropic emission, which determines the corresponding average visible haze $(AVLH_T)$ and $AVLH_R$.

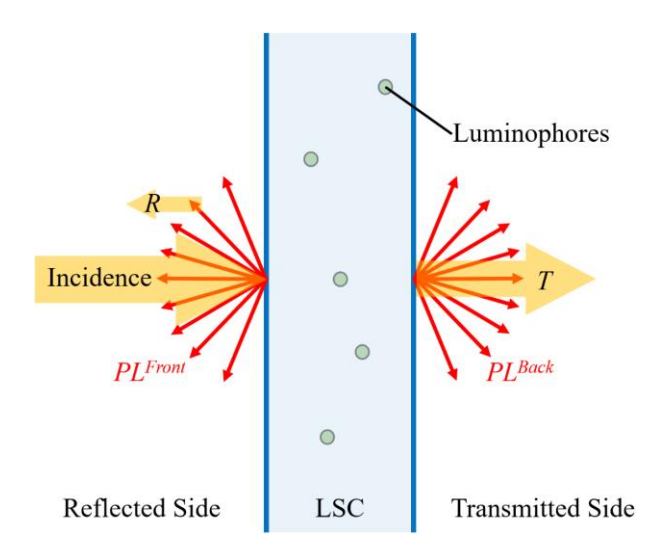


Figure 5.6 Schematic showing the transmitted and reflected light (orange arrows) and the escaped photoluminescence (red arrows).

In window and plastic industry, the scattering haze is defined as the ratio of the transmitted light that is scattered to the total transmitted light (the sum of specular transmittance and diffusive transmittance). The definition of scattering haze is therefore referenced to quantify the glowing haze. On the transmitted side:

$$AVT_{\perp} = \frac{\int AM \ 1.5G(\lambda) \cdot T(\lambda) \cdot V(\lambda) d\lambda}{\int AM \ 1.5G(\lambda) \cdot V(\lambda) d\lambda}$$

$$AVT_{Glowing} = \frac{\int PL^{Back}(\lambda) \cdot V(\lambda)d\lambda}{\int AM \ 1.5G(\lambda) \cdot V(\lambda)d\lambda}$$

where $T(\lambda)$ is the transmittance spectrum directly measured by the double-beam spectrometer and $PL^{Back}(\lambda)$ is the absolute escaped photoluminescence photon flux on the transmitted (back) side of the waveguide that is a function of the waveguide trapping efficiency (η_{Trap}) and the absolute total photoluminescence photon flux $(PL^{Total}(\lambda))$ as:

$$PL^{Back}(\lambda) = 0.5 \times \left(1 - \eta_{Trap}\right) \cdot PL^{Total}(\lambda) = 0.5 \times \left(1 - \sqrt{1 - 1/n_{Sub}^2}\right) \cdot PL^{Total}(\lambda)$$

Multiplying the factor of 0.5 accounts for each side, and the product of $0.5 \times (1 - \sqrt{1 - 1/n_{Sub}^2})$

is \sim 12.7%. The corresponding $AVLH_T$ is then defined based on the traditional definition of haze as the fraction of diffuse component to the diffuse plus specular component as:

$$AVLH_T = \frac{AVT_{Glowing}}{AVT_{\perp} + AVT_{Glowing}}$$
 (5.6)

Similarly, on the reflected side:

$$AVR_{\perp} = \frac{\int AM \ 1.5G(\lambda) \cdot R(\lambda) \cdot V(\lambda) d\lambda}{\int AM \ 1.5G(\lambda) \cdot V(\lambda) d\lambda}$$

$$AVR_{Glowing} = \frac{\int PL^{Front}(\lambda) \cdot V(\lambda) d\lambda}{\int AM \ 1.5G(\lambda) \cdot V(\lambda) d\lambda} = AVLT_{Glowing}$$

Where, $R(\lambda)$ is the reflectance spectrum, which can also be directly measured by the double-beam spectrometer. Then the corresponding $AVLH_R$ is defined as:

$$AVLH_R = \frac{AVR_{Glowing}}{AVR_{\perp} + AVR_{Glowing}}$$
 (5.7)

A typical example of how the DS $PL^{Back}(\lambda)$ and $PL^{Front}(\lambda)$ impact on the total transmitted and reflected spectra is shown in Figure 5.4B. With 20% neutral VIS single-pass absorptance ($A_I = 20\%$), the transmitted and reflected solar spectra ($AM\ 1.5G(\lambda) \cdot T(\lambda)$) and $AM\ 1.5G(\lambda) \cdot R(\lambda)$) are both determined, and the varying $PL^{Back}(\lambda)$ and $PL^{Front}(\lambda)$ as a function of emission wavelengths are then superimposed onto the transmitted and reflected solar spectra as the combined spectra $AM\ 1.5G(\lambda) \cdot T(\lambda) + PL^{Back}(\lambda)$ and $AM\ 1.5G(\lambda) \cdot R(\lambda) + PL^{Front}(\lambda)$ on the transmitted and reflected sides, respectively.

Another mechanism that can be conceptually utilized to enhance LSC performance is upconversion (UC) as introduced in Chapter 2. This effectively expands the solar spectral coverage achievable over conventional DS process.^{57–59} By assuming ideal QYs of various UC processes of 50%, the idealized absorptance and emission profiles are shown in Figure 5.4C: the $PL(\lambda)$ peaks (blue, cyan, green, orange, red and NIR) shown in Figure 3A are also used for UC emission, and spectral range between 675 nm (VIS/NIR border) and up to twice of the corresponding emission peak wavelengths (i.e., two low-energy photons are up-converted into one high-energy photon) can be potentially utilized for UC harvesting. In all these UC processes we confirm that the total absorbed NIR energy is higher than the total up-converted and emitted energy so that the energy conservation is always satisfied.

Quantum-cutting (QC) is another photoluminescence process that effectively enhances DS. In this case, one high-energy photon is absorbed and split into multiple low-energy photons. 63–67 This spectral conversion approach enables effective utilization of high-energy UV photons in LSC application, and the step-function absorptance and emission profiles for QC process with ideal *QY* of 200% is also plotted in Figure 5.4C. All the UV photons below 430 nm is split into multiple deeper NIR photons with a massive down-shift across the VIS range. Notably, because the VIS/NIR cutoff is at 675nm, quantum-cutting NIR photons results in emission past 1350 nm, and it is very challenging to spectrally match such a deep IR emission with high efficiency edgemounted PV cells. QC with emission in the visible range requires the absorbed UV light with photon energy over 3.7 eV (< 338 nm), and the corresponding high energy UV photons flux (< 0.4% of the total AM 1.5G photon flux) is negligible for electrical power generation. Therefore, these two cases are not considered in this optical model.

Similar to the DS process, the combined spectra $AM\ 1.5G(\lambda) \cdot T(\lambda) + PL^{Back}(\lambda)$ and $AM\ 1.5G(\lambda) \cdot R(\lambda) + PL^{Front}(\lambda)$ resulting from the UC and QC mechanisms are also used to calculate the

rendered color metrics affected by the escaped photoluminescence on each side. To date, DS is the most widely adopted photoluminescence mechanism in LSC design with near unity QYs. Demonstrations of TTA-UC^{4,134–136} and QC^{63–65} mechanisms in LSC applications have also been reported in literature, but TTA-UC is still far from ideal due to its relatively low up-conversion efficiency. In contrast, near 200% QYs have been shown for QC mechanism despite less ideal absorption/emission profiles.⁶³

5.3 Results

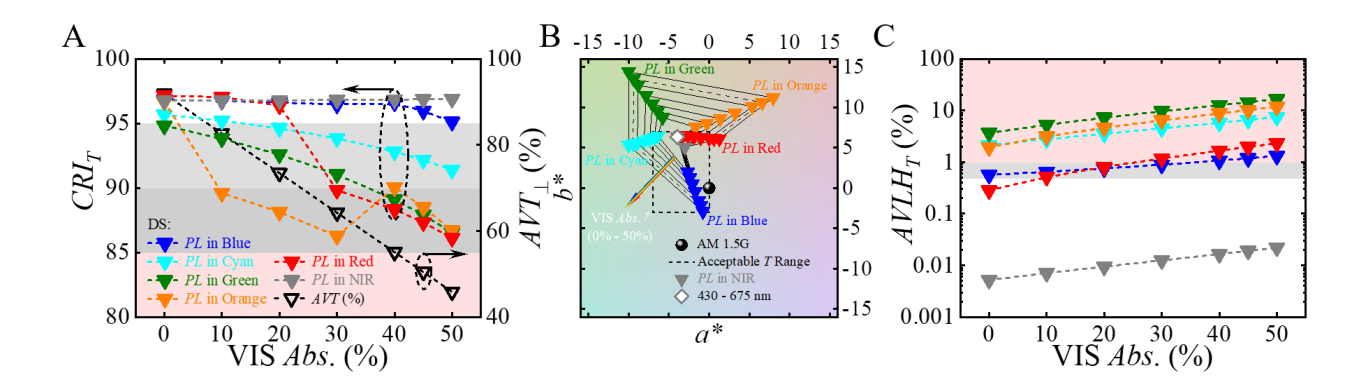


Figure 5.7 Visual impact of photoluminescence on aesthetic parameters of TLSCs on the transmitted side.

The impact of escaped down-shifting (DS) photoluminescence in different emission wavelengths on (A) CRI_T and AVT_{\perp} , (B) $(a^*, b^*)_T$, (C) average visible haze $(AVLH_T)$ as a function of degree of A_I . Note: 1) different shades of background colors in (A) indicate various CRI_T grades of transparent window glasses on the transmitted side: 95-100 for "excellent" (in white), 90-95 for "good" (in light gray), 85-90 for "acceptable" (in dark gray), and below 85 for "poor" (in red); 2) dashed boxes in (B) indicate the acceptable $(a^*, b^*)_T$ ranges: $-7 < a^* < 0$ and $-3 < b^* < 7$, which is based on the survey of many commercially available architectural glass products shown in Figure 5.2A; 3) the threshold value is 1% for $AVLH_T$ on the transmitted side, $AVLH_T$ range above 1% in red shade suggests strong visual impact from glowing haze due to escaped visible photoluminescence, which is unacceptable for window applications; $AVLH_T$ range between 0.5% and 1% in grey, is less favorable for high quality glazing systems.

Figure 5.7 shows the impact of DS photoluminescence on neutral-colored LSC aesthetics as a function of various degrees of visible contribution. Architectural glass typically requires AVT_{\perp} s above 50%, which still allows design opportunities and flexibility to effectively harvest some visible photons for TPV power generation. As shown in Figure 5.7A, the AVT_{\perp} linearly decreases as VIS contribution (A_I) increases. However, as visible absorption contribution increases, the overall intensities of $PL^{Back}(\lambda)$ and $PL^{Front}(\lambda)$ also increase, which can significantly affect the combined spectra and aesthetics on both sides (indoor and outdoor) of the LSCs.

In both the lighting and window industries, the color rendering can be categorized by the corresponding CRI ranges, typically, 95-100 is "excellent", 90-95 is "good", 85-90 is acceptable, and < 85 is "poor" for neutral-colored requirements which are indicated with different shades of color in Figure 5.7A and Figure 5.8A for the transmitted and reflected side, respectively. As more incident photons are harvested and down-shifted into the visible photoluminescence, the corresponding CRI_T and CRI_R values drop accordingly. On the transmitted side, the CRI_T s degrade with all visible PL colors but still remain within or above the acceptable range as long as the visible contribution (A_I) is below 50%. On the reflected side, however, all the CRI_R s immediately degrade to an unacceptable range even without any visible absorption contribution. We also see the impact of $PL^{Back}(\lambda)$ and $PL^{Front}(\lambda)$ on (a^*, b^*) in Figure 5.7B and Figure 5.8B, respectively. The increasing VIS photon contribution can quickly move the (a^*, b^*) away from the origin (0, 0) towards the corresponding colors of the visible photoluminescence, driving the corresponding color tinting out of the acceptable ranges on each side. On the transmitted side, we see that the aesthetics are outside the acceptable window for every emission color except the ones with $PL(\lambda)$ in the blue for A_1 50%, and $PL(\lambda)$ in the red for $A_1 < 40\%$. On the reflected side, only LSCs with $PL(\lambda)$ in the red and $A_1 < 10\%$ fall within the acceptable range.

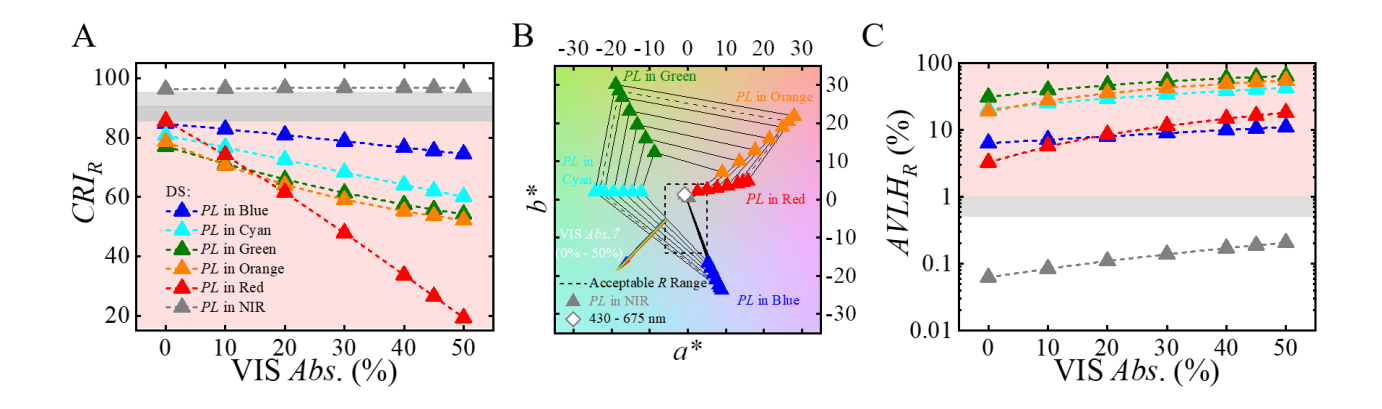


Figure 5.8 Visual impact of photoluminescence on aesthetic parameters of TLSCs on the reflected side.

The impact of escaped down-shifting (DS) photoluminescence in different emission wavelengths on (A) CRI_R , (B) $(a^*, b^*)_R$ and (C) $AVLH_R$ as a function of degree of A_I . Note: 1) different shades of background colors in (A) indicate various CRI_R grades of transparent window glasses on the reflected side: 95-100 for "excellent" (in white), 90-95 for "good" (in light gray), 85-90 for "acceptable" (in dark gray), and below 85 for "poor" (in red); 2) dashed boxes in (B) indicate the acceptable $(a^*, b^*)_R$ ranges: $-6 < a^* < 5$ and $-14 < b^* < 4$, which is based on the survey of many commercially available architectural glass products shown in Figure 5.2B; 3) the threshold value is 1% for $AVLH_R$ on the reflected side, $AVLH_R$ range above 1% in red shade suggests strong visual impact from glowing haze due to escaped visible photoluminescence, which is unacceptable for window applications; $AVLH_R$ range between 0.5% and 1% in grey, is less favorable for high quality glazing systems.

Conventionally, the threshold value for scattering haze is limited to < 1% for high quality architectural window glass (haze over 0.5-1% creates an uncomfortable "cloudiness" to the observers and therefore becomes unacceptable for high quality glazing systems.). The impact of glowing haze caused by escaped photoluminescence is also assessed, and the resulting $AVLH_{TS}$ and $AVLH_{RS}$ are plotted in logarithmic scale in Figure 5.7C and Figure 5.8 C, respectively. For all the PL colors, the $AVLH_{TS}$ and $AVLH_{RS}$ monotonously increase as more visible photons are harvested and contribute into the DS PL. The threshold requirement of 1% is also set for both $AVLH_{TS}$ and $AVLH_{RS}$ of LSCs with DS mechanisms as shown in Figure 5.7C and Figure 5.8 C, respectively. On the transmitted side, photoluminescence in cyan, green and orange can cause strong glowing haze even with no VIS contribution, and photoluminescence in blue and red is acceptable with very limited VIS contribution < 20 - 30%. On the reflected side, all visible

photoluminescence results in corresponding AVLH_R values over 1% regardless of the VIS contribution.

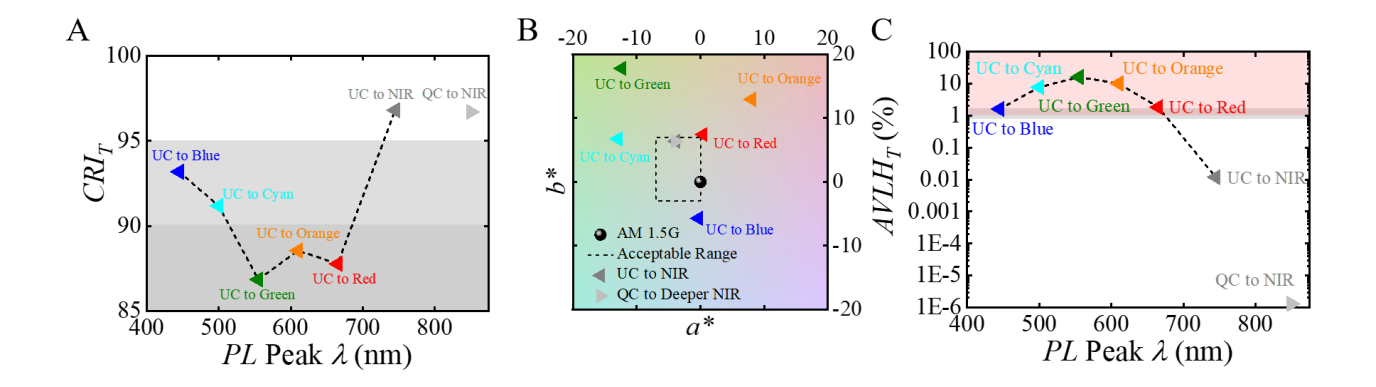


Figure 5.9 The impact of escaped photoluminescence from up-conversion (UC) and quantum-cutting (QC) processes on the aesthetics on the transmitted side. Impact on (A) CRI_T , (B) $(a^*, b^*)_T$, (C) $AVLH_T$ as a function of emission wavelength.

Figure 5.9 and Figure 5.10 summarize the aesthetic parameters of LSCs with TTA-UC and QC mechanisms as a function of $PL(\lambda)$ peak wavelength. To isolate the impact from the TTA-UC and QC photoluminescence only, no VIS contribution is included in these assessments. As shown in Figure 5.9A and Figure 5.10A, all up-converted emission in VIS range results in reduced CRI_{TS} on the transmitted side. On the reflected side, the corresponding CRI_{RS} are impacted even more strongly from the visible $PL^{Front}(\lambda)$, and all are unsuitable for window applications. Particularly, UC emission in the red results in CRI_{R} as low as 19.4. Accordingly, the (a^*, b^*) coordinates of the LSCs with visible UC emission are strongly tinted by the colors of the visible photoluminescence on both sides as shown in Figure 5.9B and Figure 5.10E and all are outside of the acceptable range. Additionally, the "glowing" effect would be very prominent to observers on both sides of the LSCs with all the corresponding $AVLH_{TS}$ and $AVLH_{RS}$ well above the threshold value of 1%. In particular, $PL^{Escaped}(\lambda)$ in green results in $AVLH_{RS}$ as high as ~70% due to the close spectral match of $V(\lambda)$ and $PL(\lambda)$.

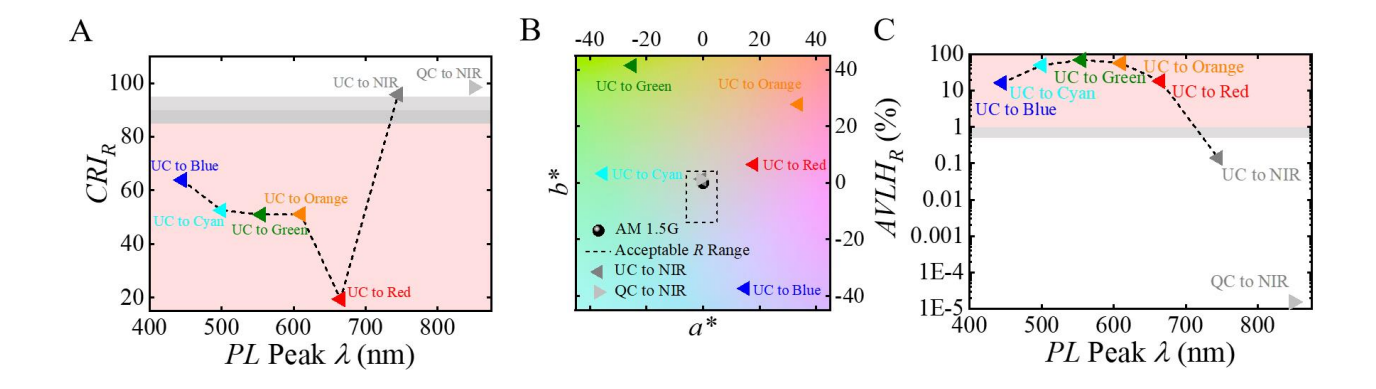


Figure 5.10 The impact of escaped photoluminescence from up-conversion (UC) and quantum-cutting (QC) processes on the aesthetics on the reflected side. Impact on (A) CRI_R , (B) $(a^*, b^*)_R$ and (C) $AVLH_R$ as a function of emission wavelength.

Absorption and emission peaks in VIS should be avoided in LSC designs where there is a preference/requirement of color neutrality.^{3,9,44,78} However, coloration can be desirable in particular LSC applications.^{137–139} On the transmitted side, the transmitted photon fluxes (AM $1.5G(\lambda) \cdot T(\lambda)$) are strongly tinted in blue, cyan, green, orange, and red, respectively. ¹²⁰ In comparison, AVT_{\perp} s of various transmittance profiles are calculated based on both AM 1.5G and D65 spectra, the absolute discrepancies are generally below 1% unless the transmission is severely tinted.

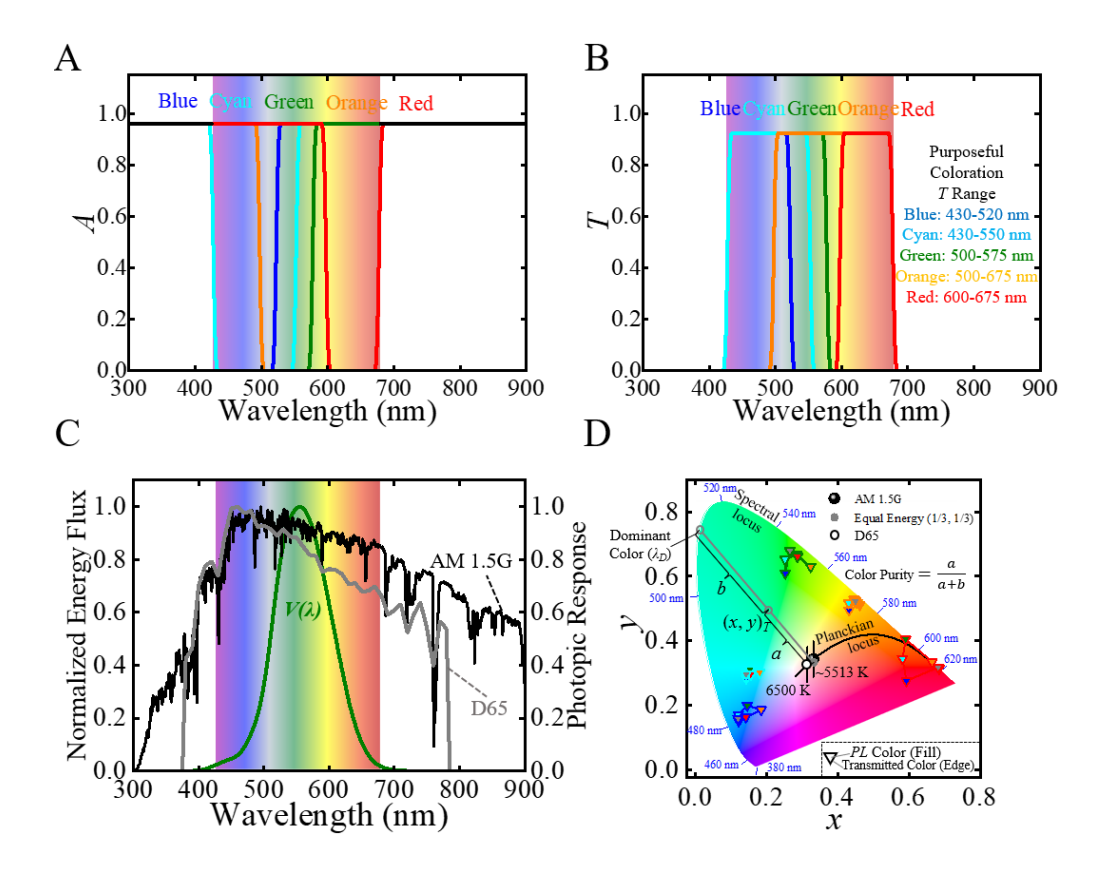


Figure 5.11 The impact of escaped photoluminescence from DS processes of LSCs with purposeful coloration on the transmitted side.

The idealized step-function (A) absorbance, (B) transmittance. (C) Comparison of normalized AM 1.5G and D65 energy fluxes. The photopic response ($V(\lambda)$) is also included as the background. (D) The impact of various escaped photoluminescence from DS process in different emission wavelengths on various transmitted colors. Note: 1) the edge colors of the down-triangle legends represent the transmitted colors, and the fill colors of triangle legends represent the photoluminescence colors; 2) CIE 1931 color chromaticity diagram is suitable to illustrate the high color purities of the transmitted colors under the impact of various escaped photoluminescence. As the example shown in (A), the color purity (i.e., color saturation) of the transmitted color is the distance in the chromaticity diagram between the $(x, y)_T$ color coordinate point of the test source and the coordinate of the equal energy point of (1/3, 1/3) as a, divided by the distance between the equal energy point and the dominant color wavelength point (x_d, y_d) as a+b. Therefore, the color purity of $(x, y)_T$ is thus calculated as $=\frac{a}{a+b} = \frac{\sqrt{(x-1/3)^2+(y-1/3)^2}}{\sqrt{(x_d-1/3)^2+(y_d-1/3)^2}}$.

As incident photons are harvested and down-shifted into visible photoluminescence, the escaped photoluminescence $(PL^{Back}(\lambda))$ exhibits impact on combined transmitted photon flux $(AM 1.5G(\lambda) \cdot T(\lambda) + PL^{Back}(\lambda))$, shifting the $(x, y)_T$ coordinates of the transmitted colors and

simultaneously impacting the corresponding color purities depending on the photoluminescence wavelength. Photoluminescence could thus reinforce, shift, or deteriorate transmissive color. Since the AM 1.5G(λ)·T(λ) is significantly stronger compared to the $PL^{Back}(\lambda)$, the shift in $(x, y)_T$ is moderate as shown in **Figure 5.11**D, but the change in color purity can still be up to ~0.2-0.25. The resulting $(x, y)_T$ coordinates of all the transmitted colors stay close to the spectral locus, suggesting relatively high color purities regardless of the impact of VIS photoluminescence colors. Although the transmitted color is dominated by the transmittance spectrum (i.e., the corresponding VIS absorption profile), the impact from the escaped photoluminescence is not negligible. Whereas the colors of reflected photon fluxes are less tinted, and the $PL^{Front}(\lambda)$ fluxes are comparable to $AM\ 1.5G(\lambda) \cdot R(\lambda)$ fluxes, as a result, the colors of $PL^{Front}(\lambda)$ can substantially affect the overall colors of combined photon fluxes $(AM\ 1.5G(\lambda)\cdot R(\lambda)+PL^{Front}(\lambda))$, significantly driving the $(a^*, b^*)_R$ towards the corresponding colors of the visible photoluminescence as shown in Figure 5.12B to F. Therefore, the impact from PL should not be simply overlooked for these types of LSCs. Moreover, the impact of PL in the VIS spectrum not only changes the color rendering and color quality (perhaps not dominantly) but will also impart substantial luminescent haze dominantly (haze at even 1% becomes significant to observers).

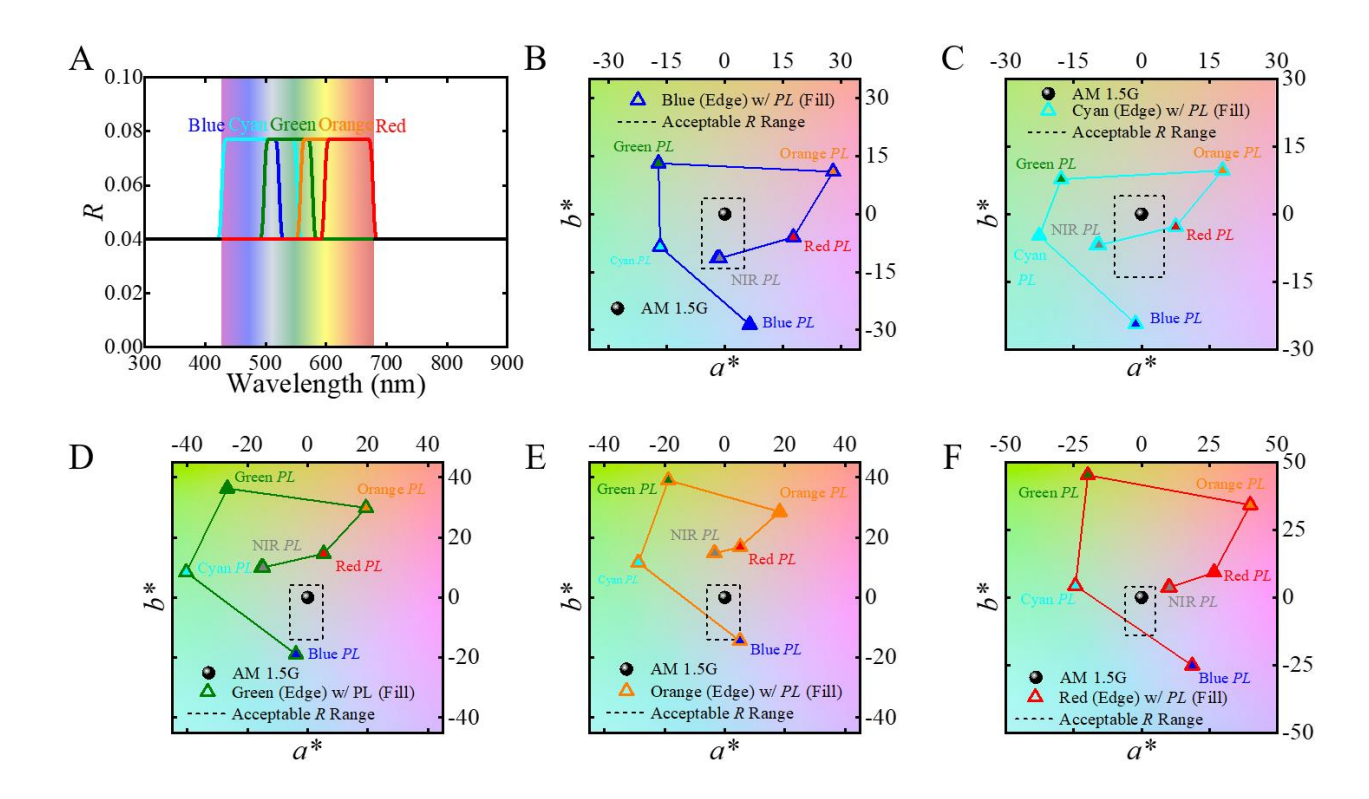


Figure 5.12 The impact of escaped photoluminescence from DS processes of LSCs with purposeful coloration on the reflected side.

(A) Idealized step-function reflected profiles of LSCs with various purposeful coloration. (B) The impact of various escaped photoluminescence from DS process in different emission wavelengths on (B) reflected blue color, (C) reflected cyan color, (D) reflected green color, (E) reflected orange color and (F) reflected red color. Note: the edge colors of the up-triangle legends represent the reflected colors, and the fill colors of triangle legends represent the photoluminescence colors.

5.4 Discussion

Significant effort and attention in LSC research have been focusing on improving luminophore QYs and suppressing reabsorption loss, however, it is also important to consider the various contributions to LSC aesthetics. As emitters are optimized and gradually approach theoretical limits for QY (100%, 50% and 200% for DS, UC, and QC mechanisms, respectively) and absorption/harvesting range, photoluminescence will continuously grow more impactful on all the key aspects of LSC aesthetics. This is particularly true when the $PL(\lambda)$ locates in the VIS.

In most cases, the impact on the (a^*, b^*) is unacceptable and is unacceptable in nearly all cases when considering haze (as shown in Figure 5.7, Figure 5.8, Figure 5.9, and Figure 5.10). In contrast, the impact on CRI_T , CRI_R , $(a^*, b^*)_T$ and $(a^*, b^*)_R$ becomes negligible (even with high levels of visible contribution) as the DS photoluminescence is redshifted into NIR range. Additionally, glowing haze (AVLH_T and AVLH_R) caused by NIR photoluminescence is also typically well below 0.5% (but depends on how much tail emission there is into the VIS). This effectively helps to maintain the high imaging fidelity and aesthetics on both sides. For DS photoluminescence, all incident photons with wavelengths shorter than the emission wavelengths can potentially contribute to the photovoltaic conversion, which results in the increasing peak height of the superimposed $PL^{Back}(\lambda)$ and $PL^{Front}(\lambda)$ as photoluminescence wavelength redshifts as shown in Figure 5.4B. With the same degree of AVT₁, LSCs with NIR photoluminescence not only minimize the visual impact, but always maximize the utilization of the VIS contribution. Similarly, the UC process with NIR emission and the QC process deeper in the NIR can also effectively ensure that these LSC devices meet all aesthetic requirements for the highest demand window applications. As shown in Figure 4, the corresponding CRIs exhibit the highest quality, the (a^*, b^*) coordinates reside very close to the origin, and the AVLHs are magnitudes below the threshold values on both sides of the LSC devices. Similar to the DS process, as the $PL(\lambda)$ redshifts, the usable solar spectrum for UC process also expands increasingly in the NIR and IR as shown in Figure 3F, e.g., photons as deep as ~1500 nm can potentially be utilized for the UC with NIR emission. In contrast, for UV-only selective harvesting TLSCs, the absorption cutoff is strictly limited to < 430 nm to avoid yellowish tint. The total photon flux at wavelengths < 430 nm is only ~3.7% of the AM 1.5G photon flux, therefore, the potential of these configurations seems limited. But there are three approaches to effectively utilize the UV photons and further enhance the LSC-PV performance:

quantum-cutting for photocurrent gain, paring with high bandgap edge-mounted PV for voltage loss reduction, and incorporating the UV component into a multi-band (tandem) LSC configuration for maximized solar spectrum coverage, which will be discussed in detail in Chapter 9.

It is important to note that some of these limitations can be partially mitigated by increasing the waveguide trapping efficiency (η_{Trap}). In theory, this can be improved to near 100% with combined anti-reflection coatings and distributed Bragg reflectors with tunable stop bands. In this case, the visual impact of photoluminescence would be effectively minimized or even eliminated for all photoluminescence mechanisms. However, such waveguiding enhancement can only be enabled when these optical designs are simultaneously applied onto both sides of the waveguide, and the stop bands need to spectrally match the PL (λ) wavelengths. If the PL (λ) and the corresponding stop bands reside within the VIS range (at normal or oblique incidence), the device will be strongly tinted from the corresponding $T(\lambda)$ and $R(\lambda)$ spectra as opposed to the PL spectra (a poor tradeoff), still exhibiting low color fidelity on both sides. While such an approach can potentially mitigate the impact of photoluminescence on the aesthetics, it comes at a substantial financial cost that would negate some or all of the low-cost advantage of an LSC approach. Similarly, the use of higher refractive index waveguides (i.e., glass) can simultaneously reduce waveguiding losses and photoluminescence impacting on the aesthetics, but also with the similar cost tradeoffs since high index windows are not commonly/commercially available at large scales.

In certain applications, surfaces with purposeful coloration are desired, and VIS luminescent haze can be incorporated to enhance such visual impact or expand the color tunability range. Herein, the VIS luminescence haze is deemed as a benefit rather than a detriment. ^{140,141} Figure 5.7B, Figure 5.8B, Figure 5.8B, Figure 5.10B, Figure 5.11D and Figure 5.12B to F show the expanded color tunability enabled by photoluminescence (in DS, UC, and QC) on the

transmitted and reflected side, respectively. Notably, for LSCs with coloration from VIS absorption, if the $AM\ 1.5G(\lambda) \cdot R(\lambda)$ and $PL^{Front}(\lambda)$ profiles are designed to overlap with each other, the preferred reflected colors can be further enhanced by the escaped VIS photoluminescence as shown in Figure 5.12B to F. Furthermore, the combination of various coloration mechanisms (selective absorption, reflective coating, and VIS photoluminescence) offers diverse approaches to modify the surface appearance (either the entire panel or only fractions of the surfaces) instead of electrical power production, for example, the artistic potential of the LSCs can be exploited by utilizing different luminophores with various absorption and emission profiles as paints on transparent waveguides as canvases. ¹⁴² Intricate patterns, special signage or even artistic creation can be applied, where luminescence can offer a unique visual perception or improved color saturation. ^{131,139–141}

5.5 Summary

Luminescent solar concentrators provide promising opportunities for widespread solar adoption due to their structural simplicity, ease of fabrication, design flexibility, and selective harvesting tunability. However, the significance of LSC aesthetics is often underestimated or ignored even though these metrics are often the key thresholds for practical applications. In this perspective, we first identify the key figures of merit for aesthetic quality of semitransparent and transparent LSC devices, and then we develop an optical model to quantitatively evaluate the rendered color fidelity and glowing haze of LSC system by incorporating the impact of escaped photoluminescence. The aesthetics of LSCs with various photoluminescence mechanisms, including down-shifting, up-conversion, and quantum-cutting processes, are systematically analyzed, and future strategies to simultaneously improve the photovoltaic performance and

aesthetic quality of LSCs are proposed. For LSC applications with the requirements of minimum visual impact from escaped photoluminescence, the optimal approach is to shift the PL into NIR, which is also beneficial to minimize the overlap between absorption and emission profiles, suppressing the corresponding reabsorption loss. Quantitative analysis based on the optical model is provided to endorse such approach. As emitter materials with various photoluminescence mechanisms develop and the corresponding photoluminescence *PLQY*s improve, the consideration of the overall LSC visual impact will start to emerge. Therefore, the goal of this chapter is to provide a roadmap for LSC development with aesthetic consideration in advance, so that the research can push the LSC technology more commercially appealing in both PV performance and aesthetic quality in the future, rather than the opposite way. Purposeful coloration enabled by visible-absorbing and emitting luminophores in LSC design is also quantitatively discussed. Visible photoluminescence could effectively reinforce, shift, or deteriorate the color rendering effects on both the transmitted and reflected sides of the LSCs. Ultimately, we expect this work helps researchers comprehensively consider all the crucial aspects in LSC design, guiding these devices advance in a market-adoptable pathway.

Chapter 6 Integration of Luminescent Solar Concentrators onto Arbitrary Surfaces

There has been a significant interest in improving the photovoltaic performance of LSC/TLSC devices, however, little attention has been focused on the challenges of integrating LSCs onto non-window surfaces or windows with significant infrared absorption coefficients. In these situations, the total internal reflection can be effectively disabled when LSCs are directly and seamlessly integrated onto surfaces that are highly absorptive or scattering to infrared light. In this chapter, we utilize a low refractive index adhesive film with high transparency between the NIR-selective TLSC waveguide and the back surface, to maintain both the device functionality and aesthetic quality of the surface underneath. Therefore, photovoltaic measurements are conducted to show that the TIR is re-enabled with the presence of such an optical design.

6.1 Introduction

Figure 6.1 illustrates operating principles of a NIR-selective harvesting TLSC system. Due to the difference of refractive index between the waveguide and the ambient environment the remitted photons are predominantly trapped within the waveguide by total internal reflection (TIR), causing them to be directed towards the waveguide edges where these re-emitted photons can be converted into electrical power in photovoltaic cells. According to Snell's law, the key to ensuring TIR is that the waveguide is made of a material with higher index of refraction (n) value than that of both the front and back claddings. The waveguide material should also have low extinction coefficient (k) or scattering coefficient at the wavelength range of the photoluminescence. Such an example is shown in Figure 6.1, where the windshield glass of a car $(n_{glass} \cong 1.50)$ in contact with air $(n_{air} = 1.0)$ on both sides can function effectively as a waveguide for TLSCs. However,

when a TLSC is integrated onto arbitrary surfaces such as the siding of a car, the back of the waveguide is no longer in contact with air but seamlessly adhered with the solid surface beneath. This results in re-emitted photons entering the back surface and being lost to absorption or scattering from that surface. Spacing an air gap between the waveguide and the surface underneath can regain this waveguide function, however, air gaps generally lack structural stability rendering them unsuitable for robust applications.¹⁴³

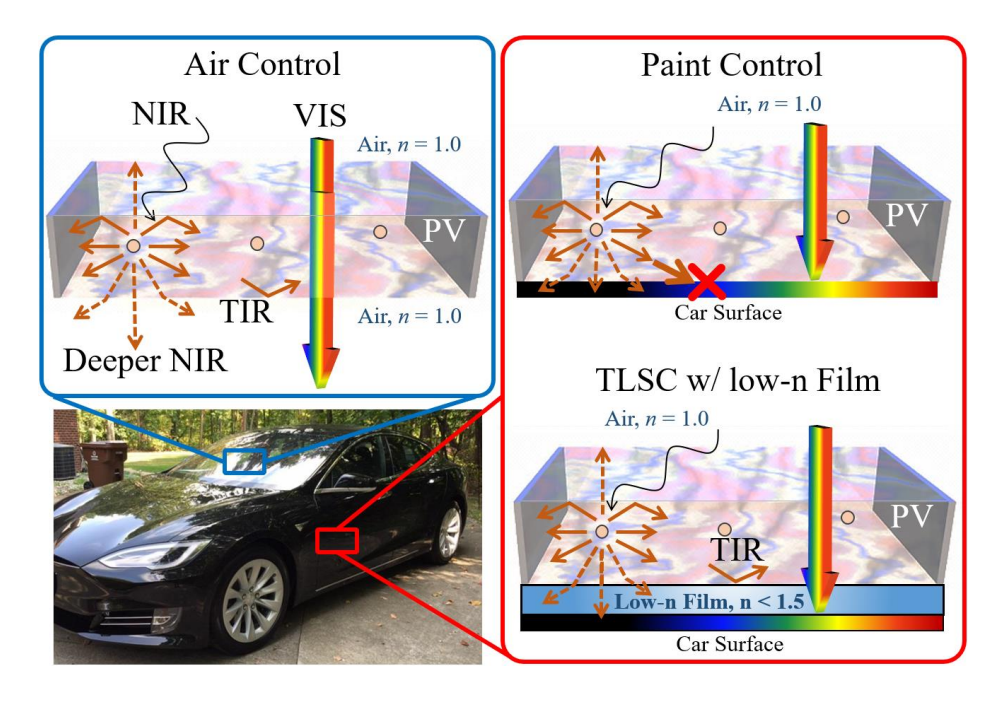


Figure 6.1 Conceptual schematic showing a TLSC integrated onto arbitrary surfaces.

(A) TLSC integrated onto window ("Air Control") and non-window ("TLSC w/ Low-n Film") parts of an automobile. While a black automobile is pictured, this could be applied to any color automobile without changing the architecture. With direct integration of LSC and TLSCs on such surfaces (included in the schematic as "Paint Control") total internal reflection (TIR) is disabled.

In this chapter, we demonstrate a route to enable the photovoltaic performance of TLSC devices as they are installed onto arbitrary surfaces. We have developed an optical approach to confine the TIR to the optically transparent waveguide and prevent surface absorption that can effectively turn off the TLSC device. Conceptually, a neat layer with a low refractive index is coated onto the back side of the TLSC to function as cladding for the waveguide (Figure 6.1). NIR-

selective harvesting organic dye/polymer host composite is then coated onto the front surface of the waveguide as the luminophore film. Due to the NIR-absorption of the organic dye combined with visible/infrared transparency of the low refractive index film, the overall visual impact of the whole TLSC device is minimized while the functionality and aesthetic quality of the surface underneath are largely unaffected. Both the current density-voltage (J-V) characteristics and distance-dependent EQE_{LSC} measurements show that the insertion of the low refractive index film can effectively re-enable the LSC device and substantially improve the η_{LSC} and scalability in comparison to the TLSC control devices without such an approach. This design provides a simple and scalable method to resolve the challenge of seamless integration of TLSCs onto any surface to help realize the full potential of LSC and TLSC devices beyond windows.

6.2 Experimental Section

Module Fabrication: "Air Control" TLSC: 200 mgL⁻¹ 1-(5-carboxypentyl)-3,3-dimethyl-2-((E)-2-((E)-3((E)-2-(1,3,3-trimethylindolin-2ylidene)ethylidene)cyclohex-1-enyl)vinyl)-3H-indolium chloride (Cy7-CA) (Lumiprobe) ethanol solution was mixed with mounting medium (Fluoroshield F6182, Sigma-Aldrich) at a volume ratio of 1:2. This mixture was drop-cast on the front surface of a 5.08 cm \times 5.08 cm \times 0.635 cm glass sheet (for photovoltaic characterization) and allowed to dry for 6 hours in a glove-box filled with nitrogen gas (O_2 , O_2) ppm), resulting in a layer thickness of 0.5 mm. Dichloromethane was mixed with (poly)-butyl methacrylate-comethyl methacrylate (PBMMA) (Sigma-Aldrich) at a volume ratio of 1:1. This mixture was then drop-cast onto the dye/waveguide composite film to make a smooth and flat surface to avoid light scattering in the waveguide and act as a protection layer. The same layer structure was applied for

2.54 cm \times 2.54 cm \times 0.1 cm (for photoluminescence (PL) measurements) or 1.27 cm \times 1.27 cm \times 0.07 cm (for QY measurements). For photovoltaic measurements, single-crystalline solar cells (Vikocell) were laser cut into 5.08 cm \times 0.635 cm strips for η_{LSC} and corresponding EQE_{LSC} measurements and 10.16 cm \times 0.635 cm strips for normalized position-dependent EQE_{LSC} measurements. For η_{LSC} measurements, two PV strips were mounted on orthogonal edges using index matching gel (Thorlabs) to attach the PV strips on glass edges and were connected in parallel. Each device was tested with the same PV cells. The remaining two edges were covered with specular film reflector (DF2000MA series, 3M). For EQE_{LSC} measurements, one PV strip was attached to one edge of the waveguide with the other three edges painted black.

Thin, low index polymer layers were coated onto the backside of the waveguide sheet by doctor blade, and the thickness of these low refractive index films ("n = 1.30" or "n = 1.38") are controlled to 0.5 mm. A PBMMA film was then formed on top of the low refractive index layer as a polymer protection film by drop-casting. This PBMMA film is necessary for good adherence of the following paint layer and to protect the previously coated low index layers from redissolution. After the PBMMA film is dried, paint is sprayed uniformly to form a dense and smooth paint film. The front surfaces and edges of "n = 1.30", "n = 1.38" and "Paint Control" TLSCs are the same as the "Air Control" TLSC.

Optical Characterization: Specular transmittance of both solutions and films were measured using a dual-beam Lambda 800 UV/VIS spectrometer in the transmission mode. The PL for Cy7-CA in both solutions and polymer films were measured by using a PTI QuantaMaster 40 spectrofluorometer with excitation at 675 nm. Quantum yield measurements were tested by using Hamamatsu Quantaurus fluorometer, excitation ranges in scan mode (10 nm per scan step) were

adjusted to 700 - 750 nm for Cy7-CA. Six QY values were collected, and the reported QY was averaged from these six QY values with corresponding excitation wavelengths.

Photovoltaic Characterization: J-V measurements were obtained using a Keithley 2420 source measurement under simulated AM1.5G solar illumination (xenon arc lamp with the spectral mismatch factor of 0.97±0.03 for all the devices tested). The light intensity was calibrated with an NREL-calibrated Si reference cell with KG5 filter. For position-dependent EQE_{LSC} measurements, the excitation beam was obtained by directing chopped incident light from a quartz tungsten halogen lamp through a monochromator. EQE_{LSC} scans were performed by positioning the monochromatic excitation beam from a fiber perpendicular to the LSC waveguide front surface at various distances from a single edge-mounted Si PV cell. As addressed in Chapter 4, the measured EQE_{LSC} was corrected by the geometric factor, $g = \pi/tan^{-1}(L/2d)$, which accounts for the different angle subtended by the solar cell at various distance d, where L is the square-shaped LSC plate length. Note both η_{LSC} and EQE_{LSC} measurements were tested by using the same TLSC to match the J_{SC} with the J_{SC}^{Int} , and a matte black background was placed on the back of the tested TLSC device to eliminate the illumination from the environment or reflection (double pass) for both η_{LSC} and EQE_{LSC} measurements. We also utilize the same PV cells mounted around the edge to eliminate any PV-to-PV variations in performance.

Optical Modeling: In considering reabsorption losses from the overlap in the absolute absorption and normalized emission spectra, the optical efficiency $\eta_{Opt}(\lambda)$ of the "Air Control" TLSC system was numerically evaluated in Matlab as a function of distance d, plate length L, plate thickness t_0 and dye/polymer film thickness t. The complete equations used in this simulation can be found in Chapter 2.9

6.3 Results

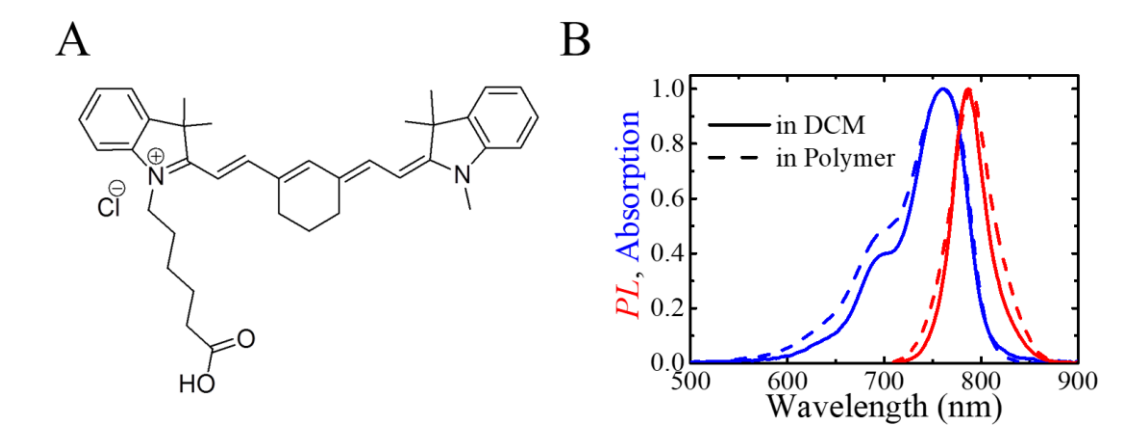


Figure 6.2 NIR luminophore utilized in this study.

(A) The molecular structure of Cy7-CA. (B) Normalized absorption (blue) and emission spectra (red) of Cy7-CA in DCM solution (solid lines) and polymer matrix film (dashed lines).

Cyanine dye Cy7-CA is used as the NIR-selective harvesting luminophore for all the TLSC devices. The molecular structure of Cy7-CA is shown in **Figure 6.2**A, and the absorption/emission spectra in both dichloromethane (DCM) solution and in polymer matrix are plotted in Figure 6.2B. The absorption and photoluminescence spectra of the Cy7-CA in polymer matrix and in DCM solution are very close to each other: the absorption spectra peak at 760 nm for DCM solution and 762 nm for dye/polymer composite film, while the NIR emission peaks are 787 nm for DCM solution and 788 nm for dye/polymer composite film. The photoluminescent quantum yield (*QY*) is 24±1 in DCM solution and 19±1 in polymer matrix.

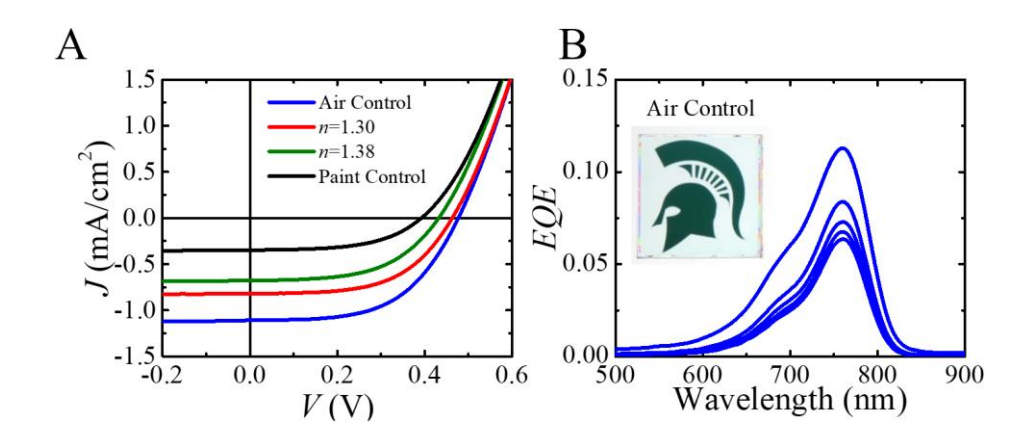


Figure 6.3 Photovoltaic performance.

(A) Current density as a function of voltage (*J-V* curves) for the fully assembled TLSC systems with different layer structures including "Air Control" (blue), "n = 1.30" (red), "n = 1.38" (olive) and "Paint Control" (black). (B) Absolute external quantum efficiency (EQE_{LSC}) of "Air Control" TLSC system as a function of wavelength (measured at d = 5 mm, 15 mm, 25 mm, 35mm and 45 mm), inset: photograph of "Air Control" TLSC.

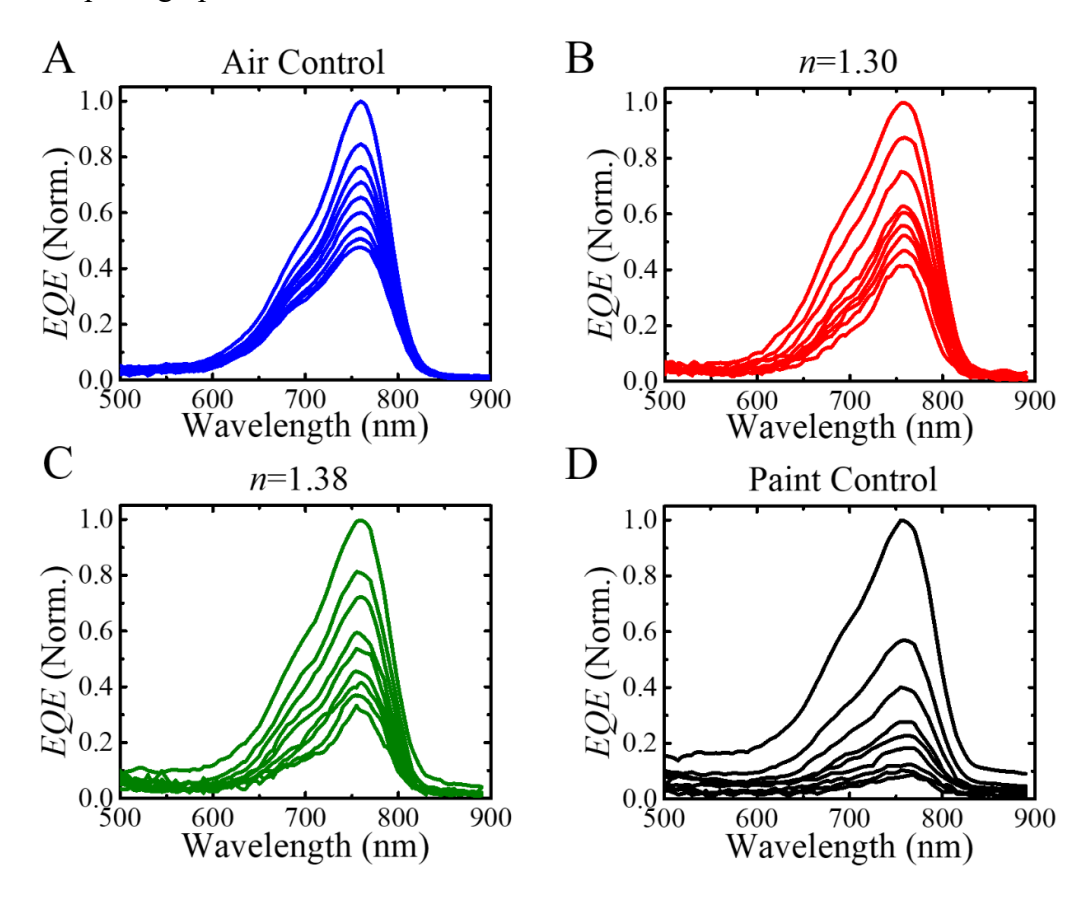


Figure 6.4 Normalized position-dependent EQE_{LSC} . (A) "Air Control". (B) "n = 1.30". (C) "n = 1.38". (D) "Paint Control". Series of EQE scans are performed as a function of wavelength from 15 mm to 95 mm, with 10 mm increments.

TLSC devices are formed on borosilicate glass sheets with an active area of 25.8 cm². To demonstrate the principle of this design, cyanine dye molecules are dissolved in ethanol, mixed with a polymer host, and then drop-cast onto glass sheets to form dye/polymer composite films. Laser-diced Si photovoltaic cells are mounted around the two orthogonal edges and connected in parallel and the other two orthogonal edges are taped with reflective films (see Section 6.2.1 for details). TLSC devices with four different layer structures (as shown in Figure 6.1) are made and

their photovoltaic characteristics are compared. We utilize two different commercially available low index polymers (n = 1.30 and n = 1.38) to compare to an air control (air as the claddings on both sides of the waveguide) and a paint control (just a paint layer on the back surface of the waveguide). The J-V characteristics of these TLSCs are shown in Figure 6.3A along with the absolute position-dependent EQE_{LSC} of the air-control in Figure 6.3B and the normalized EQE_{LSC} s for the other configurations in **Figure 6.4**. The measured J_{SC} of the device with Cy7-CA is 1.11 ± 0.02 mAcm⁻², with a V_{OC} of 0.47 ± 0.01 V and a FF of $55\pm1\%$, leading to an efficiency of 0.30±0.01%. In contrast to the "Air Control" TLSC, the "Paint Control" TLSC exhibits a very poor photovoltaic behavior, which shows a J_{SC} of 0.31±0.02 mAcm⁻², V_{OC} of 0.38±0.01 V, FF of $54\pm1\%$, and a η_{LSC} of only $0.07\pm0.01\%$. When we integrate the low-index polymers, "n=1.30" and "n = 1.38", into the TLSC devices, the corresponding η_{LSC} is improved to $0.21\pm0.03\%$ and $0.16\pm0.01\%$, with J_{SC} of 0.82 ± 0.09 mAcm⁻² and 0.62 ± 0.02 mAcm⁻², V_{OC} of 0.46 ± 0.01 V and 0.43 ± 0.01 V, and FF of $56\pm1\%$ and $55\pm1\%$, respectively. Thus, adding these low refractive index films significantly restore their photovoltaic performance compared to the "Paint Control". Figure 6.4D shows the EQE_{LSC} spectra of the "Air Control" TLSC as a function of excitation position. The EQE_{LSC} peak position of the TLSC (i.e., at 760 nm) matches the absorption spectrum of Cy7-CA in polymer matrix in Figure 6.2B and no direct excitation of the edge-mounted solar cell is observed in any of the EQE_{LSC} spectra. The calculated photocurrent density from integrating the product of the EQE_{LSC} and AM 1.5G solar spectra is 0.91 mAcm⁻² of the "Air Control" TLSC, which is in good agreement with the J_{SC} extracted from J-V measurements.

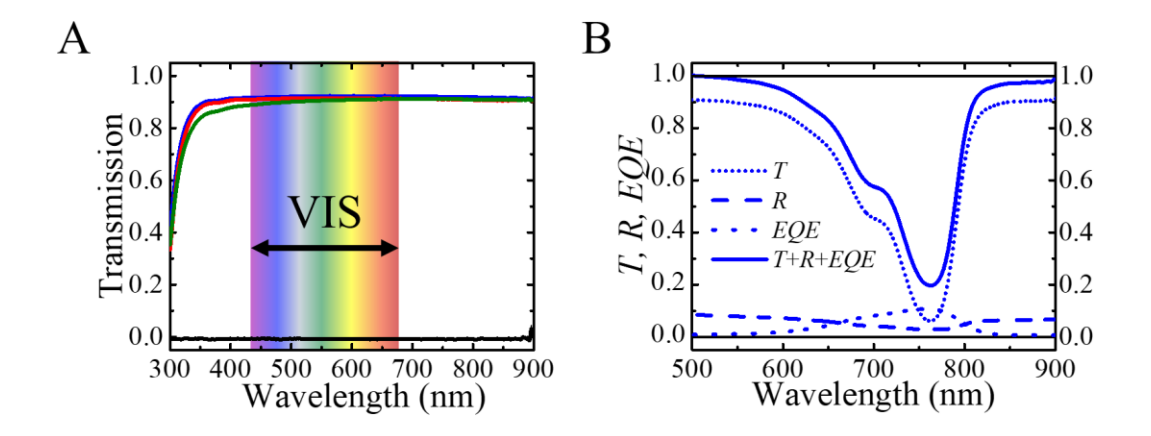


Figure 6.5 Transmittance spectrum and photon balance check.

(A) Spectra for waveguide alone (blue, solid), "n = 1.30" film coated on the backside of the waveguide (red, solid), "n = 1.38" film coated on the backside of the waveguide (green, solid), paint on the backside of the waveguide (black, solid) and "Air Control" TLSC device (blue, short dot). *AVT* and *CRI* were calculated based on these transmittance spectra. (B) $T(\lambda)$, $R(\lambda)$, $EQE(\lambda)$, and photon balance $(EQE(\lambda) + R(\lambda) + T(\lambda) \le 1)$ of the "Air Control" TLSC device.

These data show that the presence of the low refractive index film imparts minimal visual impact such as absorptive coloring or tinting. The transmission spectra of the low refractive index films are compared with that of waveguide alone in **Figure 6.5**A. The transmission spectrum curves of both the "n = 1.30" and "n = 1.38" films on the waveguide sheets nearly overlap with that of the waveguide alone across the whole visible spectrum (from 400 nm to 900 nm), so the corresponding AVT and CRI for "n = 1.30" is 91.3% and 99.8, respectively. ^{3.9,10} For "n = 1.38", its corresponding AVT is 90.6% and CRI is 99.0 compared to 92.2% and 100 for the waveguide alone, respectively. The transmission spectrum of the paint film is also included in the same plot, which indicates that the paint film completely blocks the entire incident light from 300 nm to 900 nm. As addressed previously in Chapter 3 and Chapter 4, to check the validity of photon balance from the independent EQE_{LSC} , $T(\lambda)$, and $R(\lambda)$ spectra measurements of the "Air Control" TLSC device, we show that $EQE_{LSC}(\lambda) + R(\lambda) + T(\lambda) \le 1$ is satisfied at each wavelength in Figure 6.5B. ^{3,12,124} The transmission spectrum of the "Air Control" TLSC device has a corresponding AVT of 87.7% and CRI of 92.3. For the majority of window and glazing system applications, a device should

have AVT > 65-75% and CRI > 90, and therefore the "Air Control" TLSC with Cy7-CA is well suited for this requirement. Although there is not a similar standard for transparent PVs applied to non-transparent surfaces, higher AVT and CRI will always lead to better color fidelity (quantitatively, for example, with CIE chromaticity coordinates) of the original aesthetic quality of the back surfaces, which is critical in many applications and particularly important for automobiles.

To explore the impact of the low refractive index film on device scalability, TLSC systems with the four different structures were characterized by position-dependent EQE_{LSC} as a function of the distance (d) from the excitation source to the same edge-mounted PV cell. Multiple EQE_{LSC} scans were taken for each TLSC system as d was increased from 15 mm to 95 mm (10 mm interval). The EQE_{LSC} spectra of the TLSC devices with four different layer structures are plotted in Figure 6.4A to D and the EQE_{LSC} peak values of each individual scan were extracted and plotted in **Figure** 6.6A.

6.4 Discussion

In the emission wavelength range of Cy7-CA (700 to 850 nm) the edge-mounted Si PV show a nearly constant EQE_{PV} (~90%) so that Equation 4.4 simplifies to $EQE_{LSC}(\lambda) = \eta_{opt}(\lambda) \cdot EQE_{PV}$, where $EQE_{PV} \approx 90\%$. Therefore, the position-dependent EQE_{LSC} roll-off behavior can be used to represent the decay trend of optical efficiency as a function of d. Since all four TLSC devices possess the same polymer encapsulation film, dye/polymer matrix film and waveguide, these loss factors $((1 - R_f(\lambda)), A(\lambda), \eta_{PL})$ are essentially independent of the low refractive index film. For simple waveguides, the trapping efficiency (η_{Trap}) is a function of the

refractive index of the waveguide cladding: $\eta_{Trap} = \sqrt{1 - n_{cladding}^2/n_{waveguide}^2}$. As for the case of the waveguide having two claddings with different refractive index values, η_{Trap} is dominated by the cladding side with lower refractive index due to its larger critical angle (θ_C) for TIR at the waveguide/cladding interface. The reabsorption efficiency η_{RA} is a function of both η_{Trap} and η_{PL} , but it is weakly dependent on the refractive index of the waveguide and cladding compared to η_{Trap} itself. Thus, the difference in $EQE_{LSC}(\lambda)$ roll-off behavior should be dominated by η_{Trap} .

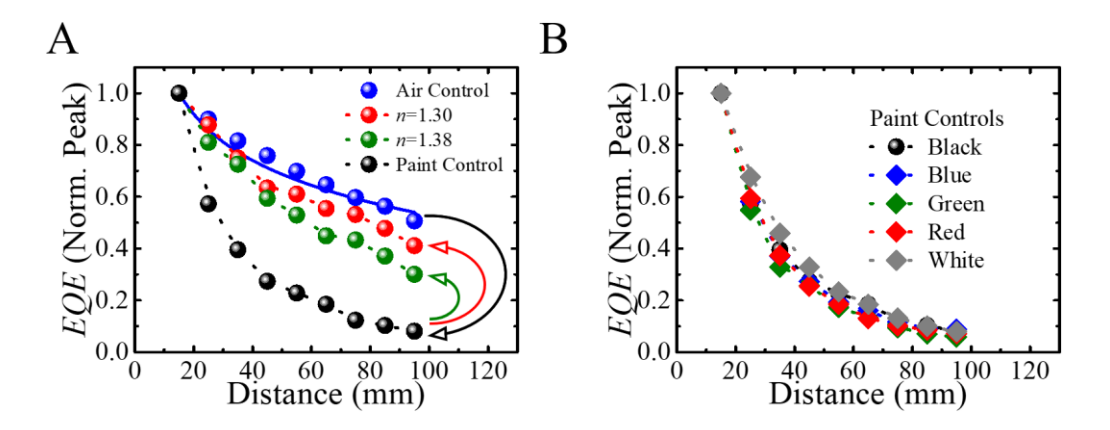


Figure 6.6 Extracted and normalized peak EQE_{LSC} value as a function of distance (d). (A) Simulated optical efficiency (solid line) as a function of distance (d) to fit the measured normalized EQE_{LSC} peak values of the "Air Control" TLSC system. The measured normalized EQE_{LSC} peak values of other TLSC systems including "n = 1.30", "n = 1.38" and "Paint Control" are also plotted for comparison. (B) The measured normalized EQE_{LSC} peak values of colored (black, blue, green, red and white) "Paint Control" TLSC systems.

As shown in Figure 6.6A the "Air Control" TLSC has the highest trapping efficiency, so the EQE_{LSC} decay trend is the slowest since it has both front and back surfaces in contact with air. Once the backside of the waveguide is configured with an absorptive paint film the TIR is no longer confined within the waveguide and the light penetrates into the paint layer. This results in the parasitic absorption and scattering of the light from the paint layer that leads to rapid EQE_{LSC} decays for the "Paint Control" and a factor of 4 lower η_{LSC} . Some remaining EQE_{LSC} signal can

still be collected at very short distances (small d) as shown in Figure 6.4D which is mainly from a very small portion of the emitted photon flux reaching the edge-mounted PV directly through the waveguide but not via TIR. This explains why some residual short-circuit current density can still be detected from the J-V measurement for the corresponding TLSC device in Figure 6.3A. This straight-through luminescent is strongly sensitive to the waveguide thickness, where there is a smaller emission angle range for photons to reach the edge as the waveguide thickness decreases or the length of the device increases. Nonetheless, the η_{LSC} is reduced by nearly 75% even for devices of 5 cm length and would be an even greater loss as the device size is increased.

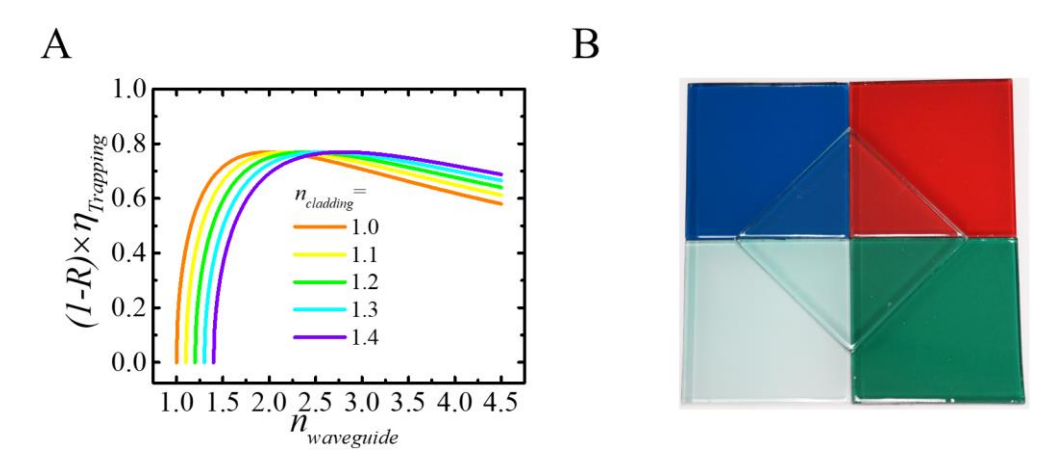


Figure 6.7 Product of the reflection and trapping efficiencies as a function of refractive index of waveguide.

(A) Product of the reflection and trapping efficiencies $((1-R) \times \eta_{Trapping})$ of simple waveguides for different $n_{cladding}$ (1.0–1.4) scenarios as a function of $n_{waveguide}$. In all cases the maximum product is 0.77. (B) A picture of four colored "Paint Control" TLSCs with an "Air Control" TLSC on top, this picture also shows the dye/polymer composite layers largely do not impact the fidelity of the original aesthetic quality of the surfaces underneath.

We also fabricated "Paint Control" TLSC devices with different colors (blue, green, red and white) to mimic the arbitrary back surfaces and extracted their EQE peak values as a function of d and plotted in **Figure 6.7**B. All the colored "Paint Control" TLSCs show very similar EQE_{LSC} decay trends compared to the black "Paint Control" in Figure 6.7A since absorption and scattering losses are effectively equivalent. With the low refractive index film inserted between the

waveguide and the paint, the EQE_{LSC} roll-off is mitigated substantially for both "n = 1.30" and "n = 1.38". For "n = 1.30", the decay is within 80-85% of the "Air control" which indicates that TIR within the waveguide is essentially fully restored. Integration of lower index could further enhance the refractive index contrast between the waveguide and its cladding and thus reduce this loss to regain the last 15-20%.

For polymers, there are several major methods to reduce the refractive index including chemical modifications and creating nano-porosity (airgaps) in the films. 144 Incorporating fluorinated functional groups into the main chains or side chains of the polymer structures can be an effective strategy where fluorine atoms can effectively reduce the dipole moment by localizing the electron density in C-F σ bond and thereby reducing the total molecular polarizability that is tied to the polarizability. 145,146 Utilizing this approach, indices in the range of 1.1-1.3 have been demonstrated. As an alternative to low-index polymer layers, inorganic optical cladding can be deposited as an interlayer. For example, the refractive indices of MgF2, CaF2 and SiO2 dense coating films are $n_{MgF_2} = 1.39$, $n_{CaF_2} = 1.44$ and $n_{SiO_2} = 1.46$, and they are among the materials with the lowest refractive index values. 127,128 Increasing the porosity volume fraction of these materials in nanoscale can further reduce the refractive index to < 1.1 and can be obtained with glancing angle deposition. 127,128,147–152 While porous polymer and inorganic films have shown quite low refraction indices, it is still difficult to synthesize mechanically robust layers with minimal haze for n < 1.3 for practical applications. For example, porous structures typically have limited mechanical stability and can become collapsed with excess pressure. Additionally, nanoporous structures can also create additional light scattering which is as detrimental for light trapping as the underlying surface. 128,144 Nonetheless, further enhancements in the waveguide could be achieved with higher complexity optical designs such as distributed Bragg reflectors with

tunable stop bands matching the luminescent wavelength range of the luminophores but with greater impact on the color coordinates that vary with angle. 153,154

To further approach the scaling of the air TLSC devices, it is possible to replace the current waveguide with higher refractive index material ($n_{waveguide} > 1.5$). The optimum of the product of the reflection and trapping efficiencies $((1-R_f)\cdot\eta_{Trap})$ of simple waveguides for different $n_{cladding}$ (1.0 to 1.4) scenarios as a function of $n_{waveguide}$ is plotted in Figure 6.7A. With the higher $n_{cladding}$ provided, the higher $n_{waveguide}$ is required to obtain the maximum product ~0.77. Polymers are often the most suitable waveguide materials since luminophores can be embedding directly into the waveguide via mixing or coated as a luminophore/matrix film onto a surface. Introduction of aromatic rings, halogen atoms (except for fluorine), and sulfur atoms are the most common ways to adjust the polymer refractive index to ~1.70 with good visible transparency. Polymer materials with refractive index > 1.70 have been developed but are typically much more costly and very few are commercially available. Practically, expanding the polymer refractive indices from 1.30 to 1.70 is wide enough for the purpose of waveguiding enhancement. 155-161 For example, if the refractive index of the waveguide is $n_{waveguide} = 1.70$ with a low refractive index film cladding of n = 1.30 coated on the backside then η_{Trap} can reach 64.5%, which is very close to the "Air Control" scenario of 74.5%.

It is worth mentioning that the strategy of adjusting the refractive index of different layers in TLSC can also be applied to 1) colorful LSC system when the LSC devices are integrated onto the areas where the aesthetic quality are not a concern and which give more freedom in the luminophore selection; 2) insertion between multi-junction LSCs as an interlayer to separate and protect the luminescent flux from each subpanel being reabsorbed by the lower bandgap luminophore; 3) integration onto the transparent surfaces where the glass does not have sufficient

transparency in the infrared spectrum; 4) incorporation of the low refractive index layer along with other flexible components (waveguide, luminophore layer and PV), resulting in a mechanically flexible LSC or TLSC devices that can be more readily integrated onto curved surfaces. Finally, it should be noted that while the goal of this work is to demonstrate the optical design which enables LSC application in these aforementioned areas, improvements in the η_{LSC} baseline by increasing the cyanine quantum yield as well as reabsorption loss will be discussed in Chapter 7.^{78,162}

6.5 Summary

In conclusion, we have shown that integrating TLSCs onto to highly absorptive and colorful painted surfaces results in nearly 80% drop in performance. To overcome this deployment limitation we have designed NIR harvesting visibly transparent LSC device that can be seamlessly integrated onto arbitrary surfaces. This is achieved by deploying a thin, low refractive index layer between the backside solid surface and the TLSC waveguide. Photovoltaic characteristic shows that the power lost to scattering or absorption of painted surfaces is notably restored with the aid of this low refractive index layer. The waveguide sheet coated with such low refractive index film show AVTs > 90% and CRIs > 99 so that these low refractive index films add very little visual impact to the overall aesthetic quality of the TLSC system. Moreover, the scalability is expected to be significantly improved while still retaining much of their photovoltaic performance. This work provides a simple and cost-effective optical design to make TLSCs deployable on any surface without visual impact on the surface underneath, further accelerating the potential for these clean, low-cost solar technologies.

Chapter 7 Impact of Stokes Shift on the Performance of Near-Infrared Harvesting Transparent Luminescent Solar Concentrators

In LSC/TLSC development, reabsorption loss currently limits the device performance and scalability. This loss is typically defined by the Stokes shift between the absorption and emission spectra of luminophores. In this chapter, the Stokes shifts (*S*) of near-infrared selective-harvesting cyanines are altered by substitution of the central methine carbon with dialkylamines. Varying *S* with values over 80 nm and ideal infrared-visible absorption cutoffs are successfully demonstrated. The photovoltaic performance of the corresponding TLSC device is measured and reported. However, experiments and simulations show that it is not simply the Stokes shift that is critical, but the total degree of overlap that depends on the shape of the absorption tails. We show with a series of *S*-modulated cyanine dyes that the *S* is not necessarily correlated to improvements in performance or scalability. Accordingly, a new parameter, the overlap integral (*OI*), is defined to sensitively correlate reabsorption losses in any LSC/TLSC system. In deriving this parameter, new approaches to improve the scalability and performance are discussed to fully optimize TLSC designs to enhance commercialization efforts.

7.1 Introduction

Recently, several approaches towards mitigating the reabsorption effect by increasing the Stokes shift with various species of luminophores have been reported for quantum dots, 7,24,86,88,92,94,95,126,163–166 rare-earth ions, 48,49,89,96–99,167 nanoclusters, 7,44,168,169 and organic molecules. 68,69,73,77,80,81 For example, inorganic semiconductor nanocrystals exhibit high photoluminescence efficiencies with absorption and emission spectra that are tunable by particle size and composition. Several strategies have been developed to increase the Stokes shift,

including most notably the formation of core/shell "giant" quantum dots (QDs) as quasi-type I or type II hetero-structures for CdSe/CdS, 85,95 PbS/CdS⁹⁴ or I-II-VI₂ ternary CdSe/Cd_xPb_{1-x}S, 88 CuInS₂/CdS, 166 CuInS₂/ZnS QDs. 92 The nanocrystal shell typically has a larger energy bandgap, acting as a photon absorbing antenna and protective carrier barrier when energy is transferred to the lower bandgap core crystal photon emitter. The energy gap difference between the core and the shell crystals results in an increase in downshift up to 150-200 nm. 88,94 Doping QDs with transition metal ions is another approach to tackle the reabsorption problem, for example, utilizing Mn-doped ZnSe, 94 Cu-doped CdSe QDs or nanoplatelets. 164 The doping impurity introduces new localized excited energy states (mid-gaps) within the original QD energy bandgap, which generates a downshifted radiative recombination pathway with respect to the absorption.

However, a key limitation of these QDs is the continuous band-like absorption profiles that hinder selective absorption of invisible infrared photons without an accompanying absorption in the visible that compromise their visible transparency and aesthetic quality. In contrast, organic molecules are a class of luminophore candidates for LSC and TLSC applications that exhibit excitonic properties and separated molecular orbitals stemming from their π -conjugated molecular structure. While the Stokes shifts of traditional and commercially available organic dyes utilized in LSCs are generally small (< 20-30nm),^{68,77,80,81} recent efforts have looked to circumvent the reabsorption loss by using an excitation energy transfer (energy migration) strategy with multiple dyes via Förster resonance energy transfer (FRET).^{22,125,170–172} Such an approach separates the absorption of the donor from the emission of the acceptor so that the reabsorption in the LSCs is reduced but the close physical coupling of the dyes along with the need for multiple dyes with high QYs creates additional challenges. Another method has also been explored via resonance shifting

in optical cavity designs for the waveguides, 173 but it requires the utilization of neat thin-film layers of luminophores which are often less suitable for achieving the highest luminescent QYs.

For many TLSC applications, high aesthetic quality and transparency are the most critical metrics.³ Thus, harvesting the invisible portion of the solar spectrum (ultraviolet (UV) and nearinfrared (NIR)) is most beneficial for such applications. TLSC with NIR selective harvesting cyanine dyes has been demonstrated in previous work but the Stokes shifts were all < 30 nm, thus limiting the larger area optimization.⁹ In this work, we develop large Stokes shift TLSCs by modifying the central methine coordination of NIR selective cyanine dyes, resulting in Stokes shifts over 80 nm with simultaneously improved QY and maintaining selective NIR harvesting. These changes in SS are explained by ab initio calculations which show that the distortion about the central amino group in the excited states decreases the energy of the lowest unoccupied molecular orbitals (LUMO) energy. The corresponding TLSC devices exhibit a 30% η_{LSC} improvement for a 25.8 cm² device that was found to stem, surprisingly, not from the changes in SS but from changes in the absorption width and improved quantum yield. These trends are quantitatively confirmed by distance dependence quantum efficiency measurements and optical modeling. Thus, we introduce a new parameter to replace the Stokes shift, the overlap integral, to more accurately correlate the true reabsorption loss, act as a fast-screening parameter, and prevent misleading expectations in performance.⁷⁸

7.2 Experimental Section

Module Fabrication, Optical and Photovoltaic Characterization: 100 mgL⁻¹ Cy7-CA (150 mgL⁻¹ Cy7-NEt₂-I or 150 mgL⁻¹ Cy7.5-NEt₂-I) ethanol solution was mixed with mounting medium

(Fluoroshield F6182, Sigma-Aldrich) at a volume ratio of 1:2. The module fabrication process, optical and photovoltaic characterization are similar to the description in Section 6.2.1 to 6.2.3 in Chapter 6 by following the standard protocols introduced in Chapter 3 and Chapter 4.

Optical Modeling: The reabsorption and forward emission losses were estimated with luminophore (Cy7-CA) absorption, emission spectra, distance d and TLSC plate length L. The TLSC system optical efficiencies, in considering reabsorption losses from the overlap in the absolute absorption and normalized emission spectra were numerically evaluated in Matlab as a function of distance d, plate length L, plate thickness t_0 and dye/polymer film thickness t. Equation 2.4 is the complete equation used in these simulations.

Electronic Structure Calculations: The geometries of Cy7-CA, Cy7-NEt₂-I, and Cy7.5-NEt₂-I were optimized in their ground and first excited electronic states to elucidate the relaxation motions responsible for the enhanced Stokes shifts of Cy7-NEt₂-I and Cy7.5-NEt₂-I. The charged side chain on the Cy7-CA and two ethyl groups on the two nitrogen atoms terminating the polymethine backbone of Cy7.5-NEt₂-I were replaced by methyl groups to reduce the cost of calculations. This is expected to have little effect on the Stokes shifts because the HOMO and LUMO do not extend to these side chains. Calculations were performed at the linear response time-dependent density functional level of theory using the TeraChem software package. 174–177 The CAM-B3LYP functional level of theory using the TeraChem software package. TDDFT is known to give an accurate description of the shape of the excited state potential energy surface (e.g., S). 179 These calculations were enabled by the Extreme Science and Engineering Discovery Environment (XSEDE). Torsion angles are defined as the mean of the two C1-C2-N-C3 dihedral angles where C2 is the central carbon atom of the polymethine chain and N is the nitrogen of the amino group.

7.3 Results

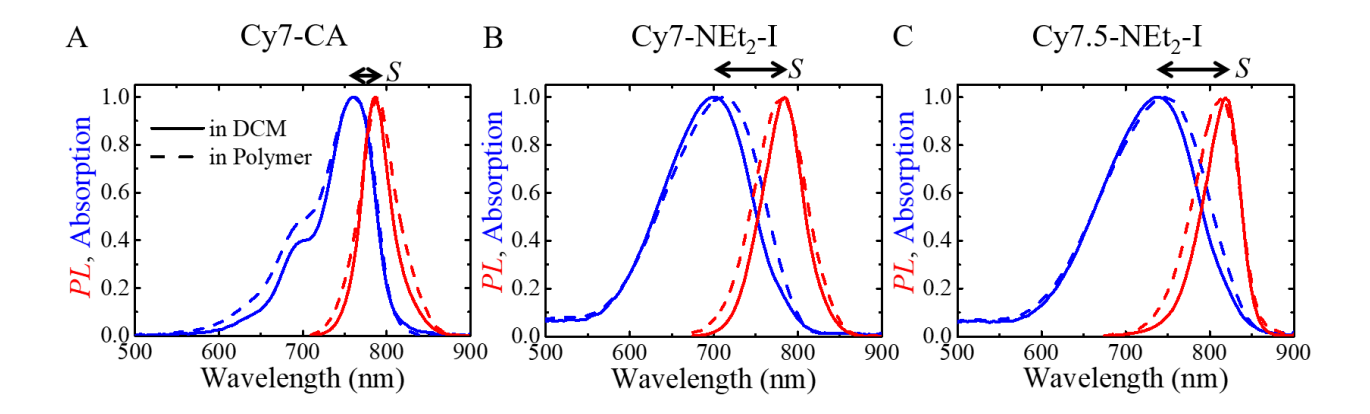


Figure 7.1 Normalized absorption and emission spectra of cyanine dyes.Normalized absorption (blue) and emission spectra (red) of Cy7-CA (A), Cy7-NEt2-I (B) and Cy7.5-NEt2-I (C) in DCM solutions (solid lines) and polymer films (dashed lines). Permission to utilize the Spartan helmet logo is kindly provided by the MSU.

We focus on two key parent cyanine salts that are derivatized to modify the Stokes shift:

2-((E)-2-((E)-2-chloro-3-(2-((E)-1,3,3-trimethylindolin-2-ylidene)ethylidene)cyclohex-1-enyl)vinyl)-1,3,3-trimethyl-3*H*-indol-1-ium iodide and 2-((E)-2-((E)-2-(E)-2-(1,1,3-(E)-2)))trimethyl-1,3-dihydro-2*H*-benzo[e]indol-2-ylidene)ethylidene)cyclohex-1-en-1-yl)vinyl)-1,1,3trimethyl-1*H*-benzo[e]indol-3-ium iodide. These parent compounds are converted via the addition/elimination reaction of the Cl on the central methine backbone to 2-((E)-2-(E)-(diethylamino)-3-(2-((E)-1,3,3-trimethylindolin-2-ylidene)ethylidene)cyclohex-1-en-1-yl)vinyl)-1,3,3-trimethyl-3H-indol-1-ium iodide (Cy7-NEt₂-I) and 2-((E)-2-(diethylamino)-3-((E)-2-(3-ethyl-1,1-dimethyl-1,3-dihydro-2*H*-benzo[*e*]indol-2-ylidene)ethylidene)cyclohex-1-en-1yl)vinyl)-3-ethyl-1,1-dimethyl-1*H*-benzo[*e*]indol-3-ium iodide (Cy7.5-NEt₂-I). In addition, 1-(5carboxypentyl)-3,3-dimethyl-2-((E)-2-((E)-3((E)-2-(1,3,3-trimethylindolin-2ylidene)ethylidene)cyclohex-1-enyl)vinyl)-3*H*-indolium chloride (Cy7-CA)introduced previously is also included for comparison. We have tested a large number of different substituents, substituted at C4 with SS ranging from <20 nm to >180 nm. ^{162,181} The result of those studies will

be described in more detail elsewhere; herein, we focus on these two particular derivatives for device integration as they provided the highest SS and QY with selective absorption in NIR range of the solar spectrum. The absorption and emission spectra in both dichloromethane (DCM) solution and in a polymer matrix of Cy7-CA, Cy7-NEt2-I and Cy7.5-NEt2-I are plotted in **Figure 7.1**A to C.

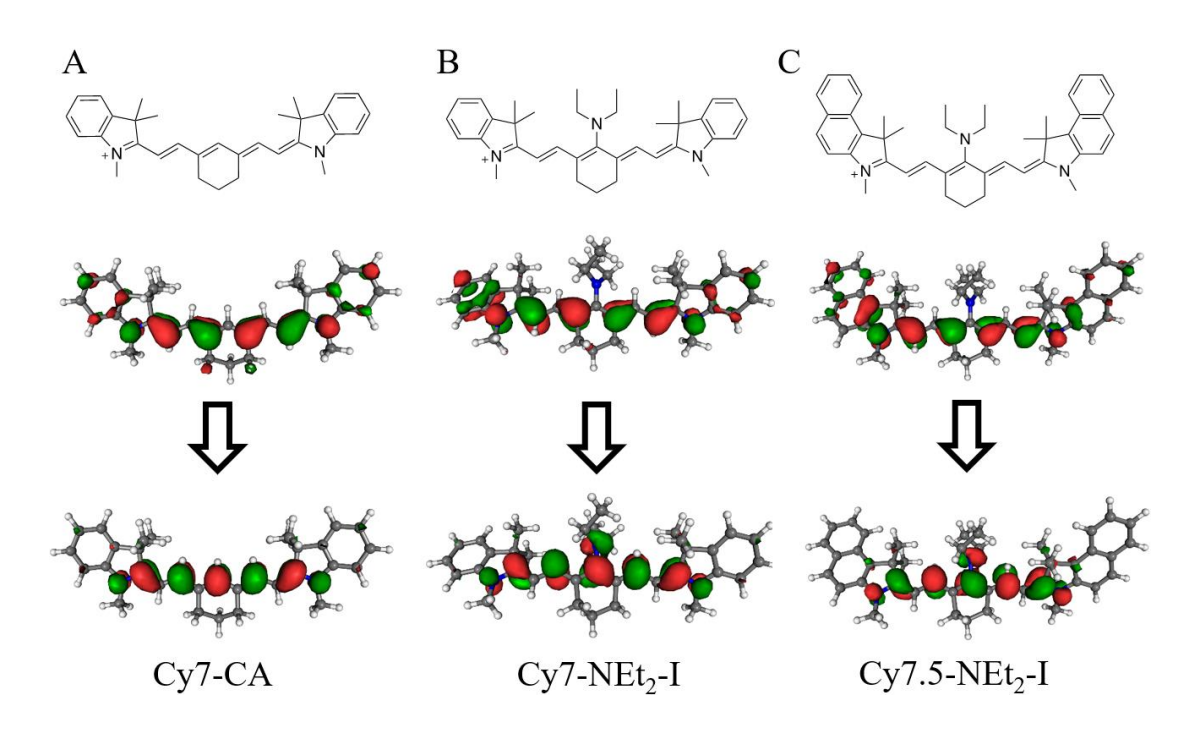


Figure 7.2 Molecular structure, HOMO and LUMO electronic orbitals. (A) Cy7-CA. (B) Cy7-NEt2-I (C) Cy7.5-NEt2-I.

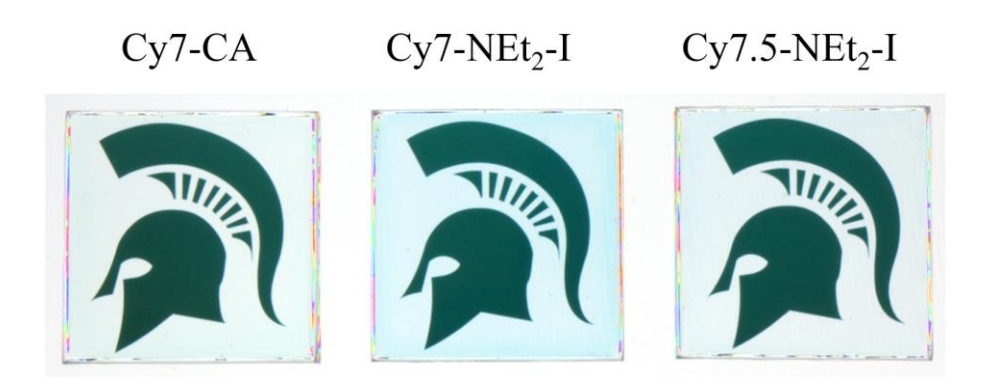


Figure 7.3 Photographs of the TLSCs.

TLSC photographs taken in front of the MSU Spartan helmet incorporating Cy7-CA, Cy7-NEt₂-I and Cy7.5-NEt₂-I luminophores (illuminated from behind the TLSC).

The truncated molecular structures of all three cyanine dyes are shown in **Figure 7.2**A to C. Cy7-CA acts as the control luminophore with a small Stoke shift of 27 nm in DCM. The Stokes shift of the diethylamino substituted analog, Cy7-NEt₂-I is increased to 84 nm with an improved *QY* of 30±2% and absorption peak of 700 nm in DCM. Similarly, the modified Cy7.5-NEt₂-I also shows an increased *S* of 81 nm with red-shifted absorption peak of 738 nm compared to Cy7-NEt₂-I. The *QY*s of these three cyanine dyes are summarized in **Table 7.1**, where the *QY*s of the three cyanine dyes in the polymer film are modestly reduced compared to that in DCM solution.

Table 7.1 Summary of the absorption λ_{max} , emission λ_{max} , Stokes shifts (S) and quantum yields (PLQYs) of Cy7-CA, Cy7-NEt₂-I and Cy7.5-NEt₂-I in DCM and polymer films.

Cyanines	Matrices	Absorption λ_{max} (nm)	Emission λ_{max} (nm)	S (nm)	<i>QY</i> (%)
Cy7-CA	Solution	760 (1.631 eV)	787 (1.575 eV)	27	24±1
	Polymer	762 (1.627 eV)	788 (1.573 eV)	26	19±1
Cy7-NEt ₂ -I	Solution	700 (1.771 eV)	784 (1.581 eV)	84	30±2
	Polymer	710 (1.746 eV)	780 (1.590 eV)	70	26±1
Cy7.5-NEt ₂ -I	Solution	738 (1.680 eV)	819 (1.514 eV)	81	23±1
	Polymer	746 (1.662 eV)	816 (1.519 eV)	70	15±1

Density functional theory-based calculations shown in Figure 7.2A to C are utilized to understand the mechanism of the Stokes shift variation. The NEt₂ substitution leads to additional relaxation in the central amino groups of Cy7-NEt₂-I and Cy7.5-NEt₂-I, which is presumably responsible for the increased Stokes shift. We note that the spectral shifts moving from the solvent to the polymer matrix are quite small (only several nm) and are expected due to the combination of solvochromatic shifts and changes in steric hindrance. When the cyanine dyes are introduced into the polymers, the more polarized environment stabilized the excited state, leading to a bathochromic shift of the absorption. However, after the dye are mounted into the polymers, the

free rotation of the dyes is highly limited, creating a vibration energy change at the ground state, thus leading to a hypsochromic shift of the photoluminescence.

The TLSC devices are formed on borosilicate glass plates with an active area of 25.8 cm². Cyanine molecules are dissolved in ethanol solutions, mixed with a polymer host, and then dropcast onto glass sheets to form luminophore/polymer composite films. The polymer mounting medium acts to separate the dye molecules and prevent aggregation-induced quenching that reduces the QY. If the solvent or polymer mounting medium (or the combination of both) are poorly chosen, large clusters of the dye molecules will form which leads to visible nonuniformities. Moreover, if the solvent and polymer poorly paired, the mounting medium can separate from the solvent, resulting in wavy films with visible ripples that detrimentally affect the device aesthetic quality. Laser-cut Si photovoltaic cells are mounted around the two orthogonal edges and connected in parallel. The photovoltaic performance of the TLSCs based on the three cyanine dyes is shown in **Figure 7.4**. The measured J_{SC} of the device with Cy7-NEt₂-I is 1.18 mAcm⁻², with a Voc of 0.51 V and a FF of 60% leading to an efficiency of 0.36%. The J-V characteristic of TLSC with Cy7-CA shows a J_{SC} of 0.93 mAcm⁻², with a V_{OC} of 0.49 V and FF of 61%, resulting in a η_{LSC} of 0.28%, which is lower than previously reported Cy7 devices due to the six-times larger device area. The second cyanine luminophore derivative Cy7.5-NEt₂-I has similar V_{OC} of 0.48 V and FF of 57% with lower J_{SC} of 1.02 mAcm⁻², and an overall efficiency of 0.28% which is similar to the Cy7-CA control TLSC device.

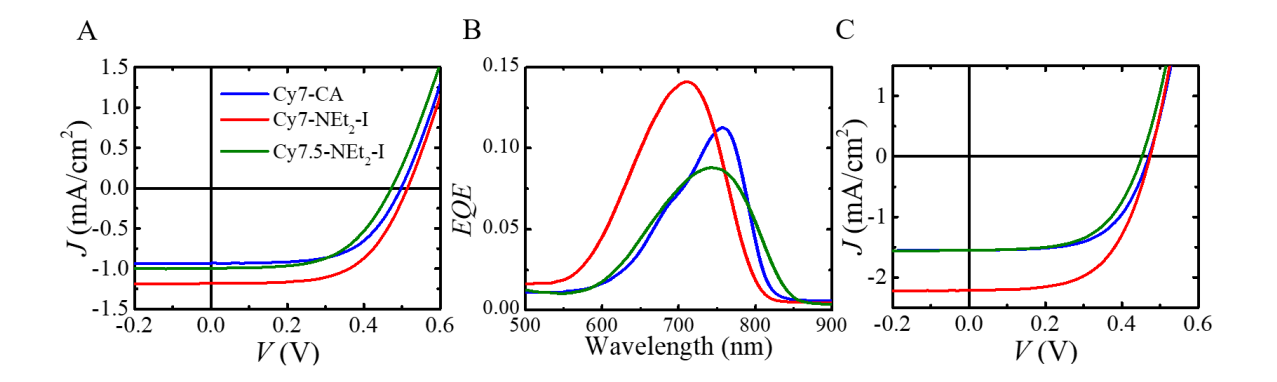


Figure 7.4 Photovoltaic performance of the TLSCs.

(A) Current density as a function of voltage (J-V curves) for the fully assembled TLSC systems with three of the cyanine dyes based on waveguide dimension of 5.08 cm \times 5.08 cm. (B) Representative external quantum efficiency (EQE) of three cyanine dye TLSC systems as a function of wavelength (measured at distance d = 5mm). (C) J-V curves for the fully assembled TLSC systems with three of the cyanine dyes based on waveguide dimension 2.54 cm \times 2.54 cm.

Figure 7.4B shows the EQE_{LSC} spectra of the three cyanine luminophores. In general, the absorption spectra of the luminophores determine where the EQE_{LSC} peaks will be. The peak positions of Cy7-CA, Cy7-NEt₂-I and Cy7.5-NEt₂-I match the absorption spectra in Figure 7.1A to C and no direct excitation of the edge-mounted solar cells is observed in the spectra. In the emission wavelength range of these three cyanine dyes (700 to 850 nm) the edge-mounted Si PV show a nearly constant EQE_{PV} ($\approx 90\%$) so that $EQE_{LSC}(\lambda) = \eta_{opt}(\lambda) \cdot EQE_{PV}$, where $EQE_{PV} \cong 0.90$. While Cy7-NEt₂-I with the highest QY in the polymer film leads to the highest EQE peak of 14.1% at 710 nm, the EQE peaks of Cy7-CA and Cy7.5-NEt₂-I are 11.3% and 8.8% at 760 nm and 745 nm, respectively. These are also consistent with the QY trend of the three cyanine dyes. The I_{SC} from integrating the product of the position-dependent and averaged I_{SC} and the AM1.5G solar spectrum is used to confirm the photocurrent density of the whole TLSC device. For TLSCs with 5.08 cm $\times 5.08$ cm active area, five EQE_{LSC} spectra were tested as a function of the distance I_{SC} from the excitation source to edge-mounted PV cell. Based on its wide absorption and high I_{SC} Cy7-NEt₂-I yields a I_{SC} of 1.22 mAcm⁻¹. The wider absorption peak of Cy7.5-NEt₂-I compensates

the slightly lower QY in the polymer film, thus exhibiting a close integrated J_{SC}^{Int} compared with Cy7-CA. All the integrated J_{SC}^{Int} values are within error of the photocurrent densities from J-V measurement.

To check the validity of photon balance from the EQE_{LSC} , $T(\lambda)$, and $R(\lambda)$ spectra measurements of these devices, we show that $EQE_{LSC}(\lambda) + R(\lambda) + T(\lambda) \le 1$ is satisfied at each wavelength. This validity check is plotted in **Figure 7.5** for each device. It is also worth noting that the TLSC devices with these three cyanine dyes have been made with a smaller active area (6.45 cm²) similar to prior work utilizing 1-(6-(2,5-dioxopyrrolidin-1-yloxy)-6-oxohexyl)-3,3-dimethyl-2-((E)-2-((E)-3-((E)-2-(1,3,3trimethylindolin-2-ylidene)ethylidene)cyclohex-1-enyl)vinyl)-3*H*-indolium chloride (Cy7-NHS) that had an active area of 4 cm² as shown in Figure 7.4C. With similar device active area, the smaller TLSC with Cy7-NEt₂-I exhibit significantly improved η_{LSC} of 0.62% (2.21 mAcm¹ of J_{SC} , 0.47 V of V_{OC} and 60% of FF) over previous work, while the TLSCs with the two other cyanine dyes, Cy7-CA and Cy7.5-NEt₂-I, have very similar photovoltaic performance ($\eta_{LSC} \sim 0.4$ %) compared to previous work (**Table 7.2**).

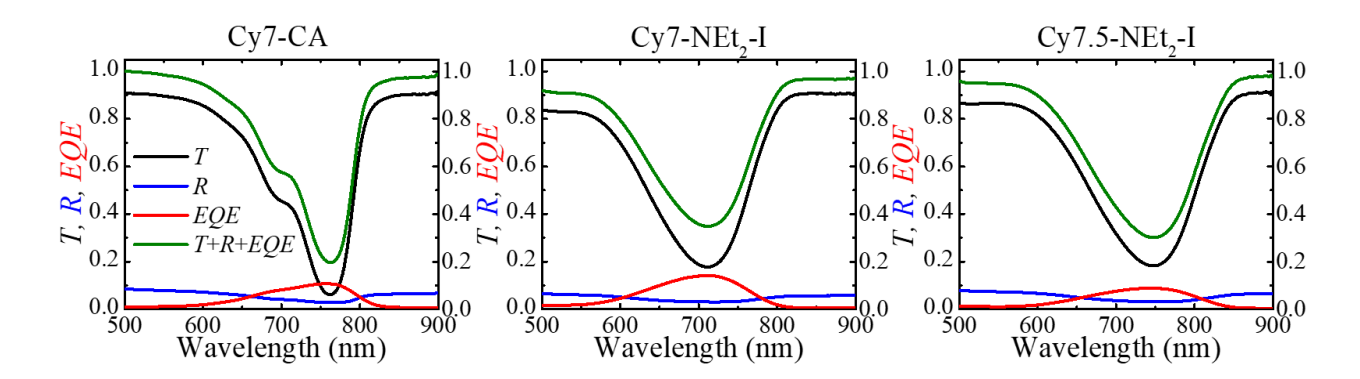


Figure 7.5 Photon balance check.

(A) TLSC with Cy7-CA. (B) TLSC with Cy7-NEt₂-I. (C) TLSC with Cy7.5-NEt₂-I. As one of the most important self-consistency checks in TPV characterization, the sum of transmittance $(T(\lambda))$, reflectance $(R(\lambda))$ and $EQE_{LSC}(\lambda)$ is below 1 at all wavelengths, which confirms the validity of the corresponding independent measurements.

Table 7.2 Summary of photovoltaic parameters and overlap parameters.

TLSCs	Area (cm²)	Jsc (mAcm ⁻²)	J_{SC}^{Int} (mAcm ⁻²)	Voc (V)	FF (%)	η _{LSC} (%)	AVT (%)	CRI	<i>J</i> (μm M -1)	OI
Cy7-NHS	4	1.2±0.1	1.00	0.50±0.01	66±2	0.40±0.03	87.7	91.0	1.49	27.9
Су7-СА	6.45	1.55±0.05	0.96	0.47±0.01	61±1	0.44±0.02	88.1	92.1	1.56	27.2
	25.8	0.93±0.02		0.49±0.01	61±1	0.28±0.02				27.2
Cy7-NEt ₂ -I	6.45	2.2±0.2	1.22	0.47±0.01	60±1	0.62±0.05	77.1	75.6	0.46	25.9
	25.8	1.18±0.01		0.51±0.01	60±1	0.36±0.01				
Cy7.5- NEt ₂ -I	6.45	1.55±0.09	0.02	0.46±0.01	59±1	0.41±0.03	84.7	89.4	0.99	20.0
	25.8	1.02±0.01	0.82	0.48±0.01	57±1	0.28±0.02				30.8

Note: *J*, *S*, *S*', and *OI* of TLSC systems with the different cyanine luminophores and Cy7-NHS (from reference ⁸). We note that only the *OI* accurately correlates to the scaling behavior measured and shown in Figure 7.6D.

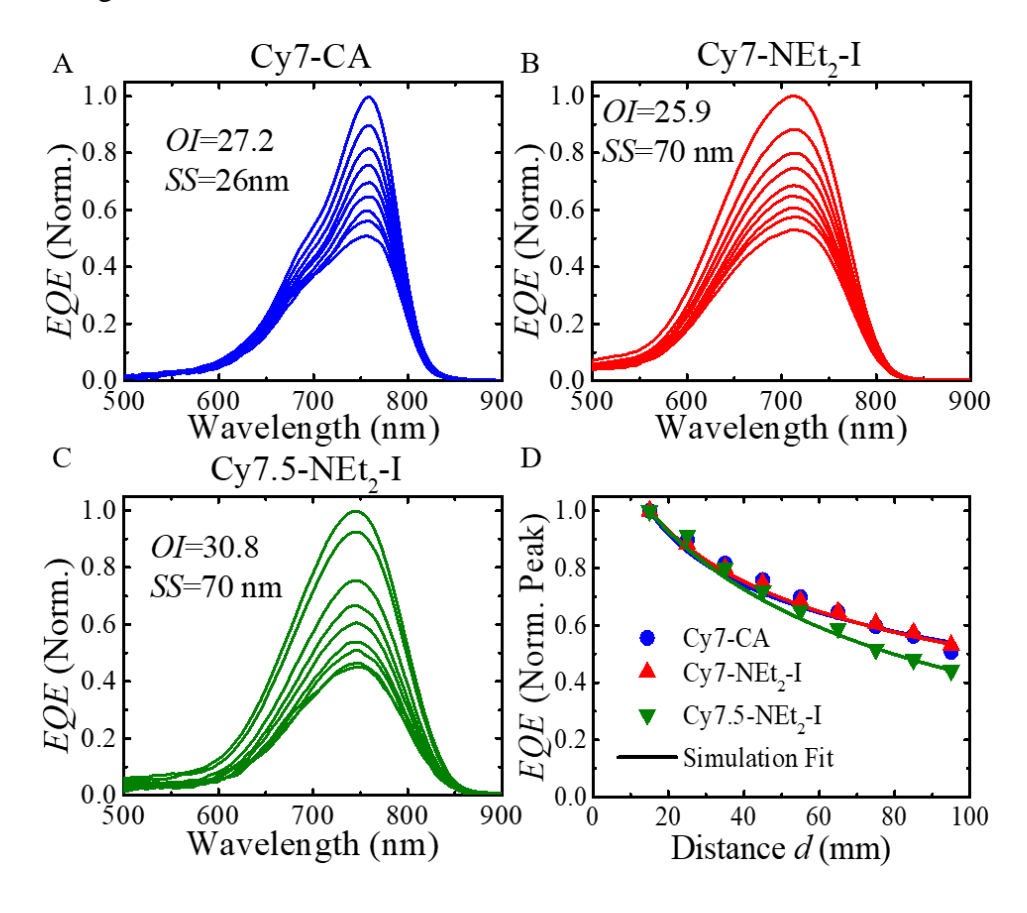


Figure 7.6 Position-dependent *EQE*_{LSC} spectra.

Extracted and normalized EQE_{LSC} peak values of Cy7-CA (A), Cy7-NEt₂-I (B) and Cy7.5-NEt₂-I (C) as a function of wavelength measured from 15 mm to 95 mm, with 10 mm increments. (D) Calculated optical efficiencies (solid lines) as a function of distance (d) of three cyanine luminophore TLSC systems to fit the measured normalized EQE_{LSC} peak values (symbols).

To explore the impact of Stokes shift on the scalability, TLSC systems were characterized by the external quantum efficiency as a function of position. Multiple EQE_{LSC} scans were taken for each TLSC system as d was increased from 15 mm to 95 mm (10 mm interval, and the same Si PV strip was used for all the EQE_{LSC} scans). The normalized EQE_{LSC} spectra of three cyanine dyes were plotted in **Figure 7.6**A-C. The EQE_{LSC} peak values of each individual scan of the three cyanine dyes were extracted and plotted in Figure 7.6D.

7.4 Discussion

The higher degree of conjugation with Cy7.5-NEt₂-I results in a lower bandgap. Therefore, both the absorption and emission spectra of Cy7.5-NEt₂-I are red-shifted compared to Cy7-NEt₂-I, and the shape of both spectra remain nearly identical. That the absorption spectrum of Cy7-NEt₂-I is blue-shifted relative to Cy7-CA can be understood via the Dewar-Knott color rule. Addition of an electron donating species to the central position of the polymethine chain destabilizes the LUMO, which has significant density on the central carbon as shown in Figure 7.2, while leaving the energy of the HOMO, which has little density on that carbon, unaffected. When the amine is oriented such that its lone pair electron is conjugated with the polymethine chain, it acts as such an electron donating group, therefore the excitation energy is increased.

The nuclear relaxation responsible for the enhanced Stokes shift of Cy7-NEt₂-I and Cy7.5-NEt₂-I compared to Cy7-CA was investigated via linear response time-dependent density functional theory calculations. The computed Stokes shifts (0.07, 0.15, and 0.17 eV for truncated models of Cy7-CA, Cy7-NEt₂-I, and Cy7.5-NEt₂-I, respectively) are in good agreement with the experimental values (0.06, 0.19, and 0.17 eV in solution). The polymethine chains of all three

molecules relax similarly in the excited state, with individual bond lengths changing by up to 0.02 \mathring{A} . Additional relaxation is observed in the central amino groups of Cy7-NEt₂-I and Cy7.5-NEt₂-I. The bond lengths between the central carbon of the polymethine chain and the amine nitrogen are lengthened by 0.02 \mathring{A} , consistent with excitation into a LUMO that is antibonding with respect to the amine bond as shown Figure 2. The amino group also twists relative to the polymethine chain upon excitation, with the torsion angles increasing from 44° to 55° in Cy7-NEt₂-I and from 44° to 56° in Cy7.5-NEt₂-I. This torsional motion reduces the conjugation of the lone pair on the nitrogen atom of the amino group to the π orbitals of the polymethine chain, thus decreasing the electron donating ability of the group. Collectively, these twisting and stretching motions destabilize the LUMO but leave the energy of the HOMO - which does not have density on the amine bond - relatively unaffected. These changes in orbital energy account for the enhanced Stokes shifts of Cy7-NEt₂-I and Cy7.5-NEt₂-I compared to Cy7-CA.

The main factor that leads to enhanced performance for the TLSC with Cy7-NEt₂-I is the increased J_{SC} (see Table 2 for detail). Several key factors are responsible for these changes: changes in quantum yield, variations in total absorption (absorption width), and reductions in reabsorption loss. Surprisingly, the Cy7-NEt₂-I with a large Stokes shift of 70 nm in the polymer film only shows slightly better reabsorption efficiency compared to Cy7-CA with a small Stoke shift of 26 nm, and Cy7.5-NEt₂-I shows even slightly more rapid EQE_{LSC} peak decay than the other two. To understand this surprising result, we remember that the EQE_{LSC} of TLSC consists of the optical efficiency, η_{Opt} (the number of photons reaching the waveguide/number of photons incident on the waveguide active area) and the EQE_{PV} of the PV at the emission wavelength. A numerical calculation of optical efficiency was performed by accounting for multiple reabsorption and emission events. Excellent agreement of the experimental EQE_{LSC} and the simulated optical

efficiency suggests that reabsorption is indeed the main loss mechanism in all of these TLSC systems and that despite the large increase in the S, the scalability is not significantly improved. Considering the other factors contributing to the photocurrent, it is primarily the increased absorption width and quantum yield that leads to the J_{SC} increase.

Both the experimental and modeling result suggests that Stokes shift is not ultimately a useful design parameter to identify how well a luminophore will perform in LSCs over large area. Here we define a new parameter, the overlap integral (*OI*) to quantify the reabsorption properties of a luminophore as:

$$OI = \int_0^\infty A(\lambda) \cdot PL^*(\lambda) d\lambda \tag{7.1}$$

As introduced in Chapter 3 and Chapter 4, $A(\lambda)$ is the absolute absorption spectrum (calculated by $A(\lambda) = 1 - R(\lambda) - T(\lambda)$) of a luminophore/host composite film, and $PL^*(\lambda)$ is the normalized emission spectrum of the luminophore in the host material. The OI then depends on the concentration of the luminophore layer and the degree of overlap between the absorption and emission spectra in the host material (rather than in solution). The calculated OI for the investigated luminophores is summarized in Table 7.2. Despite the large S between Cy7-CA and Cy7-NEt₂-I and between Cy7-CA and Cy7.5-NEt₂-I, there is only a small difference in the OI. This is because the absorption tail is broadened with the increase in the SS. Peak broadening is often observed with red-shifted chromophores, resulting from increased vibrational states and/or larger conformational flexibility and more potential isomeric states. Furthermore, a potential charge transfer process can also lead to spectral broadening, if a strong dipole is induced upon excitation. The similarity of the OI elucidates the similar optical efficiency (or EQE_{LSC} decay curves) in Figure 7.6D and show the correct correlation: increasing the OI leads to improved scalability in the EQE_{LSC} while the

measured SS shows an incorrect trend. Thus, the OI more sensitively captures and reflects the distance dependence of luminophores with differing Stokes shifts. The way the OI is defined in Equation 7.1 is not only useful for organic dyes but to all luminophores (including inorganic quantum dots) and all luminophore optical densities. For screening purposes the OI can be evaluated for fixed absolute peak (or specified wavelength) absorption values (e.g., A = 80%). It is thus a useful design parameter for quickly tracking, predicting, and understanding relative performance changes in a range of LSC systems.

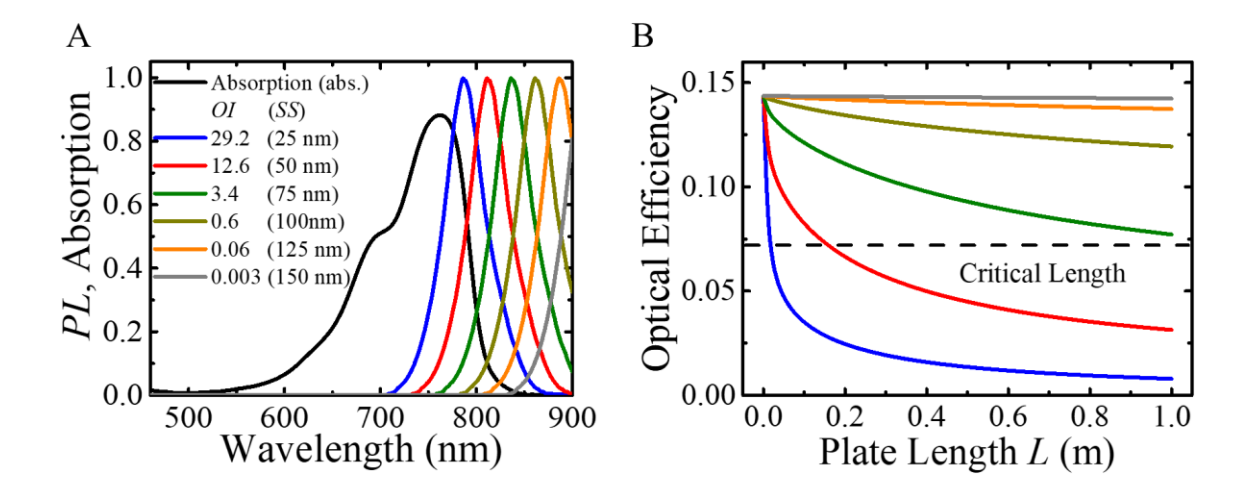


Figure 7.7 Overlap integral and scalability prediction.

(A) Different overlap integral (OI) values obtained by keeping the absolute absorption fixed and shifting the normalized emission spectrum of a luminophore (Cy7-CA). We note that the OI and S are not typically equivalent because chemical changes that lead to changes in the SS also lead to spectral changes in the tail absorption. The S values for the simulation are provided to emphasize the reason that this parameter has been misleadingly considered as a design parameter. (B) Optical efficiencies as a function of plate length L for different OI values.

It is natural to consider the FRET overlap integral (J) as a parameter to correlate the EQE scalability as it is material specific. The well-known expression for J is:

$$J = \frac{\int PL_D(\lambda)\epsilon_A(\lambda)\lambda^4 d\lambda}{\int PL_D(\lambda) d\lambda}$$
 (7.2)

where $PL_D(\lambda)$ is the emission spectrum of the donor dye, and $\epsilon_A(\lambda)$ is the molar absorptivity coefficient of the acceptor dye. Conceptually, however, J depends on both the shape and the magnitude of molar absorptivity coefficient (ϵ_A) and therefore can predict the wrong scaling. For example, if the magnitude of ϵ_A is lower for the same spectral shape, one would simply load more luminophore to maintain the same optical density (absolute absorption) leading to the same OI but lower J. Indeed, we find that J does not correlate with the scaling of the EQE with plate length. The measured trends, from lowest to highest scaling are: Cy7.5-NEt₂-I, Cy7-CA, Cy7-NEt₂-I; J predicts Cy7-CA, Cy7.5-NEt₂-I, Cy7-NEt₂-I while the OI correctly captures the trend Cy7.5-NEt₂-I, Cy7-CA, Cy7-NEt₂-I.

Given that the absorption coefficient in the NIR range for the host polymer material and targeted glass is in the range from 10^{-2} to 10^{-4} cm⁻¹ (e.g., poly(methyl methacrylate)s and certain glasses) most reabsorption losses stem from the luminophore. To qualitatively connect the trends in the OI with the EQE_{LSC} roll-off behavior, we performed an additional simulation where the absolute absorption spectrum of a sample LSC was kept fixed and the normalized emission was manually shifted to create different overlap in the modeling as shown in **Figure 7.7A**. We emphasize that while such a manual shifting of the emission corresponds to increases in the Stokes shift and creates different OI values, such an increase in the Stokes shift in practice does not necessarily lead to changes in the OI due to variations in the peak bandwidth. The calculated optical efficiency in Figure 7.7B shows the impact of overlap integral on the TLSC scalability: if the OI can be decreased from 30 to 3 (i.e., an order of magnitude), the critical TLSC plate length (L) defined as the distance at which the optical efficiency decays to half of its original value can be increased from 2 cm to > 1 m, which would be sufficient for many large-scale and window-based applications. We also note that there is a trade-off between absorption efficiency and the OI

on the total power conversion efficiency that also depends on the thickness (which dictates the optical density of the luminophore). In the case of the TLSCs, the impact on the AVT and CRI should also be considered, emphasizing that broad absorption in the invisible solar spectrum with sharp absorption cutoffs around the visible and near the bandgap are also key. Thus, strategies for sharpening the densities of states around the bandgap should be explored moving forward. The most feasible approach to minimize OI is to modify the NIR-selective harvesting luminophore so that both the absorption edges have sharp cutoffs, keeping the emission narrow as well. Adding more fused rings to lock the geometry of the cyanine dyes could potentially restrict the distribution of conformers at the ground state, and thus achieve sharper transition bandwidths. Furthermore, the restricted geometry (molecular rigidity) could lead to increased quantum efficiency and luminophore lifetime by reducing non-radiative decay pathways. The lifetime of cyanine dyes is another interesting and key area. The fabricated TLSC devices show no degradation during > 2 hours in exposure to air. Interestingly, we have shown that the stability of such compounds integrated as active layers in photovoltaic devices (a more demanding application than LSCs) are more a function of the coordinating counterion than the photoactive counterion itself. We have shown that such anion modifications can lead to photovoltaic lifetime anywhere as short as few days to > 7 years for the same photoactive cation. 185 Thus, future efforts in characterizing the lifetime of these compounds in TLSC application will need to focus on both chemical modifications as well as ion pairing.

It is also important to consider the impact of increasing the OI by simply increasing the Stokes shift. The ideal Stokes shift should not only be engineered to minimize the OI but also carefully adjusted to allow all the emission of the luminophores to coincide with the high EQE_{PV} wavelength range of the edge-mounted PV cells. If the S is too large, a portion of the emission will

have a wavelength longer than the absorption cutoff of the edge-mounted PVs and thus cannot be harvested. For example, with edge mounted Si PVs the maximum Stokes shift should be limited to < 200 nm with the selective harvesting of a 200-300 nm slice of the NIR spectrum for optimal performance. For GaAs PVs with wider band gap the maximum Stokes shift is even more restricted.

7.5 Summary

In conclusion, we have synthesized novel NIR selective harvesting cyanine dyes with selective NIR harvesting, large Stokes shift > 80 nm, and improved quantum yield of > 30%. Luminescent solar concentrators based on these cyanine dyes exhibit power conversion efficiency of up to 0.6% combined with high visible transparency > 80%. Based on the analysis of both experiment and simulation results, we show that the Stokes shift is not a suitable design parameter to quantify the reabsorption loss moving forward. Instead, we define a new parameter, the spectral "overlap integral", derived in way to accurately capture the properties of the overlap between absorption and emission of a luminophore in future LSC design and optimization. Simulations also indicates that with one order of magnitude decrease of the overlap integral the LSC plate size can be increased to ~1m, which is sufficient for most structural glazing systems. Thus, this work provides a guide to improve the efficiency and scalability of NIR-selective harvesting TLSC systems (and all LSCs) that can help fulfil the promise of low-cost transparent photovoltaics.

Chapter 8 Near-Infrared Harvesting Transparent Luminescent Solar Concentrators based on Non-Fullerene Acceptors

Recently, CO_i8DFIC (also referred to as O6T-4F) has been developed as a non-fullerene acceptor (NFA) in organic photovoltaics with unprecedented performance. In this chapter, we introduce NFAs into TLSCs as the luminophores. The impact of CO_i8DFIC concentration on photovoltaic performance, aesthetic quality, and scalability is systematically studied. After device optimization, the CO_i8DFIC TLSCs are shown to achieve a η_{LSC} over 1.2% while the AVT exceeds 74% and CRI exceeds 80. This chapter reports the highest TLSC device efficiency at the highest visibly transparency and highlights that the photoluminescent properties of these emerging low bandgap organic molecules providing an encouraging path to higher TLSC performance.

8.1 Introduction

Most of current LSC/TLSC reports focus on 1) the improvement of *PLQY*, ^{78,126,164} 2) the modulation of the absorption and emission spectra to minimize the reabsorption loss, ^{86,89,92,189} and 3) the enhancement of light absorption by matching the absorption spectrum of the luminophores with the peak of the incident solar spectrum. ^{125,170,171,190} However, the continuous-band absorption characteristics of these luminophores limit their absorption cutoff to ~435 nm, if a high aesthetic quality and transparency is targeted. As addressed in Chapter 5, bandgaps beyond 435 nm can result in rapid drops in *AVT* and *CRI*. ^{5,191} Utilizing wavelength selective absorbers makes it possible to harvest just the UV or NIR. As selective absorption redshifts beyond 675 nm, the *CRI* and *AVT* reach a maximum. ^{78,191} Therefore, NIR photons between 675 nm and the absorption cutoff of the edge-mounted PV cell can be utilized for power generation, and this range coincides

with the peak of the incident AM 1.5G photon flux. Moreover, even with tail absorption in the red-NIR below 675 nm, the resulting blue/green tint is often more visually acceptable than yellow/red tinting, which offers more design freedom for NIR selective-harvesting luminophores. 12,124,188,191

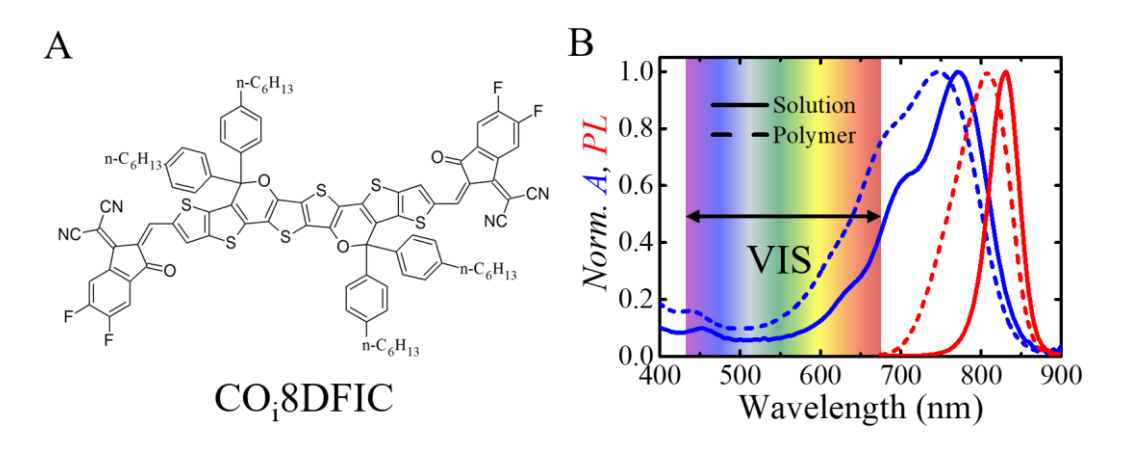


Figure 8.1 Non-fullerene acceptor utilized in this study.

(A) Molecular structure of CO_i8DFIC. (B) Normalized absorption (blue) and emission spectra (red) of CO_i8DFIC in chlorobenzene solution (solid lines) and polymer matrix (dashed lines).

In general, organic dyes can then be designed to selectively harvest NIR photons, which is not typically possible with traditional semiconductors. 44,78,143,162,188 However, organic luminophores often suffer from large self-absorption (large overlap between absorption and PL), narrow absorption peaks, and relatively low QY in NIR. 78,143,162,188 Recently, CO_i8DFIC (also referred to as O6T-4F, the molecular structure is shown **Figure 8.1**A) has been developed as a NFA in organic photovoltaics with unprecedented performance. In this chapter, we introduce NFAs (including CO_i8DFIC) as the luminescent emitters in NIR-selective harvesting TLSCs, where we more than double the η_{LSC} to 1.24%, which is the best NIR-selective harvesting TLSC to date and the highest η_{LSC} reported above 70% AVT. 186,187 Due to the high visible transparency from wavelength selective-harvesting, the LUE is also comparable to the highest LUE of quantum-dot-based LSCs. With this materials motif, efficiencies approaching 5% with a similar level of

AVT are possible solely by increasing QY from \sim 25% to closer to 100% and efficiencies above 10% are possible by additionally increasing the solar harvesting around the visible spectrum. ¹⁸⁸

8.2 Experimental Section

CO_i8DFIC powder was massed and dissolved in dichloromethane (5 min of sonication) to prepare the solution at the target concentration. For "150 mgL⁻¹" TLSC, 150 mgL⁻¹ dichloromethane solution was uniformly mixed with (poly)-butyl methacrylate-co-methyl methacrylate (PBMMA) (Sigma-Aldrich) at a volume ratio of 1:1. The CO_i8DFIC solution concentration is adjusted accordingly for other TLSCs. The module fabrication, optical and photovoltaic characterization are similar to the description in Section 6.2.1 to 6.2.3 in Chapter 6 by following the standard protocols introduced in Chapter 3 and Chapter 4.^{124,143}

8.3 Results

The normalized absorption and emission spectra of CO_i8DFIC dissolved in chlorobenzene solution and embedded in polymer matrix are plotted in Figure 8.1B. From solution to polymer matrix, there is a hypsochromic shift of both the absorption and emission spectra: the absorption peak shifts from 770 to 745 nm and the emission peak shifts from 831 to 808 nm, exhibiting Stokes shift of ~60 nm. The measured QY is $23\pm1\%$ in chlorobenzene solution and $25\pm3\%$ in polymer matrix with an increased absorption width. This is a relatively high QY for NIR emission range, considering most commercially available quantum dots with emission in this range are \leq 50%. In contrast, CO_i8DFIC bandgap decreases in neat films (as applied in organic PVs), so that external quantum efficiencies (EQE_{PV}) of reported PV devices can be extended up to 1050 nm. When spin-

coated as neat layers on glass, the corresponding absorption spectrum does exhibit an absorption onset at ~1000 nm as shown in **Figure 8.2**, but the quantum yield decreases significantly to the point where neat layers are not viable in LSC structures. There are two likely explanations for the shift of the spectra from solution to polymer matrix film – aggregation and solvatochromic shifts. Aggregation typically leads to a broadening of the absorption such that the bandgap decreases. In 8.2A we have measured the absorption spectra in different polymer hosts (Eukitt vs. Shandon) and find that the absorption/bandgap do not change while the emission does moderately shift. We also make aggregated solutions by mixing THF with water and neat films as shown in Figure S1B. The absorption cutoffs of aggregates and neat film are very close to each other (olive curves) and show a huge bathochromic shift (~100 nm) compared to the monomer in solution. In contrast, the absorption cutoffs of solution and polymer film are very close to each other (blue curves). Thus, this is more likely a solvatochromic shift related to the difference in the index of refraction of the polymer host. CO_i8DFIC bandgap decreases in neat films and aggregates compared to solution and polymer matrix, and the corresponding absorption onset also redshifts. We thus investigate the potential of this compound in doped LSC structures.

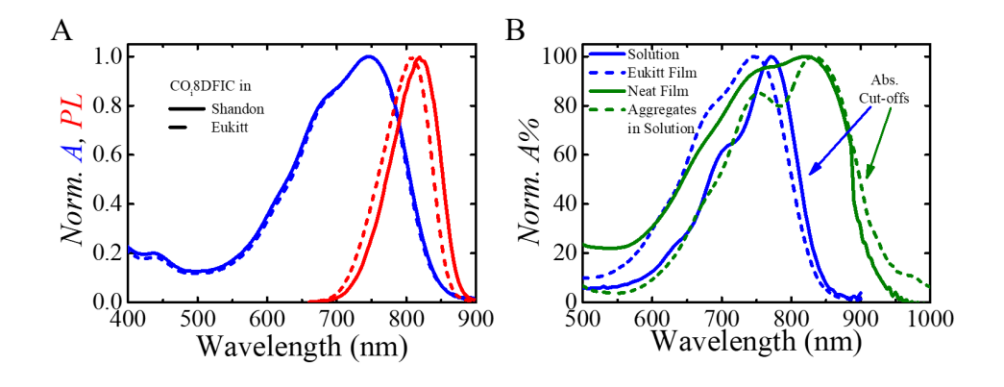


Figure 8.2 Optical Properties of the NFA utilized in this study.

(A) Normalized absorption (blue) and emission (red) spectra of CO_i8DFIC embedded in two different polymer matrices: Shandon (solid lines) and Eukitt (dashed lines). (B) Normalized absorption comparison of CO_i8DFIC in solution, polymer matrix film, neat film, and particle aggregates.

TLSC devices were formed on square-shaped borosilicate glass sheets with an active area of 25.8 cm² (the waveguide length (L) is 5.08 cm). CO_i8DFIC molecules were dissolved in dichloromethane, and uniformly mixed with the polymer host. The mixture was then drop-cast onto glass sheets to form CO_i8DFIC/polymer composite films. The CO_i8DFIC in dichloromethane solution was prepared with various luminophore concentrations to adjust the total light absorption in the NIR. Both Si and GaAs were utilized as edge-mounted PVs. Si was utilized to understand the trends in the performance and GaAs was deployed to reduce thermal losses and demonstrate maximum photovoltaic performance. We note that the utilization of GaAs is only possible as the CO_i8DFIC/polymer PL cutoff is nearly ideally positioned at 875nm with respect to the GaAs EQE_{PV} cutoff of 900nm. Laser-diced Si PV cells (or GaAs PV cells) were mounted onto two orthogonal edges and connected in parallel, while the other two orthogonal edges were painted black. TLSC devices with five different CO_i8DFIC concentrations were fabricated and their photovoltaic performance was characterized. For comparison, TLSC with cyanine dye Cy7-NHS was also added as a reference device. 8,78 The current density versus voltage (J-V) characteristics of these TLSCs are shown in **Figure 8.3**A along with average position-dependent $EQE_{LSC}(\lambda)$ spectra in Figure 8.3B. The photovoltaic parameters and aesthetic quality metrics (AVT and CRI) are summarized in **Table 8.1**. The TLSC with the lowest concentration of 50 mgL⁻¹ shows 30% higher short-circuit current density (J_{SC} : 1.29±0.03 mAcm⁻²) compared to the "Cy7-NHS" control $(1.01\pm0.07 \text{ mAcm}^{-2})$ while exhibiting similar open-circuit voltage (V_{OC}) and fill factor (FF). The corresponding AVT (84.4% vs. 88.2%) and CRI (91.3 vs. 92.0) are very close. As the CO_i8DFIC concentration increases to 150 mgL⁻¹, the J_{SC} further increases to 2.07±0.08 mAcm⁻² with a modestly reduced AVT (74.4%) and CRI (80.0), and the corresponding η_{LSC} reaches 0.54±0.03%.

Further increasing the concentration to 300 mgL⁻¹ only slightly improves the η_{LSC} to 0.61±0.05% with a significant cost in AVT (59.7%) and CRI (63), where there is an increasing blue tint.

Table 8.1 Photovoltaic and aesthetic quality parameters of the TLSCs.

Devices	J _{SC} (mAcm ⁻²)	J ^{Int} _{SC} (mAcm ⁻²)	Voc (V)	FF %	η _{LSC} %	AVT %	LUE	CRI	(a*, b*)
Cy7-NHS	1.01±0.07	1.03	0.42±0.01	57±1	0.24±0.01	88.2	0.21	92.0	(-5.5, -0.8)
50 mgL ⁻¹	1.29±0.03	1.30	0.44±0.01	57±1	0.33±0.01	84.4	0.28	91.3	(-6.01.5)
100 mgL ⁻¹	1.76±0.09	1.71	0.46±0.01	58±1	0.47±0.03	78.0	0.37	84.8	(-10.4, -2.8)
150 mgL ⁻¹	2.07±0.08	1.89	0.47±0.01	56±1	0.54±0.03	74.4	0.41	80.0	(125 27)
150 mgL ⁻¹ *	1.54±0.05	1.78	0.99±0.01	81±1	1.24±0.04	74.4	0.92	80.0	(-13.53.7)
200 mgL ⁻¹	2.13±0.06	1.88	0.47±0.01	57±1	0.57±0.03	67.4	0.38	72.0	(-18.6, -5.3)
300 mgL ⁻¹	2.24±0.04	2.12	0.48 ± 0.01	57±1	0.61±0.05	50.7	0.37	62.0	(242, 67)
300 mgL ⁻¹ *	1.56±0.08	1.77	0.99±0.01	80±1	1.24±0.07	59.7	0.74	63.0	(-24.2, -6.7)

Note: * indicates TLSCs edge-mounted with GaAs PVs.

The J_{SC} values extracted from J-V characteristics are confirmed by the integrated J_{SC} from $EQE_{LSC}(\lambda)$ (in Figure 8.3B). The EQE_{LSC} peak positions matches the absorption spectrum in Figure 8.1B, and interestingly, an amount of the EQE_{LSC} contribution originates from the visible range due to the neutral absorption profile of the CO_i8DFIC through the visible. In EQE_{LSC} measurements, scattering caused by particle aggregation or direct illumination of the edgemounted PV can be directly identified from the shape of EQE_{LSC} spectra: Rayleigh scattering decreases as wavelength increases, which superimposes an inclined background to the luminophore peaks; Direct illumination of the PV introduces a level background to the luminophore peaks that extends to the absorption cutoff of the edge-mounted PV. Both effects can cause inaccurate EQE_{LSC} measurement and overestimated integrated J_{SC} . Neither Rayleigh scattering at short wavelengths, nor direct illumination of the edge-mounted PV cell at the long

wavelengths are observed in the EQE_{LSC} spectra, which confirms that the EQE_{LSC} contribution stems only from the PL of the embedded CO_i8DFIC.

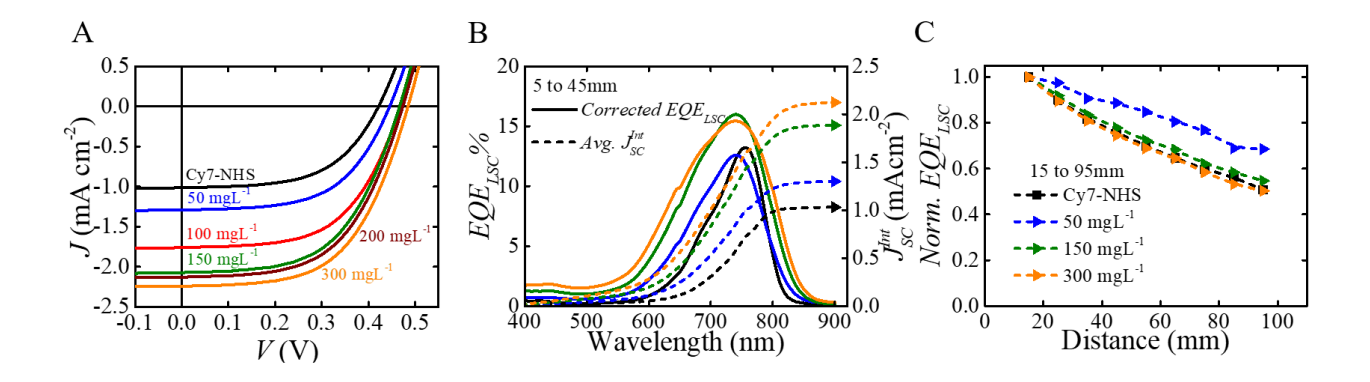


Figure 8.3 Photovoltaic performance of CO_i8DFIC TLSCs.

(A) Current density versus voltage (J-V) characteristics of CO_i8DFIC TLSCs with different concentrations. (The legends 50 to 300 mg L⁻¹ indicate the precursor solution concentration). All scans were measured under AM 1.5G illumination and all TLSCs were edge-mounted with Si PVs. (B) Average $EQE_{LSC}(\lambda)$ spectra of CO_i8DFIC TLSCs with different concentrations. The corresponding integrated J_{SC} match well with the J_{SC} extracted from J-V characteristics shown in (A). (C) The normalized position-dependent EQE_{LSC} peak values of CO_i8DFIC TLSCs with different concentrations. The Cy7-NHS TLSC is also included as reference.

To explore the impact of CO_i8DFIC concentration on device scalability, TLSC systems (dimension: 10.16×10.16 cm) with three different CO_i8DFIC concentrations (50 mgL⁻¹, 150 mgL⁻¹ and 300 mgL⁻¹) and "Cy7-NHS" were characterized by position-dependent EQE_{LSC} as a function of the distance (*d*) from the excitation source to the edge-mounted PV cell. Multiple EQE_{LSC} scans were taken for each TLSC system as *d* increases from 15 mm to 95 mm with 10 mm interval. The corrected EQE_{LSC} peak values are extracted and plotted in Figure 8.3C.

8.4 Discussion

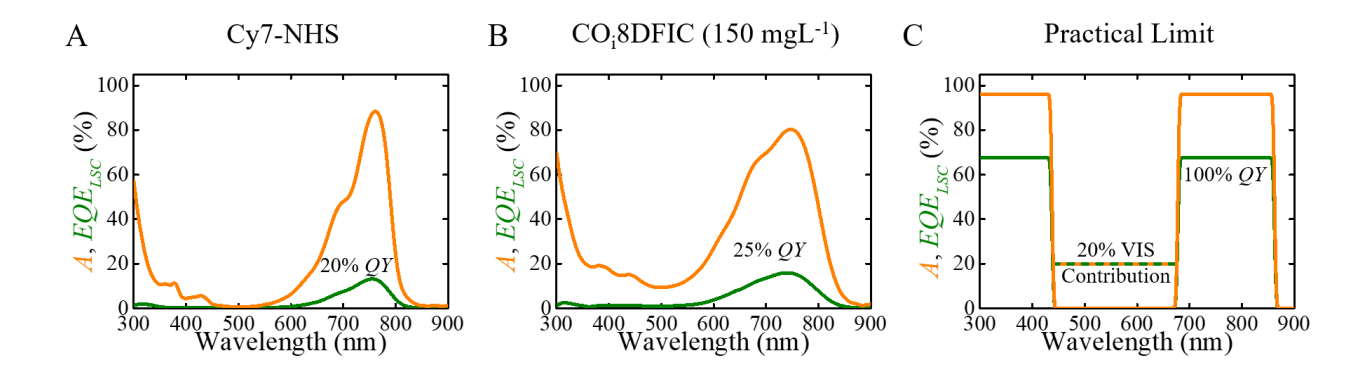


Figure 8.4 Absolute absorption and *EQELSC* **spectra for TLSCs.**(A) Cy7-NHS and (B) CO_i8DFIC 150 mgL-1. (C) TLSC reaching practical limits with GaAs as edge-mounted PV.

The absolute absorption peak height of "50 mgL⁻¹" ($A(\lambda)$ % = 49.6%) is significantly lower than that of the "Cy7-NHS" control $(A(\lambda)\% = 88.6\%)$, however, the EQE_{LSC} peak heights are similar to each other as shown in Figure 8.3B. Thus, this 30% η_{LSC} improvement mainly originates from the wider absorption peak and the higher QY of the CO_i8DFIC. The excellent luminescent properties are likely one of the reasons it has become such a high-performance acceptor in photovoltaic devices, where the high OY at notably low bandgaps signifies a reduction of nonradiative modes. For "150 mgL⁻¹", both the increased absorption peak height $(A(\lambda))\% = 80.3\%$) and width results in substantial improvement in J_{SC} . Further increasing the concentration, the absorption peak height reaches a plateau $(A(\lambda)\% = 92.0\%$ for "300 mgL⁻¹"), but the increased width leads to both color-tinting (low AVT and CRI) and greater reabsorption loss. This is reflected in the corresponding EQE_{LSC} spectra: the "300 mgL⁻¹" shows a broader EQE_{LSC} peak width but a decreased peak height compared to the "150 mgL⁻¹". The decay trends of the normalized positiondependent EOE_{LSC} peak value can help to analyze the reabsorption loss behavior: "50 mgL⁻¹" exhibits the slowest decay trend due to the lowest reabsorption in the series. With higher luminophore concentration the "150 mgL⁻¹" shows a more rapid decay curve, however, it is still

slightly slower than that of the "Cy7-NHS" control. Lastly, with the highest concentration, the "300 mgL-1" and the "Cy7-NHS" share very similar "roll-off" behavior due to the highest reabsorption loss in the series. Considering the scalability, aesthetic quality, and photovoltaic performance, 150 mgL-1 is found to be the optimal concentration. To further clarify the origin of the enhancement, we break this down further: as shown in **Figure 8.4** and **Table 8.2**, moving from the previously reported Cy7-NHS to CO_i8DFIC leads to a near doubling η_{LSC} from improved QY from 20% to 25% (increase by a factor of 1.25) and an increase in the wavelength selective absorption by a factor of 1.63.

Table 8.2 Wavelength selective absorption ratio, QY and $Int. J_{SC}$ comparison.

Luminophore	Total Solar Photon Absorbed (#m ⁻²)	QY %	J ^{Int} _{SC} (mAcm ⁻²)	V _{OC} (V)	FF (%)	η _{LSC} (%)	
Cy7-NHS	4.28×10^{20}	20±1					
CO _i 8DFIC	6.98×10^{20}	25±3	See Table 8.3 for detail		i1		
Ratio	6.98/4.28=1.63	25/20=1.25					
Practical Limit-1 (0% VIS Contribution)	9.14×10^{20}	100	10.3	1.05	80	8.65	
Practical Limit-2 (20% VIS Contribution)	1.11×10^{21}	100	13.5	1.05	80	11.34	

Note: for TLSCs with Cy7-NHS and COi₈DFIC 150 mgL⁻¹; factors to reach practical limits with and without visible contribution.

To explore the photovoltaic performance the TLSCs with different G factor, edge-mounted PV and luminophores, we also fabricated and tested square TLSC devices with a different G factor: waveguide length of 10.16 cm and thickness of 3.175 mm, and the G factor is 8. As shown in **Figure 8.5**, the averaged integrated current density is 0.95 mAcm⁻² compared to 1.78 mAcm⁻² with

the CO_i8DFIC concentration of 150mgL⁻¹. The η_{LSC} is expected to be 0.75% with similar VOC and FF.

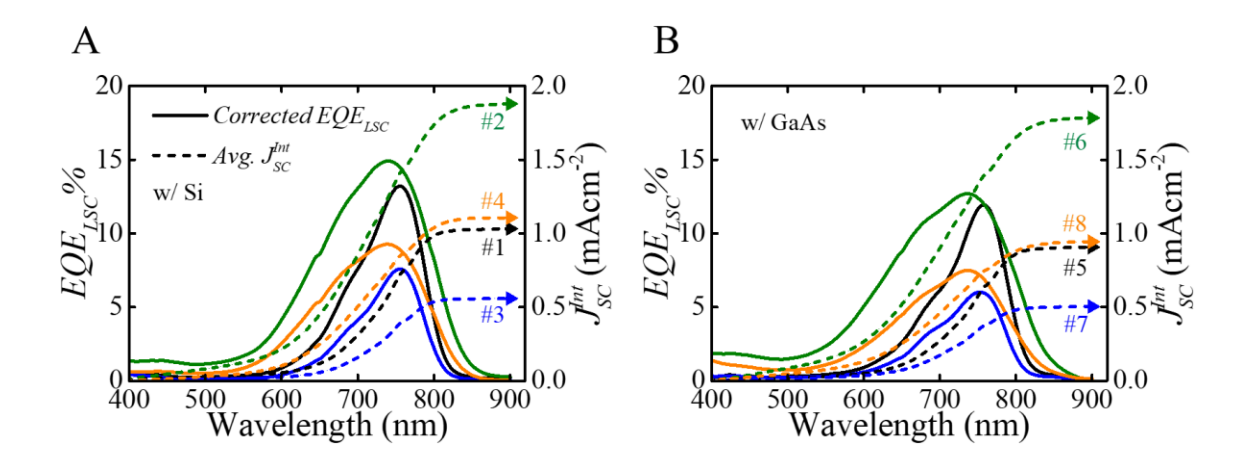


Figure 8.5 EQE_{LSC} and the averaged integrated J_{SC} comparison of TLSCs with different edge mounted PVs, G factors and luminophores.

In addition, as G factor and edge-mounted PV are kept the same, the η_{LSC} improvement from CO_i8DFIC is always 80-100% compared to Cy7-NHS as shown in **Table 8.3**. Moving from Si to GaAs leads to an improvement in the V_{OC} and FF by a factor of 2.2 and 1.4, respectively. Therefore, one can see the η_{LSC} improvement from the luminophore and matched PV cell is equally important.

Table 8.3 Summary of Photovoltaic parameters for TLSCs with different edge-mounted PV, *G* factor and luminophores as shown in Figure 8.5.

#	Luminophore	PV	G	J ^{Int} _{SC} (mAcm ⁻²)	Voc (V)	FF (%)	η _{LSC} (%)
1		Si	8	0.56	0.45	57	0.14
2	Cy7-NHS		2	1.03	0.42	57	0.25
3	Cy / TVIID	GaAs	8	0.50	0.99	80	0.40
4		GaAs	2	0.91	0.99	80	0.72

Table 8.3 (cont'd)

#	Luminophore	PV	G	J ^{Int} _{SC} (mAcm ⁻²)	V _{OC} (V)	FF (%)	η _{LSC} (%)
5		Si	8	1.10	0.45	57	0.28
6	CO _i 8DFIC	21	2	1.89	0.47	56	0.54
7	Colograp	GaAs	8	0.95	0.99	80	0.75
8		<i>Cur</i> 15	2	1.78	0.99	80	1.41

As shown in Figure 8.4C and Table 8.2, improving the QY from 25% to 100% can increase the η_{LSC} by a factor of 4 (from 1.3% to 5.2%). However, improving the UV and NIR absorption efficiency with sharper absorption spectrum cutoffs (e.g., with dielectric mirrors) would result in a factor of 1.31 (η_{LSC} from 5.2% to 6.8%), while further tuning the emission spectrum to suppress the reabsorption, would lead to an enhancement of 1.26 (η_{LSC} from 6.8% to 8.6%). By absorbing 20% of the VIS light from 435-675 nm, the integrated J_{SC} can be further improved from 10.3 mAcm⁻² to 13.5 mAcm⁻² (30% enhancement) boosting the η_{LSC} up to > 11%. This emphasizes several key points: 1) there is nearly as much to be gained by increasing the absorption efficiency as the QY and 2) selectively harvesting UV+NIR is more effective to reach the highest efficiencies. Overall, optimized efficiencies above 10% are conceptually achievable with this class of materials and an efficiency above 5% (with AVT > 70%) is achievable with modest gains as the QY approaches 50%.

Reabsorption is still a primary loss mechanism in these NIR selective-harvesting TLSC devices that can limit their application to smaller area applications. However, neither the Stokes shift nor the normalized absorption and emission spectra (Figure 8.1B) reflect the actual scalability in devices with different CO_i8DFIC concentrations.⁷⁸ To quantify this behavior, we introduced a

useful design parameter called the overlap integral (*OI*) to conveniently correlate reabsorption losses in LSC systems. Since the emission width of Cy7-NHS and CO_i8DFIC are distinctly different from each other, we normalized *OI* by their corresponding emission spectra to account for any spectral shape difference:

$$OI^* = \frac{\int_0^\infty A(\lambda)PL^*(\lambda)d\lambda}{\int_0^\infty PL^*(\lambda)d\lambda}$$
 (8.1)

where $PL^*(\lambda)$ is the normalized emission spectrum of the organic emitter in polymer matrix film, OI^* is the modified overlap integral that will be dependent on thickness and/or luminophore concentration, and lower OI^* is desirable for higher efficiency and improved scalability. The calculated OI^* trend from the lowest to highest scaling is: "50 mgL⁻¹" (0.249), "150 mgL⁻¹" (0.467), "Cy7-NHS" (0.470) and "300 mgL⁻¹" (0.618), which agrees well with the decay trend of these TLSCs.

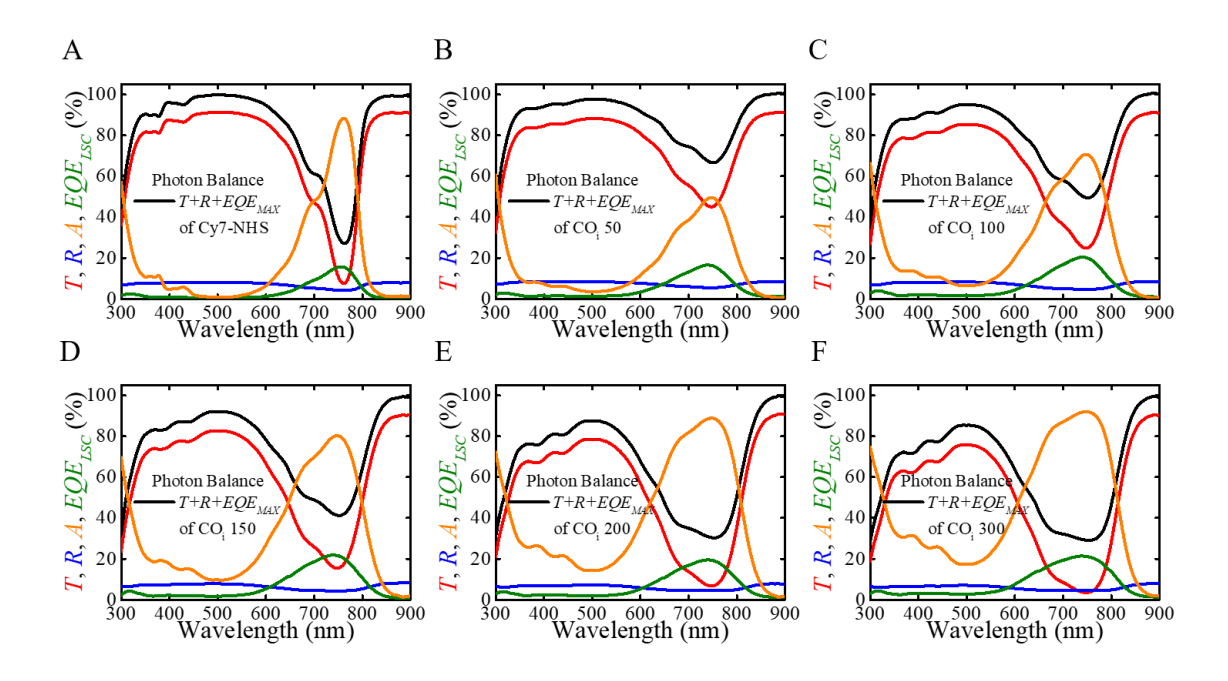


Figure 8.6 Photon balance check.

Measured transmittance $(T(\lambda))$, reflectance $(R(\lambda))$, absorption $(A(\lambda) = 1 - T(\lambda) - R(\lambda))$, $EQE_{LSC}(\lambda)$ spectrum and photon balance check $(EQE_{LSC}(\lambda) + T(\lambda) + R(\lambda) \le 1)$ of TLSCs at each wavelength.

To confirm the validity of the photon balance from the independent $EQE_{LSC}(\lambda)$, $T(\lambda)$, and $R(\lambda)$ spectra measurements of the TLSC device, $EQE_{LSC}(\lambda) + T(\lambda) + R(\lambda) \le 1$ is satisfied at each wavelength all the TLSC devices involved in **Figure 8.6**A to F. We note that the highest $EQE_{LSC}(\lambda)$ (acquired at the smallest d, rather than the average in Figure 8.3B) in the position-dependent EQE_{LSC} spectra is used in this relation to ensure that the whole series satisfy the photon balance. 12,124

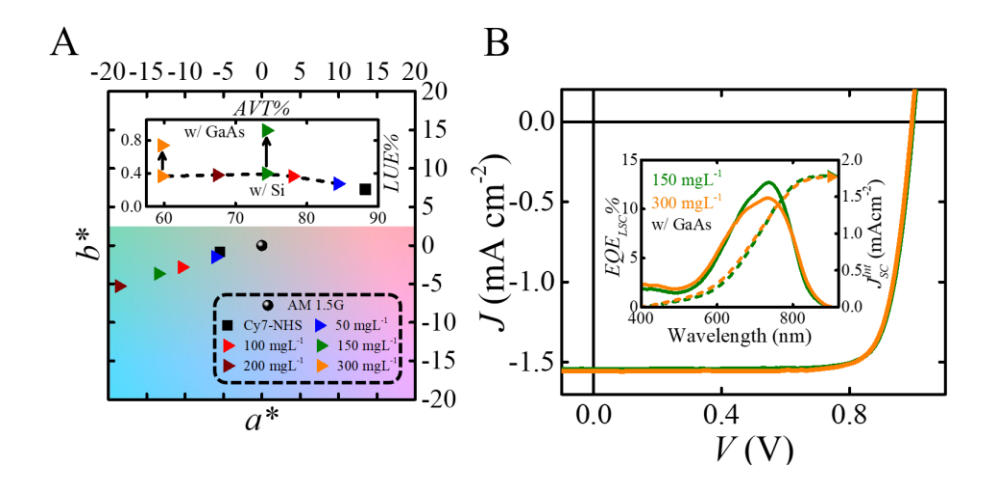


Figure 8.7 CIELAB color coordinates, LUEs and TLSCs with GaAs edge-mounted PV. (A) Color coordinates (a^* , b^*) of CO_i8DFIC TLSCs in CIELAB color space. Note: "300 mg L $^-$ 1" is strongly tinted and the corresponding CO_i8DFIC TLSCs (edge-mounted with Si or GaAs PV) versus AVT. (B) Current density versus voltage (J–V) characteristics of "150 mg L $^-$ 1" and "300 mg L $^-$ 1" TLSCs edge-mounted with GaAs PVs. Inset: averaged $EQE_{LSC}(\lambda)$ spectra of the same two TLSCs edge-mounted with GaAs PVs. The corresponding integrated J_{SC} match well with the J_{SC} extracted from J–V characteristics.

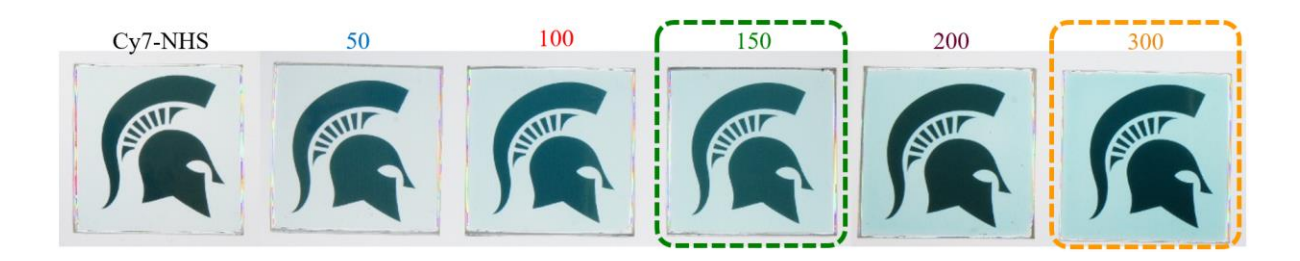


Figure 8.8 Photographs of all the TLSC devices.

Permission to utilize the Spartan helmet logo is kindly provided by MSU.

The CIELAB color space coordinates (a^*, b^*) are key figures of merit to quantify the rendered color fidelity of the transmitted light in the window industry. 3,12,124 The incident AM 1.5G is at the origin (0, 0) (as neutral) and the (a^*, b^*) positions of the TLSCs are plotted in **Figure 8.7**A. Since there is a tail absorption of the NIR absorption peak that extends into VIS (mostly in red), the TLSCs all have negative values of a^* and b^* . The coordinates of "50 mgL-1" and "Cy7-NHS" are very close to each other, which can be observed in the TLSC photographs as shown in **Figure 8.8**. As the CO_i8DFIC concentration increases, the positions move away from the origin along a nearly straight line and the rendered colors gradually become more blue-tinted. At the highest concentration the corresponding (a^*, b^*) moves outside of the scale shown, indicating that the "300 mgL-1" is no longer suitable for glazing systems.

As discussed in Chapter 2, the output voltage of an LSC device is determined by the edge-mounted PV cell. Ideally, using a PV cell with a bandgap bordering the emission edge of the luminophore can effectively reduce voltage losses (reduced thermalization loss in the PV) and improve the overall η_{LSC} . Further increasing the bandgap of the edge-mounted PV beyond that can result in a direct trade-off between the output voltage and collectable current. With the CO_i8DFIC emission peak edge at around 900 nm, GaAs is a nearly ideal PV with an EQE_{PV} cutoff closest to the CO_i8DFIC emission peak edge. We therefore integrate GaAs PV cells onto "150 mgL-1" and "300 mgL-1" TLSCs to replace the Si PVs as an example of this potential improvement. The J-V curves are plotted in Figure 8.7B. The measured J_{SC} of the "150 mgL-1" device with GaAs is 1.54 ± 0.05 mAcm-2, with significantly improved V_{OC} of 0.99 ± 0.01 V and FF of $81\pm1\%$, leading to a η_{LSC} of $1.24\pm0.04\%$. The "300 mgL-1" exhibits very similar photovoltaic performance as the "150 mgL-1". The average EQE_{LSC} spectra is provided in the inset of Figure 8.7B; with slightly broader EQE_{LSC} peak width, the peak height of "300 mgL-1" is lower than that of the "150 mgL-1" but more

contribution from the visible range, so the integrated J_{SC} values of "150 mgL⁻¹" and "300 mgL⁻¹" are 1.78 mAcm⁻² and 1.77 mAcm⁻², respectively, and these values also agree well with the J_{SC} from the J-V characteristics.

The *LUE* provides a metric for systematically comparing transparent PV devices with different overall levels of *AVT* on the same scale.^{3,12} We plot the *LUE* of the TLSC devices as a function of their *AVT* in the inset of Figure 8.7A. With Si edge-mounted PVs, the "Cy7-NHS" control TLSC has an *LUE* of 0.21, and the *LUE* of the CO_i8DFIC TLSCs peaks at 0.41 with "150 mgL⁻¹". Further increasing the concentration can slightly improve the η_{LSC} but dramatically reduce the *AVT*. With GaAs PVs, the "150 mgL⁻¹" and "300 mgL⁻¹" have *LUE* values of 0.92 and 0.74, respectively. To the best of our knowledge, the "150 mgL⁻¹" is the first report for a TLSC device with an *AVT* over 70% and a η_{LSC} over 1.2%.

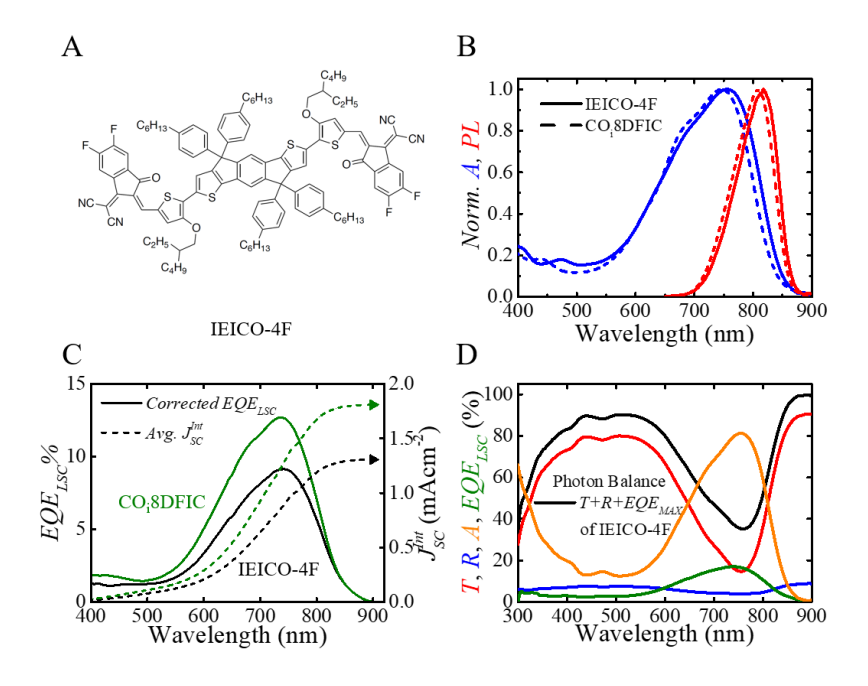


Figure 8.9 TLSC with a similar NFA IEICO-4F.

(A) Molecular structure of IEICO-4F. (B) Normalized absorption (blue) and emission (red) spectra of CO_i8DFIC (solid lines) and IEICO-4F (dashed lines) embedded in polymer matrix (Eukitt). (C) EQE_{LSC} and the averaged integrated J_{SC} comparison of TLSC with CO_i8DFIC and IEICO-4F as luminophores. (D) Photon balance of the TLSC with IEICO-4F.

To show that these NFAs are a compelling platform for LSC and TLSC development, we have characterized and integrated a second popular non-fullerene acceptor (IEICO-4F) as a luminophore for TLSCs. The corresponding $A(\lambda)$, $PL(\lambda)$, and $EQE_{LSC}(\lambda)$ are similar to CO_i8DFIC with slightly lower QY of 20±2% in polymer matrix as shown in **Figure 8.9**. This reinforces the promising properties of this class of low bandgap organic molecules and gives an important new direction for future study.

As the spectral absorption range is nearly ideal and well-coupled spectrally to the GaAs (which is already close to the Shockley-Queisser limit), the practical limit with this device arrangement/molecular-motif can be estimated by considering just an improvement of the QY of the NIR luminophore from 25% (measured) to ~90%-100%. This could be achieved, for example, with chemical modifications to the core molecular motif to reduce non-radiative modes via rigidification. In this limit, the η_{LSC} would reach an efficiency just over 5% with the same high level of AVT, while approaching the record opaque LSC of 7%. ¹⁹² Practical limits above 10% are possible with this approach as shown in Table 8.2.

8.5 Summary

In conclusion, we introduce NFAs into LSCs and TLSCs as the luminophore. We focus on CO_i8DFIC, which has emerged as a blockbuster acceptor in organic photovoltaics but which also has excellent luminescent properties. The impact of CO_i8DFIC concentration on η_{LSC} , aesthetic quality, and scalability is systematically studied. After device optimization, the TLSCs are shown to achieve a η_{LSC} over 1.2% while the *AVT* exceeds 74% and *CRI* exceeds 80. This work reports the highest TLSC device efficiency at the highest visibly transparency and highlights that the

photoluminescent properties of these emerging low bandgap organic molecules providing an encouraging path to higher TLSC performance.

Chapter 9 Ultraviolet and Near-Infrared Selective Harvesting Dual-Band Transparent Luminescent Solar Concentrators

In this chapter, we combine massive-downshifting phosphorescent nanoclusters and fluorescent organic molecules into a TLSC system as UV and NIR selective-harvesting luminophores, respectively, demonstrating UV and NIR dual-band selective-harvesting TLSCs with η_{LSC} over 3%, AVT exceeding 75% and color metrics suitable for the window industry. With distinct wavelength-selectivity and effective utilization of the invisible portion of the solar spectrum, this work reports the highest LUE of 2.6 for a TLSC system, the highest η_{LSC} of any transparent photovoltaic devices with AVT greater than 70% and outperforms the practical limit for non-wavelength-selective transparent photovoltaics.

9.1 Introduction

Many previous works on TLSCs with NIR harvesting have absorption profiles that have limited UV capture with η_{LSC} s up to around 1% and AVTs above 70% for an LUE of 0.7. The highest reported and certified semitransparent LSC devices based on inorganic nanocrystals have reported a η_{LSC} of 2.2% with an AVT of 44% (LUE of 0.97) and a brown coloring. Multiple luminophores with various wavelength-selectivity can be incorporated into the LSC waveguide to maximize the spectral coverage of light harvesting, 193–200 enhance photovoltaic performance, 125,171,201,202 and balance the color neutrality. However, the coupling or reabsorption between different luminophores often leads to a reduction in the efficacy of this approach. 203,204

Guided by the ideal TLSC design introduced in Chapter 2, we simultaneously introduce highly luminescent phosphorescent nanoclusters (NCs) and fluorescent organic molecules into TLSCs as isolated UV and NIR selective-harvesting luminophores, respectively. The nanoclusters selectively harvest UV photons while exhibiting near-unity QY and massive downshift of the luminescence into the NIR, without the use of heavy or toxic elements like lead.^{7,44,205,206} To effectively pair these emitters and prevent parasitic reabsorption loss of the nanocluster emission in the NIR absorbing organic fluorophore we show a strategy to isolate the absorption/emission bands. The corresponding dual-band selective-harvesting TLSC exhibits the highest η_{LSC} at the highest transparency, therefore, the highest LUE, and demonstrates a novel design to effectively utilize the solar spectrum in a highly aesthetical approach. Distinct UV and NIR selectivity offers the TLSC excellent aesthetic quality (AVT over 75% and CRI of 90) and the down-shifting dual-band TLSCs also show good photostability with minimal degradation over more than 700 hours of continuous 1 Sun illumination.

9.2 Experimental Section

Synthesis of Luminophores: Cs₂Mo₆I₁₄: MoI₂ powder (2A Biotech) was uniformly mixed with CsI powder (Sigma-Aldrich) with a stoichiometric ratio of 3:1. The mixture was then transferred into a quartz ampule (12 cm long, 1.5 cm diameter), and the ampule was sealed under vacuum. The ampule was heated at the reaction temperature of 750 °C for 72 hours to form Cs₂Mo₆I₁₄. After cooling down to room temperature, the powder in the ampule was dissolved in acetone (wine-colored solution) and the undissolved impurity (unreacted black powder) was

filtered out. The acetone was removed by rotary evaporation to obtain red $Cs_2Mo_6I_{14}$ powder. Powder XRD pattern of $Cs_2Mo_6I_{14}$ was collected to confirm the product.^{206,207}

 $Cs_2Mo_6I_8(CF_3CF_2COO)_6$: $Cs_2Mo_6I_{14}$ was weighed and dissolved in acetone in a flask, and silver pentafluoropropionate (CF_3CF_2COOAg) (Sigma-Aldrich) was added into the $Cs_2Mo_6I_{14}$ solution with a stoichiometric ratio of 6:1. The reaction was kept in the dark in a nitrogen atmosphere for 48 hours. After the ligand exchange reaction, the precipitated AgI was filtered out and the solution (cider-colored) was dried by rotary evaporation to obtain orange $Cs_2Mo_6I_8(CF_3CF_2COO)_6$ powder. The powder was purified by silica column chromatography (20% ethanal/80% acetone, gradually increasing to 100% ethanol) to yield the pure nanocluster product. Column chromatography was performed using Silicycle 60 Å, 35-75 μ m silica gel. The final purification step boosts the NC QY by ~10% by eliminating the non-radiative impurities from the reactions. $Cs_2Mo_6I_8(CF_3COO)_6$ and $Cs_2Mo_6I_8(CF_3CF_2CF_2COO)_6$ nanoclusters were prepared by reacting $Cs_2Mo_6I_{14}$ and silver trifluoroacetate (CF_3COOAg) or silver heptafluorobutyrate ($CF_3CF_2CF_2COOAg$) with similar procedure. All the NC products were confirmed by high resolution mass spectrometry (Xevo G2-OTOF).

Figure 9.1 General synthesis of CO_i8DFIC.

Figure 9.2 General synthesis of BODIPY.

CO_i8DFIC and BODIPY: Synthesis of CO_i8DFIC^{186,208} starts from lithiation of commercially available 3-bromothieno[3,2-b]thiophene **1**, followed by carbonylation and esterification was afforded intermediate **2** as a mixture of regioisomers. The ratio of desired isomer **2a** was enriched by recrystallization following our previous report. The obtained material was directly subjected to subsequent Stille coupling, BBr₃ demethylation, lactonization, Grignard reaction, and Vilsmeier-Haack formylation, to furnish key precursor **4**. CO_i8DFIC was afforded

by a final condensation with difluoroindanone **5**. The synthesis of **BODIPY**²⁰⁹ commenced with 2,3-dihydroxynaphthalene, which was converted to the corresponding dihydrazine **6**, and followed by formation of dihydrazone **7** for subsequent acid-catalyzed Fischer indole synthesis and decarboxylation to furnish the key building block naphthobipyrrole **8**. The BODIPY scaffold was then constructed by orthoformation in the presence of POCl₃ and following treatment with $BF_3 \cdot OEt_2$.

Module Fabrication: UV waveguide: Cs₂Mo₆I₈(CF₃CF₂COO)₆ nanocluster powder was weighed and dissolved in ethanol to prepare the solution at the target concentration (1, 2, 5, 10 and 20 mgmL⁻¹). The ethanol solution was mixed with mounting medium (Fluoroshield F6182, Sigma-Aldrich) at a volume ratio of 1:2. NIR waveguide: CO_i8DFIC or BODIPY was dissolved in dichloromethane to prepare the solution (100 mgL⁻¹ for BODIPY and 125 mgL⁻¹ for CO_i8DFIC). The dichloromethane solution was mixed with mounting medium (Shandon, Thermo Fisher Scientific) at a volume ratio of 1:1. Dual-band TLSCs: This mixture was drop-cast on 50.8 mm X 50.8 mm \times 3.175 mm (for J-V characterization and averaged EQE_{LSC} measurement) and 101.6 mm \times 101.6 mm \times 3.175 mm (for position-dependent EQE_{LSC}) borosilicate glass sheets and allowed to dry for 6h in a glovebox filled with nitrogen gas (O₂, H₂O < 1ppm). After the composite films (~0.5 mm thickness) were completely dry, two components were encapsulated together by UV-curing epoxy (DELO) around the edges, where the two composite films faced each other within the encapsulation, the nitrogen gap thickness is also ~0.5 mm. The edge-mounted GaAs PVs (Alta Devices) were used as received. For J-V measurements, two PV strips were mounted on orthogonal edges (each edge was fully covered) using index matching gel (Thorlabs) to attach the PV strips on the waveguide edges and were connected in parallel. The remaining two edges were painted black to block the light and internal reflection of light. For EQE_{LSC} measurements, one PV

strip (composed of two GaAs PVs connected in parallel) was attached to one edge of the waveguide with the other three edges painted black. Correcting the raw data to account for 4 cell integration was done according to standardized protocols reported in Chapter 4.^{44,124}

Optical characterization: Similar to the description in Section 6.2.1 to 6.2.3 in Chapter 6 by following the standard protocols introduced in Chapter 3 and Chapter 4.

Photovoltaic characterization: A Keithley 2420 SourceMeter was used to obtain J-V characteristics under simulated AM 1.5G solar illumination. A xenon arc lamp was used as the illumination source and the EQE_{LSC} spectra of each TLSCs were used as the input to calculate their corresponding mismatch factors (MF): the MF values are 1.067, 1.051 and 1.052 for NC-only, NC+CO_i8DFIC and NC+BODIPY TLSCs. The light intensity was calibrated with an NRELcalibrated Si reference diode with a KG5 filter. The position-dependent EQE_{LSC} measurements were performed using a QTH lamp with a calibrated Si detector, monochromator, chopper and lock-in amplifier. The measured $EQE_{LSC}(\lambda)$ at each distance (d) was corrected by multiplying the geometric factor $g = \pi/tan^{-1}(L/2d)$, which accounts for the different angle subtended by the edgemounted PV at various excitation distance (d), where L is the LSC waveguide length. A series of $EQE_{LSC}(\lambda)$ spectra were acquired with the same TLSC device attached to the same GaAs PV, then the averaged spectrum was used to represent the whole device and integrated to confirm the J_{SC} from the corresponding J-V characteristics of the same device. A matte black background was placed on the back of the TLSC device to eliminate illumination from the environment or reflection (double-pass) for both J-V and EQE_{LSC} measurements. All the TLSC devices were tested with the same GaAs PV cells to eliminate any PV-to-PV variation in performance. 44,124

Lifetime Test: A sulfur-plasma lamp was used to constantly illuminate the TLSCs for photostability measurements. Analogously to the xenon arc lamp, the illumination intensity of the

sulfur-plasma lamp was also calibrated to ~ 1 Sun (light intensity uniformity < $\pm 5\%$) with NREL-calibrated Si reference cell. ^{185,210} Three key parameters including $A(\lambda)$, $EQE_{LSC}(\lambda)$ and $IQE_{LSC}(\lambda)$ were monitored to evaluate the photostability of the TLSC devices.

9.3 Results

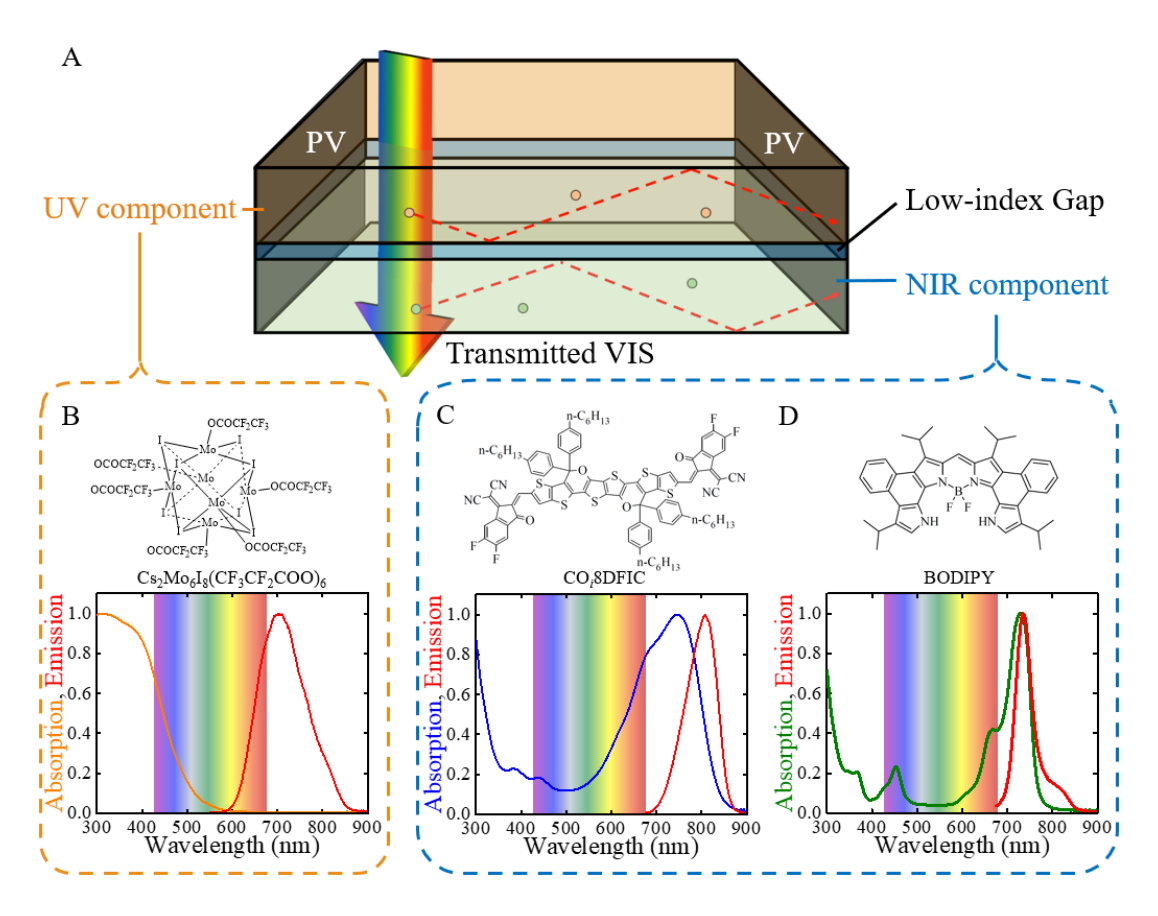


Figure 9.3 Working Principle and Luminophores of the Dual-band TLSCs.

(A) Schematic showing the structure and working principle of the dual-band selective harvesting transparent luminescent solar concentrator (TLSC). The UV component and NIR component are separated by an air gap which enables total internal reflection within each waveguide and isolation of the emission from each luminophore. Molecular structure, normalized absorption and emission spectra of (B) Cs₂Mo₆I₈(CF₃CF₂COO)₆ nanocluster, (C) CO_i8DFIC and (D) BODIPY in polymer matrix. Both the absorption and emission profiles of all the luminophores are designed to stay out of the VIS range, maximizing the visible transmission and aesthetic quality. Although a small portion of the NC PL falls into the red range, the majority of the escaped PL from the top UV component can be reabsorbed by the bottom NIR component, enhancing the light harvesting and minimizing any red glow observed from the transmitted side.

9.3A with the UV component coated in polymer matrix on one waveguide and the NIR component on the other. A nitrogen gap is utilized to optically isolate the waveguided luminescence in each panel to prevent parasitic reabsorption. For more practical deployment, this air gap can be replaced with a low refractive index polymer, ^{144–146} metal oxide, ^{128,147,149,151,209,211} or glue with slight change in the performance. ¹⁴³

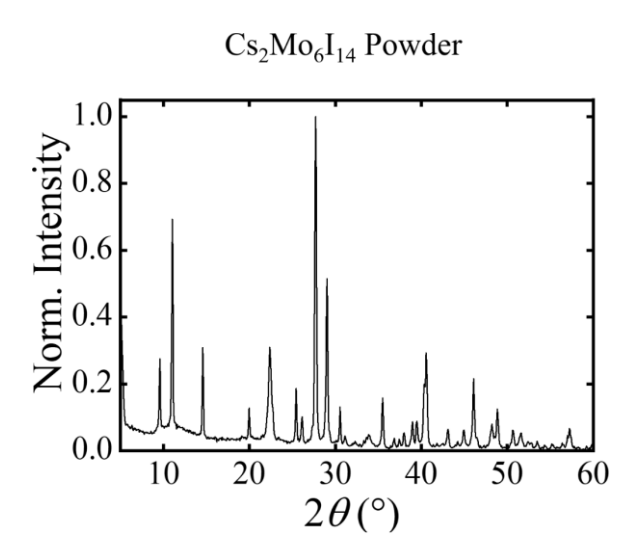


Figure 9.4 X-ray Diffraction pattern of Cs₂Mo6I₁₄ nanocluster powder.

The top UV component is based on phosphorescent hexanuclear nanoclusters, where the chemical structure of Cs₂Mo₆I₈(CF₃CF₂COO)₆ NC is shown in Figure 9.3B. Substitution of the apical halide positions has been shown previously to be an effective approach to increase *QY*s above 50%.^{7,168,205,206,212,213} Both X-ray diffraction (XRD)²¹² and mass spectrometry^{205,213} are used to confirm the formation of the synthesized products. As shown in **Figure 9.4**, the observed X-ray diffraction (XRD) pattern of Cs₂Mo₆I₁₄ nanocluster (NC) matches well with previous literature report, which confirms the formation of Cs₂Mo₆I₁₄ nanocluster from the synthesis of MoI₂ and CsI.

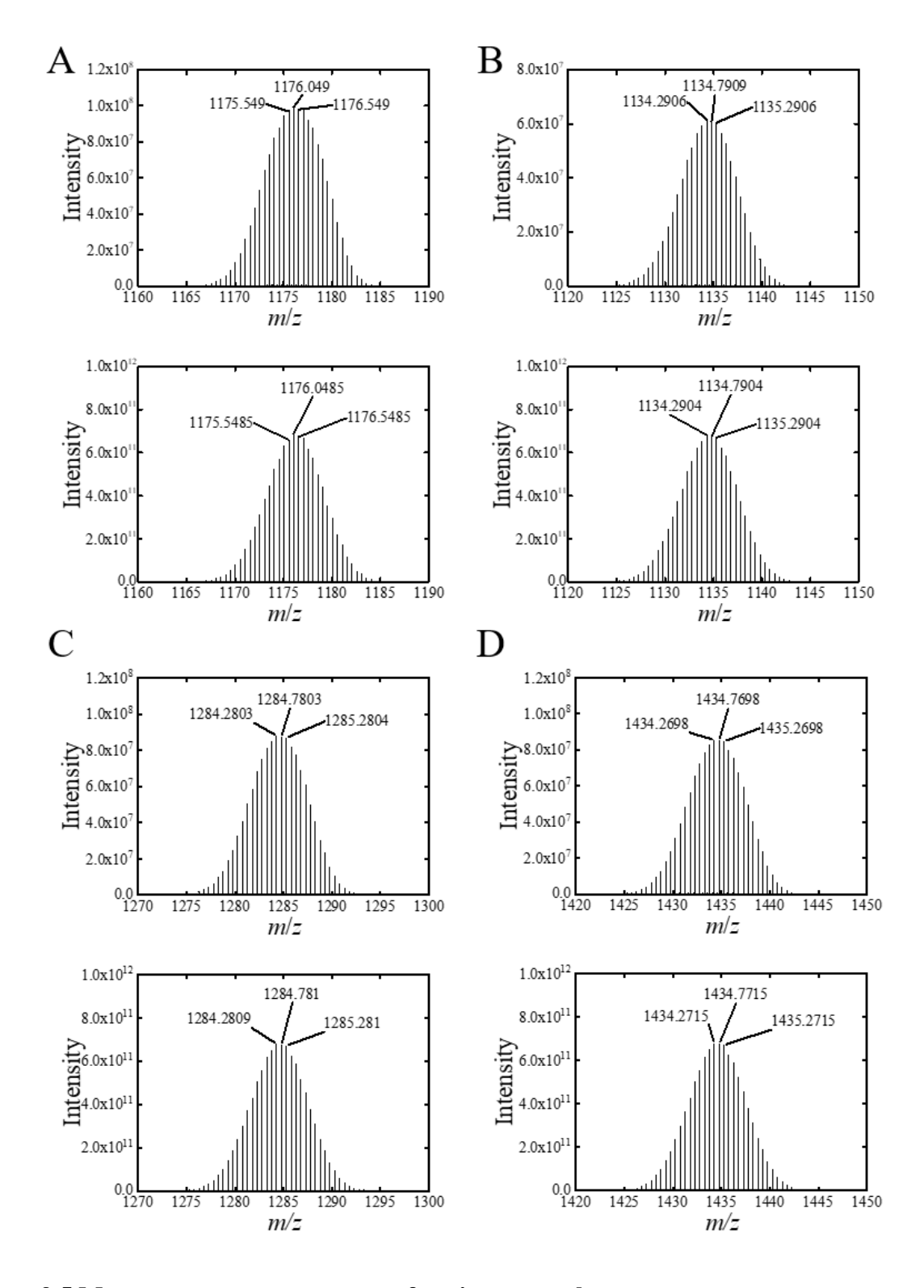


Figure 9.5 Mass spectrometry patterns of various nanoclusters. (A) $Cs_2Mo_6I_{14}$, (B) $Cs_2Mo_6I_8(CF_3COO)_6$, (C) $Cs_2Mo_6I_8(CF_3CF_2COO)_6$ and (D) $Cs_2Mo_6I_8(CF_3CF_2COO)_6$ NCs with the experimental measured data (top) compared with the theoretical isotopic distribution (bottom) in each plot.

High resolution mass spectrometry scans as a function of m/z were measured and plotted in **Figure 9.5**. Mo has rich isotope distribution (92Mo, 94Mo, 95Mo, 96Mo, 97Mo and 98Mo are the six main and stable isotopes of Mo), and there are six Mo sites in each NC. Various combination of these isotopes therefore results in the distribution in the corresponding mass spectrometry plot. Various terminating ligands ((CF₃)_n chain length) were synthesized and tested to maximize the QYwith the composition above providing the highest value. The experimentally measured mass spectrometry patterns of the Cs₂Mo₆I₁₄, Cs₂Mo₆I₈(CF₃COO)₆, Cs₂Mo₆I₈(CF₃CF₂COO)₆ and Cs₂Mo₆I₈(CF₃CF₂CF₂COO)₆ NCs all match well with theoretical peaks, confirming the successful synthesis of CsMo₆I₁₄ NC and subsequent substitution of the apical halide positions with various ligands (including CF₃COO⁻, CF₃CF₂COO⁻, and CF₃CF₂CF₂COO⁻). We note that the chemical composition of the NC does not contain any hazardous heavy metal ions, which makes the deployment more environment-friendly. The TLSC waveguide was made by drop-casting NC/polymer mixture onto square borosilicate glass sheets to form uniform composite films. The normalized absorption and emission spectra of the NC in polymer are shown in Figure 9.3B. The spectra show band absorption cutoff at the UV/VIS border and NIR emission onset at the VIS/NIR border with a massive downshift over 300 nm and a corresponding QY of 80±5 in polymer matrix (75±5% in acetonitrile), which makes these NCs an excellent UV selective-harvesting luminophore for TLSC applications.⁷

The bottom waveguide is based on fluorescent organic small molecules. In organic and molecular semiconductors light absorption originates from the transition from the ground state to excited molecular orbitals. The energy difference between the excited molecular states forms discontinuities in the density of states. Therefore, these energy gaps can be tuned to transmit visible photons in TPV applications. In this work, two different organic luminophores are demonstrated

as NIR selective-harvesters: CO_i8DFIC (also referred to as O6T-4F), which has been developed as a NFA in organic photovoltaics with excellent performance; 186,187,208,214 and a BODIPY derivative with high QY in the NIR.²⁰⁹ The molecular structures, normalized absorption, and emission spectra of these NIR components in polymer matrix are shown in Figure 9.3C and D, respectively. Similarly, the NIR selective-harvesting waveguide was also made by drop-casting dye/polymer mixture onto glass sheets to form a uniform composite film. The absorption peak of CO_i8DFIC is at 745 nm and the emission peak is at 808 nm, resulting in a Stokes shift of ~60 nm and QY of 25±3% in polymer matrix (23±1% in chlorobenzene). Compared to CO_i8DFIC, the absorption and emissions peaks of BODIPY are narrower with a smaller Stokes shift (10 nm), but the significantly higher QY of $40\pm3\%$ in polymer matrix ($41\pm2\%$ in hexane) is among the highest values for this NIR emission range. Moreover, we have shown previously that Stokes shift is not always well correlated to performance and a more important parameter to analyze is the overlap integral (OI: 0.015, 0.40 and 0.56 for UV component with NC, NIR component with CO_i8DIFC and NIR component with BODIPY, respectively.), 188 which indicates a similar level of reabsorption probability between the two NIR emitters due to the balance between Stokes shift and absorption/emission widths. 78 Indeed, to reach the theoretical SQ limits actually requires small Stokes shifts, narrow emission, and sharp absorption cutoffs so that the OIs approach zero and still enable scalability.9

For optimizing LSCs it is advantageous to select an edge-mounted PV cell with a bandgap bordering the emission edge of the luminophores. This allows all the waveguided PL to be collected and converted to electricity while minimizing the voltage losses due to thermalization. Thus, the voltage of the LSC system is increased. With all three emission edges of NC, CO_i8DFIC and BODIPY below 900 nm as shown in Figure 9.3B-D, GaAs is a nearly ideal edge-mounted PV

cell choice for these luminophores to maximize the overall photovoltaic performance. GaAs cells are mounted on two edges for J-V measurements and on one edge of the dual waveguide for EQE_{LSC} measurements following the standardized procedures outline elsewhere, where both are accordingly corrected for the equivalent four-edge mounting by following the methods discussed in detail in Chapter 4. 124

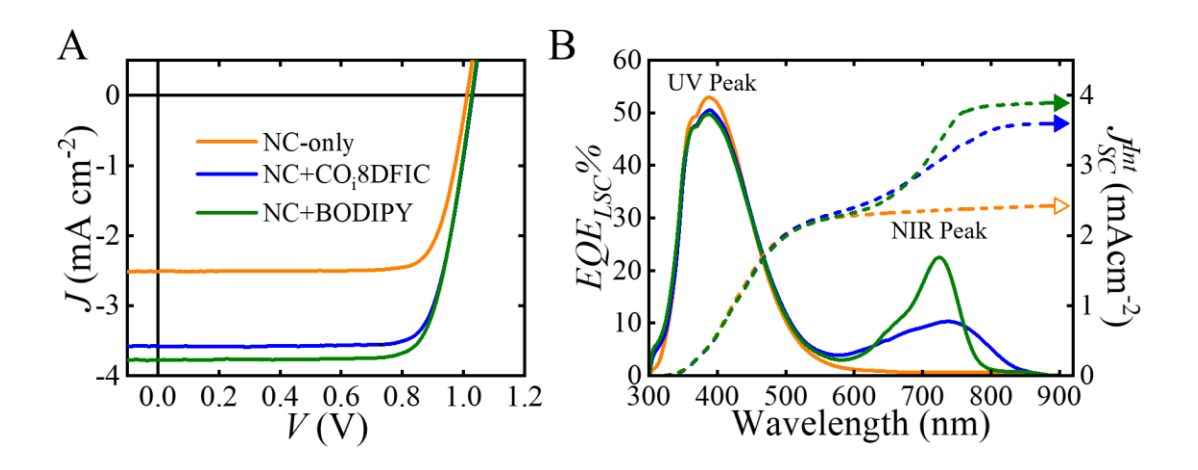


Figure 9.6 Photovoltaic Performance of the Dual-band TLSCs.

(A) Current density versus voltage (J-V) characteristics of NC-only, NC+CO_i8DFIC and NC+BODIPY TLSCs. All scans were measured under AM 1.5G illumination and all TLSCs were edge-mounted with the same GaAs PV cells. (B) Average $EQE_{LSC}(\lambda)$ spectra of NC-only, NC+CO_i8DFIC and NC+BODIPY TLSCs. The corresponding integrated short-circuit current density (I_{SC}^{Int}) matches well with the J_{SC} extracted from J-V characteristics shown in (A).

Single-band TLSC devices with one luminophore were first fabricated and optimized based on concentration. Dual-band TLSC devices with two luminophore combinations (NC+CO_i8DFIC and NC+BODIPY) were then fabricated and their photovoltaic performance was characterized. For comparison, the TLSC with NC-only (10 mgmL⁻¹) was added as a reference device. The *J-V* characteristics of these TLSCs (active area of 5.08×5.08 cm² and total waveguide thickness of 0.635 cm) measured under AM 1.5G illumination are shown in **Figure 9.6**A. When a PV cell is edge-mounted onto an LSC waveguide, the LSC-PV system should be treated as an integrated photovoltaic device, and the input solar photon flux is received by the area of the front surface of

the LSC waveguide (A_{LSC}) rather than the area of the edge-mounted PV (A_{Edge}), just as with any PV system. The NC-only TLSC shows J_{SC} of 2.5±0.2 mAcm⁻², V_{OC} of 1.01±0.01 V and FF of 80±1%, resulting in a η_{LSC} of 2.0±0.1%. As the organic molecules are added into TLSCs with the same UV component (NC concentration is kept at 10 mgmL⁻¹), the J_{SC} values are improved to 3.6±0.2 mAcm⁻² and 3.8±0.1 mAcm⁻² while exhibiting similar V_{OC} and FF. This results in corresponding η_{LSC} s that reach 2.9±0.1% and 3.01±0.07% for NC+CO_i8DFIC and NC+BODIPY TLSCs, respectively, with color metrics suitable for the window industry. A champion device η_{LSC} of 3.65% is reached with higher NC concentration, however, the corresponding color metrics are outside the range of suitable for the window industry. All the photovoltaic performance and aesthetic quality parameters are summarized in **Table 9.1**.

Table 9.1 Photovoltaic and aesthetic quality parameters of the TLSCs.

Luminophore(s)	G	J_{SC}	J_{SC}^{Int}	Voc	FF	PCE	AVT	AVT LUE %	CRI	(a*, b*)
		(mAcm ⁻²)	(mAcm ⁻²)	(V)	%	%	%			
NC (1) ^a -only	4	_c	0.50	1.00 ^d	80e	0.40	85.3	0.34	96.5	(-0.8, 3.0)
NC (2) ^a -only	4	_c	0.81	$1.00^{\rm d}$	80°	0.64	85.0	0.55	98.3	(-1.5. 4.9)
NC (5) ^a -only	4	_c	1.51	$1.00^{\rm d}$	80e	1.21	83.7	1.01	95.3	(-3.6, 13.0)
NC (10) ^a -only	4	2.0±0.1	2.42	1.01±0.01	80±1	1.94	81.9	1.59	91.3	(-5.6, 23.3)
	8 ^b	_c	2.10	$1.00^{\rm d}$	80e	1.68		1.38		
NC (20) ^a -only	4	_c	2.93	$1.00^{\rm d}$	80e	2.34	78.7	1.84	84.0	(-7.6, 40.7)
NC (1) ^a +CO _i 8DFIC	2	_c	1.86	1.00 ^d	80e	1.49	68.5	1.02	81.5	(-13.3, -0.8)
NC (2) ^a +CO _i 8DFIC	2	_c	2.18	$1.00^{\rm d}$	80e	1.75	68.0	1.19	80.8	(-15.1, 2.4)
NC (5) ^a +CO _i 8DFIC	2	_c	2.88	1.00 ^d	80e	2.30	67.9	1.56	81.8	(-15.8, 5.8)
NC (10) ^a +CO _i 8DFIC	2	3.6±0.2	3.60	1.02±0.01	79±1	2.9±0.1	65.6	1.89	82.9	(-18.8, 22.2)
	4 ^b	_c	3.00	1.00 ^d	80e	2.40		1.58		
CO _i 8DFIC+NC (10) ^a	2	3.26±0.03	3.26	1.01±0.01	79±1	2.59±0.01	66.4	1.72	84.2	(-18.0, 22.9)

Table 9.1 (cont'd)

2	_c	4.27	1.00 ^d	80e	3.42	62.1	2.12	80.4	(-20.6, 33.7)
2	_c	2.07	1.00 ^d	80e	1.66	78.4	1.30	89.8	(-9.5, 7.5)
2	_c	2.40	1.00^{d}	80°	1.92	77.9	1.49	90.1	(-10.1. 10.1)
2	_c	3.10	1.00^{d}	80°	2.48	77.2	1.92	90.2	(-11.1, 14.7)
2	3.8±0.1	3.89	1.02±0.01	78±1	3.01±0.07	75.0	2.36	00.2	(12.2.25.5)
4 ^b	_c	3.32	1.00 ^d	80°	2.66	/5.8	2.02	88.3	(-13.3, 25.5)
2	3.55±0.06	3.57	1.02±0.01	79±1	2.84±0.05	73.4	2.08	86.1	(-15.4, 28.4)
2	_c	4.56	1.00^{d}	80°	3.65	71.6	2.61	82.9	(-15.1, 42.7)
4	1.55±0.04	1.50	1.00±0.01	81±1	1.26±0.03	76.3	0.92	81.6	(-12.4, -3.7)
4	1.84±0.03	1.83	1.00±0.01	81±1	1.48±0.03	86.4	1.26	92.2	(-7.2, 5.2)
	2 2 2 4 ^b 2 2 4	2 _c 2 _c 2 _c 2 _s 2 _s 2 _s 2 _s 2 _s 2 _s 3.8±0.1 4b _c 2 _s 3.55±0.06 2 _c 4 _1.55±0.04	2 -c 2.07 2 -c 2.40 2 -c 3.10 2 3.8±0.1 3.89 4b -c 3.32 2 3.55±0.06 3.57 2 -c 4.56	2 -c 2.07 1.00 ^d 2 -c 2.40 1.00 ^d 2 -c 3.10 1.00 ^d 2 3.8±0.1 3.89 1.02±0.01 4 ^b -c 3.32 1.00 ^d 2 3.55±0.06 3.57 1.02±0.01 2 -c 4.56 1.00 ^d 4 1.55±0.04 1.50 1.00±0.01	2 -c 2.07 1.00d 80e 2 -c 2.40 1.00d 80e 2 -c 3.10 1.00d 80e 2 3.8±0.1 3.89 1.02±0.01 78±1 4b -c 3.32 1.00d 80e 2 3.55±0.06 3.57 1.02±0.01 79±1 2 -c 4.56 1.00d 80e 4 1.55±0.04 1.50 1.00±0.01 81±1	2 -c 2.07 1.00d 80c 1.66 2 -c 2.40 1.00d 80c 1.92 2 -c 3.10 1.00d 80c 2.48 2 3.8±0.1 3.89 1.02±0.01 78±1 3.01±0.07 4b -c 3.32 1.00d 80c 2.66 2 3.55±0.06 3.57 1.02±0.01 79±1 2.84±0.05 2 -c 4.56 1.00d 80c 3.65 4 1.55±0.04 1.50 1.00±0.01 81±1 1.26±0.03	$\begin{array}{cccccccccccccccccccccccccccccccccccc$	$\begin{array}{c ccccccccccccccccccccccccccccccccccc$	2 -c 2.07 1.00d 80c 1.66 78.4 1.30 89.8 2 -c 2.40 1.00d 80c 1.92 77.9 1.49 90.1 2 -c 3.10 1.00d 80c 2.48 77.2 1.92 90.2 2 3.8±0.1 3.89 1.02±0.01 78±1 3.01±0.07 2.36 75.8 88.3 4b -c 3.32 1.00d 80c 2.66 2.02 2 3.55±0.06 3.57 1.02±0.01 79±1 2.84±0.05 73.4 2.08 86.1 2 -c 4.56 1.00d 80c 3.65 71.6 2.61 82.9 4 1.55±0.04 1.50 1.00±0.01 81±1 1.26±0.03 76.3 0.92 81.6

Note:

The averaged position-dependent $EQE_{LSC}(\lambda)$ spectra are shown in Figure 9.6B. For NC-only TLSC the EQE_{LSC} contribution originates only from the light absorption of the UV selective-harvesting NC. Neither Rayleigh scattering (caused by particle aggregation) nor direct illumination of the edge-mounted PV is observed from the EQE_{LSC} profile. For the NC+CO_i8DFIC and NC+BODIPY TLSCs, both UV and NIR peaks appear in their corresponding EQE_{LSC} spectra, which result from the dual-band selective-harvesting. The EQE_{LSC} peak positions match the absorption spectra of the corresponding luminophores. The EQE_{LSC} peak heights are constrained by both the luminophore QY values and the absolute absorption spectra. With the same NC concentration, the UV contribution is nearly the same for all three TLSCs. Both slightly higher

^a Inside each () is the concentration of NC (in mgmL⁻¹) in the precursor solution.

^b 10.16×10.16 cm² TLSCs for position-dependent EQE_{LSC} roll-off behavior study.

^c J_{SC} values integrated from the corresponding EQE_{LSC} spectra were used for PCE and LUE calculation.

^d V_{OC} of 1.00 V is assumed for *PCE* and *LUE* calculation comparison, consistent with the range of V_{OC} s experimentally measured (1.00-1.02 V)

^e FF of 80% is assumed for PCE and LUE calculation and comparison, consistent with the range of FFs experimentally measured (79-81%).

absolute absorption peak and significantly higher QY of the BODIPY results in a substantially higher EQE_{LSC} peak compared to that of the CO_i8DFIC for this device size. As one of the most important consistency checks for any photovoltaic device, the J_{SC} values extracted from J-V characteristics are confirmed by the integrated $J_{SC}(J_{SC}^{Int})$ from $EQE_{LSC}(\lambda)$. The J_{SC}^{Int} values are 2.42 mAcm⁻², 3.60 mAcm⁻² and 3.89 mAcm⁻² for NC-only, NC+CO_i8DFIC and NC+BODIPY TLSCs, respectively, and match well with the J_{SC} from the J-V curves. Although the EQE_{LSC} peak of BODIPY in the NC+BODIPY TLSC is higher than that of the NC+CO_i8DFIC TLSC, the broad absorption width of CO_i8DFIC compensates for the lower absorption peak and QY, resulting in similar contributions from the NIR components but different aesthetic quality.

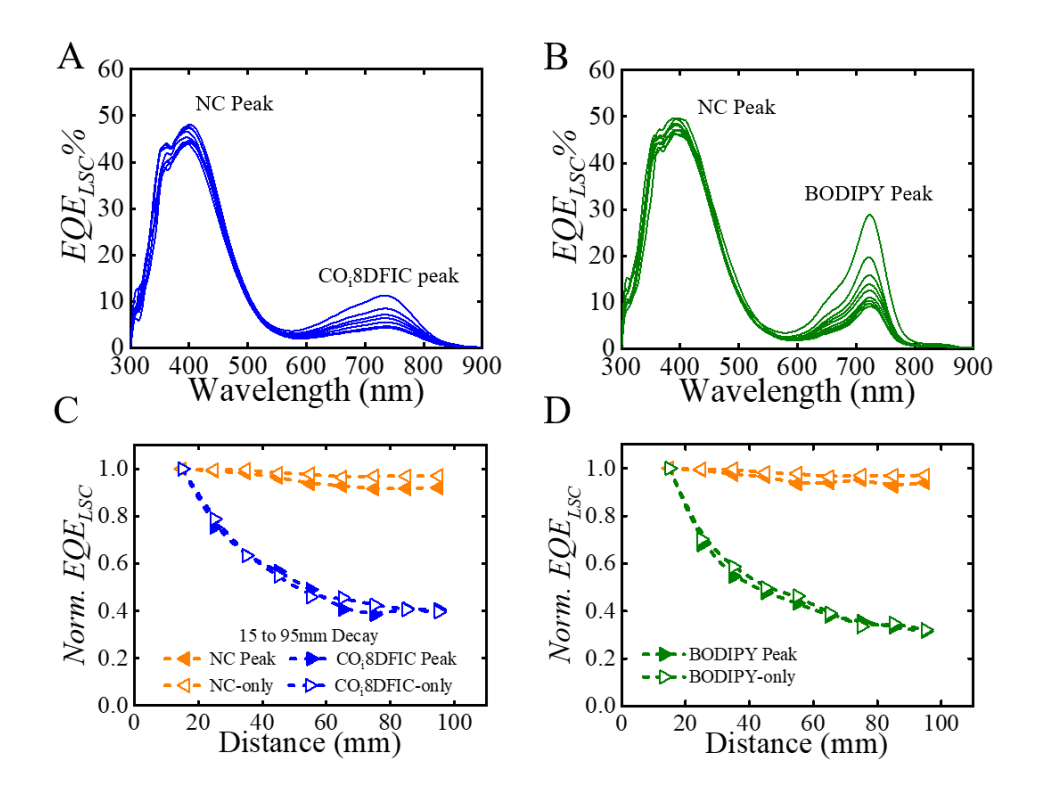


Figure 9.7 Position-dependent *EQELSC* spectra.

The series of absolute position-dependent EQE_{LSC} spectra of (A) NC+CO_i8DFIC and (B) NC+BODIPY TLSCs, where d increases from 15 mm to 95 mm, with 10 mm interval. The position-dependent EQE_{LSC} peak values of NC+CO_i8DFIC and NC+BODIPY TLSCs are extracted, normalized and plotted in (C) and (D), respectively. A NC-only, a CO_i8DFIC-only and a BODIPY-only TLSC are included as references.

Figure 9.7 (cont'd)

The UV and NIR peak decay behaviors of the dual-band TLSCs closely resemble those of the NC-only, CO_i8DFIC-only and BODIPY-only reference TLSCs, respectively, confirming the effective isolation of the two components by the air gap.

The series of position-dependent EQE_{LSC} spectra can be used to understand the scalability of LSC systems. The dual-band TLSC systems were fabricated with larger dimension (active area of $10.16 \times 10.16 \text{ cm}^2$), and the series of EQE_{LSC} at various d are plotted in **Figure 9.7**A and B for NC+CO_i8DFIC and NC+BODIPY TLSCs, respectively, where d is the distance between the incident excitation beam and the edge-mounted PV cell along the centerline of the square waveguide (the corresponding PV performance, geometric and flux gain (G) are tabulated in Table 9.1). Both UV and NIR peak values of each individual scan were extracted, normalized and plotted as a function of d in Figure 9.7C and D.

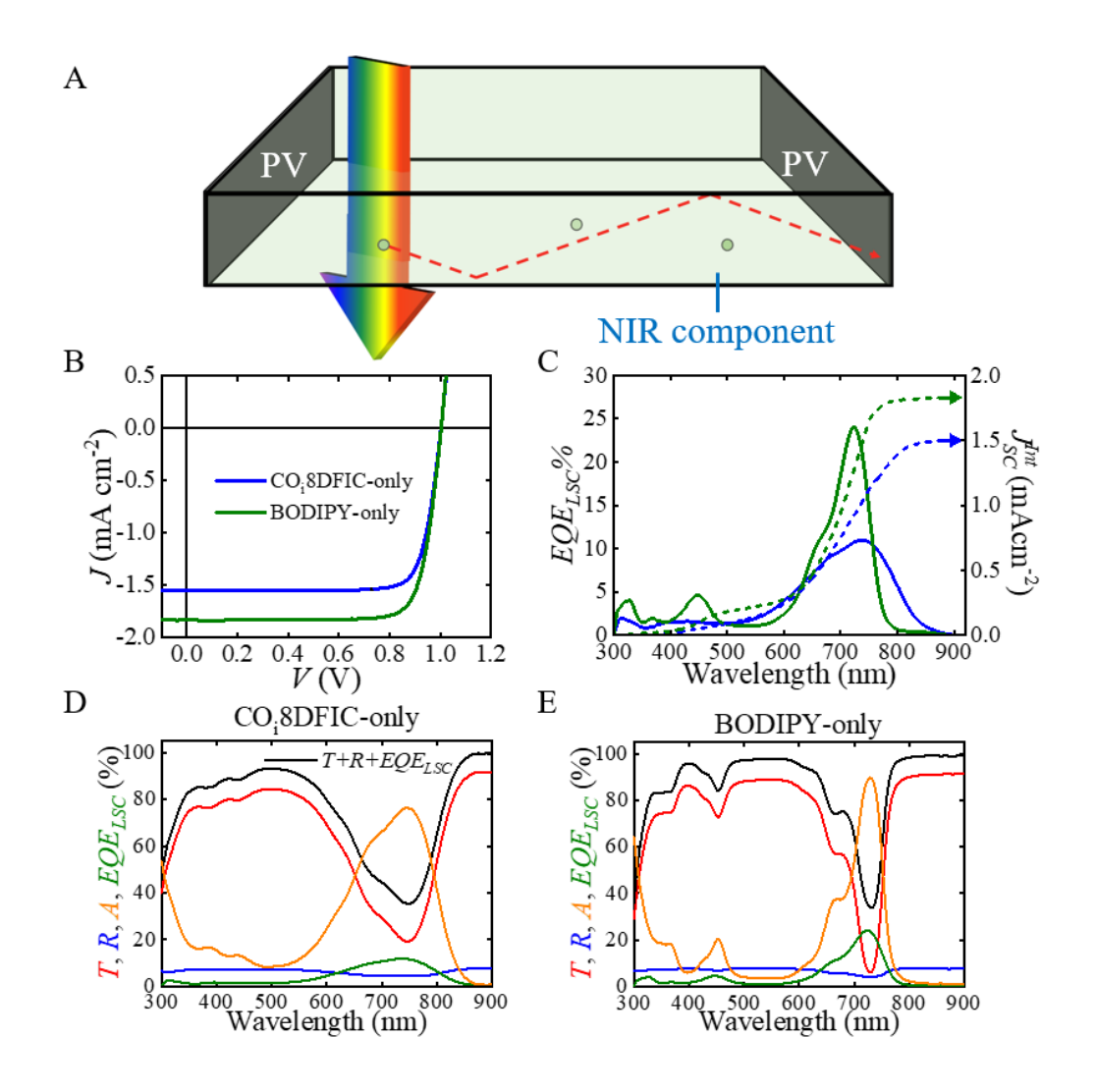


Figure 9.8 Single-pane NIR-only TLSCs.

(A) Schematic of NIR component only TLSC. (B) Current density versus voltage (J-V) characteristics of CO_i8DFIC-only and BODIPY-only TLSCs under AM 1.5G illumination. (C) Average external quantum efficiency ($EQE_{LSC}(\lambda)$) spectra of CO_i8DFIC-only and BODIPY-only TLSCs. The corresponding integrated short-circuit current density (J_{SC}^{Int}) match well with the J_{SC} extracted from J-V characteristics shown in (B). Photon balance check for (D) CO_i8DFIC-only and (E) BODIPY-only TLSCs.

The NC-only, CO_i8DFIC-only and BODIPY-only TLSCs were also fabricated as references. As shown in **Figure 9.8**B the CO_i8DFIC-only TLSC shows J_{SC} of 1.55±0.04 mAcm⁻², V_{OC} of 1.00±0.01 V and FF of 81±1%, resulting in a η_{LSC} of 1.26±0.03%. With significantly higher QY of BODIPY compared to CO_i8DFIC, the BODIPY-only TLSC shows improved J_{SC} of 1.84±0.03 mAcm⁻² with similar V_{OC} and FF, leading to a corresponding PCE of 1.48±0.03%. The

 J_{SC} values extracted from J-V characteristics are also confirmed by the J_{SC}^{Int} from the $EQE_{LSC}(\lambda)$ as shown in Figure 9.8C. The peaks of EQE_{LSC} match with the peaks of the absorption spectra of the corresponding organic luminophores, and the J_{SC}^{Int} values are 1.50 mAcm⁻² and 1.83 mAcm⁻² for CO_i8DFIC -only and BODIPY-only TLSCs, respectively, which are in good agreement of the J_{SC} values from the J-V curves. The photon balance for CO_i8DFIC -only and BODIPY-only TLSCs is consistent $(EQE_{LSC}(\lambda) + T(\lambda) + R(\lambda) \le 1)$ as shown in Figure 9.8D and E, respectively.

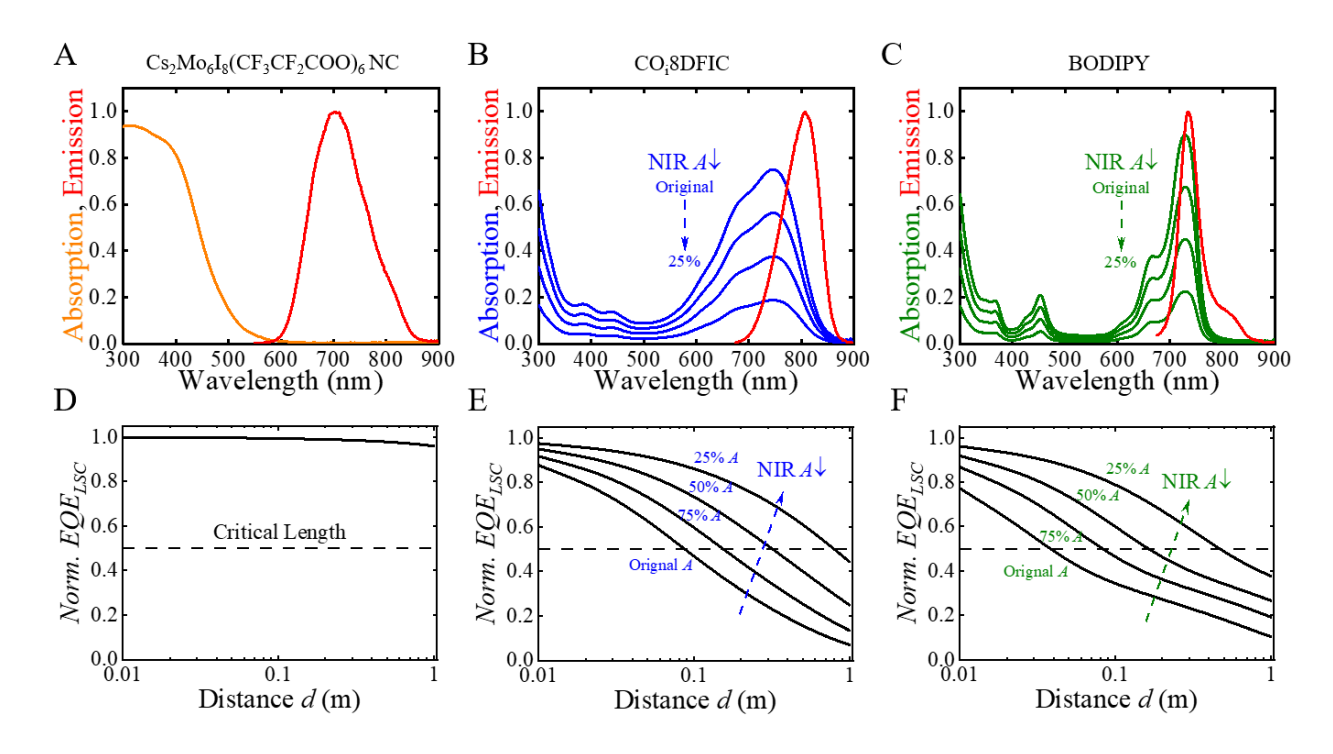


Figure 9.9 Optical simulation for TLSC scalability. Absolute absorption and normalized emission profiles of (A) NC in UV component TLSC, (B) CO_i8DFIC in NIR component TLSCs with various concentrations and (C) BODIPY in NIR component TLSCs with various concentrations, respectively. (D) to (F) the corresponding normalized EQE_{LSC} as a function of plate length for (A) to (C).

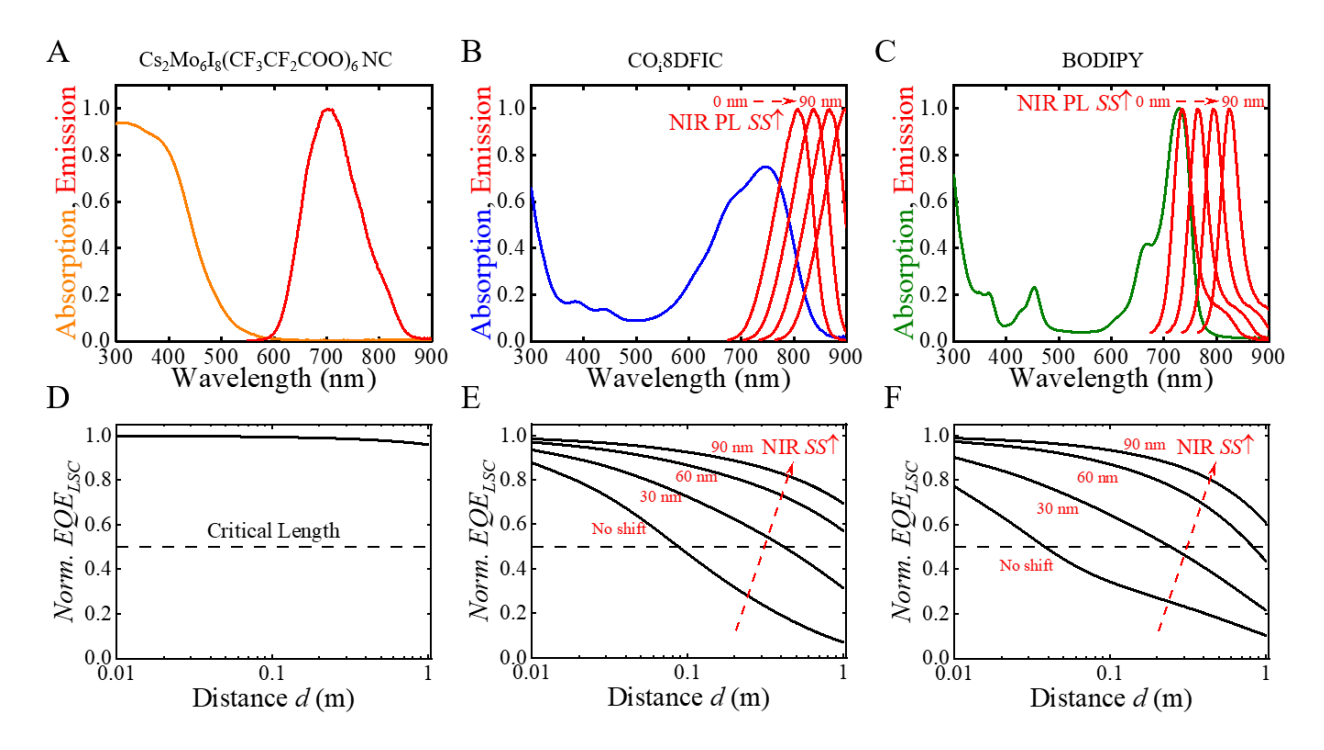


Figure 9.10 Optical simulation for TLSC scalability. Absolute absorption and normalized emission profiles of (A) NC in UV component TLSC, (B) CO_i8DFIC in NIR component TLSCs with various SSs (assuming no changes to absorption tail or emission width) and (C) BODIPY in NIR component TLSCs with various SSs, respectively. (D) to (F) the corresponding normalized EOE_{LSC} as a function of plate length for (A) to (C).

With the massive downshift of the NC, the reabsorption loss is so negligible that the *EQE_{LSC}* peak values in the UV of the NC-only, NC+CO_i8DFIC and NC+BODIPY TLSCs stay nearly constant as *d* increases. With the absorption and emission profiles of all the luminophores as input, Optical simulation is provided in **Figure 9.9** and **Figure 9.10**, the practical size for the UV component with NC is over 1 m, which is ready for practical deployment. The NIR contribution can be balanced by reducing the concentration (balancing absorption and reabsorption) or increasing Stokes shift (*S*, or spectral overlap). Due to significantly stronger overlap between the absorption and emission spectra for both CO_i8DFIC and BODIPY, the reabsorption loss leads to a more pronounced decay of the NIR peak values compared to the UV peaks. As shown in Figure 9.7C and D, the UV and NIR peak decay behaviors of the dual-band TLSCs strongly resemble those of the NC-only, CO_i8DFIC-only and BODIPY-only TLSCs, respectively. Given

the similarity in the decay trend in each range of the EQE_{LSC} spectra, the isolation of the waveguides effectively enables total internal reflection within each waveguide so that the UV and NIR components operate nearly independently.

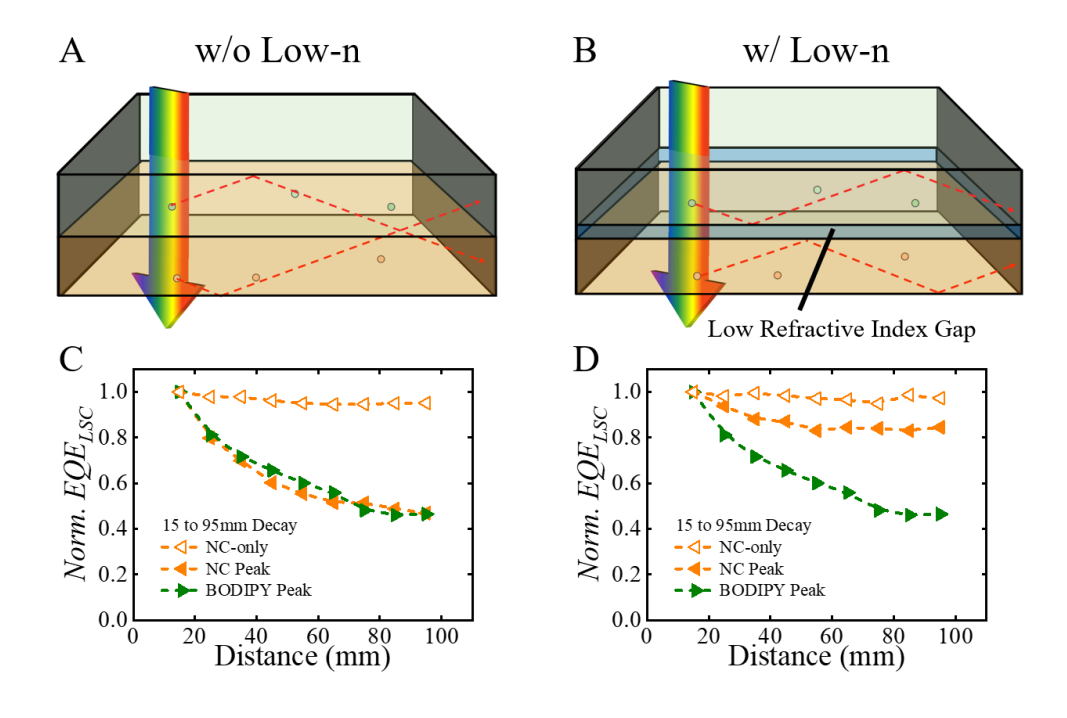


Figure 9.11 Impact of optical isolation on the performance of dual-band TLSCs. Schematics showing the dual-band TLSCs (A) without optical isolation and (B) with optical isolation realized by inserting a low refractive index (low-n, n = 1.30) polymer layer between two waveguides. (C) The extracted and normalized position-dependent EQE_{LSC} peak values of the TLSCs in (A) and (B) are shown in (C) and (D), respectively. The NC-only TLSC is also included as reference for comparison.

Notably, such optical isolation was also realized by seamlessly inserting a low refractive index layer (n = 1.30) between the two waveguides as shown in **Figure 9.11**, which can enhance the device structural stability for a greater range of applications.²⁰⁶ Improvements in scalability to the largest device sizes are likely achievable via Stokes shift engineering which has led to values over 100 nm for single-fluorescent emitters (see Figure 9.10 for detail), and more specifically, following chemical approaches that reduce overlap integrals. The UV and NIR components cannot operate independently without the low-n gap. As shown in **Figure 9.11**C, the photoluminescence

of the NC in the UV component is reabsorbed by the BODIPY in the NIR component due to the lack of optical isolation. As a result, the decay trend of the NC peak resembles that of the BODOPY peak. Once the low-n layer is inserted between these two waveguides, the optical isolation is reenabled, the number of the NC peak decay behavior recovers and resembles that of the NC-only TLSC as shown in Figure 9.11D.

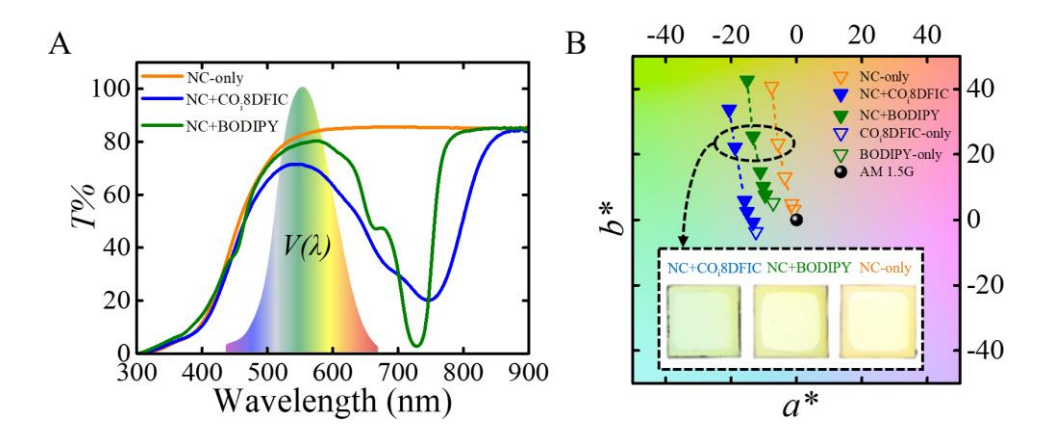


Figure 9.12 Aesthetic Quality of the Dual-band TLSCs.

(A) The transmittance spectra $(T(\lambda))$ of the NC-only, NC+CO_i8DFIC and NC+BODIPY TLSCs along with the normalized photopic response of the human eye $(V(\lambda))$ for comparison. (B) The (a^*, b^*) coordinates of NC-only group, NC+CO_i8DFIC group and NC+BODIPY group TLSCs in CIELAB color space. Within each group the NC concentration $(1, 2, 5, 10 \text{ and } 20 \text{ mgmL}^{-1})$ is the only variable. The (a^*, b^*) of CO_i8DFIC-only and BODIPY-only TLSCs are included as references. Inset: photographs of NC-only, NC+CO_i8DFIC and NC+BODIPY edge-encapsulated TLSCs with NC concentration at 10 mgmL⁻¹.

Aesthetic quality is equally important as photovoltaic performance for any TPV device, which determines whether a TPV device can be deployed in certain practical applications. 3,12,124,215 The transmittance spectra ($T(\lambda)$) of the NC-only, NC+CO_i8DFIC and NC+BODIPY TLSCs are plotted in **Figure 9.12**A along with the photopic response of the human eye ($V(\lambda)$) for comparison. NC shows an absorption cutoff edge at the UV/VIS border and BODIPY exhibits a NIR-band absorption onset at the VIS/NIR border. However, the broad NIR-band absorption of CO_i8DFIC extends into the red/NIR range, leading to lower visible transmittance with a slight blue tint. $T(\lambda)$ is used to quantify the main figures of merit for aesthetic quality: AVT, CRI and CIELAB color

space coordinates (*a**, *b**). All three parameters are prominently utilized metrics in the window industry to assess overall transparency and color quality of glazing systems. With good UV selectivity, the NC-only TLSC shows *AVT* of 81.9% and *CRI* of 91.3. For the dual-band TLSCs, the *AVT* and *CRI* of the NC+CO_i8DFIC TLSC drop to 65.6% and 82.9. With the better NIR selectivity of BODIPY, the *AVT* and *CRI* of the NC+BODIPY TLSC is improved to 75.8% and 88.3, respectively. Even more important are the color coordinates, which are discussed in the next section in detail.

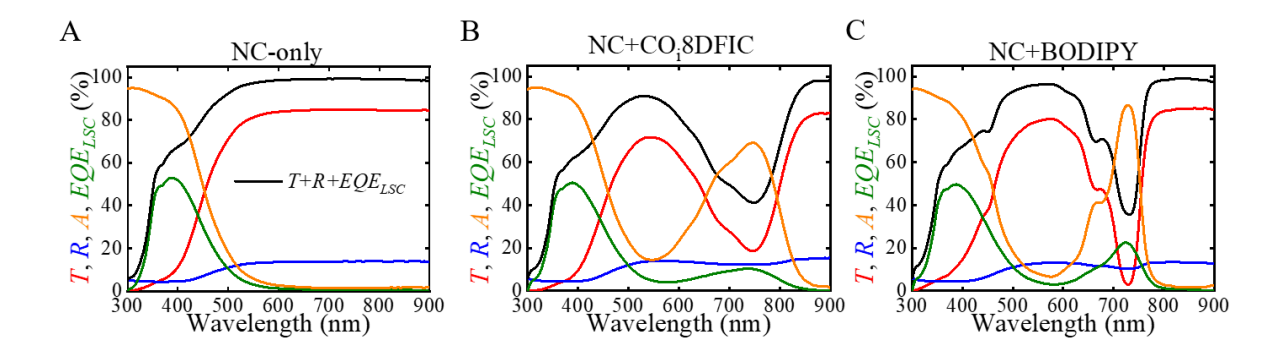


Figure 9.13 Photon balance check.(A) NC-only. (B) NC+CO_i8DFIC. (C) NC+BODIPY TLSCs.

The photon balance is a necessary consistency check to confirm the validity of independent measurements including $EQE_{LSC}(\lambda)$, $T(\lambda)$ and $R(\lambda)$ at every wavelength $(EQE_{LSC}(\lambda) + T(\lambda) + R(\lambda) \le 1)$. The photon balance for all the TLSC devices in this work is shown to be consistent in **Figure 9.13**.

9.4 Discussion

Because color coordinates of glazing systems are often utilized as a strict criteria for product viability in the window industry, the impact of NC concentration on aesthetic quality and

photovoltaic performance of the NC-only, NC+CO_i8DFIC and NC+BODIPY TLSCs is systematically studied for both performance and aesthetics. The CIELAB color space coordinates (a^*, b^*) are commonly utilized to assess acceptable ranges of color tinting for products in the glass and glazing industries (-15 $< a^* < 1$ and -15 $< b^* < 15$ for many mass market architectural glass products). As the "reference light source" for TPVs, the incident AM 1.5G is at the origin (0, 0) (as colorless or neutral), 3,12 and the (a^*, b^*) coordinates are plotted in Figure 9.12B as a function of NC concentration. These TLSCs are categorized into three groups: NC-only group, NC+CO_i8DFIC group and NC+BODIPY group, within each group NC concentration (1, 2, 5, 10 and 20 mgmL⁻¹) is the only variable. Additionally, the CO_i8DFIC-only and BODIPY-only TLSCs are included as references. As shown in Figure 9.12B, the incorporation of CO_i8DFIC or BODIPY leads to negative values of a^* due to the tail NIR absorption into red range. The b^* of NC-only, NC+CO_i8DFIC and NC+BODIPY TLSCs moderately increases as NC concentration increases from 1 to 5 mg mL⁻¹, while further increasing the concentration above 10 mg mL⁻¹ causes a dramatic drop in TLSC aesthetic quality and b^* values that are less acceptable to the window industry (b*>15).

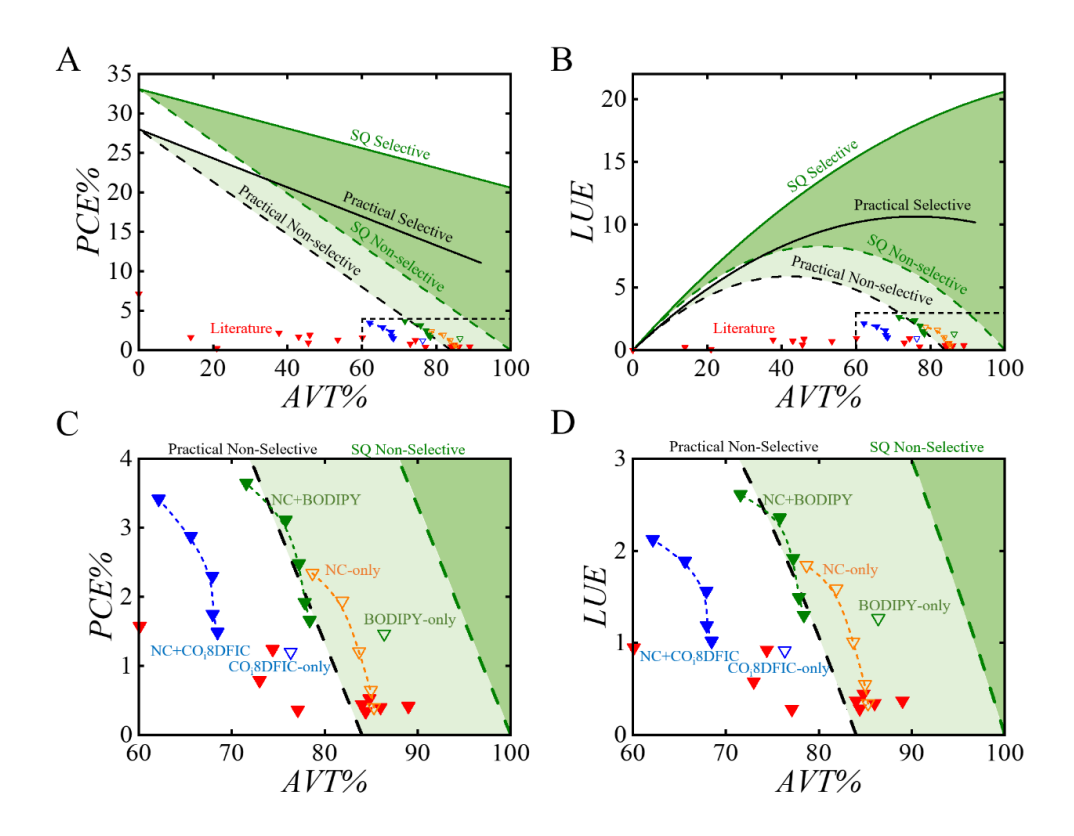


Figure 9.14 Comprehensive Analysis of Photovoltaic Performance and Aesthetic Quality. (A) Power conversion efficiency (PCE) versus average visible transmittance (AVT) and (B) Light utilization efficiency ($LUE = PCE \times AVT$) versus AVT for NC-only group, NC+CO_i8DFIC group,

utilization efficiency ($LUE = PCE \times AVT$) versus AVT for NC-only group, NC+CO_i8DFIC group, NC+BODIPY group, CO_i8DFIC-only and BODIPY-only TLSCs in full-scale. (C) Zoomed-in PCE vs. AVT plot and (D) zoomed-in LUE vs. AVT plot for all the TLSCs. Note: The olive dash line is the Shockley-Queisser (SQ) PCE (or LUE) limit for non-wavelength-selective TPV with partial visible transmittance; the black dashed line is the practical PCE (or LUE) limit for non-wavelength-selective TPV with partial visible transmittance. The dark shaded green region indicates the target PCE and AVT (or LUE and AVT) combination only achievable with the wavelength-selective approach (theoretical). The light shaded green region indicates the target PCE and PCE a

Visibly absorbing semiconductor materials can also be utilized as active layers in TPV applications. As introduced in Chapter 1, active layers with thin enough thickness or microsegmented structure permits the transmission of a portion of visible light, which creates partial visible transparency.^{2,53,111,131,139,216,217} However, there is a direct trade-off between photovoltaic performance and visible transmission in this approach. As shown in Figure 9.12B, any non-neutral

absorption profile within 435-675 nm range can result in sharp drops in AVT, CRI, and increased deviation of (a^*, b^*) from the CIELAB origin. Therefore, this type of device is sometimes referred to as "semitransparent" PV or non-wavelength-selective TPV. Although the theoretical Shockley-Queisser (SQ) limit for an opaque PV is 33.1%, the PCE of a non-wavelength-selective TPV approaches 0% as the AVT approaches 100% - in the practical limit these devices approach 0% at AVTs around 85-90% due to reflections of double-pane encapsulation.^{3,9,10} Similar to the discussion in Section 1.5, the SQ and practical PCE limit lines for non-wavelength-selective TPVs are shown in **Figure 9.14**A. For wavelength-selective TPVs or TLSCs which harvest only UV (< 435 nm) and NIR photons (> 675 nm), the corresponding SQ PCE limit is 20.6% with an AVT > 99%. The light shaded green regions reflect the practically achievable *PCE* and *AVT* combination with the wavelength-selective approach only, and the dark shaded green regions indicates the theoretically achievable *PCE* and *AVT* combination with the wavelength-selective approach only. The PCE values as a function of AVT (60-100% range) of all three groups of TLSCs (including CO_i8DFIC-only and BODIPY-only references) are plotted in Figure 9.14C. Among all these devices, BODOIPY-only, NC-only, and NC+BODIPY (with 5 and 10 mgL⁻¹ NC concentrations) TLSCs are all above the practical PCE limit line for non-wavelength-selective TPVs for the first time due to the good NIR selectivity and high QYs. As the NC concentration increases from 1 to 10 mgmL⁻¹, the *PCE* vs. AVT trend line of the NC-only group maintains a trend nearly parallel to the practical SQ PCE limit line until it starts to deviate above 10 mgmL⁻¹ due to tail absorption extending into the visible range. The NC+CO_i8DFIC group and NC+BODIPY groups also show a similar trend as NC concentration increases, and the incorporation of the NIR component significantly improves the PCE of the dual-band selective-harvesting TLSC system over 3% (up to 3.65% with 20 mgmL⁻¹ NC concentration) with modestly reduced AVT. In practical deployment the edge-mounted PV cells, encapsulation, and framing to stabilize the integrated TLSC-PV system can add manufacturing complexity and cost, which should not be overlooked. However, the benefit of eliminating device patterning, large area electrodes, and increasing defect tolerance should far outweigh these added steps, which will ultimately be automated similarly to manufacturing insulated glass units (IGU).

Light utilization efficiency provides a metric for systematically comparing TPVs with different levels of *AVT* values on the same scale. 3,12,124 *LUE* of all the TLSCs as a function of their corresponding *AVT* along with the SQ and practical *LUE* limit lines are plotted in Figure 9.14B and D. Although both the air gap and the tail of the NIR absorption into red range leads to a slightly reduced *AVT* level, the *LUE* still gains significant improvement stemming from the dual-band selective-harvesting. Literature reports are included as background in both *PCE* vs. *AVT* and *LUE* vs. *AVT* plots for comparison. The corresponding performance parameters are also tabulated in **Appendix B**.

Among all the TLSCs, the NC+BODIPY shows the best LUE of 2.61 at an AVT of 71.6%, the highest LUE value reported for a TLSC system by over a factor of $2.^{126}$ However, it is a balanced combination of PCE, AVT, and CRI or (a^*, b^*) that is important to consider when choosing optimal and deployable devices. As shown in Table 9.1 the NC+BODIPY with 5 mgmL⁻¹ NC concentration is expected to be the most suitable TLSC device for real-world deployment as b^* is < 15. We also note that the aesthetics of a TLSC depends on its $T(\lambda)$, $R(\lambda)$ and $PL(\lambda)$ spectra. $T(\lambda)$ determines the aesthetic quality observed from the transmitted side of the device as discussed above; whereas $R(\lambda)$ affects the aesthetic quality observed from the incident side, which can also be quantitatively evaluated using CRI and (a^*, b^*) based calculations. Since $T(\lambda) + R(\lambda) + A(\lambda) = 1$, where $A(\lambda)$ is the absorption spectrum of the TPV device, distinct UV and NIR wavelength-

selectivity with a neutral absorption profile in VIS can lead to good color rendering observed from both sides for a TPV device. However, due to the working principle of LSC devices, a portion of the photoluminescence (~26%) can escape from the top and bottom of the waveguide (via the escape cone), which can be observed as "glow" if the PL (or a portion of PL) resides in the VIS range. Such glow can also affect the aesthetics of a TLSC device and create an effectively colorful haze under illumination. In our case, we have designed all the emitters to effectively emit outside of the visible range. While there is a slight advantage in being able to recapture NIR emitted light from the escape cone of the top waveguide with the NIR absorber in the bottom waveguide, this effect is relatively small.

Looking ahead we consider strategies for further increasing the performance to approach the TPV and TLSC limit. The total photon flux at wavelengths < 435 nm is only ~4% of the AM 1.5G, 63,65,67,93 and the UV contribution can be potentially doubled with multi-exciton generation or singlet-fission. Harvesting light at wavelengths > 435 nm can rapidly cause a yellowish or brown tint (large positive b^* values), which are unacceptable for the majority of window applications. In contrast, the NIR range between 675 nm and the absorption cutoff of the edge-mounted PV cell (EQE_{PV} , e.g., ~1100 nm for Si and ~900 nm for GaAs, etc.) coincides with the peak of AM 1.5G photon flux, which has significantly more potential for power generation. Even with absorption extending into the red range, a resulting blue tint (negative a^* value) is more visually acceptable, which offers more design freedom for NIR selective-harvesting luminophores and can even help to compensate poor b^* values from yellow tinting. The QYs of various UV-absorbing luminophores including quantum-dots and nanoclusters have been gradually improved to more than 80% in recent years, and further improvement will likely be rather limited. 128,197,198,200,213,214,218,219 By comparison, the QY of NIR luminophores currently ranges from

20 to 40% (in this work). However, there is still promise via chemical design to improve the OY closer to 60-80%. Improving the QY of NIR luminophores can effectively lead to performance improvement without changing the optical properties. This is reflected in Figure 9.6B for the NC+BODIPY TLSC: although the NC peak is much stronger than the BODIPY peak (due to higher QY and less reabsorption loss of the NC), the contribution from the NIR component is comparable to that from the UV component (with 5.08 cm × 5.08 cm waveguide size, 2.4 mAcm ² from NC vs. 1.5 mAcm⁻² from BODIPY). Currently, the overlap between the absorption and emission spectra of the NIR-selective luminophores is relatively large, especially compared to that of the UV-selective luminophores. The main drawback is the reabsorption loss as the corresponding module size increases. However, there are scaling losses for all PV technologies as the module size increases, typically on the order of 20-40% (depending on the technology). At the size of $10.16 \text{ cm} \times 10.16 \text{ cm}$ (Table 9.1), the contribution from the NIR component is still significant (2.10 mAcm⁻² from NC vs. 1.22mAcm⁻² from BODIPY). For applications with larger size, the practical size for the UV component with NC is over 1 m, while the NIR components can still contribute significantly (50% of its original value) to a size of ~0.1 m and (30% of its original value) up to a size of ~0.3 m, which could still enable tiling in window facades. Thus, future improvements in TLSCs can result from: 1) the improvement of the QY of the NIR selectiveharvesting luminophores (allowing 2-3 times of enhancement in the NIR contribution without changing the aesthetics); 2) sharper wavelength-selectivity near the UV/VIS and VIS/NIR borders for higher visible transmittance and better color rendering; 3) separation of the absorption and emission spectra of the NIR luminophores to suppress the reabsorption loss (reduce the overlap integral), where we have demonstrated that the Stokes shifts can be increased to > 150 nm via decoupling the absorption/emission in small bandgap emitters. 162 Considering a dual-band TLSC

with QYs of >80% in both UV and NIR components and nearly ideal wavelength-selectivity, the overall PCE would be ~7% with AVT > 80% and CRI > 90. This PCE and AVT combination is well above the practical and theoretical SQ PCE, and LUE limit lines shown in Figure 9.14A and B, and would be suitable for deployment in many practical applications, particularly as the overlap integral is reduced further.

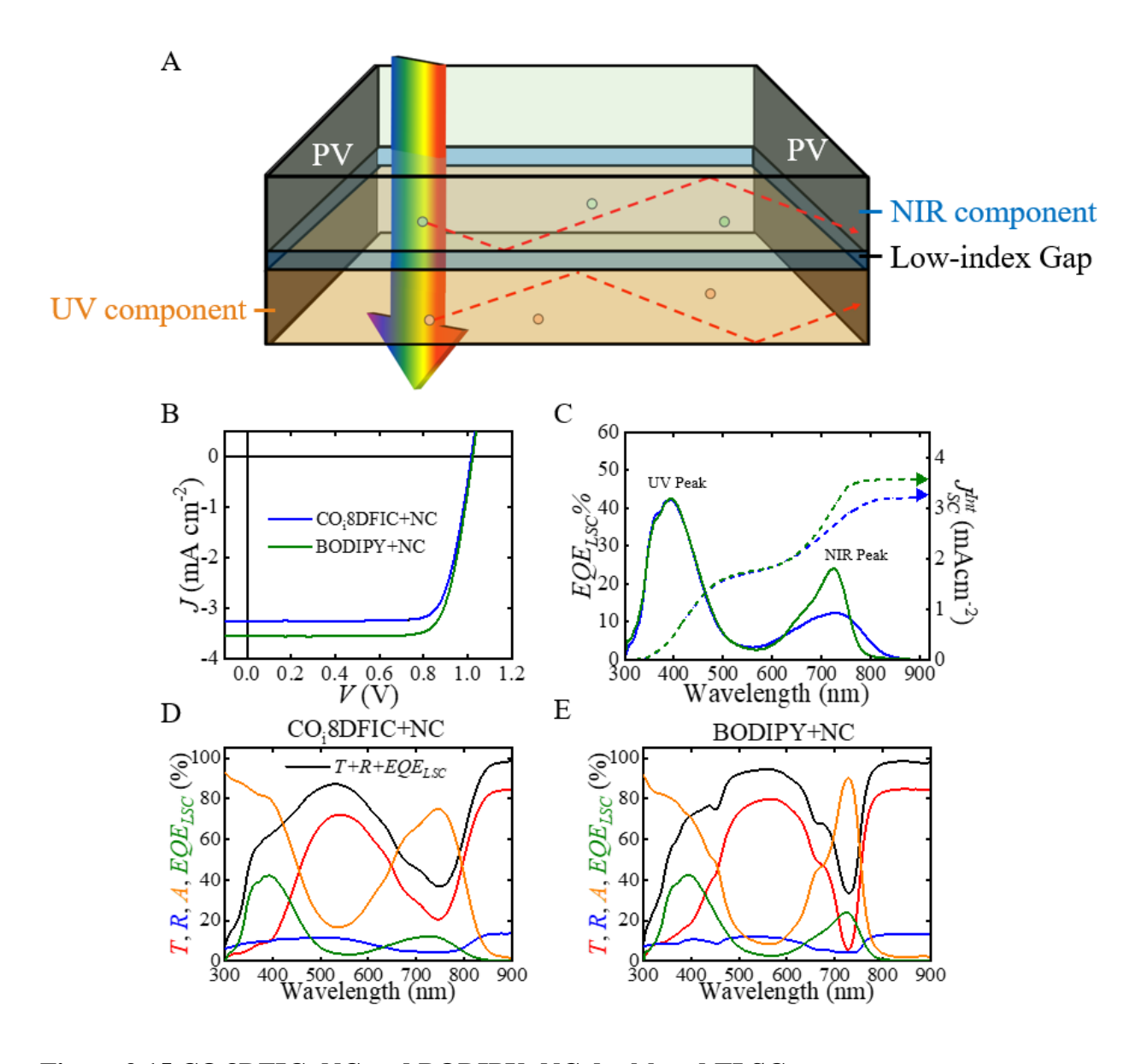


Figure 9.15 CO_i8DFIC+NC and BODIPY+NC dual-band TLSCs.(A) Schematic showing the dual-band TLSCs with NIR component as the top waveguide and UV component as the bottom waveguide. (B) *J-V* characteristics of CO_i8DFIC+NC and BODIPY+NC

Figure 9.15 (cont'd)

TLSCs under AM 1.5G illumination. (C) Average $EQE_{LSC}(\lambda)$ spectra of CO_i8DFIC+NC and BODIPY+NC TLSCs. The corresponding integrated short-circuit current density (J_{SC}^{Int}) match well with the J_{SC} extracted from J-V characteristics shown in (B). Photon balance check for (D) CO_i8DFIC+NC and (E) BODIPY+NC TLSCs.

Interestingly, since the absorption profiles of the UV and NIR components are spectrally separated from each other, switching the sequence of the incident light passing through (NIR component as the top waveguide and UV component as the bottom waveguide as shown in Figure **9.15**A) can still maintain good photovoltaic performance, which maintains the same aesthetic quality of the TLSC observed from the transmitted side. We note that in CO_i8DFIC+NC and BODIPY+NC TLSCs: CO_i8DFIC or BODIPY is used as the top waveguide luminophore and NC is used as the bottom waveguide luminophore, and all the luminophore concentrations are kept the same as the NC+CO_i8DFIC and NC+BODIPY TLSCs shown in Figure 9.6. In Figure 9.15B the CO_i8DFIC+NC TLSC shows J_{SC} of 3.26±0.03 mAcm⁻², V_{OC} of 1.01±0.01 V and FF of 79±1%, resulting in a η_{LSC} of 2.59±0.01%. With slightly higher J_{SC} of 3.55±0.06 mAcm⁻² and similar V_{OC} and FF values, the BODIPY+NC TLSC shows a η_{LSC} of 2.84±0.05%. Figure 9.15C shows the $EQE_{LSC}(\lambda)$ spectra of these two TLSCs, compared to Figure 9.6B the NC peaks decrease by ~10% due to more reflection loss of the UV photons, and the CO_i8DFIC and BODIPY peaks increase by ~10% resulting from less reflection loss of the NIR photons. Therefore, the contribution to the overall J_{SC}^{Int} from UV and NIR ranges becomes more balanced. The J_{SC}^{Int} values of the CO_i8DFIC+NC and BODIPY+NC TLSCs are 3.26 mAcm⁻² and 3.57 mAcm⁻², which are in great agreement of the J_{SC} values extracted from the corresponding J-V characteristics. The photon balance for CO_i8DFIC+NC and BODIPY+NC TLSCs is consistent as shown in Figure 9.15D and E, respectively.

Although the η_{LSC} s of CO_i8DFIC+NC and BODIPY+NC TLSCs are slightly lower than those of the NC+CO_i8DFIC and NC+BODIPY TLSCs shown in Figure 9.6A, moving forward, with improved spectral coverage, QY and distinct separation of the absorption and emission spectra of the NIR selective-harvesting luminophores, the advantage of placing NIR component as the top waveguide could become more impactful and lead to superior η_{LSC} with the same aesthetic quality. However, as we note below it is also important to consider the impact of panel arrangement on lifetime, as putting the NC panel first can prevent the UV from reaching the NIR panel and in some cases help to extend the lifetime.

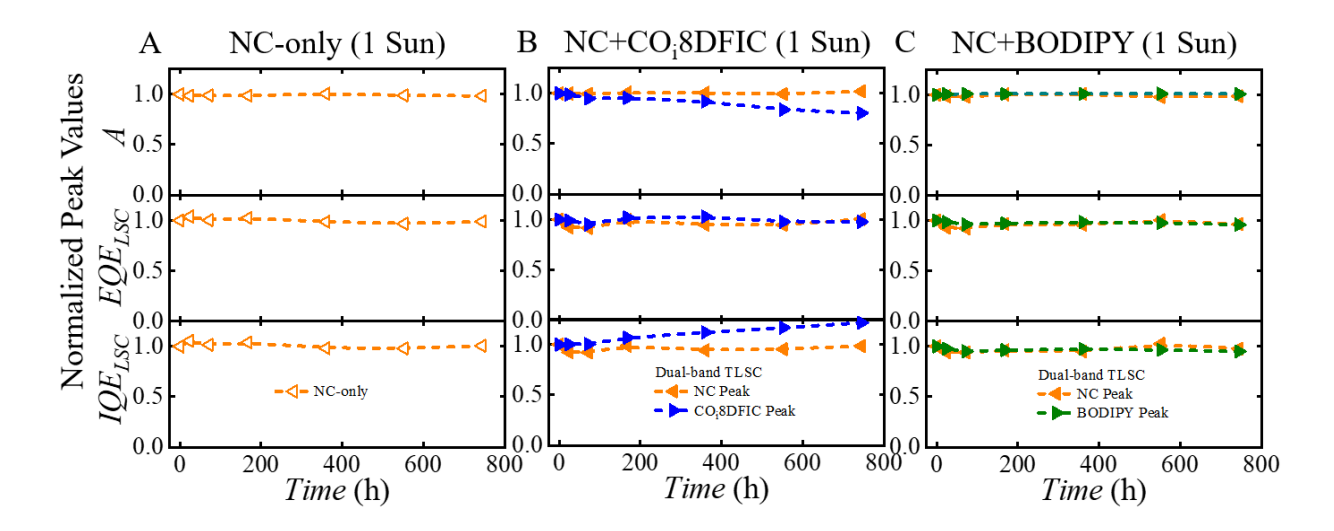


Figure 9.16 Photostability study of dual-band TLSCs. Normalized peak values of absorption spectra $(A(\lambda))$, $EQE_{LSC}(\lambda)$ and $IQE_{LSC}(\lambda)$ for (A) NC-only, (B) NC+CO_i8DFIC and (C) NC+BODIPY TLSCs as a function of time under constant illumination.

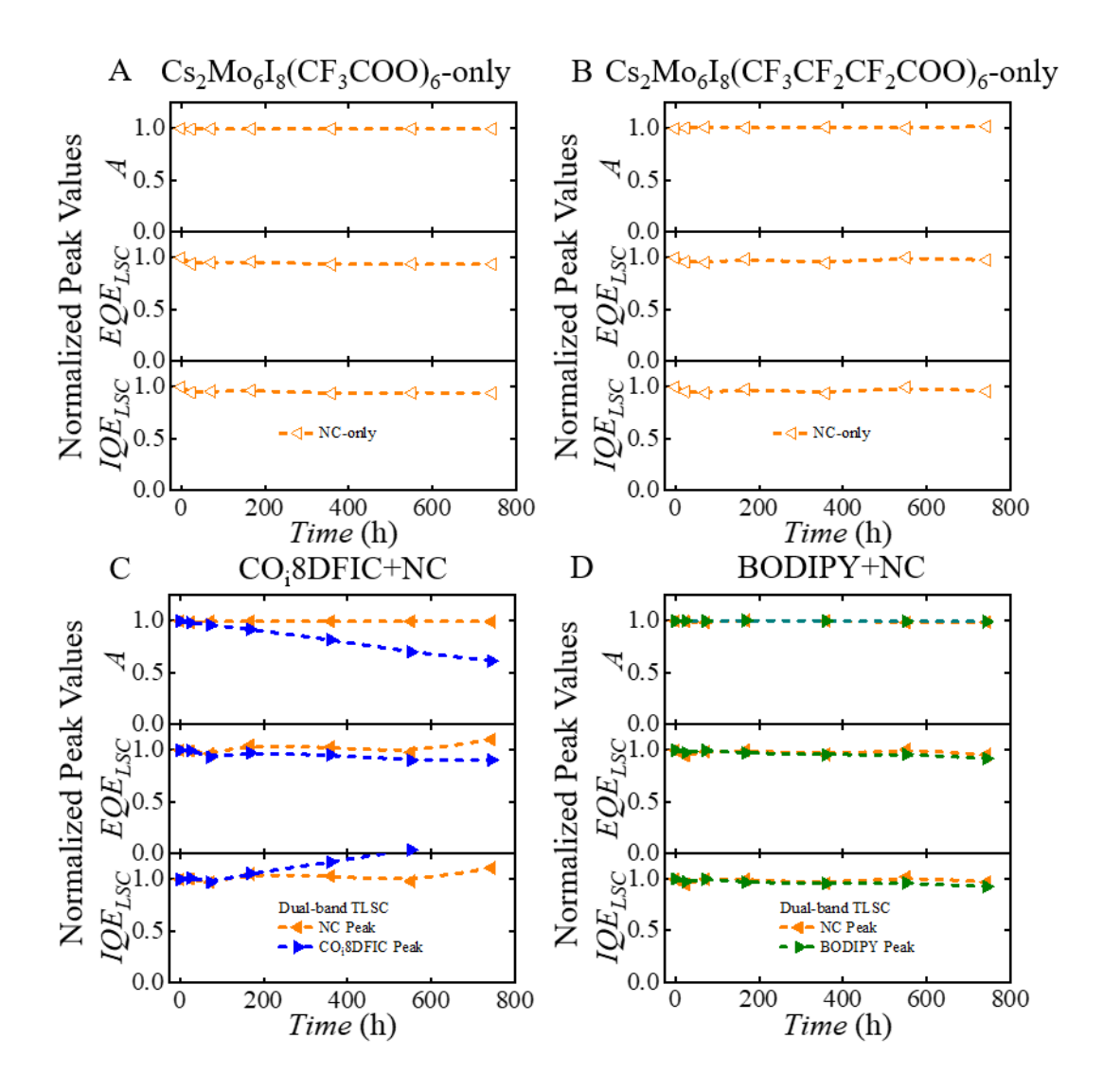


Figure 9.17 Photostability study of dual-band TLSCs. Normalized peak values of absorption spectra $(A(\lambda))$, $EQE_{LSC}(\lambda)$ and internal quantum yield $(IQE_{LSC}(\lambda))$ for (A) NC $(Cs_2Mo_6I_8(CF_3COO)_6)$ -only, (B) NC $(Cs_2Mo_6I_8(CF_3CF_2COO)_6)$ -only and (C) $Co_18DFIC+NC$ $(Cs_2Mo_6I_8(CF_3CF_2COO)_6)$ and BODIPY+NC $(Cs_2Mo_6I_8(CF_3CF_2COO)_6)$ TLSCs as a function of time under constant 1 Sun illumination.

Long lifetime performance is another key feature in real-world deployment. ^{141,185,210} The photostability of all the NC-only (with three different ligands), NC+CO_i8DFIC, CO_i8DFIC+NC, BODIPY+NC, NC+BODIPY TLSCs were studied and are shown in **Figure 9.16** and **Figure 9.17**. The lifetime of an LSC is directly a function of the absorption efficiency (bleaching) of the luminophore, quantum yield of the luminophore, and lifetime of the edge-mounted PV. Since we are utilizing edge-mounted PVs with lifetimes of greater than 20 years we track the absorption

profile and quantum efficiency of each luminophore combination. Three key parameters were chosen to evaluate the photostability of the TLSC devices, and these parameters were normalized by the corresponding initial values: $A(\lambda)$ spectrum is used to monitor the degradation of total light absorption for each luminophore; $EQE_{LSC}(\lambda)$ spectrum can be used to represent the degradation of the contribution of each luminophore to the overall photovoltaic performance; internal quantum efficiency $(IQE_{LSC}(\lambda) = EQE_{LSC}(\lambda)/A(\lambda))$ is the $EQE_{LSC}(\lambda)$ value normalized by the $A(\lambda)$ at each wavelength, is used to analyze the photoluminescence stability of each luminophore under constant illumination of 1 Sun.

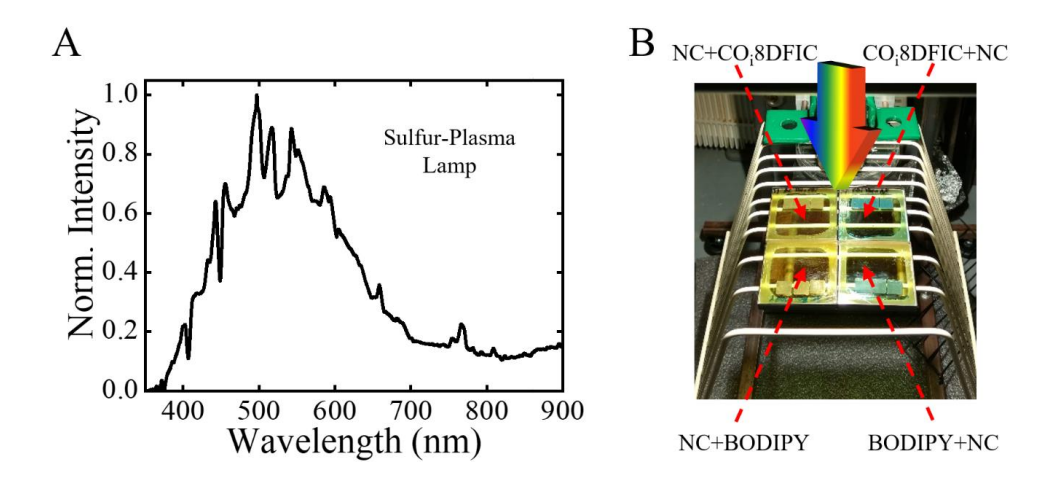


Figure 9.18 Photostability test setup.
(A) The sulfur-plasma lifetime testing lamp spectrum. (B) Photographs of four dual-band TLSCs under constant illumination in lifetime testing.

A sulfur-plasma lamp is used for lifetime testing. The light intensity of the lamp was calibrated to 1 Sun with NREL-calibrated Si reference cell, and the corresponding lamp spectrum measured by a calibrated Ocean Optics spectrometer (USB4000) is shown in **Figure 9.18**. All three parameters of all the NC-only (with various ligands) and the UV components of both dualband TLSCs remain nearly constant after 700 hours of constant illumination. In BODIPY+NC TLSC, the BODIPY peak also does not show any significant degradation. However, in

CO_i8DFIC+NC TLSC with the NIR component as the top waveguide, the CO_i8DFIC is not protected by the NC from the UV light, a more pronounced $A(\lambda)$ decay of the CO_i8DFIC is observed compared to that of the NC+CO_i8DFIC TLSC. Compared to $A(\lambda)$, the $EQE_{LSC}(\lambda)$ of the CO_i8DFIC peak shows a less pronounced decay trend due to less reabsorption loss, therefore, the corresponding $IQE_{LSC}(\lambda)$ even slightly increases at this time scale.

Figure 9.16 combined with Figure 9.17 provide some key information: 1) UV component - all the NCs with different ligands show excellent photostability with no sign of degradation after 744 hours of constant 1 Sun illumination; 2) NIR component - BODIPY shows superior photostability compared to CO_i8DFIC, with no sign of degradation after 744 hours of constant 1 Sun illumination, while CO_i8DFIC degrades to about 50% in the same timeframe; 3) Combined – using the UV component as the top waveguide can effectively alleviate the degradation of the CO_i8DFIC component underneath, notably, the $A(\lambda)$ peak degrades much slower in NC+CO_i8DIFC (UV component on top) than in CO_i8DFIC+NC (NIR component on top), which clearly suggests that NC in the top waveguide can function as a UV filter to protect the NIR organic molecules beneath from high energy photo-degradation. Interestingly, as photo-degradation proceeds, the $A(\lambda)$ peak of the CO_i8DFIC gradually decreases, which leads to less reabsorption loss due to less spectral overlap between the absorption and emission profiles (lower overlap integral), and subsequently results in a slight increase in the $IOE_{LSC}(\lambda)$. However, we note that such a trend should only be short lived as further reductions in $A(\lambda)$ will dominate the $EOE_{LSC}(\lambda)$ and saturate in the $IOE_{LSC}(\lambda)$ trends.

9.5 Summary

In conclusion, by combining highly emissive phosphorescent hexanuclear metal halide nanoclusters and organic luminophores as isolated UV and NIR selective-harvesting luminophores, we have designed and demonstrated dual-band selective-harvesting TLSC devices. Harvesting invisible photons from both UV and NIR portions of solar spectrum leads to $\eta_{LSC} > 3\%$, with good wavelength-selectivity that results in AVT > 75% and CRI of 90 (LUE > 2.5). This approach could lead to devices with efficiency approaching 10% as NIR QYs are further improved. This work demonstrates the potential of TLSCs to be deployed as power-generating sources in multiple applications with high photovoltaic performance, excellent aesthetic quality, and long-term photostability. With simple and low-cost manufacturing, this technology is able to offer a promising approach to utilize solar energy in entirely new ways.

Chapter 10 Future Outlook and Conclusions

In this chapter, we provide several promising proposals for the future development of transparent luminescent solar concentrators, with a focus to improve the photovoltaic stability, expand novel adoption opportunities, and facilitate the seamless integration. Based on the projects discussed in the prior chapters, a final summary of the findings of this thesis research will be given in the end.

10.1 Future Outlook

10.1.1 Mechanically Flexible TLSCs

Flexibility is another important and underexplored feature in practical TPV/TLSC deployment, especially when the modules are required to be integrated onto architectural surfaces with curvature. ²²⁰ In the previous chapters, drop-casting luminophore/polymer composite thin-films onto transparent waveguide is convenient for the purpose of research demonstration, however, it is more practical to imbed the luminophore directly into flexible transparent waveguides for fabrication, storage, transportation, and deployment. This motivation drives us to find a combination of luminophore/matrix by developing a processing method to fabricate LSCs with mechanical flexibility and visible transparency.

As a proof of concept, optically transparent thermoplastic (TPU) pellets were mixed and heated with cyanine dye (Cy7) and hot-pressed into sheets. Combined with flexible GaAs solar cells and flexible reflective film onto the edges of these dye/composite sheets, the whole TLSC system exhibits mechanical flexibility. As shown in **Figure 10.1**, photoluminescent properties and

optical transparency were measured. To determine the impact of bending on TLSC properties, key metrics including optical transmission and photovoltaic performance have been investigated as a function of the radius of curvature and number of bending cycles. This preliminary investigation suggests a promising route to produce flexible TLSC devices in large scale. In the next step, various UV and NIR selective-harvesting luminophores described in Chapter 7 to Chapter 9 will be incorporated to fabricate flexible TLSCs, and the fabrication process will be further optimized to simultaneously increase the scalability and reduce energy consumption.

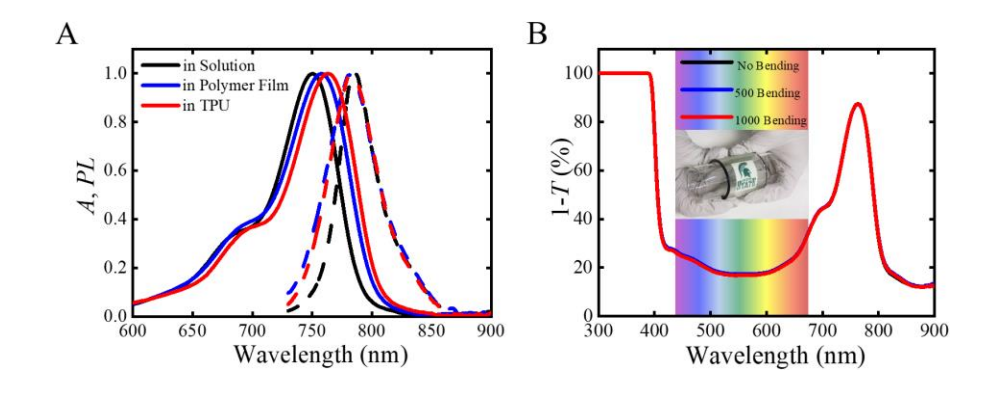


Figure 10.1 Mechanically flexible TLSC prototype.(A) Normalized absorption (solid lines) and emission (dashed lines) spectra of Cy7-CA in solution, polymer film and TPU. (B) The transmittance (1-*T*) spectra of Cy7/TPU composite sheets in bending test.

10.1.2 TLSCs Integrated with Micro-Segmented Opaque PVs

One of the most significant bottlenecks in LSC/TLSC design is the reabsorption loss. This loss is more significant for NIR selective-harvesting TLSCs due to more restrictive absorption and emission spectral overlap. Integrating micro-segmented opaque PV into TLSC can effectively alleviate the reabsorption loss. As shown in **Figure 10.2**A, with the integration of high-performance micro-segmented opaque PV (i.e., PV mesh) in TLSC waveguide, the distance for

the emitted and waveguided photoluminescence to reach a PV cell is substantially reduced. The spacings between the segmented PV mesh are determined by the reabsorption length of the emitters, which also creates various degrees of neutral visible transmittance. The coverage ratio of the mesh to the LSC waveguide area on the integrated module active area can be adjusted according to different efficiency and transparency requirement. Notably, the micro-segmented PV itself can also harvest incident solar irradiance and generate electric power, and demonstrations of the segmentation design have been shown in the PV community. This approach is a good example of the combination of wavelength-selective and non-wavelength-selective TPVs. However, a key challenge with this approach is developing micro-segmented PV arrays that are thin enough (~50 µm feature sizes) so that they are not discernable to the human eye and produce only minimal amounts of haze.

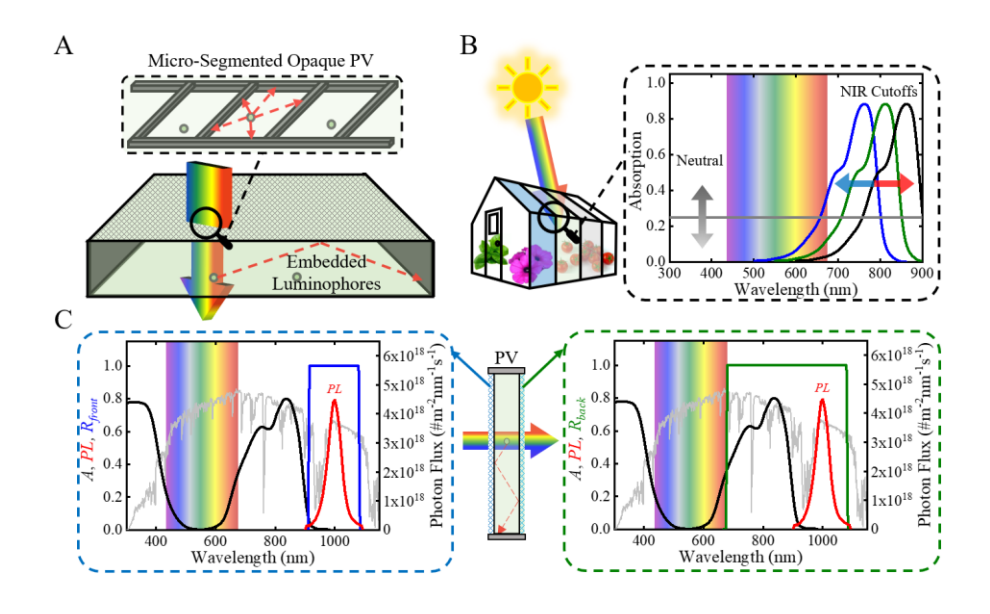


Figure 10.2 TLSCs with Micro-segmented PV, greenhouse application and photon management.

(A) Schematic showing the NIR selective-harvesting TLSC coupled with micro-segmented PV, this design can reduce the distance for the waveguided photoluminescence to reach a nearby PV, significantly alleviating the reabsorption loss. (B) Schematic showing NIR selective-harvesting TPVs for greenhouse deployment, absorption profiles with various NIR onsets and varying levels of neutral transmission are included in this study. (C) Schematic showing NIR selective-harvesting TLSC with ideal reflector configuration for enhanced waveguide trapping.

10.1.3 Research on TPVs for Greenhouse Deployment

There are over 390 billion ft² of total commercial greenhouses area worldwide. We envision that transparent photovoltaics can be seamlessly laminated onto existing greenhouses for facile retrofitting and replacement or new greenhouses being built. Motivated by power demand, energy autonomy, environmental concerns and economic development, widespread commercial deployment of TPV technologies would offer greenhouse owners the choice to retrofit, substantially improving the overall potential for incorporation. Ultimately, these technologies offer the potential to achieve compelling payback periods (< 5 years) and levelized energy costs near \$0.05 - 0.15 per kWh by piggybacking on the materials, framing, and maintenance of the greenhouse. Moreover, by selectively harvesting NIR range of the incident solar irradiance, TPV greenhouse roofs can dramatically reduce unwanted solar heating inside greenhouses from infrared flux and utilize this energy for electricity generation, moreover, give the potential of deploying over agricultural land.

There are key differences between the photopic response of the human eye and photosynthesis of the plant. It is not entirely clear at what wavelength the NIR harvesting for electricity generation is allowed without significantly impacting the plant growth underneath, yield, and flowering. In this early-stage project as outlined in Figure 10.2B, we chose NIR selective-harvesting luminophores with various NIR absorption onsets and encapsulated them into glass sheets as greenhouse roofs. Additionally, varying levels of neutral transmission profiles are also included as a parameter in this investigation. Several archetypal plant species in commercial greenhouses including petunia, basil, and mini tomato are grown under these sheet samples. After the completion of the growth process, research results can be analyzed to generate transparent PV design guidelines (absorption cutoff, total average transparency), which will enable solar

generating greenhouses to simultaneously maximize electric power generation and plant production.

10.1.4 Trapping Efficiency Enhancement with Photon Management

For LSCs/TLSCs with simple waveguides and isotropic emitters, the light trapping efficiency is limited to ~74.5%. This can be improved to ~100% with fine-tuned complex optical designs. As shown in Figure 10.2C, distributed Bragg reflectors (DBR) with different reflection spectral ranges can be coated on the front and back surfaces of the LSC waveguide. 4.21,151,153,154 The front surface coating allows the transmission of the NIR photons to enter the waveguide but reflects the escaped photoluminescence back into the waveguide where the back surface coating reflects all the PL NIR photons back into the waveguide. Therefore, emitted photons can be trapped (nearly perfectly) within the waveguide, and the luminophore concentration can be reduced due to the double-pass effect. Such design can simultaneously enhance the photovoltaic performance and device scalability. Moreover, these coatings are similar to low-E coatings, which isolates the indoor environment from the excess heat outside in summer and keeps the heat indoor in winter. However, designing and implanting such optical trapping coatings will require careful consideration of cost, and oblique angle aesthetic impact.

10.1.5 Performance Enhancement via Spectral Conversion Approaches

As shown in the prior chapters, the photoluminescence quantum yield of NIR selectiveharvesting luminophores is another limiting factor in TLSC design. Currently, our best *QY* values are in the range of 20-40%, and novel molecular structure designs are expected to gradually improve the QYs with decoupled absorption and emission spectra (i.e., minimized spectral overlap), e.g., from Cy7 to COi8DFIC to BODIPY as shown in this work. There is another promising approach to improve the QYs of NIR emitters: as shown in Chapter 9, the NC exhibit near-unity QY with UV selective-harvesting. Docking NIR molecular organic dyes onto inorganic phosphorescent emitters with high QY could effectively resolve this problem: as shown in **Figure 10.3**A, the NIR organic dyes function as absorber (or donor) and transfer the harvested NIR photon energy to the inorganic emitter (or acceptor), and then then the energy is re-emitted via phosphorescence with high QY. This spectral conversion not only can improve the utilization of NIR photons, but it can also potentially suppress the reabsorption loss between absorption and emission spectra.

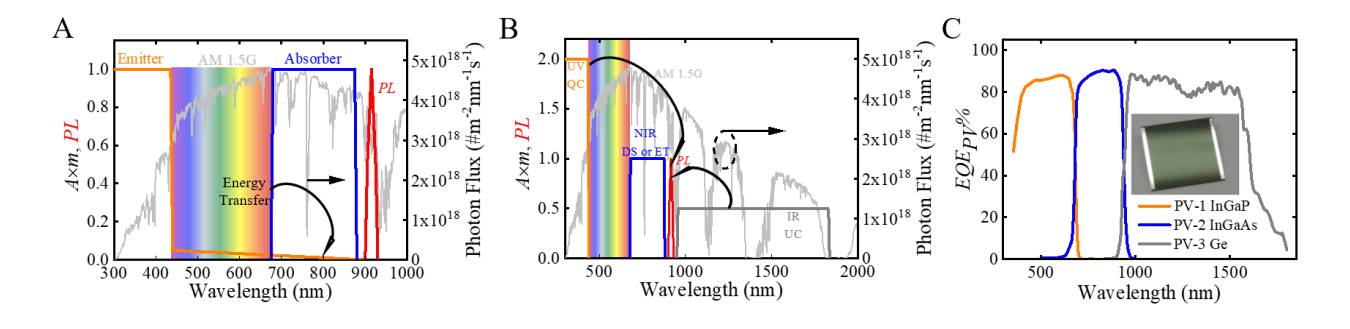


Figure 10.3 TLSCs performance enhancement via spectral conversion approaches.

(A) Ideal absorption and emission profiles of the absorber and emitter species in energy transfer approach. (B) Combination of various spectral conversion photoluminescence mechanisms (downshifting, up-conversion and quantum-cutting) in one TLSC device. (C) *EQE_{PV}* spectrum of a tandem InGaP/InGaAs/Ge triple-junction PV, which can be potentially utilized as the edgemounted PV for TLSCs in the future.

Moreover, the combination of various spectral conversion mechanisms could potentially lead to superior photovoltaic performance. As shown in Figure 10.3B, UV photons can be quantum-cut, NIR photons can be down-converted (or via energy transfer), and deeper IR photons can be up-converted, all the emission of these spectral conversion mechanisms can be adjusted in

NIR range with an optimized bandgap. In this scenario, one UV photon can contribute two NIR photons, and IR photons below the emitter (edge-mounted PV) bandgap can also contribute to photovoltaic process, the resulting efficiency can exceed the Shockley-Queisser limit.⁵⁹

In addition to spectral conversion of the luminophores with multi-band absorption profiles, tandem (multi-junction) PV with extended spectra response and ultra-high efficiency can be edge-mounted to LSCs. The EQE_{PV} spectrum of a typical example of tandem InGaP/InGaAs/Ge triple-junction PV is shown in Figure 10.3C, the spectral response extends to over 1800 nm. However, it is particularly difficult to current-match all the PV sub-cells with various monochromatic emission. One solution to circumvent this problem is to use inverter to connect all the sub-cells of the edge-mounted PV, the output direct-circuit (DC) current from each sub-cell will first be converted alternating-current (AC) current, and then connected in parallel to supply the external loads, which allows more freedom in luminophore selection and design.

10.1.6 Photodynamic Therapy for On-site Cancer Curing

Many of the luminescent materials we have developed in this thesis could find additional applications in imaging and photodynamic therapy of various diseases, including cancer. According to Centers for Disease Control and Prevention (CDC), for every 100,000 people in the United States, 438 new cancer cases were reported and 153 of them died of cancer in 2017. Cancer is now the second cause of death in the United States, exceeded only by heart disease. Currently, approximately 38.4% of men and women will be diagnosed with cancer at some point during their lifetimes. Therefore, cancer impacts people of all races, ethnicities, and sexes. The burden of

cancer also shows economic impact on the U.S. society, according to National Cancer Institute, the estimated national expenditures for cancer care in 2017 were \$147.3 billion.

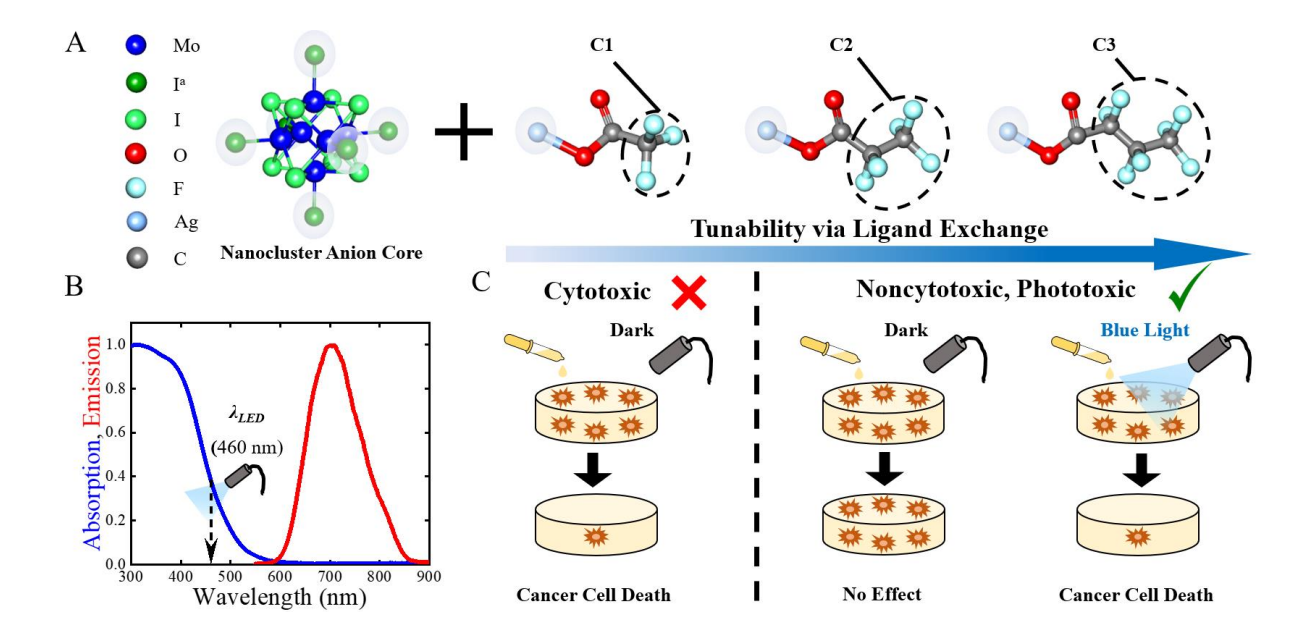


Figure 10.4 Photodynamic therapy for on-site cancer curing.

(A) Ball-and-stick schematics of nanocluster (NC) core (Mo₆I₈I^a₆²-) and three ligand structures (C1: CF₃COO-Ag, C2: CF₃CF₂COO-Ag, and C3: CF₃CF₂CF₂COO-Ag) involved in this study. Note: I^a represents six apical iodine of the NC core, which can react with the Ag of the ligand molecules to form different NCs (blue shaded area). (B) Absorption and emission spectra of the NCs. (C) Schematic showing cytotoxicity versus phototoxicity. The tunability between cytotoxicity and phototoxicity is enabled via ligand exchange.

Traditional cancer treatments include surgical intervention, radiation therapy, chemotherapy, immunotherapy, however, serious side effects can be caused when these treatments start to affect healthy tissues or organs. In contrast, photodynamic cancer therapy (PDT) is a minimally invasive alternative to these traditional cancer treatments. ^{223,224} The illumination of light at specific wavelength can trigger the phototoxicity of the sensitizer absorbed by the target cancer cells. The photoluminescent property of photoactive materials offers great potential as both diagnostic and therapeutic agents for PDTs. Moreover, photoactive materials can also be utilized as contrast agents for tumor imaging, and the combination of therapy and diagnostics is commonly referred as "Theranostics".

In preliminary studies shown in Figure 10.4 (in collaboration with Dr. Sophia Lunt's laboratory from the Department of Biochemistry and Molecular Biology at MSU) metal halide nanoclusters are applied for the first time in photodynamic therapy for on-site cancer treatment. We find that the toxicity for cancer cells can be surprisingly tuned from cytotoxicity to phototoxicity via ligand exchange on NC core. Heating CsI and MoI₂ at 750 °C to form Cs₂Mo₆I₁₄ first, then six apical position iodine react with silver trifluoroacetate (CF₃COOAg), silver pentafluoropropionate (CF₃CF₂COOAg) or silver heptafluorobutyrate (CF₃CF₂CF₂COOAg) in solution, forming Cs₂Mo₆I8(CF₃COO)₆, Cs₂Mo₆I₈(CF₃CF₂COO)₆ and Cs₂Mo₆I₈(CF₃CF₂CGOO)₆ nanoclusters (NC). 44,205 All the NCs absorb light in blue range (400-500 nm) and emit phosphorescent light in the near-infrared (NIR: 600-900 nm) with high photoluminescent quantum yield (~55-60% in acetonitrile solution). With blue light illumination, these NCs can be used to treat various cancer cell lines, showing a promising strategy for next generation photodynamic therapy. Based on the preliminary data collected in this study, utilization of photoactive materials as light-activated theranostics offer promising opportunities for disease diagnostic, imaging-guided surgery, and site-specific personalized therapy.

10.2 Final Conclusions

Visibly transparent photovoltaic technologies can be readily integrated onto our built environment to effectively convert the passive surfaces into power generating sources without compromising the current aesthetics or functionalities. Transparent luminescent solar concentrators as a key transparent solar technology feature the highest visible transparency, structural simplicity, superior scalability, and affordability. In this thesis research, following the

theoretical calculation as a roadmap, we synthesize a series of organic/inorganic excitonic photoactive materials and incorporate them into the development of TLSC devices as UV and NIR selective-harvesting luminophores, the device efficiency has been gradually improved with excellent aesthetic quality suitable for glazing systems and other deployments. Moreover, we also established standard characterization protocols for transparent photovoltaics, which will ultimately help the TPV research advance in a sustainable, reliable, and repeatable way. Collectively, all these efforts can substantially push the widespread solar adoption towards broader commercial reality.

APPENDICES

APPENDIX A Checklist for Luminescent Solar Concentrator Manuscripts

Please supply a response to each item of the checklist alongside the submitted article. 225

LSC Data Collection and Report	Description
1. Have the current density-voltage (J-V)	
characteristics been provided to calculate the	
power conversion efficiency (PCE) of the	
luminescent solar concentrator-photovoltaic (LSC-	
PV) systems? The type of the side-mounted PV	
(i.e., Si, GaAs, CIGS, perovskite or dye-sensitized	
solar cells) should be clearly addressed, and the	
corresponding PV performance parameters and	
spectral response (EQE_{PV}) of the side-mounted PV	
cells should also be reported. Does the edge-	
mounted PV show any clear hysteresis in the	
corresponding J-V characteristic? If so, stabilized	
PCE near the maximum power point (MPP) should	
be provided, along with the corresponding $J-V$	
curves, identifying scan speed and direction. The <i>J</i> -	
V characteristics of an LSC-PV system devoid of	
emitters (i.e., a blank) under the same testing	
condition should also be provided.	

- 2. Is the area of the lightguide front surface (A_{LSC}) used for the photocurrent density and PCE calculations? Please provide the dimensions (length, width, and thickness) of the lightguide and the edge-mounted PV cell. Based on these, the geometric gain ($G = A_{LSC}/A_{Edge}$, where A_{Edge} is the entire edge area, not only the area mounted with PV cells) should also be provided for reference. Using a square-shaped LSC lightguide with length of at least 5 cm or larger is highly recommended.
- 3. For *J-V* measurements, please address the number of lightguide edges mounted with PV cells. Are the unmounted edges taped/painted black or covered with reflectors to block the incident illumination during *J-V* measurements? Any blackened edges should be roughened or applied with index matching gel to the blackened surface to avoid reflections. If reflectors are mounted onto the rest of the edges, no multiplication correction factor should be applied for the *J-V* characteristics. Please indicate whether and which type of index matching material was utilized between the lightguide and the PV cells.

4. For <i>J-V</i> measurements, has an opaque mask or	
aperture with well-defined area been placed	
directly and closely in front of the LSC lightguide	
to minimize the impact from any direct incident	
light on the edge-mounted PV? Has a matte black	
backdrop been placed behind the tested LSC	
lightguide to avoid double-pass of light as a	
baseline measurement?	
5. Has position-dependent or average external	
quantum efficiency ($EQE_{LSC}(\lambda)$) data for the LSC-	
PV system been provided? Has any geometric	
correction factor been applied to correct the	
measured EQE_{LSC} profile? Does the photocurrent	
density integrated from the average EQE_{LSC} (J_{SC}^{Int})	
match the short-circuit current density extracted	
from the corresponding J - V characteristic (J _{SC})?	
The current density discrepancy should not exceed	
20%.	
6. Please state the light source and the reference	
cell used for the J - V characteristic. We recommend	
providing the intensity and the spectrum of the test	
light source (AM 1.5G, 1000 W/m ² at 25 °C are	
highly recommended). Inclusion of the	

illumination beam homogeneity over the testing	
area is also encouraged. Based on the spectrum of	
the test light source and the average $EQE_{LSC}(\lambda)$ of	
the LSC-PV system, what is the calculated spectral	
mismatch factor (MF)?	
7. Please provide the absolute absorptance	
spectrum of the entire device (e.g., $A(\lambda) = 1 - T(\lambda)$	
- $R(\lambda)$, where $T(\lambda)$ and $R(\lambda)$ are the transmittance	
and reflectance spectra of the entire device,	
respectively), normalized emission spectrum, and	
the photoluminescence quantum yield (PLQY) for	
the luminophores in the lightguide matrix at the	
selected concentration. Does the $EQE_{LSC}(\lambda)$ peak	
wavelength match the absorption peak	
wavelength? Is the peak value of the absolute	
EQE_{LSC} limited by the corresponding $PLQY$ (i.e.,	
$EQE_{LSC} < PLQY$)?	
8. Please provide a photon balance check: $T(\lambda)$ +	
$R(\lambda) + EQE_{LSC}(\lambda)/m < 1$, where m accounts for	
down-converting, multi-exciton generation, up-	
conversion, quantum cutting, or singlet fission	
cases for the LSC-PV system, and $EQE_{LSC}(\lambda)$ is the	
maximum position-dependent EQE_{LSC} . If a double-	
	i e e e e e e e e e e e e e e e e e e e

beam spectrometer is used to measure the	
transmittance spectrum, please confirm that no	
blank sample is placed on the reference side.	
9. How many LSC-PV devices have been	
fabricated and tested for the statistical analysis of	
the photovoltaic performance? Has a stability	
analysis been performed? If so, please address the	
test conditions used for this characterization in	
detail (for example, light source type and intensity,	
temperature and humidity, contained in inert gas or	
exposed to ambient air environment, indoors vs.	
outdoors, under open-circuit, short-circuit, MPP,	
or stabilized MPP conditions). Data from at least a	
second measurement 24 h after the initial test is	
recommended in the same identical conditions,	
clearly specifying the storing conditions.	
10. Is transparency an attribute of the LSC-PV	
system? If so, please provide the average visible	
transmittance (AVT) calculated from the	
corresponding transmittance $(T(\lambda))$ of the entire	
device. If a double-beam spectrometer is used to	
measure the transmittance spectrum, please	
confirm that no blank sample is placed on the	

reference side. Is aesthetic quality from either side
an attribute of the LSC-PV system? If so, please
provide color rendering index (CRI) or CIELAB
coordinates (a^* , b^*) calculated from the
appropriate transmittance and/or reflectance
spectrum of the entire device.

APPENDIX B An Overview of Literature Reports for LSC/TLSC Devices

Table A.1 State-of-the-art LSC/TLSC work for reference

References	Luminophore(s)	QY%	Size (cm ²)	G	AVT%	CRI	PCE%	EQE_{LSC}	LUE
This Work	$Cs_2Mo_6I_8(CF_3CF_2COO)_6$ NCs BODIPY	80±5 40±3	5.08×5.08	2	75.8	88.3	3.11	Yes	2.36
7	$(TBA)_2Mo_6Cl_{14}\ NCs$	50-55	2.5×2.5	6.25	84.0	94.0	0.44	Yes	0.37
8	Cy7-NHS	20±1	2.0×2.0	5	86.0	94.0	0.40	Yes	0.34
78	Cy7-NEt ₂ -I	26±1	5.08×5.08	2	77.1	75.6	0.36	Yes	0.28
188	CO _i 8DFIC	25±3	5.08×5.08	2	74.4	80.0	1.24	Yes	0.92
189	$CdSe/Cd_{1-x}Zn_xS$	~70	20.32×20.32	31	84.8	91.0	0.525 ^d	N/A	0.45
226	Si QDs	46±5	12×12	11.54	73.0 ^a	84.1	0.79 ^d	N/A	0.58
56	CdSe/CdS	45	21.5×1.35	1.23	84.9ª	89.2	N/A ^e	N/A	N/A
190	SINc:t-U(5000)	16 (UV) 8 (NIR)	7.6×2.6	9.69	89.0ª	97.7	0.414 ^d	Yes	0.37
126	CuInS ₂ /ZnS	66	10×10	17.85	37.7ª	76.9	2.18^{f}	Yes	0.82
196	$Mn:Cd_xZn_{1-x}S/ZnS$ (Top)	78±2	15.24×15.24	23.23	88.8 ^b	95.5	1.3 ^g	N/A	N/A
1,70	CuInSe ₂ /ZnS (Bottom)	65-75		23.23	8.5 ^b	0.42	1.8 ^g	N/A	N/A
227	CuInSe _x S _{2-x} /ZnS	40±4	12×12	10	45.6	77.1	0.93 ^d	N/A	0.412
228	CuInS ₂ /CdS NCs	~45	7.5×7.5	6.7	60.1ª	82.2	1.57 ^d	N/A	0.95
94	PbS/CdS	40-50	2.0×1.5	2.14	43.0ª	65.6	1.68 ^d	N/A	0.72
229	bPDI-3 LR 305	97.7	20×20	50	46.0ª	57.0	1.90 ^d	N/A	0.87
230	LR 305 LO 240	~95	3.5×10	1.30	21.0ª	19.0	0.23	N/A	0.05
215	BODIPY Derivatives	64±1	10×10	6.25	14.0	N/A	1.63 ^g	N/A	0.23
					53.5	75.3	1.31 ^g	IV/A	0.70
231	Zn Al co-doped CuInS ₂	N/A	1.8×1.8	4.1	82.5	99.1	N/A^h	N/A	N/A
232	N-doped Carbon Dots	N/A	2.0×2.0	2.5	78.4	93.5	$N\!/A^h$	N/A	N/A
163	N-doped Carbon Dots	N/A	2.5×1.6	3.03	77.7	95.6	$N\!/A^h$	N/A	N/A
136	BPEA Down-conversion	85	5.0×1.0	4.17	82.3ª	50.3	N/A^h	N/A	N/A

Table A.1 (cont'd)

References	Luminophore(s)	QY%	Size (cm ²)	G	AVT%	CRI	PCE%	EQE_{LSC}	LUE
136	BPEA Down-conversion PdTPBP Up-Conversion	85 4	5.0×1.0	4.17	68.7ª	42.5	N/Ah	N/A	N/A
233	CdSe@ZnS/ZnS QDs	79-83 (solution)	10.0×9.0	7.9	84.4	89.7	0.337 ^d	N/A	0.284

^a Transmission spectrum was acquired with a reference on the reference side of the double-beam spectrometer, so that there is an 8-10% absolute overestimation in *AVT*. These *AVT* values have been corrected accordingly.

^b Tandem LSC consists of top and bottom sub-LSCs, however, the total transmission spectrum is not provided.

^c Reflector placed behind the test LSC as the backdrop therefore, the AVT and CRI are 0.

^d Optical efficiencies (η_{OPT}) were provided. η_{OPT} is defined as the ratio of the number of emitted photons reaching the waveguide edge to the number of photon incident on the waveguide front surface over the entire solar spectrum. Therefore, the *PCE* of the LSC device is estimated as: $PCE = \eta_{OPT} \times \eta_{PV}^*$, where η_{PV}^* is the efficiency of edge-mounted PV cell under the waveguided and downshifted flux of the luminophore. η_{PV}^* is estimated to be 27.6% assuming the highest commercially available Si PV with 22.5% efficiency illuminated under AM 1.5.9,124

^e Neither *PCE* nor η_{OPT} were provided.

^f This *PCE* value is certified.

^g Area of the edge-mounted PV was used instead of the area of the front surface of the waveguide in *PCE* calculation.

^h Although *PCE* values calculated from *J-V* characteristics were given, the reported J_{SC} values are above the theoretical SQ limits given the bandgaps (even if their EQE_{LSC} of the corresponding absorption range is 100%, which is impossible given the lower quantum yield and waveguiding losses). Reported data is overestimated by 4-10 \times , due to dividing the I_{SC} by the PV area and not the LSC active area.

List of Publications from this Thesis

Research Journals

- 1. <u>Yang, C.</u> & Lunt, R. R.* *et al.* Consensus Statement: Standardized Reporting of Power-Producing Luminescent Solar Concentrator Performance. *Joule* **6**, 1-15 (2022).
- 2. <u>Yang, C.</u>, Barr, M. C. & Lunt, R. R.*. Comprehensive Analysis of Semitransparent and Transparent Luminescent Solar Concentrator Aesthetics. *Physical Review Applied* (Accepted 2022).
- 3. <u>Yang, C.</u> & Lunt, R. R.* Comment on "Upconversion-Assisted Dual-Band Luminescent Solar Concentrator Coupled for High Power Conversion Efficiency Photovoltaic Systems". *ACS Photonics* **8**, 678–681 (2021).
- 4. <u>Yang, C.</u> & Lunt, R. R.* Comment on "An Overview of Various Configurations of Luminescent Solar Concentrators for Photovoltaic Applications". *Optical Mateirals* **112**, 110752 (2021).
- 5. <u>Yang, C.</u>, Lunt, R. R.* *et al.* Ultraviolet and Near-Infrared Dual-Band Selective-Harvesting Transparent Luminescent Solar Concentrators. *Adv. Energy Mater*, 2003581 (2021).
- 6. Zhang, J. Moemeni, M., Yang, C. et al. General Strategy for Tuning the Stokes Shifts of Near Infrared Cyanine Dyes. J. Mater. Chem. C. 8, 16769-16773 (2020)
- 7. Yang, C., Lunt, R. R.* *et al.* High-Performance Near-Infrared Harvesting Transparent Luminescent Solar Concentrators. *Adv. Opt. Mater.* **8**, 1901536 (2020).
- 8. **Yang, C.**, Liu, D., Bates, M., Barr, M. C. & Lunt, R. R.* How to Accurately Report Transparent Solar Cells. *Joule* **3**, 1803–1809 (invited 2019).
- 9. <u>Yang, C.</u>, Liu, D. & Lunt, R. R.* How to Accurately Report Transparent Luminescent Solar Concentrators. *Joule* 3, 2871–2876 (invited 2019).
- 10. Liu, D., <u>Yang, C.</u>, Lunt, R. R.* *et al.* Lead Halide Ultraviolet-Harvesting Transparent Photovoltaics with an Efficiency Exceeding 1%. *ACS Appl. Energy Mater.* **2**, 3972–3978 (2019).
- 11. <u>Yang, C.</u>, Liu, D., Renny, A., Kuttipillai, P. S. & Lunt, R. R.& Integration of near-infrared harvesting transparent luminescent solar concentrators onto arbitrary surfaces. *J. Lumin.* **210**, 239–246 (2019).
- 12. Liu, D., <u>Yang, C.</u>, Bates, M. & Lunt, R. R.* Room temperature processing of inorganic perovskite films to enable flexible solar cells. *iScience* **6**, 272–279 (2018).

- 13. Kuttipillai, P. S., <u>Yang, C.</u>, Lunt, R. R.* *et al.* Enhanced Electroluminescence Efficiency in Metal Halide Nanocluster Based Light Emitting Diodes through Apical Halide Exchange. *ACS Appl. Energy Mater.* **1**, 3587–3592 (2018).
- 14. <u>Yang, C.</u>, Lunt, R. R.* *et al.* Impact of Stokes Shift on the Performance of Near-Infrared Harvesting Transparent Luminescent Solar Concentrators. *Sci. Rep.* **8**, 16359 (2018).
- 15. Liu, D., <u>Yang, C.</u> & Lunt, R. R.* Halide Perovskites for Selective Ultraviolet-Harvesting Transparent Photovoltaics. *Joule* **2**, 1827–1837 (2018).
- 16. Renny, A., <u>Yang, C.</u>, Anthony, R. & Lunt, R. R.* Luminescent solar concentrator paintings: connecting art and energy. *J. Chem. Educ.* **95**, 1161–1166 (2018).
- 17. <u>Yang, C.</u> & Lunt, R. R.* Limits of Visibly Transparent Luminescent Solar Concentrators. *Adv. Opt. Mater.* **5**, 1600851 (2017).
- 18. Herrera, C. K., <u>Yang, C.</u>, Lunt, R. R.* *et al.* Enhanced Lifetime of Near-Infrared-Selective Cyanine Dyes in Transparent Luminescent Solar Concentrators via Counterion Substitution. (in preparation 2022).
- 19. Catarine, H., <u>Yang, C.</u> *et al.* Engineering Tunable Phosphorescent Nanoclusters for Next-generation Imaging and photodynamic Therapy. (in preparation 2022).

Filed Patents

- 1. **Yang, C.**, Lunt, R. R. *et al.* Near-Infrared Harvesting Transparent Luminescent Solar Concentrators with Engineered Stokes Shift. US Patent (Application No. 17053493).
- 2. <u>Yang, C.</u>, Lunt, R. R. *et al.* High Performance Near-Infrared Harvesting Transparent Luminescent Solar Concentrators. US provisional patent (filed in Jan 2020).
- 3. <u>Yang, C.</u> & Lunt, R. R. Transparent Luminescent Solar Concentrator. US provisional patent (filed in Sept 2020).

BIBLIOGRAPHY

BIBLIOGRAPHY

- 1. Green, M. A. *et al.* Solar cell efficiency tables (Version 58). *Prog. Photovoltaics Res. Appl.* **29**, 657–667 (2021).
- 2. Almora, O. *et al.* Device Performance of Emerging Photovoltaic Materials (Version 1). *Adv. Energy Mater.* **11**, 2002774 (2021).
- 3. Traverse, C. J., Pandey, R., Barr, M. C. & Lunt, R. R. Emergence of highly transparent photovoltaics for distributed applications. *Nat. Energy* **2**, 849–860 (2017).
- 4. Lunt, R. R. & Bulovic, V. Transparent, near-infrared organic photovoltaic solar cells for window and energy-scavenging applications. *Appl. Phys. Lett.* **98**, (2011).
- 5. Liu, D., Yang, C. & Lunt, R. R. Halide Perovskites for Selective Ultraviolet-Harvesting Transparent Photovoltaics. *Joule* **2**, 1827–1837 (2018).
- 6. Liu, D. *et al.* Lead Halide Ultraviolet-Harvesting Transparent Photovoltaics with an Efficiency Exceeding 1%. *ACS Appl. Energy Mater.* **2**, 3972–3978 (2019).
- 7. Zhao, Y. & Lunt, R. R. Transparent Luminescent Solar Concentrators for Large-Area Solar Windows Enabled by Massive Stokes-Shift Nanocluster Phosphors. *Adv. Energy Mater.* **3**, 1143–1148 (2013).
- 8. Zhao, Y., Meek, G. A., Levine, B. G. & Lunt, R. R. Near-infrared harvesting transparent luminescent solar concentrators. *Adv. Opt. Mater.* **2**, 606–611 (2014).
- 9. Yang, C. & Lunt, R. R. Limits of Visibly Transparent Luminescent Solar Concentrators. *Adv. Opt. Mater.* **5**, 1600851-n/a (2017).
- 10. Lunt, R. R. Theoretical limits for visibly transparent photovoltaics. *Appl. Phys. Lett.* **101**, 43902 (2012).
- 11. Lunt, R. R., Osedach, T. P., Brown, P. R., Rowehl, J. a. & Bulović, V. Practical roadmap and limits to nanostructured photovoltaics. *Adv. Mater.* **23**, 5712–5727 (2011).
- 12. Yang, C., Liu, D., Bates, M., Barr, M. C. & Lunt, R. R. How to Accurately Report Transparent Solar Cells. *Joule* **3**, 1803–1809 (2019).
- 13. Xue, J., Uchida, S., Rand, B. P. & Forrest, S. R. 4.2% efficient organic photovoltaic cells with low series resistances. *Appl. Phys. Lett.* **84**, 3013–3015 (2004).
- 14. Menke, S. M. & Holmes, R. J. Exciton diffusion in organic photovoltaic cells. *Energy Environ. Sci.* **7**, 499–512 (2014).
- 15. Lunt, R. R., Giebink, N. C., Belak, A. A., Benziger, J. B. & Forrest, S. R. Exciton

- diffusion lengths of organic semiconductor thin films measured by spectrally resolved photoluminescence quenching. *J. Appl. Phys.* **105**, 53711 (2009).
- 16. Feron, K., Belcher, W. J., Fell, C. J. & Dastoor, P. C. Organic Solar Cells: Understanding the Role of Förster Resonance Energy Transfer. *International Journal of Molecular Sciences* vol. 13 (2012).
- 17. Shockley, W. & Queisser, H. J. Detailed Balance Limit of Efficiency of p-n Junction Solar Cells. *J. Appl. Phys.* **32**, 510–519 (1961).
- 18. Richter, A., Hermle, M. & Glunz, S. W. Reassessment of the Limiting Efficiency for Crystalline Silicon Solar Cells. *IEEE J. Photovoltaics* **3**, 1184–1191 (2013).
- 19. Green, M. A. Limits on the open-circuit voltage and efficiency of silicon solar cells imposed by intrinsic Auger processes. *IEEE Trans. Electron Devices* **31**, 671–678 (1984).
- 20. Shiraki, T., Shiraishi, T., Juhász, G. & Nakashima, N. Emergence of new red-shifted carbon nanotube photoluminescence based on proximal doped-site design. *Sci. Rep.* **6**, 28393 (2016).
- 21. Debije, M. G. & Verbunt, P. P. C. Thirty years of luminescent solar concentrator research: Solar energy for the built environment. *Adv. Energy Mater.* **2**, 12–35 (2012).
- 22. Currie, M. J., Mapel, J. K., Heidel, T. D., Goffri, S. & Baldo, M. A. High-Efficiency Organic Solar Concentrators for Photovoltaics. *Science* (80-.). **321**, 226 LP 228 (2008).
- 23. Smestad, G., Ries, H., Winston, R. & Yablonovitch, E. The thermodynamic limits of light concentrators. *Sol. Energy Mater.* **21**, 99–111 (1990).
- 24. Batchelder, J. S., Zewail, A. H. & Cole, T. Luminescent solar concentrators. 2: Experimental and theoretical analysis of their possible efficiencies. *Appl. Opt.* **20**, 3733–3754 (1981).
- 25. Ries, H. Thermodynamic limitations of the concentration of electromagnetic radiation. *J. Opt. Soc. Am.* **72**, 380–385 (1982).
- 26. Goetzberger, A. & Greube, W. Solar energy conversion with fluorescent collectors. *Applied Physics* vol. 14 123–139 (1977).
- 27. Beard, M. C., Johnson, J. C., Luther, J. M. & Nozik, A. J. Multiple exciton generation in quantum dots versus singlet fission in molecular chromophores for solar photon conversion. *Philos. Trans. R. Soc. A Math. Phys. Eng. Sci.* **373**, (2015).
- 28. Nozik, A. J. Multiple exciton generation in semiconductor quantum dots. *Chem. Phys. Lett.* **457**, 3–11 (2008).
- 29. Shpaisman, H., Niitsoo, O., Lubomirsky, I. & Cahen, D. Can up- and down-conversion and multi-exciton generation improve photovoltaics? *Sol. Energy Mater. Sol. Cells* **92**,

- 1541–1546 (2008).
- 30. Binks, D. J. Multiple exciton generation in nanocrystal quantum dots controversy, current status and future prospects. *Phys. Chem. Chem. Phys.* **13**, 12693–12704 (2011).
- 31. Beard, M. C. Multiple Exciton Generation in Semiconductor Quantum Dots. *J. Phys. Chem. Lett.* **2**, 1282–1288 (2011).
- 32. Davis, N. J. L. K. *et al.* Multiple-exciton generation in lead selenide nanorod solar cells with external quantum efficiencies exceeding 120%. *Nat. Commun.* **6**, 8259 (2015).
- 33. Nozik, A. J. *et al.* Semiconductor Quantum Dots and Quantum Dot Arrays and Applications of Multiple Exciton Generation to Third-Generation Photovoltaic Solar Cells. *Chem. Rev.* **110**, 6873–6890 (2010).
- 34. Busby, E. *et al.* A design strategy for intramolecular singlet fission mediated by charge-transfer states in donor–acceptor organic materials. *Nat Mater* **14**, 426–433 (2015).
- 35. Nozik, A. J. Nanoscience and Nanostructures for Photovoltaics and Solar Fuels. *Nano Lett.* **10**, 2735–2741 (2010).
- 36. Zimmerman, P. M., Zhang, Z. & Musgrave, C. B. Singlet fission in pentacene through multi-exciton quantum states. *Nat Chem* **2**, 648–652 (2010).
- 37. Thorsmølle, V. K. *et al.* Morphology Effectively Controls Singlet-Triplet Exciton Relaxation and Charge Transport in Organic Semiconductors. *Phys. Rev. Lett.* **102**, 17401 (2009).
- 38. Smith, M. B. & Michl, J. Singlet Fission. *Chem. Rev.* **110**, 6891–6936 (2010).
- 39. Goetzberger, A. & Wittwer, V. Fluorescent planar collector-concentrators for solar energy conversion BT Festkörperprobleme 19: Plenary Lectures of the Divisions "Semiconductor Physics" "Metal Physics" "Low Temperature Physics" "Thermodynamics and Statistical Physics" "Thin Films" ". in (ed. Treusch, J.) 427–451 (Springer Berlin Heidelberg, 1979). doi:10.1007/BFb0108339.
- 40. El-Shahawy, M. A. & Mansour, A. F. Optical properties of some luminescent solar concentrators. *J. Mater. Sci. Mater. Electron.* **7**, 171–174 (1996).
- 41. Vollmer, F. & Rettig, W. Fluorescence loss mechanism due to large-amplitude motions in derivatives of 2,2'-bipyridyl exhibiting excited-state intramolecular proton transfer and perspectives of luminescence solar concentrators. *J. Photochem. Photobiol. A Chem.* **95**, 143–155 (1996).
- 42. Batchelder, J. S., Zewai, A. H. & Cole, T. Luminescent solar concentrators. 1: Theory of operation and techniques for performance evaluation. *Appl. Opt.* **18**, 3090–3110 (1979).
- 43. Slooff, L. H. *et al.* The luminescent concentrator illuminated. in vol. 6197 61970K-

- 61970K-8 (2006).
- 44. Yang, C. *et al.* Ultraviolet and Near-Infrared Dual-Band Selective-Harvesting Transparent Luminescent Solar Concentrators. *Adv. Energy Mater.* **n/a**, 2003581 (2021).
- 45. Osedach, T. P. *et al.* Near-infrared photodetector consisting of J-aggregating cyanine dye and metal oxide thin films Near-infrared photodetector consisting of J-aggregating cyanine dye and metal oxide thin films. *Applied Physics Letters* vol. 101 113303 (2012).
- 46. Chang, J.-F. *et al.* Process dependence of morphology and microstructure of cyanine dye J-aggregate film: correlation with absorption, photo- and electroluminescence properties. *Opt. Express* **22**, 29388–29397 (2014).
- 47. Supran, G. J. *et al.* QLEDs for displays and solid-state lighting. *MRS Bull.* **38**, 703–711 (2013).
- 48. Saengkerdsub, S., Im, H.-J., Willis, C. & Dai, S. Pechini-type in-situ polymerizable complex (IPC) method applied to the synthesis of Y2O3:Ln (Ln = Ce or Eu) nanocrystallites. *J. Mater. Chem.* **14**, 1207–1211 (2004).
- 49. Ronda, C. R., Jüstel, T. & Nikol, H. Rare earth phosphors: fundamentals and applications. *J. Alloys Compd.* **275–277**, 669–676 (1998).
- 50. Inoue, T., Matsuda, K., Murakami, Y., Maruyama, S. & Kanemitsu, Y. Diameter dependence of exciton-phonon interaction in individual single-walled carbon nanotubes studied by microphotoluminescence spectroscopy. *Phys. Rev. B* **73**, 233401 (2006).
- 51. Raut, H. K., Ganesh, V. A., Nair, A. S. & Ramakrishna, S. Anti-reflective coatings: A critical, in-depth review. *Energy Environ. Sci.* **4**, 3779–3804 (2011).
- 52. Sheppard, C. J. R. Approximate calculation of the reflection coefficient from a stratified medium. *Pure Appl. Opt. J. Eur. Opt. Soc. Part A* **4**, 665 (1995).
- 53. Galagan, Y., Debije, M. G. & Blom, P. W. M. Semitransparent organic solar cells with organic wavelength dependent reflectors. *Appl. Phys. Lett.* **98**, (2011).
- 54. Green, M. A., Emery, K., Hishikawa, Y. & Warta, W. Solar cell efficiency tables (version 36). *Prog. Photovoltaics Res. Appl.* **18**, 346–352 (2010).
- 55. Woei Leow, S. *et al.* Analyzing luminescent solar concentrators with front-facing photovoltaic cells using weighted Monte Carlo ray tracing. *J. Appl. Phys.* **113**, (2013).
- 56. Meinardi, F. *et al.* Large-area luminescent solar concentrators based on / Stokes-shift-engineered/' nanocrystals in a mass-polymerized PMMA matrix. *Nat Phot.* **8**, 392–399 (2014).
- 57. Goldschmidt, J. C. & Fischer, S. Upconversion for Photovoltaics a Review of Materials, Devices and Concepts for Performance Enhancement. *Adv. Opt. Mater.* **3**, 510–535

(2015).

- 58. de Wild, J., Meijerink, A., Rath, J. K., van Sark, W. G. J. H. M. & Schropp, R. E. I. Upconverter solar cells: materials and applications. *Energy Environ. Sci.* **4**, 4835–4848 (2011).
- 59. Tayebjee, M. J. Y., McCamey, D. R. & Schmidt, T. W. Beyond Shockley–Queisser: Molecular Approaches to High-Efficiency Photovoltaics. *J. Phys. Chem. Lett.* **6**, 2367–2378 (2015).
- 60. Jiang, X., Guo, X., Peng, J., Zhao, D. & Ma, Y. Triplet–Triplet Annihilation Photon Upconversion in Polymer Thin Film: Sensitizer Design. *ACS Appl. Mater. Interfaces* **8**, 11441–11449 (2016).
- 61. Wen, S. *et al.* Future and challenges for hybrid upconversion nanosystems. *Nat. Photonics* **13**, 828–838 (2019).
- 62. Ye, C., Gray, V., Mårtensson, J. & Börjesson, K. Annihilation Versus Excimer Formation by the Triplet Pair in Triplet–Triplet Annihilation Photon Upconversion. *J. Am. Chem. Soc.* **141**, 9578–9584 (2019).
- 63. Kroupa, D. M., Roh, J. Y., Milstein, T. J., Creutz, S. E. & Gamelin, D. R. Quantum-Cutting Ytterbium-Doped CsPb(Cl1–xBrx)3 Perovskite Thin Films with Photoluminescence Quantum Yields over 190%. *ACS Energy Lett.* **3**, 2390–2395 (2018).
- 64. Cohen, T. A. *et al.* Quantum-cutting Yb3+-doped perovskite nanocrystals for monolithic bilayer luminescent solar concentrators. *J. Mater. Chem. A* **7**, 9279–9288 (2019).
- 65. Milstein, T. J., Kroupa, D. M. & Gamelin, D. R. Picosecond Quantum Cutting Generates Photoluminescence Quantum Yields Over 100% in Ytterbium-Doped CsPbCl3 Nanocrystals. *Nano Lett.* **18**, 3792–3799 (2018).
- 66. Cai, T. *et al.* Mn2+/Yb3+ Codoped CsPbCl3 Perovskite Nanocrystals with Triple-Wavelength Emission for Luminescent Solar Concentrators. *Adv. Sci.* **7**, 2001317 (2020).
- 67. Zhou, D. *et al.* Cerium and Ytterbium Codoped Halide Perovskite Quantum Dots: A Novel and Efficient Downconverter for Improving the Performance of Silicon Solar Cells. *Adv. Mater.* **29**, 1704149 (2017).
- 68. Kubin, R. F. & Fletcher, A. N. Fluorescence quantum yields of some rhodamine dyes. *J. Lumin.* 27, 455–462 (1982).
- 69. Weber, W. H. & Lambe, J. Luminescent greenhouse collector for solar radiation. *Appl. Opt.* **15**, 2299–2300 (1976).
- 70. Hermann, A. M. Luminescent solar concentrators—A review. *Sol. Energy* **29**, 323–329 (1982).

- 71. Levitt, J. A. & Weber, W. H. Materials for luminescent greenhouse solar collectors. *Appl. Opt.* **16**, 2684–2689 (1977).
- 72. Carrascosa, M., Unamuno, S. & Agullo-Lopez, F. Monte Carlo simulation of the performance of PMMA luminescent solar collectors. *Appl. Opt.* **22**, 3236–3241 (1983).
- 73. Swartz, B. A., Cole, T. & Zewail, A. H. Photon trapping and energy transfer in multiple-dye plastic matrices: an efficient solar-energy concentrator. *Opt. Lett.* **1**, 73–75 (1977).
- 74. Olson, R. W., Loring, R. F. & Fayer, M. D. Luminescent solar concentrators and the reabsorption problem. *Appl. Opt.* **20**, 2934–2940 (1981).
- 75. Kinderman, R. *et al.* I-V Performance and Stability Study of Dyes for Luminescent Plate Concentrators. *J. Sol. Energy Eng.* **129**, 277–282 (2006).
- 76. Baumberg, I. *et al.* Effect of polymer matrix on photo-stability of photo-luminescent dyes in multi-layer polymeric structures. *Polym. Degrad. Stab.* **73**, 403–410 (2001).
- 77. Mansour, A. F., Killa, H. M. A., Abd El-Wanees, S. & El-Sayed, M. Y. Laser dyes doped with poly(ST-Co-MMA) as fluorescent solar collectors and their field performance. *Polym. Test.* **24**, 519–525 (2005).
- 78. Yang, C. *et al.* Impact of Stokes Shift on the Performance of Near-Infrared Harvesting Transparent Luminescent Solar Concentrators. *Sci. Rep.* **8**, 16359 (2018).
- 79. Sanguineti, A. *et al.* High Stokes shift perylene dyes for luminescent solar concentrators. *Chem. Commun.* **49**, 1618–1620 (2013).
- 80. Reisfeld, R. *et al.* A new solid-state tunable laser in the visible. *Chem. Phys. Lett.* **160**, 43–44 (1989).
- 81. Debije, M. G. *et al.* Promising fluorescent dye for solar energy conversion based on a perylene perinone. *Appl. Opt.* **50**, 163–169 (2011).
- 82. Benjamin, W. E. *et al.* Sterically Engineered Perylene Dyes for High Efficiency Oriented Fluorophore Luminescent Solar Concentrators. *Chem. Mater.* **26**, 1291–1293 (2014).
- 83. Sark, W. G. J. H. M. van *et al.* Luminescent Solar Concentrators A review of recent results. *Opt. Express* **16**, 21773–21792 (2008).
- 84. Sanguineti, A. *et al.* NIR emitting ytterbium chelates for colourless luminescent solar concentrators. *Phys. Chem. Chem. Phys.* **14**, 6452–6455 (2012).
- 85. Coropceanu, I. & Bawendi, M. G. Core/Shell Quantum Dot Based Luminescent Solar Concentrators with Reduced Reabsorption and Enhanced Efficiency. *Nano Lett.* **14**, 4097–4101 (2014).
- 86. Erickson, C. S. et al. Zero-Reabsorption Doped-Nanocrystal Luminescent Solar

- Concentrators. ACS Nano 8, 3461–3467 (2014).
- 87. Meinardi, F. *et al.* Highly efficient large-area colourless luminescent solar concentrators using heavy-metal-free colloidal quantum dots. *Nat Nano* **10**, 878–885 (2015).
- 88. Zhao, H. *et al.* Absorption Enhancement in "Giant" Core/Alloyed-Shell Quantum Dots for Luminescent Solar Concentrator. *Small* n/a-n/a (2016) doi:10.1002/smll.201600945.
- 89. Wang, T. *et al.* Luminescent solar concentrator employing rare earth complex with zero self-absorption loss. *Sol. Energy* **85**, 2571–2579 (2011).
- 90. Berends, A. C. *et al.* Radiative and Nonradiative Recombination in CuInS2 Nanocrystals and CuInS2-Based Core/Shell Nanocrystals. *J. Phys. Chem. Lett.* **7**, 3503–3509 (2016).
- 91. Bronstein, N. D. *et al.* Luminescent Solar Concentration with Semiconductor Nanorods and Transfer-Printed Micro-Silicon Solar Cells. *ACS Nano* **8**, 44–53 (2014).
- 92. Li, C. *et al.* Large Stokes Shift and High Efficiency Luminescent Solar Concentrator Incorporated with CuInS2/ZnS Quantum Dots. *Sci. Rep.* **5**, 17777 (2015).
- 93. Chen, D. *et al.* High-Purity, Thick CsPbCl3 Films toward Selective Ultraviolet-Harvesting Visibly Transparent Photovoltaics. *ACS Appl. Energy Mater.* (2021) doi:10.1021/acsaem.1c01649.
- 94. Zhou, Y. *et al.* Near Infrared, Highly Efficient Luminescent Solar Concentrators. *Adv. Energy Mater.* **6**, 1501913-n/a (2016).
- 95. Bradshaw, L. R., Knowles, K. E., McDowall, S. & Gamelin, D. R. Nanocrystals for Luminescent Solar Concentrators. *Nano Lett.* **15**, 1315–1323 (2015).
- 96. Chengelis, D. A., Yingling, A. M., Badger, P. D., Shade, C. M. & Petoud, S. Incorporating Lanthanide Cations with Cadmium Selenide Nanocrystals: A Strategy to Sensitize and Protect Tb(III). *J. Am. Chem. Soc.* **127**, 16752–16753 (2005).
- 97. Reisfeld, R. & Kalisky, Y. Nd3+ and Yb3+ germanate and tellurite glasses for fluorescent solar energy collectors. *Chem. Phys. Lett.* **80**, 178–183 (1981).
- 98. Sun, L.-N. *et al.* Near-infrared luminescent mesoporous materials covalently bonded with ternary lanthanide [Er(III), Nd(III), Yb(III), Sm(III), Pr(III)] complexes. *Microporous Mesoporous Mater.* **98**, 156–165 (2007).
- 99. Zhang, J., Badger, P. D., Geib, S. J. & Petoud, S. Sensitization of Near-Infrared-Emitting Lanthanide Cations in Solution by Tropolonate Ligands. *Angew. Chemie Int. Ed.* **44**, 2508–2512 (2005).
- 100. ten Kate, O. M., Krämer, K. W. & van der Kolk, E. Efficient luminescent solar concentrators based on self-absorption free, Tm2+ doped halides. *Sol. Energy Mater. Sol. Cells* **140**, 115–120 (2015).

- 101. Li, Y. Q. *et al.* Luminescence properties of red-emitting M2Si5N8:Eu2+ (M = Ca, Sr, Ba) LED conversion phosphors. *J. Alloys Compd.* **417**, 273–279 (2006).
- 102. Ye, S., Xiao, F., Pan, Y. X., Ma, Y. Y. & Zhang, Q. Y. Phosphors in phosphor-converted white light-emitting diodes: Recent advances in materials, techniques and properties. *Mater. Sci. Eng. R Reports* **71**, 1–34 (2010).
- 103. de Boer, D. K. G. *et al.* Progress in phosphors and filters for luminescent solar concentrators. *Opt. Express* **20**, A395--A405 (2012).
- 104. Lauret, J.-S. *et al.* Bandgap photoluminescence of semiconducting single-wall carbon nanotubes. *Phys. E Low-dimensional Syst. Nanostructures* **21**, 1057–1060 (2004).
- 105. Lefebvre, J., Homma, Y. & Finnie, P. Bright Band Gap Photoluminescence from Unprocessed Single-Walled Carbon Nanotubes. *Phys. Rev. Lett.* **90**, 217401 (2003).
- 106. Arnold, M. S., Green, A. A., Hulvat, J. F., Stupp, S. I. & Hersam, M. C. Sorting carbon nanotubes by electronic structure using density differentiation. *Nat Nano* **1**, 60–65 (2006).
- 107. Tu, X., Manohar, S., Jagota, A. & Zheng, M. DNA sequence motifs for structure-specific recognition and separation of carbon nanotubes. *Nature* **460**, 250–253 (2009).
- 108. Avouris, P., Freitag, M. & Perebeinos, V. Carbon-nanotube photonics and optoelectronics. *Nat Phot.* **2**, 341–350 (2008).
- 109. Piao, Y. *et al.* Brightening of carbon nanotube photoluminescence through the incorporation of sp3 defects. *Nat Chem* **5**, 840–845 (2013).
- 110. Miyauchi, Y. *et al.* Brightening of excitons in carbon nanotubes on dimensionality modification. *Nat Phot.* **7**, 715–719 (2013).
- 111. Yuan, L. *et al.* Semi-transparent perovskite solar cells: unveiling the trade-off between transparency and efficiency. *J. Mater. Chem. A* **6**, 19696–19702 (2018).
- 112. Liu, F. *et al.* Efficient Semitransparent Solar Cells with High NIR Responsiveness Enabled by a Small-Bandgap Electron Acceptor. *Adv. Mater.* **29**, 1606574 (2017).
- 113. Ubiquitous Energy Certifies New World Record Performance for Transparent Solar Cell https://www.apnews.com/f664cb6090f343369072278345ed4abc. *AP News* (2019).
- 114. Wang, W. *et al.* Fused Hexacyclic Nonfullerene Acceptor with Strong Near-Infrared Absorption for Semitransparent Organic Solar Cells with 9.77% Efficiency. *Adv. Mater.* **29**, 1701308 (2017).
- 115. Zimmermann, E. *et al.* Erroneous efficiency reports harm organic solar cell research. *Nat. Photonics* **8**, 669–672 (2014).
- 116. Snaith, H. J. How should you measure your excitonic solar cells? *Energy Environ. Sci.* 5,

- 6513-6520 (2012).
- 117. Snaith, H. J. The perils of solar cell efficiency measurements. *Nat. Photonics* **6**, 337–340 (2012).
- 118. Shrotriya, V. *et al.* Accurate Measurement and Characterization of Organic Solar Cells. *Adv. Funct. Mater.* **16**, 2016–2023 (2006).
- 119. Finlayson, E. U., Arasteh, D. K., Huizenga, C., Rubin, M. D. & Reilly, M. S. Window 4.0: Documentation of Calculation Procedures. (1993).
- 120. Schubert, E. F. *Light-Emitting Diodes*. (Cambridge University Press, 2006). doi:DOI: 10.1017/CBO9780511790546.
- 121. International Glazing Database. Date accessed 14/05/2014 (2014).
- 122. Xia, R. *et al.* Optical Analysis for Semitransparent Organic Solar Cells. *Sol. RRL* **3**, 1800270 (2019).
- 123. Kawamura, Y., Sasabe, H. & Adachi, C. Simple Accurate System for Measuring Absolute Photoluminescence Quantum Efficiency in Organic Solid-State Thin Films. *Jpn. J. Appl. Phys.* **43**, 7729–7730 (2004).
- 124. Yang, C., Liu, D. & Lunt, R. R. How to Accurately Report Transparent Luminescent Solar Concentrators. *Joule* **3**, 2871–2876 (2019).
- 125. Banal, J. L., Zhang, B., Jones, D. J., Ghiggino, K. P. & Wong, W. W. H. Emissive Molecular Aggregates and Energy Migration in Luminescent Solar Concentrators. *Acc. Chem. Res.* **50**, 49–57 (2017).
- 126. Bergren, M. R. *et al.* High-Performance CuInS2 Quantum Dot Laminated Glass Luminescent Solar Concentrators for Windows. *ACS Energy Lett.* **3**, 520–525 (2018).
- 127. Schubert, E. F. & Kim, J. K. Low-refractive-index materials: A new class of optical thinfilm materials. in 2007 International Conference on Numerical Simulation of Optoelectronic Devices 1–2 (2007). doi:10.1109/NUSOD.2007.4348994.
- 128. Xi, J.-Q. *et al.* Very low-refractive-index optical thin films consisting of an array of SiO2 nanorods. *Opt. Lett.* **31**, 601–603 (2006).
- 129. Luo, X., Ding, T., Liu, X., Liu, Y. & Wu, K. Quantum-Cutting Luminescent Solar Concentrators Using Ytterbium-Doped Perovskite Nanocrystals. *Nano Lett.* **19**, 338–341 (2019).
- 130. Debije, M. G., Verbunt, P. P. C., Rowan, B. C., Richards, B. S. & Hoeks, T. L. Measured surface loss from luminescent solar concentrator waveguides. *Appl. Opt.* **47**, 6763–6768 (2008).

- 131. Li, Z., Ma, T., Yang, H., Lu, L. & Wang, R. Transparent and Colored Solar Photovoltaics for Building Integration. *Sol. RRL* **5**, 2000614 (2021).
- 132. ISO 14782:1999.
- 133. ASTM D1003 13.
- 134. Yang, C. & Lunt, R. R. Comment on "Upconversion-Assisted Dual-Band Luminescent Solar Concentrator Coupled for High Power Conversion Efficiency Photovoltaic Systems". *ACS Photonics* **8**, 678–681 (2021).
- 135. Kim, K., Nam, S. K., Cho, J. & Moon, J. H. Photon upconversion-assisted dual-band luminescence solar concentrators coupled with perovskite solar cells for highly efficient semi-transparent photovoltaic systems. *Nanoscale* **12**, 12426–12431 (2020).
- 136. Ha, S.-J. *et al.* Upconversion-Assisted Dual-Band Luminescent Solar Concentrator Coupled for High Power Conversion Efficiency Photovoltaic Systems. *ACS Photonics* **5**, 3621–3627 (2018).
- 137. Vossen, F. M., Aarts, M. P. J. & Debije, M. G. Visual performance of red luminescent solar concentrating windows in an office environment. *Energy Build.* **113**, 123–132 (2016).
- 138. Reinders, A., Kishore, R., Slooff, L. & Eggink, W. Luminescent solar concentrator photovoltaic designs. *Jpn. J. Appl. Phys.* **57**, 08RD10 (2018).
- 139. Schiphorst, J. ter *et al.* Printed luminescent solar concentrators: Artistic renewable energy. *Energy Build.* **207**, 109625 (2020).
- 140. Kanellis, M., de Jong, M. M., Slooff, L. & Debije, M. G. The solar noise barrier project: 1. Effect of incident light orientation on the performance of a large-scale luminescent solar concentrator noise barrier. *Renew. Energy* **103**, 647–652 (2017).
- 141. Debije, M. G., Evans, R. C. & Griffini, G. Laboratory protocols for measuring and reporting the performance of luminescent solar concentrators. *Energy Environ. Sci.* **14**, 293–301 (2021).
- 142. Renny, A., Yang, C., Anthony, R. & Lunt, R. R. Luminescent solar concentrator paintings: connecting art and energy. *J. Chem. Educ.* **95**, 1161–1166 (2018).
- 143. Yang, C., Liu, D., Renny, A., Kuttipillai, P. S. & Lunt, R. R. Integration of near-infrared harvesting transparent luminescent solar concentrators onto arbitrary surfaces. *J. Lumin.* **210**, 239–246 (2019).
- 144. Walheim, S., Schäffer, E., Mlynek, J. & Steiner, U. Nanophase-Separated Polymer Films as High-Performance Antireflection Coatings. *Science* (80-.). **283**, 520 LP 522 (1999).
- 145. Groh, W. & Zimmermann, A. What is the lowest refractive index of an organic polymer?

- Macromolecules 24, 6660–6663 (1991).
- 146. Sydlik, S. A., Chen, Z. & Swager, T. M. Triptycene Polyimides: Soluble Polymers with High Thermal Stability and Low Refractive Indices. *Macromolecules* **44**, 976–980 (2011).
- 147. Xi, J.-Q. *et al.* Optical thin-film materials with low refractive index for broadband elimination of Fresnel reflection. *Nat. Photonics* **1**, 176 (2007).
- 148. Xi, J.-Q., Kim, J. K. & Schubert, E. F. Silica Nanorod-Array Films with Very Low Refractive Indices. *Nano Lett.* **5**, 1385–1387 (2005).
- 149. Yan, X. *et al.* Enhanced Omnidirectional Photovoltaic Performance of Solar Cells Using Multiple-Discrete-Layer Tailored- and Low-Refractive Index Anti-Reflection Coatings. *Adv. Funct. Mater.* **23**, 583–590 (2012).
- 150. Guillemot, F. *et al.* Latex-Templated Silica Films: Tailoring Porosity to Get a Stable Low-Refractive Index. *Chem. Mater.* **22**, 2822–2828 (2010).
- 151. Xi, J.-Q. *et al.* Omnidirectional reflector using nanoporous SiO2 as a low-refractive-index material. *Opt. Lett.* **30**, 1518–1520 (2005).
- 152. Falcaro, P., Grosso, D., Amenitsch, H. & Innocenzi, P. Silica Orthorhombic Mesostructured Films with Low Refractive Index and High Thermal Stability. *J. Phys. Chem. B* **108**, 10942–10948 (2004).
- 153. Schubert, M. F., Xi, J.-Q., Kim, J. K. & Schubert, E. F. Distributed Bragg reflector consisting of high- and low-refractive-index thin film layers made of the same material. *Appl. Phys. Lett.* **90**, 141115 (2007).
- 154. Xu, L. *et al.* Enhanced Photon Collection in Luminescent Solar Concentrators with Distributed Bragg Reflectors. *ACS Photonics* **3**, 278–285 (2016).
- 155. You, N.-H., Higashihara, T., Oishi, Y., Ando, S. & Ueda, M. Highly Refractive Poly(phenylene thioether) Containing Triazine Unit. *Macromolecules* **43**, 4613–4615 (2010).
- 156. Liu, J. & Ueda, M. High refractive index polymers: fundamental research and practical applications. *J. Mater. Chem.* **19**, 8907–8919 (2009).
- 157. Badur, T., Dams, C. & Hampp, N. High Refractive Index Polymers by Design. *Macromolecules* **51**, 4220–4228 (2018).
- 158. Griebel, J. J. *et al.* New Infrared Transmitting Material via Inverse Vulcanization of Elemental Sulfur to Prepare High Refractive Index Polymers. *Adv. Mater.* **26**, 3014–3018 (2014).
- 159. Higashihara, T. & Ueda, M. Recent Progress in High Refractive Index Polymers. *Macromolecules* **48**, 1915–1929 (2015).

- 160. Javadi, A., Shockravi, A., Rafieimanesh, A., Malek, A. & Ando, S. Synthesis and structure–property relationships of novel thiazole-containing poly(amide imide)s with high refractive indices and low birefringences. *Polym. Int.* **64**, 486–495 (2014).
- 161. Okutsu, R., Suzuki, Y., Ando, S. & Ueda, M. Poly(thioether sulfone) with High Refractive Index and High Abbe's Number. *Macromolecules* **41**, 6165–6168 (2008).
- 162. Zhang, J. *et al.* General Strategy for Tuning the Stokes Shifts of Near Infrared Cyanine Dyes. *J. Mater. Chem. C* (2020) doi:10.1039/D0TC03615C.
- 163. Li, Y., Miao, P., Zhou, W., Gong, X. & Zhao, X. N-doped carbon-dots for luminescent solar concentrators. *J. Mater. Chem. A* **5**, 21452–21459 (2017).
- 164. Sharma, M. *et al.* Near-Unity Emitting Copper-Doped Colloidal Semiconductor Quantum Wells for Luminescent Solar Concentrators. *Adv. Mater.* **29**, 1700821-n/a (2017).
- 165. Coropceanu, I. & Bawendi, M. Core/Shell Quantum Dot Based Luminescent Solar Concentrators with Reduced Reabsorption and Enhanced Efficiency. *Nano Lett.* (2014) doi:10.1021/nl501627e.
- 166. Knowles, K. E., Kilburn, T. B., Alzate, D. G., McDowall, S. & Gamelin, D. R. Bright CuInS2/CdS nanocrystal phosphors for high-gain full-spectrum luminescent solar concentrators. *Chem. Commun.* **51**, 9129–9132 (2015).
- 167. Sheng, X. *et al.* Silicon-Based Visible-Blind Ultraviolet Detection and Imaging Using Down-Shifting Luminophores. *Adv. Opt. Mater.* **2**, 314–319 (2014).
- 168. Kuttipillai, P. S. *et al.* Phosphorescent Nanocluster Light-Emitting Diodes. *Adv. Mater.* **28**, 320–326 (2016).
- 169. Sokolov, M. N. *et al.* Highly luminescent complexes [Mo6X8(n-C3F7COO)6]2- (X = Br, I). *Dalt. Trans.* **40**, 6375–6377 (2011).
- 170. Banal, J. L., White, J. M., Ghiggino, K. P. & Wong, W. W. H. Concentrating aggregation-induced fluorescence in planar waveguides: A proof-of-principle. *Sci. Rep.* **4**, 4635 (2014).
- 171. Banal, J. L. *et al.* Energy Migration in Organic Solar Concentrators with a Molecularly Insulated Perylene Diimide. *J. Phys. Chem. C* **120**, 12952–12958 (2016).
- 172. Zhang, B. *et al.* Highly Fluorescent Molecularly Insulated Perylene Diimides: Effect of Concentration on Photophysical Properties. *Chem. Mater.* **29**, 8395–8403 (2017).
- 173. Giebink, N. C., Wiederrecht, G. P. & Wasielewski, M. R. Resonance-shifting to circumvent reabsorption loss in luminescent solar concentrators. *Nat. Photonics* **5**, 694–701 (2011).
- 174. Ufimtsev, I. S. & Martinez, T. J. Quantum Chemistry on Graphical Processing Units. 3.

- Analytical Energy Gradients, Geometry Optimization, and First Principles Molecular Dynamics. *J. Chem. Theory Comput.* **5**, 2619–2628 (2009).
- 175. Isborn, C. M., Luehr, N., Ufimtsev, I. S. & Martínez, T. J. Excited-State Electronic Structure with Configuration Interaction Singles and Tamm–Dancoff Time-Dependent Density Functional Theory on Graphical Processing Units. *J. Chem. Theory Comput.* 7, 1814–1823 (2011).
- 176. Titov, A. V, Ufimtsev, I. S., Luehr, N. & Martinez, T. J. Generating Efficient Quantum Chemistry Codes for Novel Architectures. *J. Chem. Theory Comput.* **9**, 213–221 (2013).
- 177. Kästner, J. *et al.* DL-FIND: An Open-Source Geometry Optimizer for Atomistic Simulations. *J. Phys. Chem. A* **113**, 11856–11865 (2009).
- 178. Yanai, T., Tew, D. P. & Handy, N. C. A new hybrid exchange–correlation functional using the Coulomb-attenuating method (CAM-B3LYP). *Chem. Phys. Lett.* **393**, 51–57 (2004).
- 179. Le Guennic, B. & Jacquemin, D. Taking Up the Cyanine Challenge with Quantum Tools. *Acc. Chem. Res.* **48**, 530–537 (2015).
- 180. Towns, J. *et al.* XSEDE: Accelerating scientific discovery. *Computing in Science and Engineering* vol. 16 62–74 (2014).
- 181. Peng, X. *et al.* Heptamethine Cyanine Dyes with a Large Stokes Shift and Strong Fluorescence: A Paradigm for Excited-State Intramolecular Charge Transfer. *J. Am. Chem. Soc.* **127**, 4170–4171 (2005).
- 182. Dewar, M. J. S. 478. Colour and constitution. Part I. Basic dyes. *J. Chem. Soc.* 2329–2334 (1950) doi:10.1039/JR9500002329.
- 183. Knott, E. B. 227. The colour of organic compounds. Part I. A general colour rule. *J. Chem. Soc.* 1024–1028 (1951) doi:10.1039/JR9510001024.
- 184. Olsen, S. A quantitative quantum chemical model of the Dewar–Knott color rule for cationic diarylmethanes. *Chem. Phys. Lett.* **532**, 106–109 (2012).
- 185. Traverse, C. J., Chen, P. & Lunt, R. R. Lifetime of Organic Salt Photovoltaics. *Adv. Energy Mater.* **8**, 1703678 (2018).
- 186. Xiao, Z. *et al.* 26 mA cm⁻² Jsc from organic solar cells with a low-bandgap nonfullerene acceptor. *Sci. Bull.* **62**, 1494–1496 (2017).
- 187. Meng, L. *et al.* Organic and solution-processed tandem solar cells with 17.3% efficiency. *Science* (80-.). **361**, 1094–1098 (2018).
- 188. Yang, C. *et al.* High-Performance Near-Infrared Harvesting Transparent Luminescent Solar Concentrators. *Adv. Opt. Mater.* **8**, 1901536 (2020).

- 189. Li, H., Wu, K., Lim, J., Song, H.-J. & Klimov, V. I. Doctor-blade deposition of quantum dots onto standard window glass for low-loss large-area luminescent solar concentrators. *Nat. Energy* **1**, 16157 (2016).
- 190. Rondão, R. *et al.* High-Performance Near-Infrared Luminescent Solar Concentrators. *ACS Appl. Mater. Interfaces* **9**, 12540–12546 (2017).
- 191. Lunt, R. R. Theoretical limits for visibly transparent photovoltaics. *Applied Physics Letters* vol. 101 (2012).
- 192. Slooff, L. H. *et al.* A Luminescent Solar Concentrator with 7.1% power conversion efficiency. *Phys. Status Solidi Rapid Res. Lett.* **2**, 257–259 (2008).
- 193. Liu, C. & Li, B. Multiple dyes containing luminescent solar concentrators with enhanced absorption and efficiency. *J. Opt.* **17**, 25901 (2015).
- 194. Liu, G., Zhao, H., Diao, F., Ling, Z. & Wang, Y. Stable tandem luminescent solar concentrators based on CdSe/CdS quantum dots and carbon dots. *J. Mater. Chem. C* 6, 10059–10066 (2018).
- 195. Mateen, F. *et al.* Tandem structured luminescent solar concentrator based on inorganic carbon quantum dots and organic dyes. *Sol. Energy* **190**, 488–494 (2019).
- 196. Wu, K., Li, H. & Klimov, V. I. Tandem luminescent solar concentrators based on engineered quantum dots. *Nat. Photonics* **12**, 105–110 (2018).
- 197. Zhou, Y. *et al.* Colloidal carbon dots based highly stable luminescent solar concentrators. *Nano Energy* **44**, 378–387 (2018).
- 198. Ma, W. *et al.* Carbon dots and AIE molecules for highly efficient tandem luminescent solar concentrators. *Chem. Commun.* **55**, 7486–7489 (2019).
- 199. Desmet, L., Ras, A. J. M., de Boer, D. K. G. & Debije, M. G. Monocrystalline silicon photovoltaic luminescent solar concentrator with 4.2% power conversion efficiency. *Opt. Lett.* **37**, 3087–3089 (2012).
- 200. Zhao, H. *et al.* Efficient and stable tandem luminescent solar concentrators based on carbon dots and perovskite quantum dots. *Nano Energy* **50**, 756–765 (2018).
- 201. Currie, M. J., Mapel, J. K., Heidel, T. D., Goffri, S. & Baldo, M. A. High-efficiency organic solar concentrators for photovoltaics. *Science* (80-.). **321**, 226–228 (2008).
- 202. Zhang, B. *et al.* Aggregation-induced emission-mediated spectral downconversion in luminescent solar concentrators. *Mater. Chem. Front.* **2**, 615–619 (2018).
- 203. Goetzberger, A. & Greube, W. Solar energy conversion with fluorescent collectors. *Appl. Phys.* **14**, 123–139 (1977).

- 204. Giebink, N. C., Wiederrecht, G. P. & Wasielewski, M. R. Resonance-shifting to circumvent reabsorption loss in luminescent solar concentrators. *Nat. Photonics* **5**, 694 (2011).
- 205. Kirakci, K. *et al.* A Highly Luminescent Hexanuclear Molybdenum Cluster A Promising Candidate toward Photoactive Materials. *Eur. J. Inorg. Chem.* **2012**, 3107–3111 (2012).
- 206. Kuttipillai, P. S. *et al.* Enhanced Electroluminescence Efficiency in Metal Halide Nanocluster Based Light Emitting Diodes through Apical Halide Exchange. *ACS Appl. Energy Mater.* **1**, 3587–3592 (2018).
- 207. Neaime, C. *et al.* Time-gated luminescence bioimaging with new luminescent nanocolloids based on [Mo6I8(C2F5COO)6]2– metal atom clusters. *Phys. Chem. Chem. Phys.* **18**, 30166–30173 (2016).
- 208. Wang, J. *et al.* Effect of Isomerization on High-Performance Nonfullerene Electron Acceptors. *J. Am. Chem. Soc.* **140**, 9140–9147 (2018).
- 209. Sarma, T., Panda, P. K. & Setsune, J. Bis-naphthobipyrrolylmethene derived BODIPY complex: an intense near-infrared fluorescent dye. *Chem. Commun.* **49**, 9806–9808 (2013).
- 210. Khenkin, M. V *et al.* Consensus statement for stability assessment and reporting for perovskite photovoltaics based on ISOS procedures. *Nat. Energy* **5**, 35–49 (2020).
- 211. Schubert, E. F., Kim, J. K. & Xi, J.-Q. Low-refractive-index materials: A new class of optical thin-film materials. *Phys. status solidi* **244**, 3002–3008 (2007).
- 212. Saito, N. *et al.* Lattice and Valence Electronic Structures of Crystalline Octahedral Molybdenum Halide Clusters-Based Compounds, Cs2[Mo6X14] (X = Cl, Br, I), Studied by Density Functional Theory Calculations. *Inorg. Chem.* **56**, 6234–6243 (2017).
- 213. Riehl, L., Ströbele, M., Enseling, D., Jüstel, T. & Meyer, H.-J. Molecular Oxygen Modulated Luminescence of an Octahedro-hexamolybdenum Iodide Cluster having Six Apical Thiocyanate Ligands. *Zeitschrift für Anorg. und Allg. Chemie* **642**, 403–408 (2016).
- 214. Chen, W. *et al.* A Semitransparent Inorganic Perovskite Film for Overcoming Ultraviolet Light Instability of Organic Solar Cells and Achieving 14.03% Efficiency. *Adv. Mater.* **30**, 1800855 (2018).
- 215. Brzeczek-Szafran, A., Richards, C. J., Lopez, V. M., Wagner, P. & Nattestad, A. Aesthetically Pleasing, Visible Light Transmissive, Luminescent Solar Concentrators Using a BODIPY Derivative. *Phys. status solidi* **215**, 1800551 (2018).
- 216. Lee, K. *et al.* Neutral-Colored Transparent Crystalline Silicon Photovoltaics. *Joule* **4**, 235–246 (2020).

- 217. Papakonstantinou, I., Portnoi, M. & Debije, M. G. The Hidden Potential of Luminescent Solar Concentrators. *Adv. Energy Mater.* **11**, 2002883 (2021).
- 218. Yan, X. *et al.* Enhanced Omnidirectional Photovoltaic Performance of Solar Cells Using Multiple-Discrete-Layer Tailored- and Low-Refractive Index Anti-Reflection Coatings. *Adv. Funct. Mater.* **23**, 583–590 (2013).
- 219. Zhao, H., Zhou, Y., Benetti, D., Ma, D. & Rosei, F. Perovskite quantum dots integrated in large-area luminescent solar concentrators. *Nano Energy* **37**, 214–223 (2017).
- 220. Liu, D., Yang, C., Bates, M. & Lunt, R. R. Room temperature processing of inorganic perovskite films to enable flexible solar cells. *iScience* **6**, 272–279 (2018).
- 221. Ravishankar, E. *et al.* Achieving Net Zero Energy Greenhouses by Integrating Semitransparent Organic Solar Cells. *Joule* **4**, 490–506 (2020).
- 222. Corrado, C. *et al.* Power generation study of luminescent solar concentrator greenhouse. *J. Renew. Sustain. Energy* **8**, 43502 (2016).
- 223. Broadwater, D., Medeiros, H. C. D., Lunt, R. R. & Lunt, S. Y. Current Advances in Photoactive Agents for Cancer Imaging and Therapy. *Annu. Rev. Biomed. Eng.* **23**, 29–60 (2021).
- 224. Broadwater, D. *et al.* Modulating cellular cytotoxicity and phototoxicity of fluorescent organic salts through counterion pairing. *Sci. Rep.* **9**, 15288 (2019).
- 225. Yang, C. *et al.* Consensus statement: Standardized reporting of power-producing luminescent solar concentrator performance. *Joule* **6**, 8–15 (2022).
- 226. Meinardi, F. *et al.* Highly efficient luminescent solar concentrators based on earthabundant indirect-bandgap silicon quantum dots. *Nat. Photonics* **11**, 177 (2017).
- 227. Meinardi, F. *et al.* Highly efficient large-area colourless luminescent solar concentrators using heavy-metal-free colloidal quantum dots. *Nat. Nanotechnol.* **10**, 878–885 (2015).
- 228. Sumner, R. *et al.* Analysis of Optical Losses in High-Efficiency CuInS2-Based Nanocrystal Luminescent Solar Concentrators: Balancing Absorption versus Scattering. *J. Phys. Chem. C* **121**, 3252–3260 (2017).
- 229. Zhang, B. *et al.* High-Performance Large-Area Luminescence Solar Concentrator Incorporating a Donor–Emitter Fluorophore System. *ACS Energy Lett.* 1839–1844 (2019) doi:10.1021/acsenergylett.9b01224.
- 230. Krumer, Z., van Sark, W. G. J. H. M., Schropp, R. E. I. & de Mello Donegá, C. Compensation of self-absorption losses in luminescent solar concentrators by increasing luminophore concentration. *Sol. Energy Mater. Sol. Cells* **167**, 133–139 (2017).
- 231. Zhu, M. et al. Deep-red emitting zinc and aluminium co-doped copper indium sulfide

- quantum dots for luminescent solar concentrators. *J. Colloid Interface Sci.* **534**, 509–517 (2019).
- 232. Gong, X. *et al.* Fabrication of high-performance luminescent solar concentrators using N-doped carbon dots/PMMA mixed matrix slab. *Org. Electron.* **63**, 237–243 (2018).
- 233. Brennan, L. J. *et al.* Large area quantum dot luminescent solar concentrators for use with dye-sensitised solar cells. *J. Mater. Chem. A* **6**, 2671–2680 (2018).